LBL-31035

Lawrence Berkeley Laboratory

UNIVERSITY OF CALIFORNIA

EARTH SCIENCES DIVISION

Array Analysis of Regional Pn and Pg Wavefields from the Nevada Test Site

M.A. Leonard
(Ph.D. Thesis)

June 1991

LOAN COPY
Circulates
for 4 weeks
Bldg. 50 Library.
Copy 2
LBL-31035

Prepared for the U.S. Department of Energy under Contract Number DE-AC03-76SF00098

DISCLAIMER

This document was prepared as an account of work sponsored by the United States Government. While this document is believed to contain correct information, neither the United States Government nor any agency thereof, nor the Regents of the University of California, nor any of their employees, makes any warranty, express or implied, or assumes any legal responsibility for the accuracy, completeness, or usefulness of any information, apparatus, product, or process disclosed, or represents that its use would not infringe privately owned rights. Reference herein to any specific commercial product, process, or service by its trade name, trademark, manufacturer, or otherwise, does not necessarily constitute or imply its endorsement, recommendation, or favoring by the United States Government or any agency thereof, or the Regents of the University of California. The views and opinions of authors expressed herein do not necessarily state or reflect those of the United States Government or any agency thereof or the Regents of the University of California.

LBL-31035

Array Analysis of Regional Pn and Pg Wavefields from the Nevada Test Site

Michael Allen Leonard
Ph.D. Thesis

Department of Geology and Geophysics
University of California

and

Center for Computational Seismology
Earth Sciences Division
Lawrence Berkeley Laboratory
University of California
Berkeley, CA 94720

June 1991

This work was supported by the Institute of Global Conflict and Cooperation Fellowship from the University of California, by the Defense Advanced Research Projects Agency monitored by the Air Force Geophysics Laboratory under Contract No. F19628-89-K-0017, and by the Director, Office of Basic Energy Sciences, Division of Engineering, Mathematics and Geosciences, of the U.S. Department of Energy under Contract No. . DE-AC03-76SF00098.

Copyright © 1991 by Michael Allen Leonard

The United States Department of Energy has the right to use this thesis
for any purpose whatsoever, including the right to reproduce all or any part thereof.

Array Analysis of Regional Pn and Pg Wavefields from the Nevada Test Site

Michael Allen Leonard

ABSTRACT

Small-aperture high-frequency seismic arrays with dimensions of a few kilometers or less, can improve our ability to seismically monitor compliance with a low-yield Threshold Test Ban Treaty. This work studies the characteristics and effectiveness of array processing of the regional Pn and Pg wavefields generated by underground nuclear explosions at the Nevada Test Site. Waveform data from the explosion HARDIN (m_b = 5.5) is recorded at a temporary 12-element, 3-component, 1.5 km-aperture array sited in an area of northern Nevada. The explosions VILLE (m_b = 4.4) and SALUT (m_b = 5.5) are recorded at two arrays sited in the Mojave desert, one a 96-element vertical-component 7 km-aperture array and the other a 155-element vertical-component 4 km-aperture array.

Within the aperture of each array spectral amplitudes vary significantly among sensors, with differences of a factor of 10 over 4 km typical. Among the mean spectra for the m_b = 5.5 events there are significant differences in low-frequency spectral amplitudes between array sites, reflecting the relative site effects. However, the spectra become nearly identical beyond about 6 Hz. Spectral ratios are used to briefly examine seismic source properties and the partitioning of energy between Pn and Pg.

Frequency-wavenumber analysis at the 12-element array is used to obtain estimates of signal gain, phase velocity, and source azimuth. This analysis reveals frequency-dependent biases in velocity and azimuth of the coherent Pn and Pg arrivals. Incoherent scattering occurs after a little over one second into the Pn wavefield and throughout the Pg wavefield. The lack of signal correlation on the horizontal components severely limits the utility of 3-component processing.

The principal factor governing array performance is signal correlation, and it is examined here in terms of spatial coherence estimates. The coherence is found to vary between the three

sites. In all cases the coherence of Pn is greater than that for Pg. The coherence estimates are used to construct spatially-continuous frequency-dependent models of cross-spectra, which can be used to simulate array processing performance for arbitrary sensor configurations. Simulations are used to rank the three locations in terms of their potential as regional monitoring array sites.

Lane R. Johnson

Lane Johnson

Dissertation Committee Chair

for Terri

You are the cream in my coffee,

and the sugar of my life

Acknowledgements

This dissertation represents the culmination of a 12-year college career. To acknowledge all those who were significant and encouraged me along the way might take me another 12. Therefore I'll restrict myself to only the most notable.

I am most grateful to Professor Lane Johnson, my committee chairman, for his financial support, his expertise, and his eternal patience as I found my way. He will always have my respect. I also thank Lane's charming wife Dotty for her delectable Journal Club desserts and overall affability. Professor Tom McEvilly served as a vivacious example of a scientist who enjoys his work, and I guess he's pretty smart too. His insight is always helpful. I appreciate the support of both Lane and Tom with my decision to pursue a career in science education.

I benefited greatly from courses taught by Professor Bruce Bolt and enjoyed our collaboration, along with Nick Gregor, on the educational seismology video. Many thanks to Russell Sell, John Friday, and Marvin Hilger at the Seismographic Station for their lessons on the operation of seismic recording equipment. I especially thank Russ for his expertise and companionship during my field work at Kaiser Quarry. Norm Abrahamson and Bob Darragh were very obliging in their time spent with me discussing signal processing.

I am indebted to the California Consortium for Crustal Studies (CALCRUST) for the use of the Savahia Mountain and Rice Valley data sets, without which much of this study would not have been possible. I thank Dave Okaya for his help with this data.

This research was supported by the Defense Advanced Research Projects Agency and was monitored by the Air Force Geophysics Laboratory under Contract F19628-89-K-0017 and by the Director of Basic Energy Sciences, Division of Engineering, Mathematics and Geosciences, of the U.S. Department of Energy under contract DE-AC03-76SF00098. Two years of support came from an Institute of Global Conflict and Cooperation (IGCC) Fellowship from the University of California. All computations were carried out at the Center for Computational Seismology, Lawrence Berkeley Laboratory.

With her devotion and support, my wife and best friend Terri made what could have been a rather grueling last month of graduate school into one that I will remember fondly as we worked and dined side by side.

Lastly, I would like to thank Edgar Alan Poe, who, through his poem "The Raven", has given me a vehicle to now address those friends I have thus far neglected:

Seven Years Now Hence

Once upon a midnight dreary, while I pondered, weak and weary,
Over many a quaint and curious volume of seismologic lore -
As I sat, my attention wandered, my brain bemused, my thoughts soon pondered
The sweatshirt I had that day laundered, and the symbol that it bore;
For in blue and gold nostalgic was "CAL", my alma mater dear of yore.
It was a sweatshirt I often wore.

Ah, distinctly I remember it was in the bleak September;
Of many I was just one member, the first-year students of '84.
Not a fool I stayed in school, the Ph.D. a precious jewel;
A treasured gem buried deep within a massive ore.
I was young, but not forever. How long, how long to dig the ore?
0 years down, just 7 more.

Presently my mind grew stronger; hesitating then no longer,
'Lane', said I, 'or Tom, your attention, I implore';
For the fact is I was learning, my mental soul within me burning,
Newfound knowledge I was yearning, novel concepts to explore -
Deep I looked through many doors.

Now all these smarts are fine and dandy; with P waves I am very handy;
With S waves I am often randy, but in grad life there is something more.
I speak, of course, of friends befriended; time together spent so splendid;
Times I wish had never ended, but times by now that are no more -
I'll hold these dear forever more.

I write these lines, seven years now hence, to do for me that which makes sense;
To tell my friends, with no pretense, their company I did adore.
Beginning now I'll get specific; I'll speak of friends I found terrific,
Wish peace to those I found pacific, not one of them a single bore -
Much I should have said before.

Long ago was Johnny Schiener, nary a gent you'll find much finer;
My memories of old Flint's Diner - barbecue ribs, please give me more.
And Dan the Man, who liked to putt;
2 am and putt, putt, putt; putting in and out the door.
Look out there Dan! Uh-oh, Fore!

Dave would rarely miss a game, (PROLIX was his wordy name),
And I am surely glad I came to know him and the smile he wore.
And John was such a friendly type, so calm and cool, so little hype;
For me he was an archetype, his feet placed firmly on the floor -
Though shoes on them he seldom wore.

Ann Kirkpatrick – so much fun, golfing in the noonday sun,
Rafting down a river run, bowling when our brains were sore.
Was Fred a friend? The answer yes; we got the bomb from NTS;
I miss him too, I must confess, his manner, and a good deal more.
Our time in Ruby Valley is a time I still pine for.

Phil I met in '83 – a genial kindhearted man was he,
That saddened I was when he left this place, drifted to the Aussie shore.
Don, I'm glad, sits by my side, and love for friends he does not hide,
And neither does his lovely bride, the bride I know he does adore –
She'll be glad forever more.

Joel's a friend who knows no fear, a man yet gentle, kind, sincere;
Soon to wed with Stacey, I wish them love forever more.
Jay and I began together, a prince, a friend – in any weather;
For him in life I see no tether. He can open any door.
Enjoy, you three, what life has store.

Bill is not your typical lad, and I don't think I've ever had
A friend so giving of himself; it's part of what he's living for.
Alberto is a friend I'll toast, a smart man, though he'd never boast,
And what a charming dinner host; his kindness – it exudes, outpours.
These Euro-friends give more, and more.

I know there's no refuting the lovely time I had commuting,
With Miss Ann Becker driving, I stepped fondly in her door.
And I think that I will always know how good a friend I had in Chiou;
I will miss him when he goes, parting for the Taiwan shore –
'Till then I hope to see him more.

If you're feeling down and low, talk with Ernie – soon you'll know
That here you've got a friend who's laugh's contagious, and your spirits soar.
Overflows with warmth, compassion, does Janet in her friendly fashion,
Time with me she did not ration – latte, please, and pastries more.
With Kathryn and Lizzy these two make four.

There's other too in SOE – Eleni, Tom, and Rich are three
Who make working here a pleasure, more so than it was before.
As gregarious a man you'll never find, Shimon is the loquacious kind,
And his is a creative mind; work for him is not a chore –
I wish for him success, and more.

Dahlia's is a lovely face, her presence helps define this place,
Her character is silk and lace – as pretty as the clothes she wore.
Andre and Pat are also here, time with them is full of cheer;
To both I'd gladly raise a beer to wish them joy forever more.
Staffers, three, I do adore.

Here the head of sciences earth – Tom McEvilly, a man of mirth,
He often makes us think in ways we've never thought before.
I also know a gent urbane, I speak of course of he called Lane.
His faith in me did never wane; this I'd like to thank him for.

So now it's over, I've got my jewel, but still I can be found in school
Teaching kids the countless rules of science – and a good deal more.
I thank again those mentioned here. My gratitude is quite sincere,
and I find that now I shed a tear for the comradeship in days of yore –
I've learned from you what friends are for.

Table of Contents

Chapter 1: Introduction 1
1.1 Background on Nuclear Testing 1
1.2 Regional Seismic Monitoring 5
1.3 Regional Arrays 7

Chapter 2: Regional Data Sets 11
2.1 Introduction 11
2.2 Recording Sites 11
2.3 Explosions SALUT and VILLE 14
2.3.1 Pn Array Recordings 15
2.3.2 Pg Array Recordings 16
2.4 Explosion HARDIN 17
2.4.1 Pn Array recordings 18
2.4.2 Pg Array recordings 18

Chapter 3: Spectral Amplitude Characteristics 45
3.1 Introduction 45
3.2 Spectra at Savahia Mountain and Ruby Valley 46
3.2.1 Pn Spectra 46
3.2.2 Pg Spectra 48
3.3 Spectra at Ruby Valley 49
3.3.1 Pn Spectra 50
3.3.2 Pg Spectra 51
3.4 Pg/Pn spectral Ratios 52
3.4.1 Savahia Mountain and Rice Valley 53

3.4.2 Ruby Valley 54
3.5 VILLE/SALUT Spectral Ratios 55
3.6 Summary Discussion 59

Chapter 4: Pn and Pg Propagation Characteristics at the Ruby Valley Array 83
4.1 Introduction 83
4.2 Array Power Estimation 84
4.3 Pn Wavefield 88
4.3.1 Signal Correlation 89
4.3.2 Phase Velocity and Source Azimuth 90
4.3.3 Slowness Stacking 92
4.4 Pg Wavefield 94
4.4.1 Signal Correlation 95
4.4.2 Phase Velocity and Source Azimuth 96
4.4.3 Slowness Stacking 97
4.5 Summary Discussion 98

Chapter 5: Spatial Coherence of Pn and Pg 123
5.1 Introduction 123
5.2 Coherence Estimation and Modeling Procedure 124
5.3 Pn coherence 129
5.4 Pg coherence 132
5.5 Modeling Array Gain 134
5.5.1 Pn Array Gain 134
5.5.2 Pg Array Gain 137
5.5.3 Array Gain Simulations 139
5.6 Summary Discussion 140

Chapter 6: Recommendations 179

References 183

Appendix A: Spectral Amplitude Estimation 189
Appendix B: Bandpass Filtering Example of a Regional Waveform 209
Appendix C: Coherence Estimation and Statistics 213
Appendix D: Estimates of $\tanh^{-1}|\gamma|$ Used in Chapter 5 Inversions 223

Chapter 1

Introduction

This dissertation addresses seismic monitoring of underground nuclear weapons testing. Specifically, the focus here is on array analysis of high-frequency regional seismic data from nuclear weapons tests conducted at the Nevada Test Site. Before introducing the technical aspects of this research, some background information is provided on nuclear testing. More complete background can be found in Bolt (1976), Dahlman & Israelson (1977), and U.S. Congress (1988).

1.1 Background on Nuclear Testing

There are currently five countries in the world with acknowledged nuclear weapons capability. They are the United States, the Soviet Union, Great Britain, China, and France. Each of these countries maintains a nuclear testing program. In the United States nuclear weapons testing takes place almost exclusively at the Nevada Test Site (NTS) in southwest Nevada. The majority of these tests are conducted for the purposes of weapons development: 75% to 80% of the nuclear tests conducted each year contribute to the engineering of specific new warheads or new weapons systems. The remaining tests are conducted to determine the survivability of military systems under the effects of nuclear explosions, to improve the understanding of the physical phenomena associated with nuclear explosions, and to ensure that existing weapons systems are working correctly. It has been argued that continued nuclear testing is required for national security and to enhance the effectiveness of nuclear deterrence. However, these arguments have been in question for more than thirty years, since the beginning of negotiations toward a Comprehensive Test Ban Treaty (CTBT), banning all nuclear testing. There was at that time, and still is, a great concern that the continued development of more powerful and sophisticated nuclear weapons systems through continued testing can increase both the

likelihood and the destructive power of a nuclear war. Today, despite extensive negotiations and a great deal of progress, a Comprehensive Test Ban Treaty has not yet been achieved.

Efforts were made by the United States, Britain, and the Soviet Union between 1958 and 1963 to achieve a CTBT, however, ostensibly because of disagreements on verification procedures, no such treaty was achieved. These parties instead produced the 1963 Limited Test Ban Treaty (LTBT), which banned testing in the atmosphere, in outer space, and under water, but placed no limit on the size, or yield, of nuclear tests. This treaty greatly reduced the danger of radioactive fallout and has since been signed by over 100 countries, though China and France are not currently among them. The Nuclear Non-Proliferation Treaty (NPT) of 1970 has served as a deterrent to conducting nuclear weapons testing of any kind. Non-nuclear weapons countries who are party to this treaty (there are currently 138) pledge not to use nuclear energy for the purpose of weapons development. The treaty further states that the three weapon states that are party to the treaty, the United States, Britain, and the Soviet Union, are to work toward nuclear disarmament and a discontinuance of nuclear testing. The two other declared nuclear-weapon states of China and France have not signed this treaty. In 1995 the NPT will be examined to decide to what extent to reform, strengthen, or expand it. Yield limits were finally placed on nuclear tests by the 1974 Threshold Test Ban Treaty (TTBT), which bans underground tests by the United States and Soviet Union having an explosive yield greater than 150 kilotons (kt). The 1976 Peaceful Nuclear Explosions Treaty (PNET) restricts individual peaceful nuclear explosions by the United States and the Soviet Union (for engineering and demolition purposes) to yields also no greater that 150 kt. (One kt represents 1000 tons of TNT, or about a million sticks of dynamite. The yield of the bombs dropped on Japan in World War II was about 13 kt.) To date, the Threshold Test Ban and Peaceful Nuclear Explosion Treaties have not been ratified, though both parties have apparently abided by the set regulations.

In the late 1970's, during the Carter administration, a good deal of progress was made in the tri-lateral negotiations for a comprehensive test ban between the United States, Britain, and

the Soviet Union. However a setback to the furthering of these negotiations, and to U.S.-Soviet relations in general, came in July 1982, when the Reagan Administration announced that the United States was withdrawing from efforts to ban all nuclear tests. The principal reason given was that further development of U.S. nuclear weapons systems was required to ensure the stability of nuclear deterrence. An additional reason was the feeling that the Soviets had cheated on the 1974 TTBT by exceeding 150 kt with a number of explosions. This has been countered by many seismologists, who find that this claim was based on a misinterpretation of seismic data (e.g., Sykes and Davis, 1987). Also significant was the Administration's lack of faith in the verifiability of a CTBT. An important point to make here is that, practically speaking, technical verification of a CTBT cannot be achieved; verification measurements from very, very small explosions, will either be within the noise of the measurements, or the uncertainty in identification and yield estimation will be so large as to make the measurements meaningless. Instead, one should think of a CTBT as a low-yield TTBT with the maximum allowable yield set below that required for militarily significant weapons tests, but not so low as to present significant verification uncertainties. Notice, then, that the two primary factors controlling the threshold level, the yields of militarily significant tests and the allowable degree of uncertainty, are ultimately based upon political, not technical, judgements. It is generally accepted among seismologists that, using seismic methods, compliance with a low-yield TTBT can be successfully monitored, with the maximum allowable yield set between about 10 kt and 15 kt, and quite possibly lower depending on the distance of the monitoring network to the testing area (U.S. Congress, 1988).

Despite the absence of formal negotiations, beginning in August of 1985 and extending for 19 months, the Soviet Union observed a unilateral moratorium on nuclear testing. The United States, however, declined the offer to join the moratorium. In May of 1986 another significant event occurred when the Natural Resources Defense Council, an environmental organization, and the Soviet Academy of Sciences signed an agreement to establish jointly-manned seismic monitoring stations near the the principal testing areas in each country (see

Berger *et al.*, 1987). The success of this venture in the very sensitive area of arms control came as a welcome surprise to many, and may well set a precedent for future private actions on publicly, though not necessarily politically, supported international issues. Finally in September of 1987, with much improvement in U.S.-Soviet relations and under great political and public pressure, a joint U.S.-Soviet statement was issued on the resumption of negotiations on the limitations of nuclear testing. The first goal was to ratify the TTBT and PNET, which required agreement on effective verification measures. Towards this end, unprecedented experiments have taken place in which U.S. and Soviet scientists have visited each others' testing sites and cooperated in a collection and exchange of test-monitoring data (e.g., Priestley *et al.*, 1990). It now appears that ratification of the Threshold Test Ban and Peaceful Nuclear Explosion Treaties is imminent.

The future of a Comprehensive Test Ban is much less certain. During the 1990 review of the NPT a large amount of pressure was applied to the nuclear weapon states by many non-weapon states to bring a halt to nuclear testing (Epstein, 1991). Though the Soviet Union claims it is willing to do so, the United States and Britain currently remain committed to testing programs and regard a CTBT as a long-term objective. Neither China or France is party to the NPT and their role in a future CTBT is unknown. An additional concern are the six other countries with advanced nuclear programs: India, Argentina, Brazil, South Africa, Pakistan, and Israel. Though all currently deny any nuclear-weapon intentions, none are part of the PNT. These countries are however bound to the 1963 PTBT, and if current efforts by some non-aligned nations towards amending the 1963 PTBT into a CBTB are eventually successful, these nuclear nations may find themselves party to a CTBT by default.

In the mean time, seismologists are continuing research to improve, and so further establish, the ability of seismic networks to monitor compliance with a low-yield testing treaty. This is still a fairly young area of research, and much remains to be done. Some general background information on low-yield seismic monitoring is given below. A more complete overview can be found in U.S. Congress (1988).

1.2 Regional Seismic Monitoring

When one considers that a buried nuclear explosion will generate waves in the earth much in the same way as an earthquake, it is not surprising that the science of seismology has provided the principal means for monitoring underground nuclear explosions. A seismic monitoring system has three primary tasks: (1) to detect that a seismic event has taken place, (2) to discriminate, i.e., to identify that seismic event as either a nuclear explosion or something else, such as an earthquake or mining explosion, and (3) if it is a nuclear test, to determine whether the size of the explosion exceeds that allowed by the prevailing nuclear test ban treaty. A great advantage of seismic measurements is that they can be made well outside of the immediate testing area. Other so-called "on-site" monitoring techniques exist, such as radiochemical and hydrodynamical methods, but these methods are much more intrusive and so are inherently more difficult to negotiate into a treaty. To date, U.S. and Soviet compliance with the 1974 TTBT has been successfully monitored through the use of teleseismic measurements made around the world. To reliably monitor a treaty in which the maximum allowable explosive size is in the range of say 1-10 kt, much less than the 150 kt currently allowed by the TTBT, seismic recordings must be made much closer to the testing sites, at so called regional distances, i.e., at distances less than about 2000 kilometers, and new seismic discrimination methods must be employed.

In addition to placing seismic stations at regional distances to monitor low-yield explosions, it is advantageous to measure the high frequencies of ground motion. This is because (1) for small-magnitude events the signal to noise ratio typically increases with increasing frequency, before eventually dropping back to very low values, (2) the most likely way to hide a weapons test is by placing the explosion in a large cavity, which muffles the explosion, reducing the amount of ground motion produced at seismic monitoring stations; however, theory predicts (e.g., Evernden *et al.*, 1986) and observations have confirmed (Garbin, 1986; Glen *et al.*, 1987) that the amount of muffling is reduced greatly for high frequencies of ground motion, and (3) potentially useful methods may exist to discriminate weapons tests from non-

weapons related seismic sources, such as earthquakes and mining blasts, based on differences in relative frequency content at high frequencies of ground motion (see references below).

The most important regional phases are referred to as the Pn, Pg, Sn, and Lg waves. Figure 1 is an example of high-frequency waveform data from NTS being used in this study.

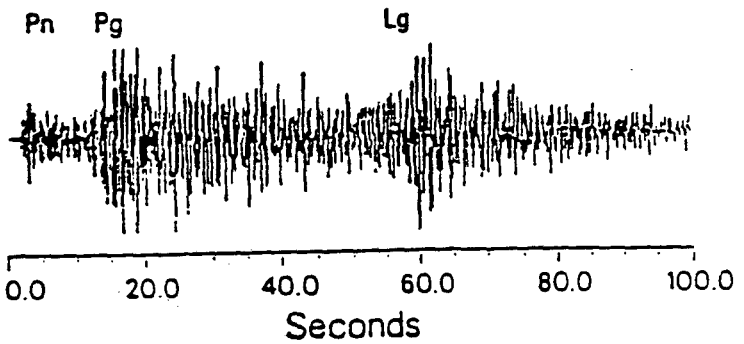

FIGURE 1: Example of a regional high-frequency seismic recording.

Regional wavefields are influenced very much by the regional characteristics of the crustal structure through which they propagate. This is why, for example, Sn is not a prominent phase in the tectonically active western U.S., but it is in the more geologically stable eastern U.S. and other shield-like environments. Notice that regional phases do not correspond to discrete arrivals. They consist instead of a train of arrivals lasting from a few to tens of seconds. Beyond a cross-over distance of about 100-200 km, depending on the crustal thickness, Pn is the first arriving wavetrain. Its phase velocity of between about 7.6 and 8.4 km/sec, depending on the regional area, indicates that Pn derives from critically refracted energy traveling along or just below the Mohorovicic discontinuity. Multiple reflections due to crustal layering will continuously feed energy into Pn refractions and so prolong the duration of the wavetrain. Additionally there are indications that much of the Pn coda, and in fact the coda of the other

regional phases as well, is derived from scattering of the wavefields (e.g., Baumgardt, 1990, Dainty and Toksoz, 1990, this study). Pg is a crustal wave, arriving after Pn beyond the cross-over distance. Its apparent velocity is typical of crustal P velocities. P-SV reflections due to crustal layering contribute to the prolonged and complex structure of Pg. Lg is regarded as being made up of multiply-reflected post-critical S waves, and has phase velocities typical of crustal S velocities. Lg is usually the largest amplitude arrival of the regional phases and it shows great promise as a reliable estimator of explosive yield (Nuttli 1986, Hansen *et al.*, 1990). All of the regional phases show promise as effective discriminants, though again because of their sensitivity to variations in crustal structure, the effectiveness of many discriminants is region, or even site, specific. The subject of regional discriminants will not be pursued in this study, but further information can be found in Nuttli (1981), Pomeroy *et al.*, (1982), Evernden *et al.*, (1986), Bennet and Murphy (1986), Pulli and Dysart (1987), Taylor *et al.*, (1988), Taylor *et al.*, (1989), Bennet *et al.*, (1989), and Baumgardt and Young (1990).

1.3 Regional Arrays

Below is some background on seismic arrays and a brief discussion of the motivation behind this study. More detailed discussions will be found in the ensuing chapters. The fundamental point here is that low-yield monitoring capability can be significantly enhanced through the use of arrays of instruments at regional monitoring sites. Seismic arrays have a number of advantages over single instruments for the purposes of monitoring low-magnitude seismic events. By applying various signal processing methods to array data, improved detection capability of a monitoring site can be achieved. Specifically, array processing methods can be used to increase the amplitude of seismic signals relative to the background noise. Therefore, an array can potentially detect much smaller events than can a single-instrument site. In addition, there a number of ways in which an array can improve discrimination and yield-estimation capability. For example, as we can seen in Figure 1.1, a regional waveform contains different types of seismic waves, traveling along different paths through the earth to

arrive at the recording site. Seismic discrimination and yield estimates require that the regional wave type be known; this becomes more difficult as the signal amplitude decreases relative to the background noise level, as it would for very low-magnitude events. However, the propagation velocity of the different wave types across the earth's surface differ, and with an array this velocity can be measured. Therefore, the wave type can be identified by its velocity and the appropriate spectral discriminate and yield measure can be applied. Secondly, array processing methods can also be used to estimate the epicentral location of seismic sources, much more reliably than a single three-component monitoring site. A reliable estimate of location alone can be a very useful discriminate if the geographic areas of weapons testing and earthquake and mining activity are known. This location ability is especially important if the event is so small that it is recorded at only one or two monitoring sites, thus making network location impossible. Additionally, estimation of seismic source type through the use of discriminants, and estimation of source size will be statistically more reliable given the greater number of recordings and lowered noise levels that can be achieved through array processing. Arrays also provide a more detailed sampling of the wavefield and so allows us to better understand the nature and extent of propagation effects which tend to obscure the source-related information by distorting and randomizing the wavefield.

These kinds of advantages in monitoring became apparent over twenty years ago with large aperture arrays such as LASA in Montana (525 short-period seismometers over an aperture of 200 km) and NORSAR in Norway (132 short-period seismometers over an aperture of 100 km). The large-aperture for these arrays is appropriate for teleseismic monitoring, however much smaller apertures on the order of a few kilometers are required to sustain the signal correlation required for successful regional high-frequency array processing. Serious work into the development of regional arrays began in 1979 with the NORESS array, located in the Baltic Shield in southern Norway. This array supports a 25-sensor geometry over an aperture of 3 km. The Noress array was later complemented by the near-identical ARCESS array in northern Norway in 1987, the 15-element 2-km aperture FINESA array in southern Finland in 1985, and

the 25-element 4-km aperture GRESS array in the Bavarian Forest area of Germany in 1990.

To date, the bulk of the work done in high-frequency seismic array processing has been done on data recorded at the Scandanavian arrays. These arrays are located on a geologic shield, which is thought to represent the best propagation environment for high-frequency waves. In the tectonically active western United States the crustal structure is profoundly different, and one should therefore expect significantly different high-frequency signal characteristics for a regional array monitoring underground weapons tests from the Nevada Test Site. However, little work has been done to study the performance characteristics of high-frequency regional arrays within areas like the Basin and Range. Given this lack of information this study was undertaken, wherein we will examine the array performance characteristics of the Pn and Pg wavefields at three distinct array sites located at regional distances from the Nevada Test Site. Research of this kind is required for optimally designing future high-frequency arrays in similar geologic settings, and for studies which attempt to estimate the overall monitoring capability of a hypothetical network of seismic arrays located in the western United States.

In this study we will find that working against effective array processing are complications and irregularities in the geologic structure which can scatter and distort the wave field, causing less than optimal signal enhancement, atypical propagation velocities, mislocations of the source epicenter, and therefore degraded detection and discrimination capability. These geologic irregularities can exist on a variety of scales, from the very local structure surrounding the array site, such as hills and valleys, to more deep-seated structural variations extending tens of kilometers into the earth's crust. Much of this dissertation will be concerned with the extent and manner in which the wavefields are distorted and randomized at the array sites. We will begin in Chapter 2 with a description and brief discussion of the regional data sets used in this study. In Chapter 3 will be an analysis of how spectral amplitude estimates vary over the aperture of the arrays and between the different array locations. An appreciation and understanding of the sensitivity of spectral amplitude estimates to changes in receiver location is

important given their use as regional source discriminants and yield measures. Also in Chapter 3 we will examine briefly the division of energy between Pn and Pg and indirectly compare two explosions to a simple explosive source model. In Chapter 4 we will focus in on one array having a design similar to that of the NORESS-type arrays, but again, located in a very different environment. We will examine the Pn and Pg signal correlation and propagation characteristics at this array and suggest relationships to local site effects and scattering. A more detailed signal correlation analysis follows in chapter 5, where we will study the spatial and frequency dependence of intersensor wavefield coherence at each of the three array sites. The coherence is parameterized and used to simulate array processing characteristics for arbitrary array configurations. Chapter 6 offers recommendations based on the findings of this study. Four appendices (A through D) are also included. Appendices A and C describe and explore the advantages of the spectral estimation method used for amplitude spectra and coherence. Appendix B displays an example of the relative frequency content of regional phases through bandpass filtering. And finally, Appendix D displays the coherence data analyzed in Chapter 5.

Chapter 2

Regional Data Sets

2.1 Introduction

In this chapter we will first describe the recording sites and recording system parameters used in this study. Next the Pn and Pg regional wavefield data will be displayed with brief comments on waveform differences due to differences in recording location, source parameters, and wavetype. More detailed analyses of spectral characteristics and coherence structure will follow in subsequent chapters. All the wavefields displayed were recorded at nearly the same epicentral distance, between 340 km and 387 km.

2.2 Recording Sites

Three temporary arrays sited in the Basin and Range province of the western U.S. are included in this study. Each array recorded explosions from the Nevada Test Site. The configurations of the array sites and the location of the arrays relative to the recorded explosions are shown in Figure 2.1. We will also look briefly at data from one explosion recorded at a permanently-installed regional instrument site operated by Lawrence Livermore National Laboratory (LLNL). Receiver and source specifications are given in Tables 1 and 2, respectively.

The Savahia Mountain array and the Rice Valley array were deployed in the Mojave Desert of southern California as part of a CALCRUST (California Consortium for Crustal Studies) crustal exploration survey. The Savahia Mountain array consisted of 145 vertical-component stations. The intersensor spacing at this array site was 25 meters. The maximum difference in station elevation was 69 meters. The Rice Valley array consisted of 96 vertical-component stations. The intersensor spacing at this array site was 100 meters. The maximum

difference in station elevation here was 59 meters.

Descriptions of the geology and tectonic evolution of the area surrounding the Mojave Desert arrays can be found in Davis *et al.* (1982, 1988), Howard and John (1987), a number of studies contained in Coward *et al.* (1987), and Wang *et al.* (1989). A geologic map of this area is shown in Figure 2.2 (after Howard and John, 1987). The area shown is dominated by extensional fault systems which resulted in the formation of many of the mountain ranges. The Savahia Mountain array was sited near Savahia Mountain, between the Turtle Mountains to the west and the Whipple Mountains to the east. The Rice Valley array was sited within Rice Valley, which lies at the southern base of the Turtle Mountains. The difference in elevation between each array site and the surrounding mountains is nominally between about 400 and 1000 meters.

Advance notice of detonation times allowed these two arrays to record the two NTS explosions SALUT ($m_b = 5.5$) and VILLE ($m_b = 4.4$). SALUT was detonated at a depth of 608 meters in the Pahute Mesa area of NTS, 371 km and 385 km to the north of the Savahia Mountain and Rice Valley arrays, respectively. VILLE was detonated at a depth of 293 meters in the Yucca Valley area of NTS, 340 km and 355 km to the north of the Savahia Mountain and Rice Valley arrays, respectively. These two explosions were separated by a distance of 40 km. The system response at these two arrays was flat to velocity from approximately 9 Hz up to the 12-pole anti-alias filter at 62.5 Hz. The normalized amplitude response to velocity at these, and the other, instrument sites is shown in Figure 2.3. Not shown in Figure 2.3 for these two arrays is a notch filter applied at 60 Hz. The data were sampled at 250 samples per second. The two arrays were separated by a distance of about 35 km. The large number of instruments and peculiar configurations make the Savahia Mountain and Rice Valley arrays unlikely models for future low-yield TTBT recording system configurations. However, the dense spatial sampling of these two arrays will allow us to study regional wavefield characteristics in detail.

The Ruby Valley array was a temporary 12-station, three-component array with an aperture of 1.5 km. The array was designed in the same manner as the NORESS array, that is, stations placed in concentric rings at log-periodic intervals in radius (Kværna, 1989). However the aperture of this array is half that of NORESS. This array was located in the Basin and Range province in northern Nevada within Ruby Valley, approximately 54 km southeast of the city of Elko, Nevada. Descriptions and analyses of the geology surrounding this area are given by Snoke (1980) and Howard (1980). A regional geologic map of the area is shown in Figure 2.4 (after Snoke, 1980). Immediately to the west of the array site lie the northern Ruby Mountains, which represent one of a number of metamorphic complexes mapped in this region. These mountains rise approximately 1400 meters in elevation above the array site. There was no significant change in station elevation across the array. The array recorded the explosion HARDIN (m_b = 5.5), detonated at a depth of 625 m in the Pahute Mesa area of the Nevada Test Site, 387 km to the south of the array. The system response at this array site was flat to velocity from approximately 5 Hz up to the 5-pole anti-alias filter at 50 Hz (see Figure 2.3). The data were sampled at 200 samples per second. The Ruby Valley array, with its small number of three-component high-frequency instruments spread over 1.5 km, may be representative of future recording system configurations emplaced to monitor nuclear test sites at regional distances.

The explosion HARDIN was also recorded by the LLNL station ELKO (lat.= 40.745, long.= -115.239) located approximately 15 km to the northwest of the Ruby Valley array at a hard rock site at the base of the Ruby Mountains. The system response at this site is flat to velocity between approximately 0.05 Hz and 10 Hz and was sampled at a rate of 40 samples per second. Referring to Figure 2.3, the LLNL response is essentially a low pass filter of velocity ground motion relative to the array site, which is effectively a high pass filter. The siting of the Ruby Valley array near this LLNL station was intentional. The seismic path from NTS to Ruby Valley is a well recorded one and the ELKO station is the quietest of the LLNL regional network (Rodgers and Rohrer, 1987).

2.3 Explosions SALUT and VILLE

We'll begin by displaying the SALUT and VILLE Pn and Pg wavefields recorded at the Savahia Mountain and Rice Valley arrays. Though we will be analyzing only the first few seconds of these wavefields in the later chapters, we will nevertheless display them here in their entirety. Keep in mind that because the Savahia and Rice arrays recorded the same sources, any differences in wavefield between the arrays for either SALUT or VILLE is due only to the slight differences in propagation path arising from the 35 km separation of the arrays and, perhaps more significantly, to differences in the geologic structure surrounding the arrays. Conversely, any differences between SALUT and VILLE for either array site are due to differences in the seismic source and the difference in propagation path arising from the 40 km separation between the two explosions. These comparisons will be further quantified in the spectral analysis which follows in Chapter 3.

Before focusing in on the Pn array recordings, refer to Figure 2.5, which shows typical recordings of both the Pn and Pg wavetrains at the Savahia Mountain and Rice Valley arrays. Contrasting explosions, there are two noticeable differences. First is the somewhat lower quality of the VILLE data. Due to recording difficulties, the first couple seconds of the VILLE Pn wavefield were not recorded at Savahia. Also, the signal to noise ratio is lower for this smaller yield explosion; the Pn arrival is only barely visible above the noise at Rice Valley. Secondly, the time to maximum Pg amplitude from the time of the Pg arrival differs between events. For example, at Rice Valley the SALUT Pg wavetrain increases to its peak amplitude in about two seconds, while for VILLE the time is doubled, to about four seconds. This behavior is similar for the Savahia Mountain recordings and may be a result of differences in source properties and/or slight differences in propagation path. Contrasting recording sites, the principal difference appears to be that the duration of relatively large amplitudes is greater at Savahia for both the Pn and Pg waves. For example, at Rice the SALUT Pg wave decays from its peak amplitude to a fairly constant background level in about 8 seconds, while at Savahia Pg is still above the background level after 15 seconds. Also, the peak amplitudes are somewhat greater

at Savahia, particularly for VILLE. These figures suggest significant amplification and possibly greater scattering effects at Savahia Mountain relative to Rice Valley.

2.3.1 Pn Array Recordings

The complete SALUT Pn wavefield recorded at Savahia is shown in Figure 2.6. The figure also includes the onset of Pg. Three more Pn waveform panels like this will follow, followed by four similar panels for Pg in section 2.3.2. In all cases the waveform data are displayed as recorded; no processing has been done other than trace alignment. The traces have been aligned using the known source azimuth and reduction velocities of 8 km/sec for Pn and 6 km/sec for Pg. Also, for visual clarity, each of the panels has been scaled differently in amplitude. True relative amplitudes can be inferred from Figure 2.5. The trace separation in Figure 2.6 is 25 meters, the greatest station separation being about 4 km. All 145 recordings are shown. Note that there is a ten-station break in recordings beyond station #96. The onset of Pn is at about 0.8 seconds and Pg near 10 seconds in the figure. The Pn onset is soon followed by a coherent, larger amplitude arrival approximately 0.5 seconds later. This arrival is more prominently displayed in Figure 2.7, which shows typical recordings of the first 4 seconds of the SALUT Pn wave at the Savahia and Rice arrays. Based on the near-surface velocity at Pahute Mesa (Leonard and Johnson, 1987), this secondary arrival occurs near the predicted time for pPn. Alternatively, Doombos and Kvæma (1987), examining a group of mining explosions in Norway, have interpreted delayed and prolonged regional Pn energy of this kind as due to scattering by topographic relief of the Moho. Therefore, care must be taken not to mistake possibly Moho scattered energy as due to pPn, as this would result in erroneous estimates of source depth, which is an important parameter in seismic discrimination. The advantage of an array here is that the phase velocity of this delayed arrival can be measured, and if it differs significantly from that for Pn then Moho scattering may be indicated.

The SALUT Pn and early Pg wavefields at Rice Valley are shown in Figure 2.8. Here the trace separation is 100 meters, four times the trace separation at Savahia. Stations #17 and

#49 through #96 did not properly record the SALUT wavefield and so are omitted from the figure. Here the maximum separation of displayed waveforms is again about 4 km. The onset of Pn is at about 0.5 seconds in the figure, again quickly followed by coherent, larger amplitude ground motion. The onset of Pg is near 11 seconds; notice that relative to the SALUT recordings at Savahia, the Pg wavefield at Rice is much more emergent (see also Fig. 2.5). Also notice in Figure 2.7 the relative difference in frequency content between the array sites, indicating a relative site effect between the two.

The VILLE Pn and early Pg wavefields at Savahia Mountain are shown in Figure 2.9. The onset of Pn is absent due to late recording, but would have occurred near 1.0 seconds in the figure. The VILLE Pn and early Pg wavefields at Rice Valley are shown in Figure 2.10. Here 94 of the 96 stations recorded useful data and the maximum waveform separation is about 7 km. The onset of Pn is just barely discernible at about 0.5 seconds. The amplitudes of Pn are quite variable across the array. A pocket of relatively large Pn amplitude is apparent in the lower left of Figure 2.10.

2.3.2 Pg Array Recordings

The first 17 seconds of the SALUT Pg wavefield at Savahia is shown in Figure 2.11. Only the first 96 recordings are shown; the remaining 49 recordings display similar characteristics and have been omitted from the figure for clarity. As is true for all of the following Pg panels, the first two seconds of the Pg waveforms shown overlap with approximately the last two seconds of data displayed in the corresponding previous Pn data panel, with changes in amplitude scale, and are aligned using a reduction velocity of 6 km/sec. Beyond about three seconds in Figure 2.11, the Pg wavefield becomes quite complex and maintains significant amplitudes well into the wavetrain. Relative to Pn, Pg appears to be richer in low-frequency energy. The Salut Pg wavefield at Rice Valley, shown in Figure 2.12, is also quite complex, though as noted in Figure 2.5, it decays in amplitude faster than at Savahia. Like Pn, Pg at Rice Valley appears to lack low-frequency energy relative to Savahia Mountain.

The first 96 VILLE Pg waveforms recorded at Savahia are shown in Figure 2.13. Again, the remaining recordings display similar characteristics and have been omitted from the figure for clarity. This wavefield appears similar in its complexity to the SALUT Pg wavefield in Figure 2.11 (note that Figure 2.13 is normalized to a lower amplitude scale than Figure 2.11). The VILLE Pg wavefield at Rice Valley is shown in Figure 2.14. Notice that the high-amplitude pocket we saw for the Pn wavefield is also visible for the Pg wavefield between about two and six seconds in Figure 2.14, suggesting a similar site effect.

2.4 Explosion HARDIN

As described earlier, the explosion HARDIN ($m_b = 5.5$) was recorded by the Ruby Valley array. Recall that the LLNL ELKO station, located 15 km away, also recorded this event. The three-component recordings of HARDIN at the LLNL station are shown in Figure 2.15. The regional phases Pn, Pg, Lg and longer period surface waves are evident on these recordings. A typical 3-component recording of HARDIN at the Ruby Valley array is shown in Figure 2.16. Because of the different instrument response, the longer period surface waves are not visible at the array site. As at the LLNL Elko station, Pg and Lg are of comparable amplitude.

Both the LLNL ELKO site and the array site recorded significant transverse motion, presumably generated by scattering and multipathing. The array recording shows a strong amplification of the horizontal ground motion relative to the LLNL site. The amplification at the array site is most likely due to the fact that the array is a soft rock site and its position in the center of the valley makes it more susceptible to complicating resonance and interference effects resulting from the boundaries of the valley. These differences attest to the strong sensitivity of regional wavefields on local site effects. Similar basin amplification effects on regional phases have been observed and modeled by Barker *et al.* (1981).

2.4.1 Pn Array Recordings

For reference, the configuration of the Ruby Valley array is shown expanded in Figure 2.17 with station numbers indicated. The first four seconds of the vertical, radial, and transverse components of the Pn wavefield at all twelve stations are shown in Figures 2.18a, 2.18b, and 2.18c respectively. Station numbers are given to the left of the figure. The waveforms are manually aligned on the early arrivals on the the vertical component and the resulting array beam is shown at the bottom. The LLNL Elko recording is also included for comparison; it has been convolved with the instrument response at Ruby Valley to facilitate comparison. The first motion of Pn at the array takes place at about 0.2 seconds in the figure and has very low amplitude. Like the recordings of SALUT and VILLE discussed earlier, we see a larger arrival about 0.5 seconds after the first motion, near the expected pPn arrival time. The waveforms have been roughly grouped by similarity to more clearly show an interesting variation in amplitude, namely that there is a gradual attenuation of amplitude moving towards the eastern side of the array. This effect will be examined further in subsequent chapters. The first 1.5 seconds or so of Pn ground motion at the array site is predominantly vertical, unlike the LLNL recording, which has significant radial ground motion. This difference is likely a consequence of a higher velocity gradient within the low-velocity valley sediments beneath the array site. Beyond about 1.5 seconds at the array is an onset of increased radial and transverse ground motion. The low-amplitude array beams indicate that either this motion is incoherent, and is therefore due to random scattering, or is actually coherent but has a much different phase velocity, as would be the case for multipathing. This also will be explored in the following chapters.

2.4.2 Pg Array Recordings

The early portions of the Pg wavefield recorded at all twelve stations at the array site are shown in Figures 2.19a, 2.19b, 2.19c for the vertical, radial, and transverse components, respectively. Here there is no obvious grouping so the waveforms are simply ordered

sequentially by station number. This time window corresponds to the 10 to 20 second window in Figure 2.16. The waveforms have been aligned along the known source-to-receiver azimuth using a reducing velocity of 6 km/sec. The onset of Pg is at about 1.6 seconds in the figure. These waveforms are plotted to a different scale than the Pn waveforms shown earlier. The relative difference in scale can be inferred from Figure 2.16 which shows Pg having a peak amplitude about two times greater than Pn on the horizontal components. Of the three components, the superposition of the vertical displays the most constructive interference, as was the case for Pn. However, for all components the degree of overlap among the waveforms is not great, as reflected in the low amplitude of the waveform beams.

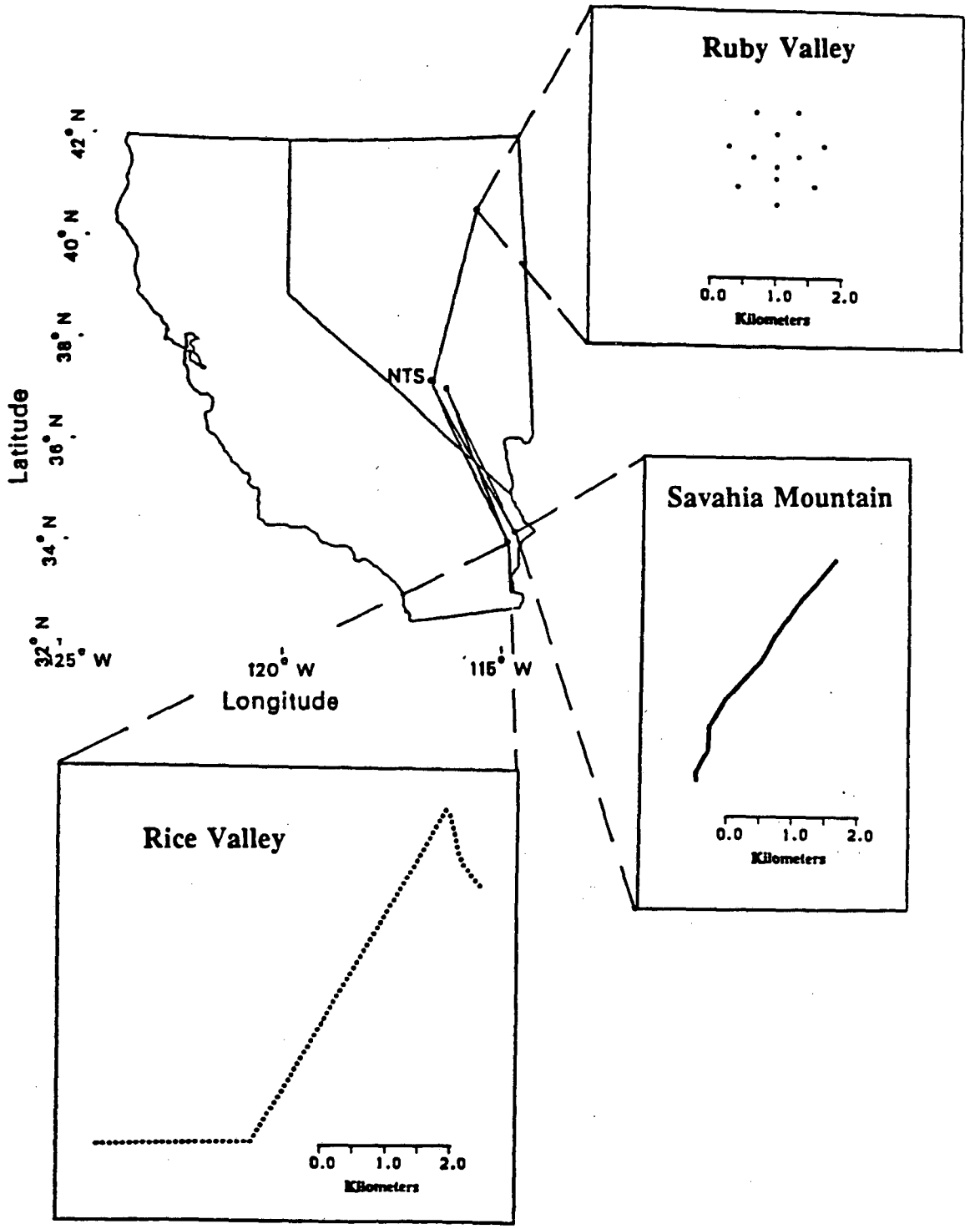

FIG. 2.1 Locations of the regional seismic arrays used in this study, connected by solid lines to the locations of nuclear tests each array recorded. The configuration of each array is also shown; each solid dot denotes the placement of one seismometer.

Table 1: NTS Explosions					
shot	GMT	latitude	longitude	depth (m)	m_b
SALUT	1985 163:15:15:0.1	37.248	-116.489	608	5.5
VILLE	1985 163:17:30:0.1	37.088	-116.084	293	4.4
HARDIN	1987 120:13:30:0.1	37.233	-116.423	625	5.5

Table 2: Recording Sites					
site name	latitude	longitude	SALUT Δ	VILLE Δ	HARDIN Δ
Ruby Valley	40.603	-115.191	*	*	387
Rice Valley	34.000	-114.756	385	355	*
Savahia Mountain	34.250	-114.588	371	340	*

* array did not record explosion

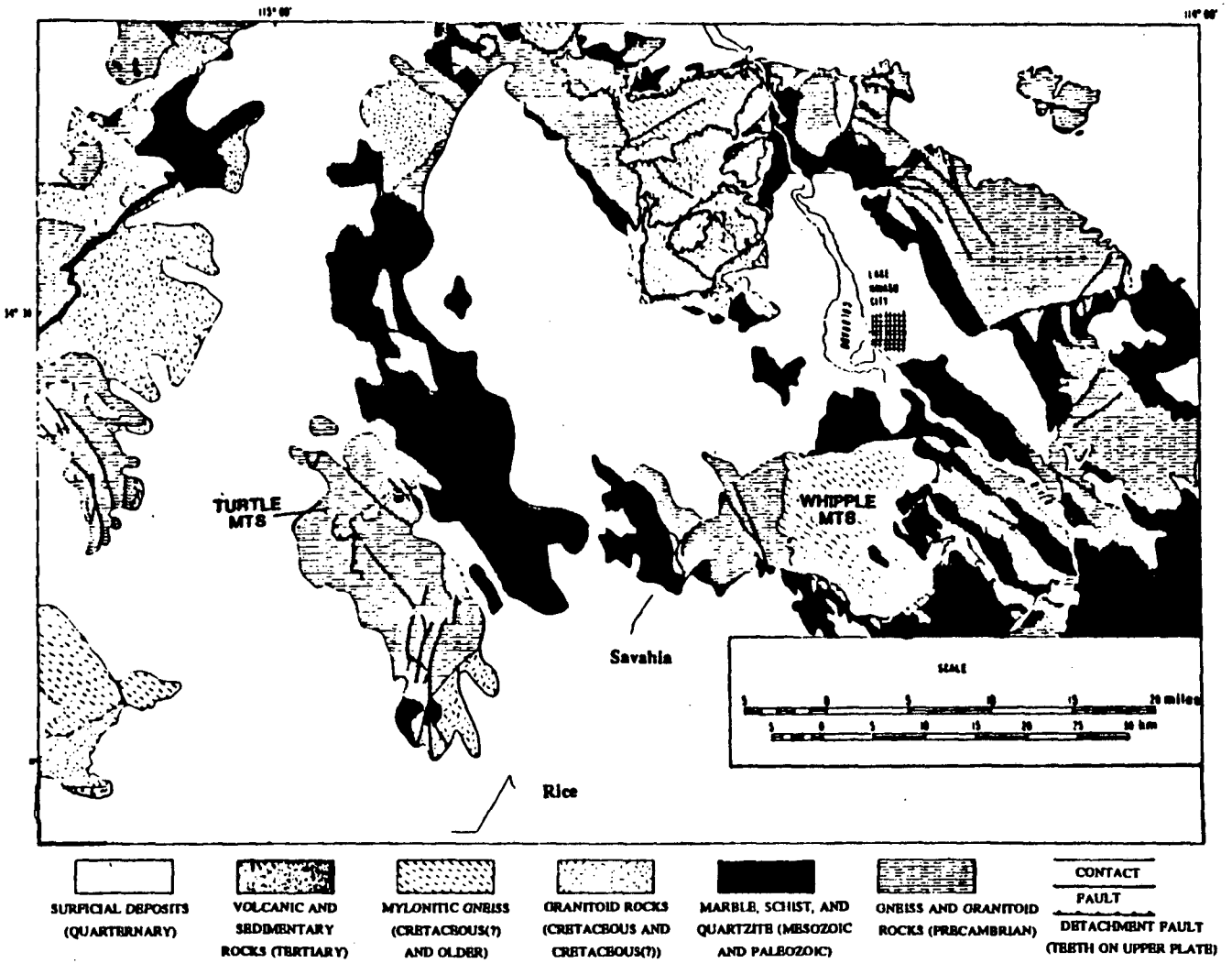

FIG. 2.2 Regional geologic map of the area surrounding the Savahia Mountain and Rice Valley array sites (after Howard and John, 1987). The Savahia Mountain and Rice Valley arrays are indicated in the lower center of the figure.

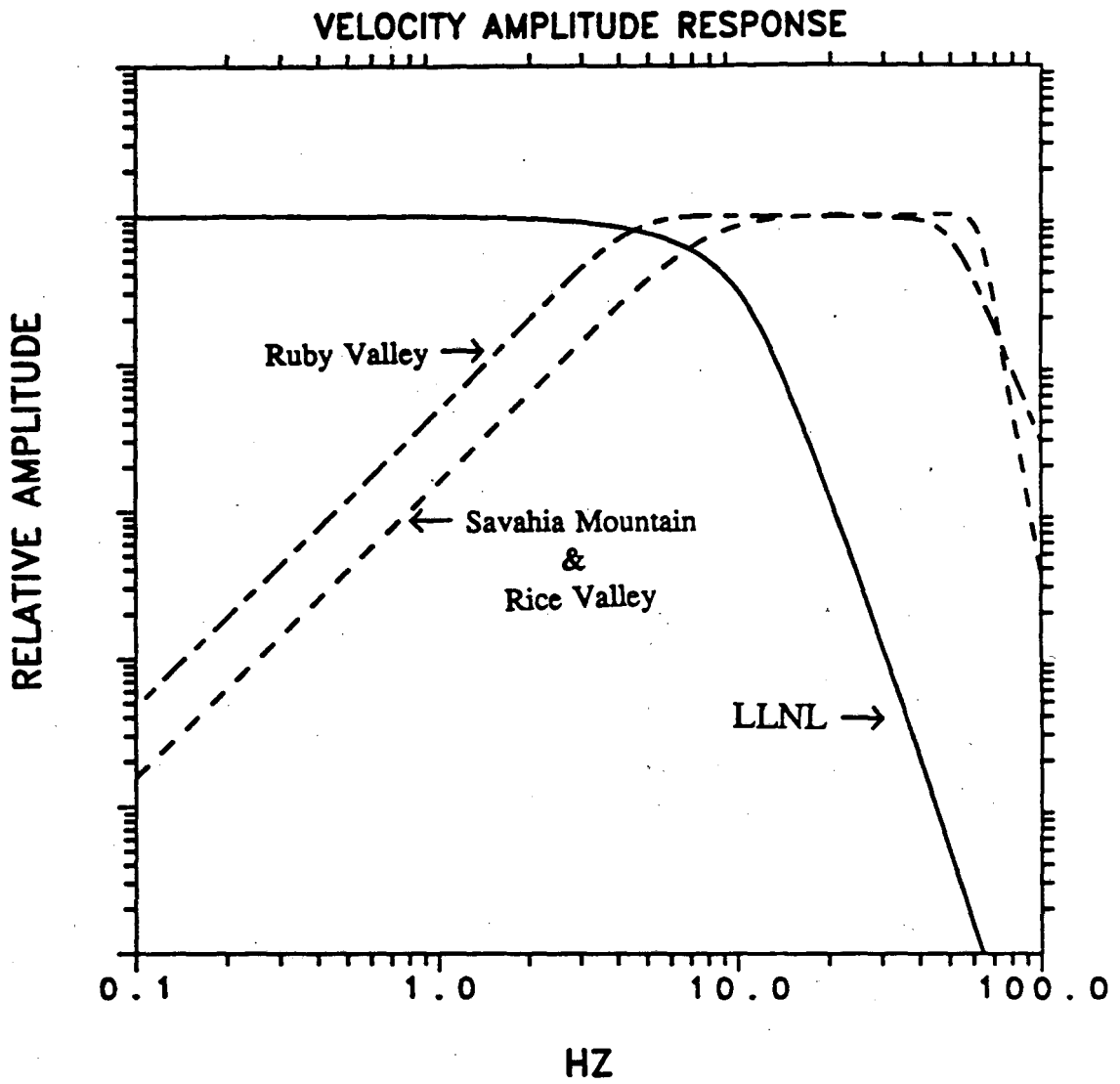

FIG. 2.3 Recording system amplitude response to velocity ground motion at each of the array sites and at the Lawrence Livermore National Laboratory (LLNL) ELKO station. The responses have been normalized for this figure.

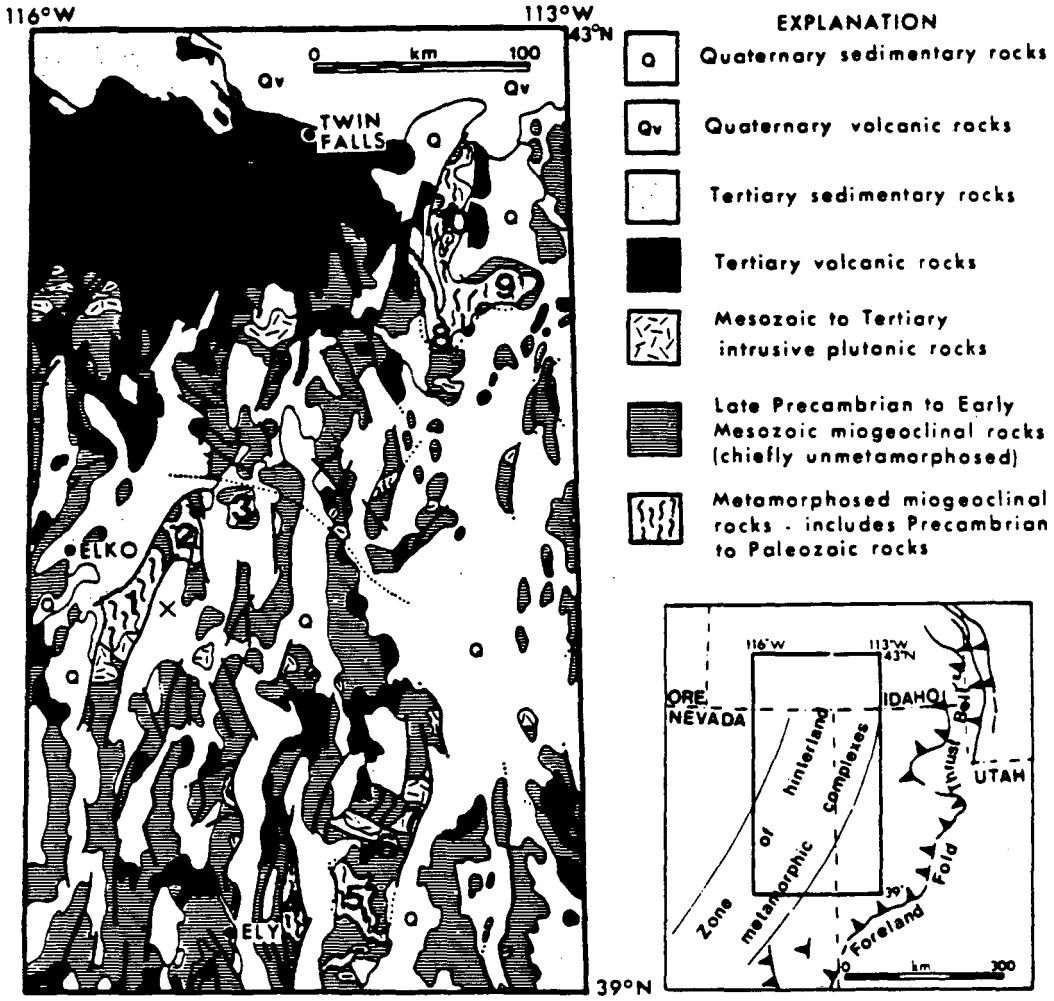

× **Ruby Valley array site**

FIG. 2.4 Regional geologic map of the area surrounding the Ruby Valley array site (from Snoke, 1980). The numbers denote metamorphic core complexes - e.g., 1, Ruby Mountains; 2, East Humboldt Range; 3, Wood Hills. The Ruby Valley array site is indicated by a cross just east of the Ruby Mountains core complex.

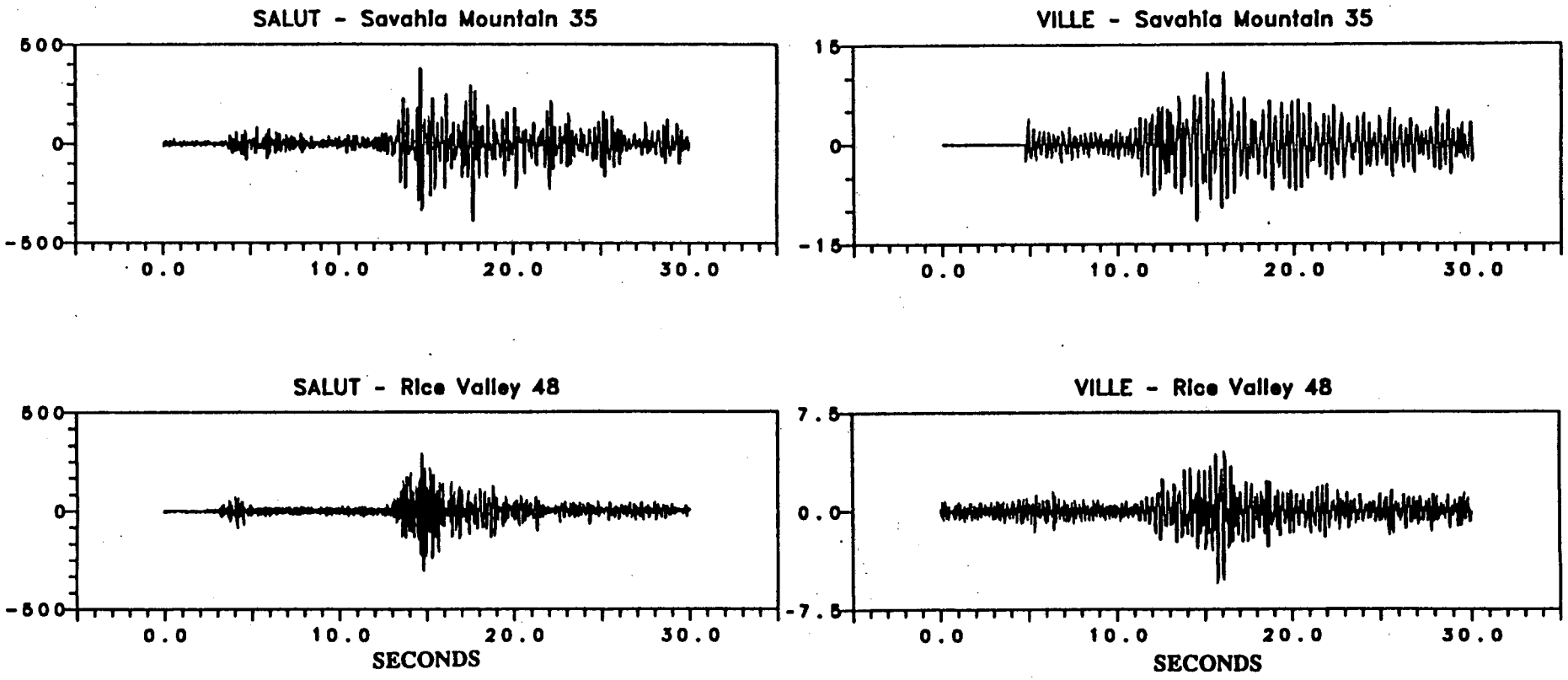

FIG. 2.5 Recordings of Pn and Pg for the explosions SALUT and VILLE at station #35 of the Savahia Mountain array and station #48 of the Rice Valley array. Approximately four seconds of pre-event noise is included, except at for VILLE at the Savahia Mountain array which did not record the early portion of Pn due to recording problems.

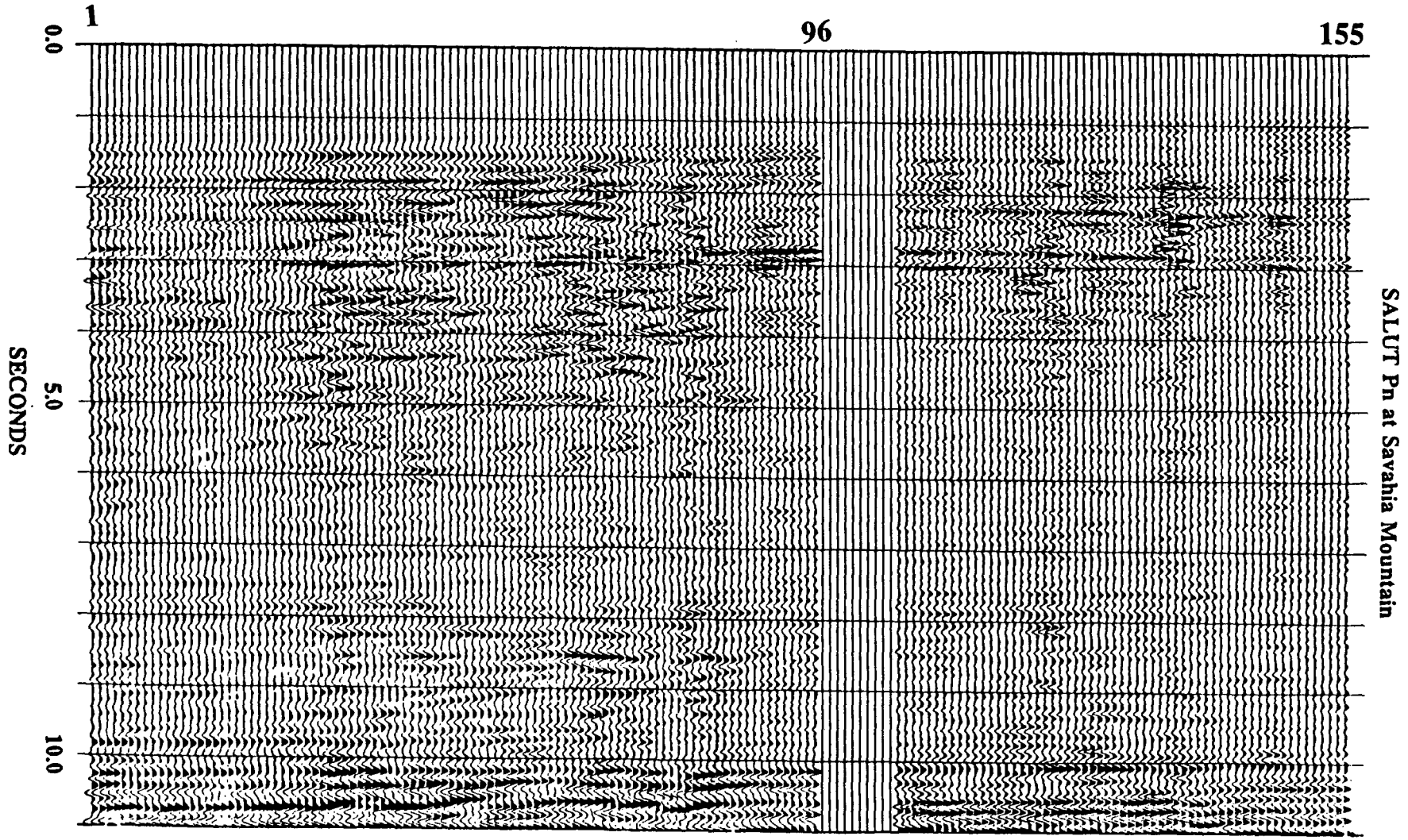

FIG. 2.6 Pn and early Pg wavefields of SALUT recorded at the Savahia Mountain array. The wavefield has been aligned using the known source azimuth and a phase velocity of 8 km/sec. The onset of Pn is near 0.8 seconds and Pg near 10 seconds in the figure. The bottom recording corresponds to station #1, the southern-most station in Figure 2.1. Subsequent recordings are spaced in 25 meter segments. Following station #96 a ten-station break occurs where no data were recorded. The maximum station separation is approximately 4 km between stations #1 and #155.

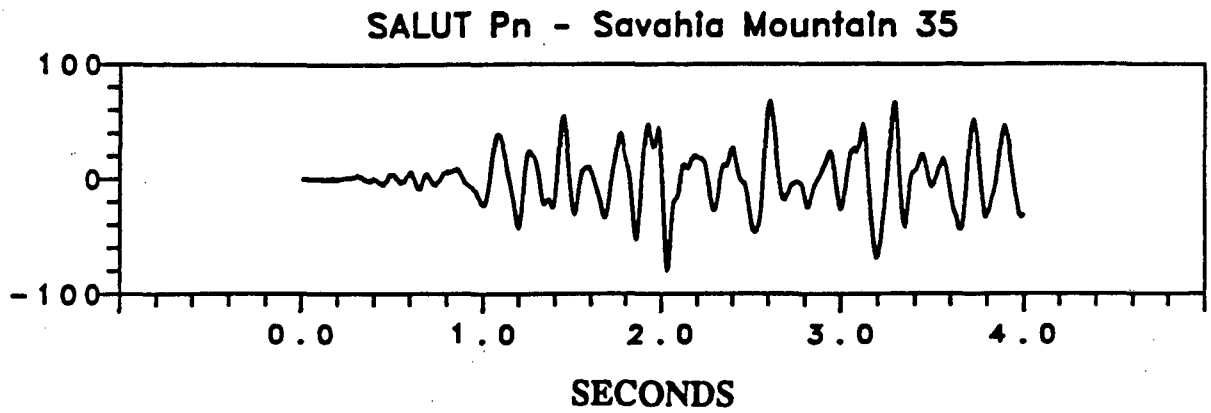

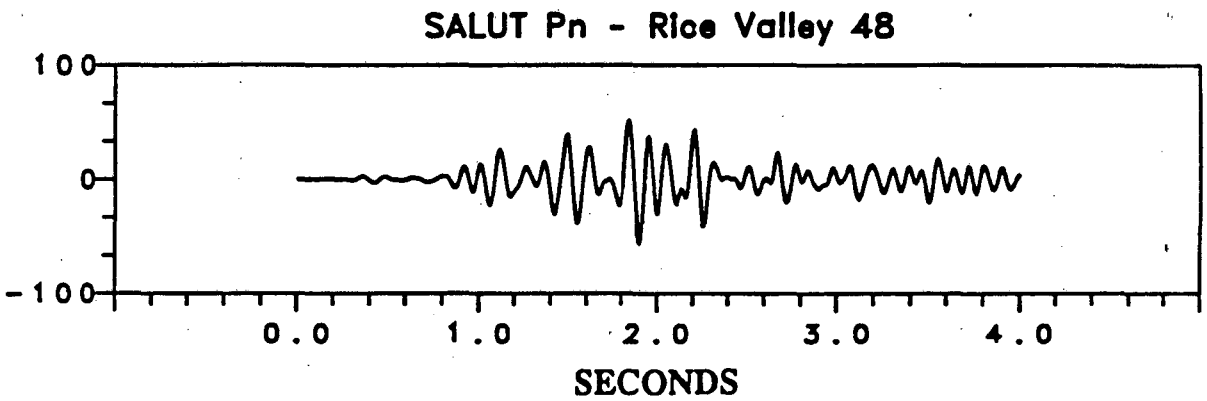

FIG. 2.7 Early SALUT Pn at station #35 of the Savahia Mountain array and station #48 of the Rice Valley array. Note the onset of the relatively large amplitude arrival near 0.7 seconds. This arrival coincides with the expected arrival time of pPn.

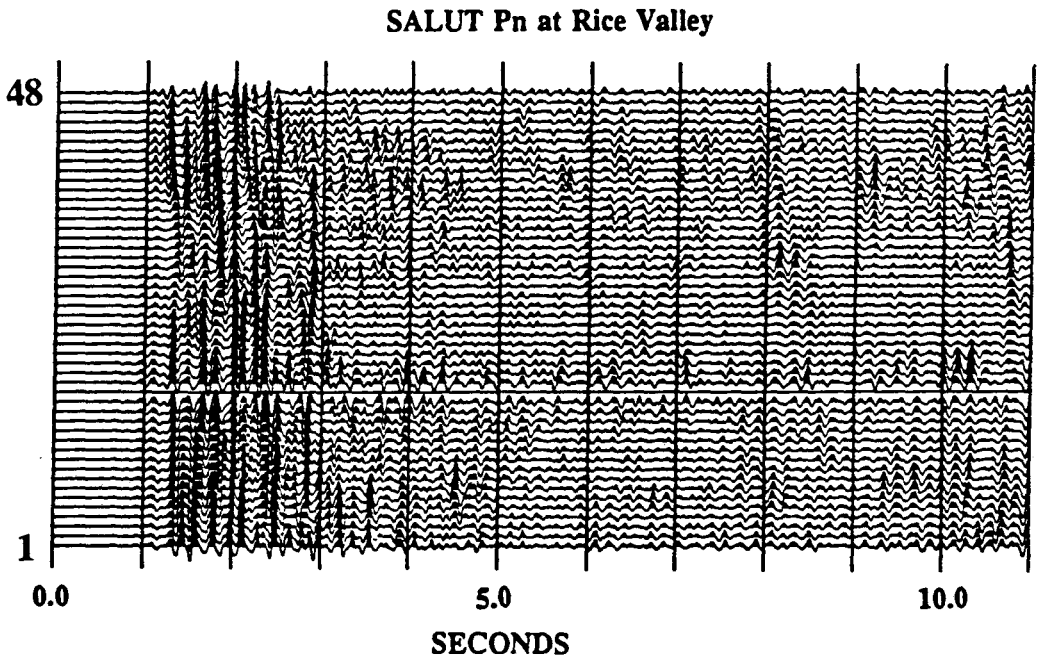

FIG. 2.8 Pn and early Pg wavefields of SALUT recorded at the Rice Valley array. The wavefield has been aligned using the known source azimuth and a phase velocity of 8 km/sec. The onset of Pn is near 0.6 seconds and Pg near 11 seconds in the figure. The bottom recording corresponds to station #1, the southwestern-most station in Figure 2.1. Subsequent recordings are spaced in 100 meter intervals. For SALUT only the first 48 stations properly recorded the wavefield, and recordings at stations #49 through #96 are therefore omitted. The maximum station separation is approximately 4 km between stations #1 and #48.

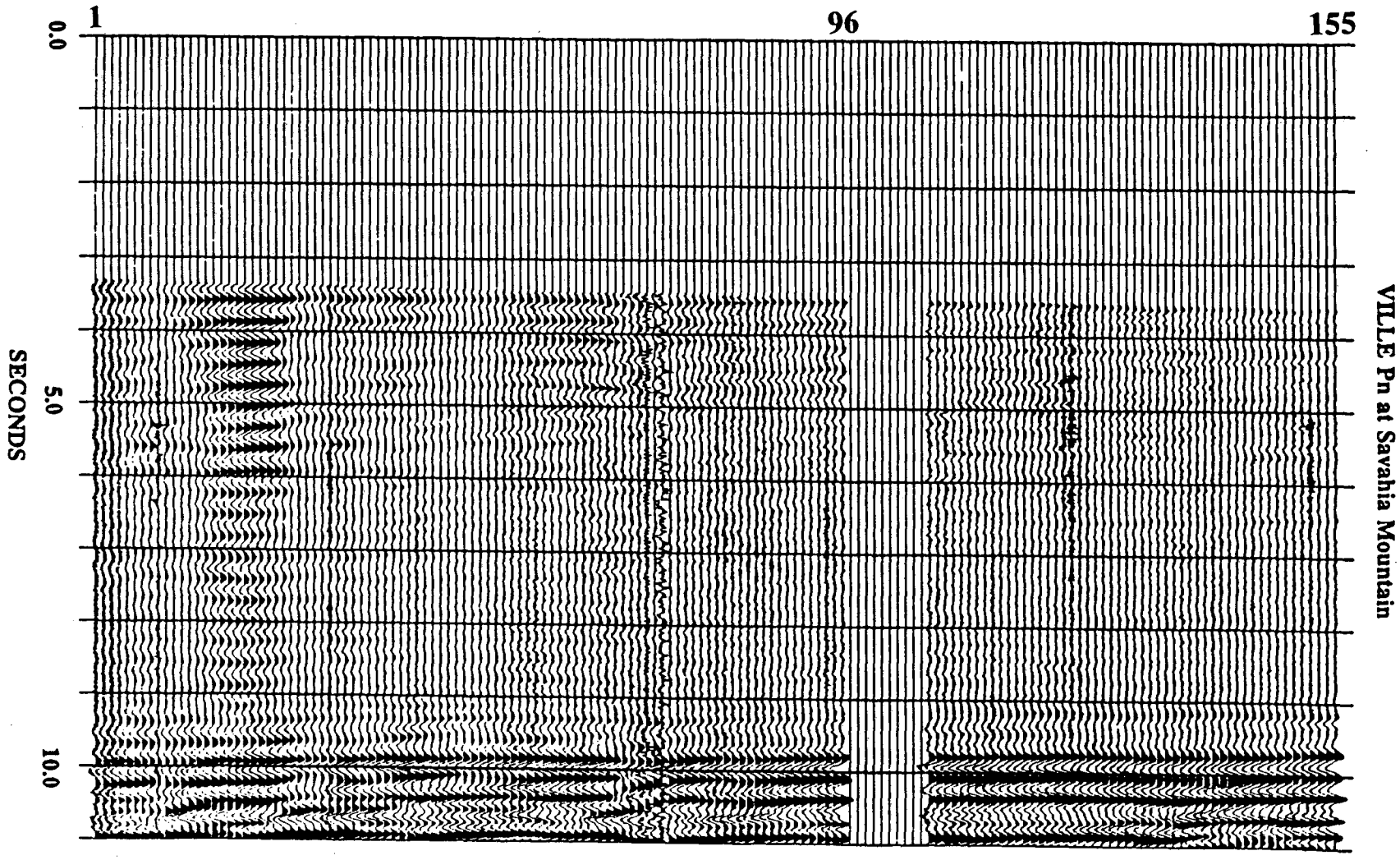

FIG. 2.9 Pn and early Pg wavefields of VILLE recorded at the Savahia Mountain array. The wavefield has been aligned using the known source azimuth and a phase velocity of 8 km/sec. The early portion of Pn, approximately 3 seconds of it, was not recorded at the array due to recording problems. The onset of Pg is near 9 seconds in the figure.

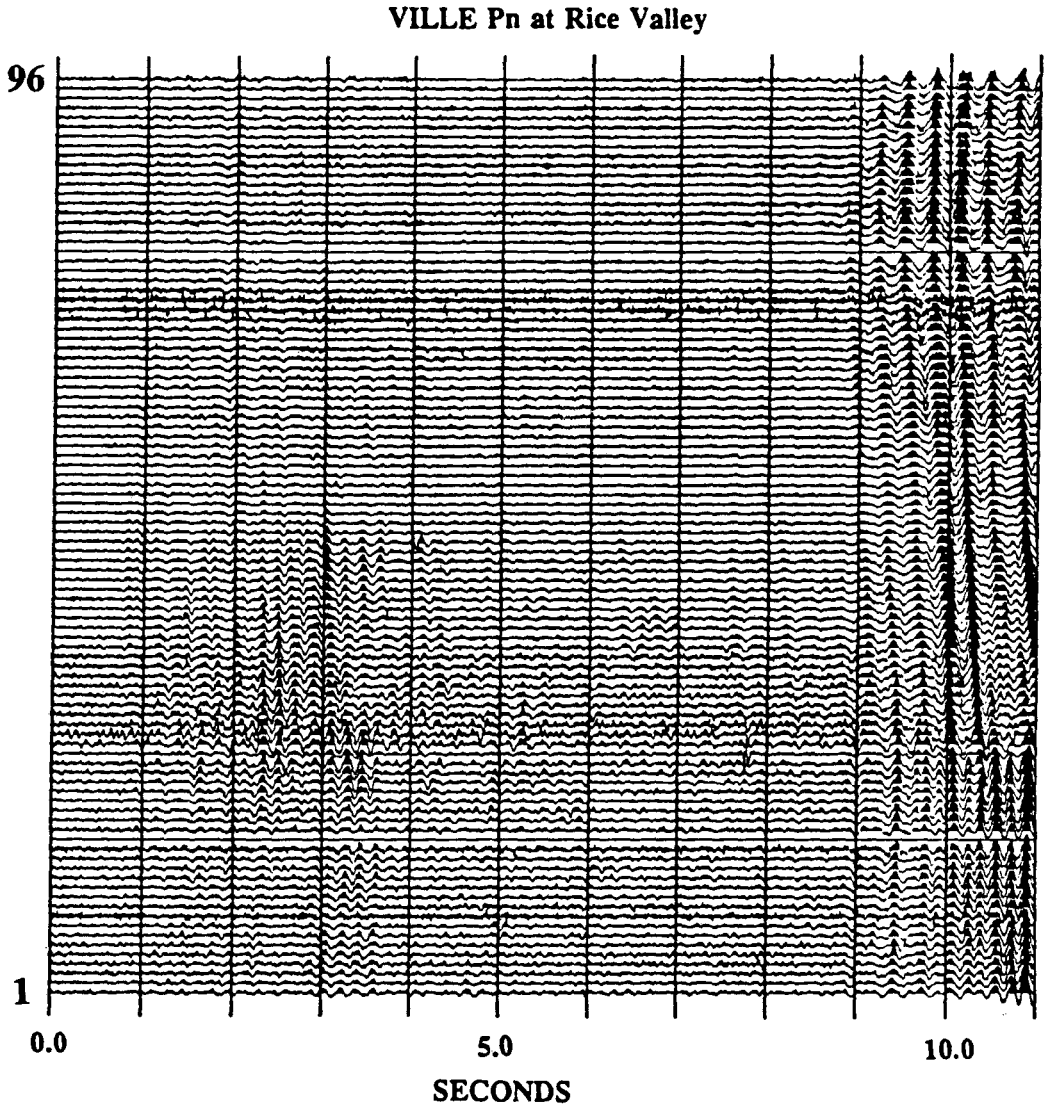

FIG. 2.10 Pn and early Pg wavefields of VILLE recorded at the Rice Valley array. Recordings from all 96 stations are shown here. The wavefield has been aligned using the known source azimuth and a phase velocity of 8 km/sec. The onset of Pn is near 0.5 seconds and Pg near 9 seconds in the figure.

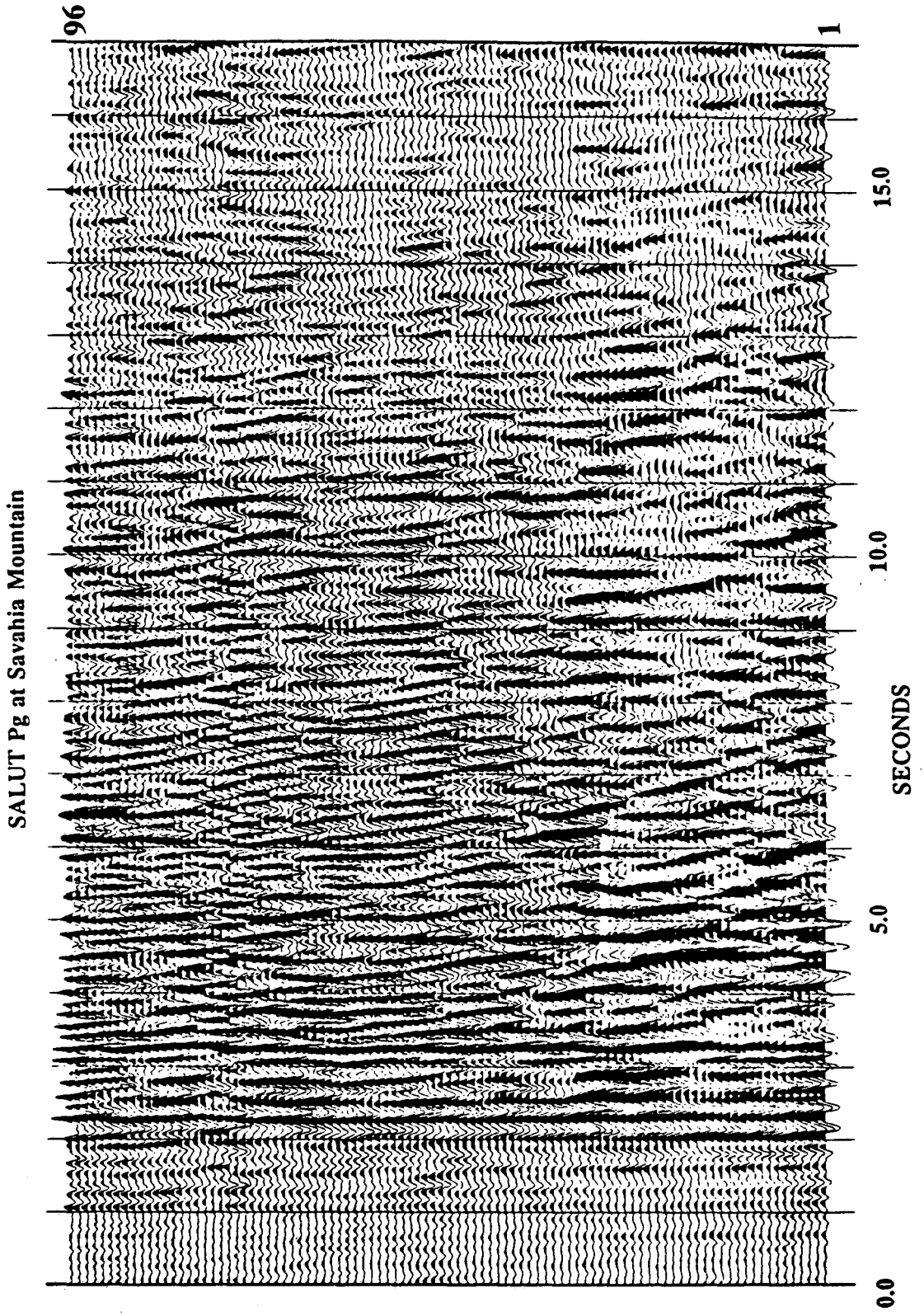

FIG. 2.11 Portion of the SALUT Pg wavefield recorded at Savahia Mountain. Only stations #1 through #96 are displayed. The wavefield has been aligned using the known source azimuth and a phase velocity of 6 km/sec. The first two seconds displayed correspond to the last two seconds in Figure 2.6, however the amplitude scale in these two figures differ.

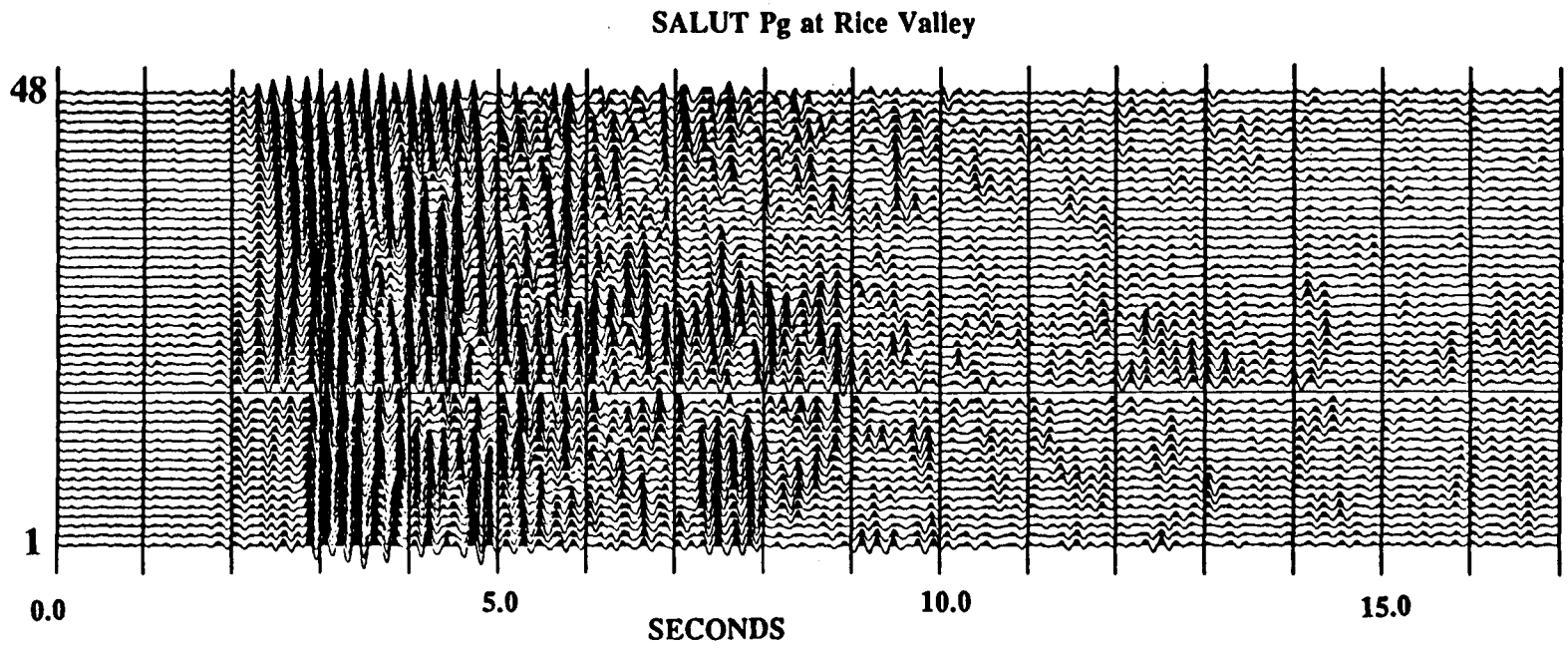

FIG. 2.12 Portion of the SALUT Pg wavefield recorded at stations #1 through 48 at the Rice Valley array. The wavefield has been aligned using the known source azimuth and a phase velocity of 6 km/sec. The first two seconds displayed correspond to the last two seconds in Figure 2.8, however the amplitude scale in these two figures differ.

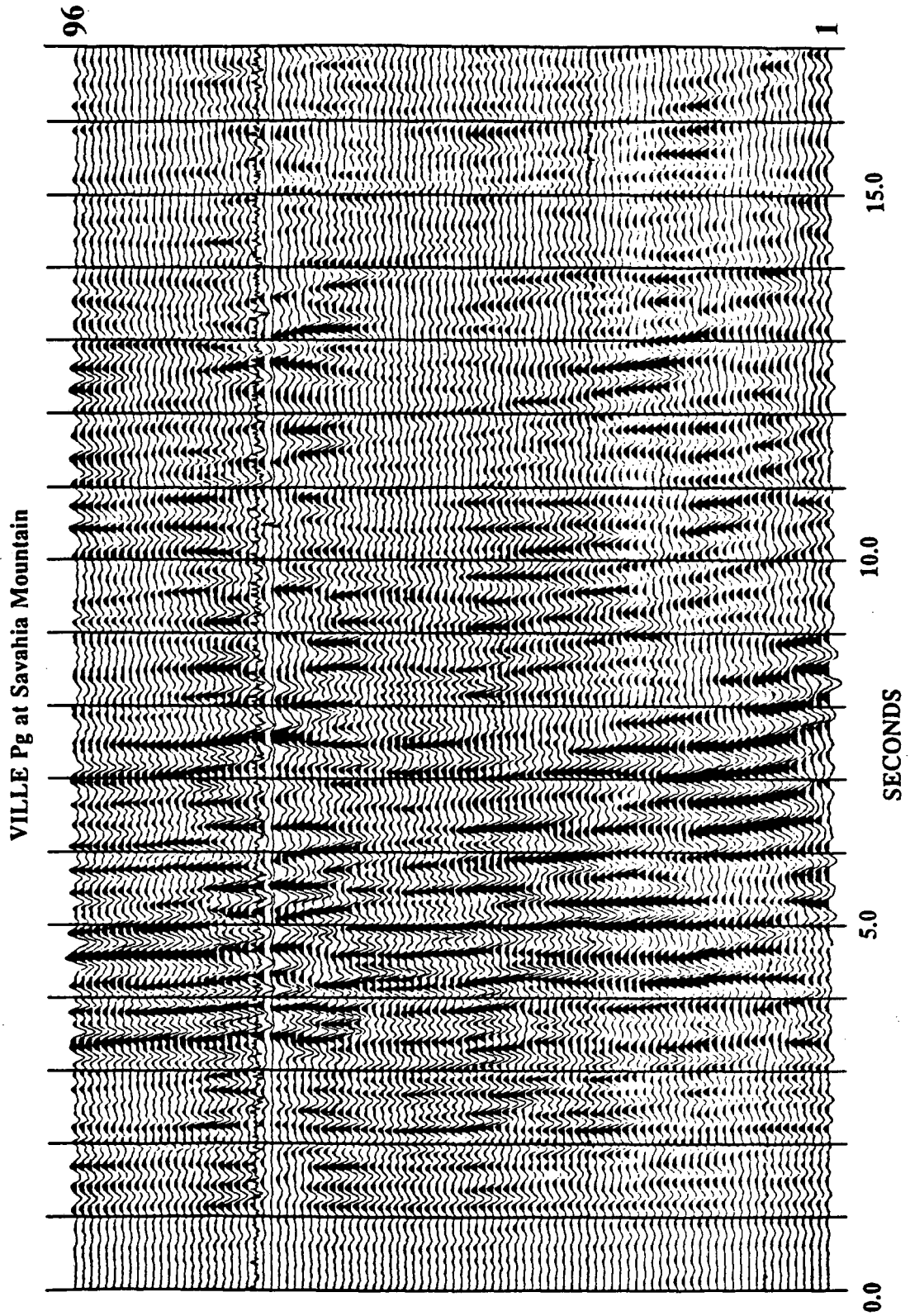

FIG. 2.13 Portion of the VILLE Pg wavefield recorded at Savahia Mountain. Only stations #1 through #96 are displayed. The wavefield has been aligned using the known source azimuth and a phase velocity of 6 km/sec. The first two seconds displayed correspond to the last two seconds in Figure 2.9, however the amplitude scale in these two figures differ.

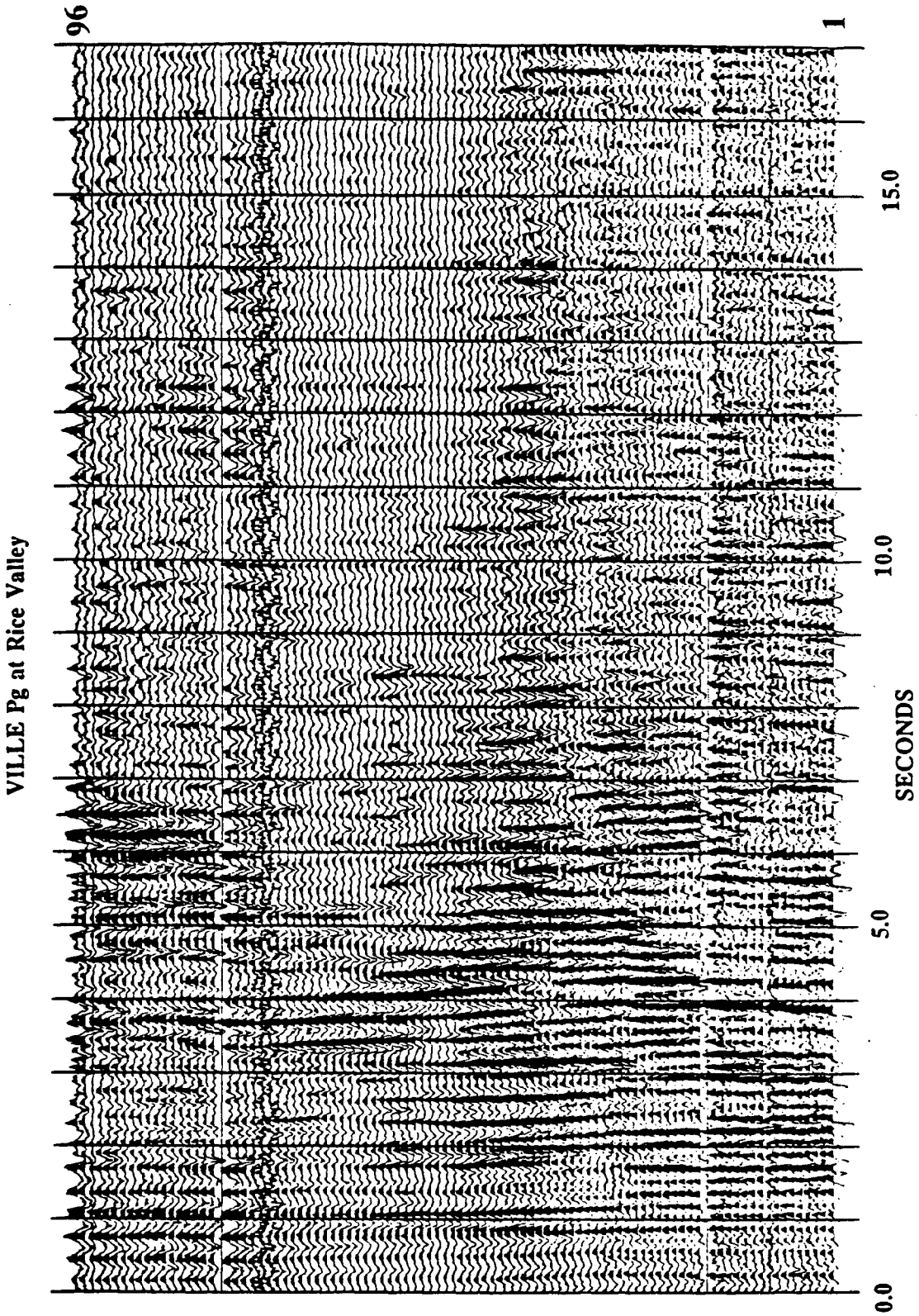

FIG. 2.14 Portion of the VILLE Pg wavefield recorded at stations #1 through 96 at the Rice Valley array. The wavefield has been aligned using the known source azimuth and a phase velocity of 6 km/sec. The first two seconds displayed correspond to the last two seconds in Figure 2.10, however the amplitudes in these two figures differ.

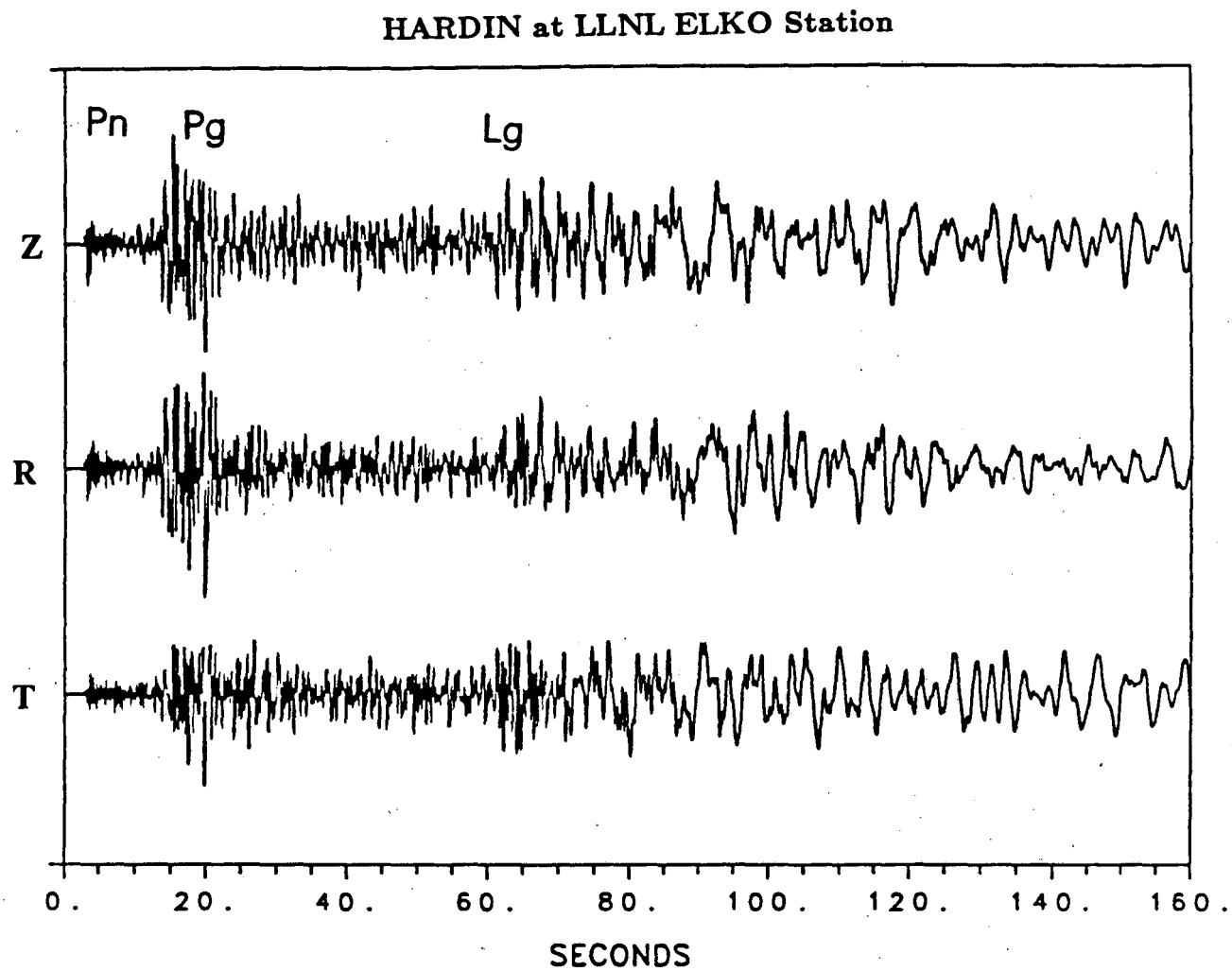

FIG. 2.15 Three-component broadband recording of HARDIN at the LLNL seismic station. The regional phases Pn, Pg, and Lg are indicated. Z = vertical, R = radial, and T = transverse.

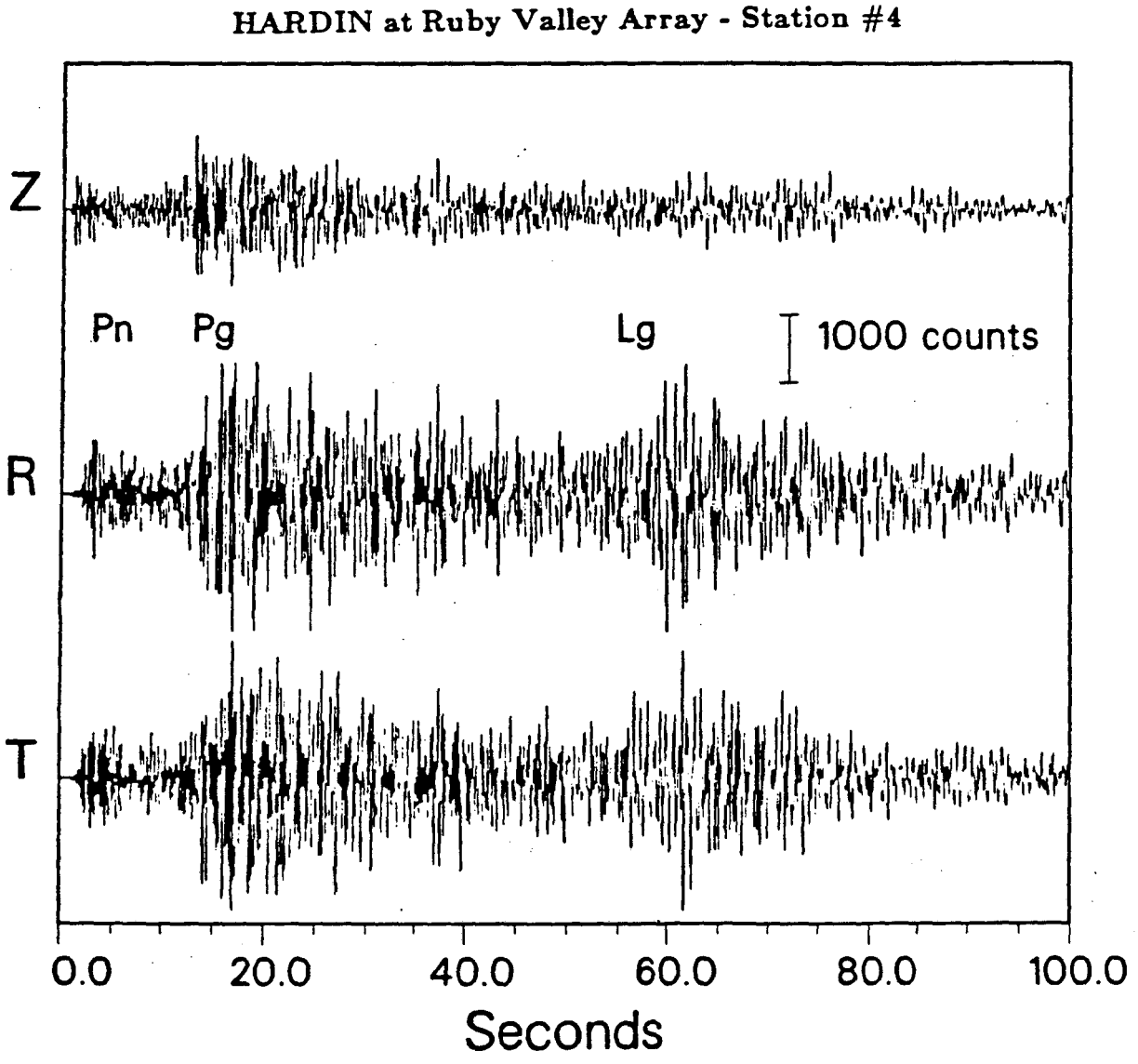

FIG. 2.16 Example of a three-component recording of HARDIN at the Ruby Valley array. The regional phases Pn, Pg, and Lg are indicated, as is the amplitude scale in digital counts.

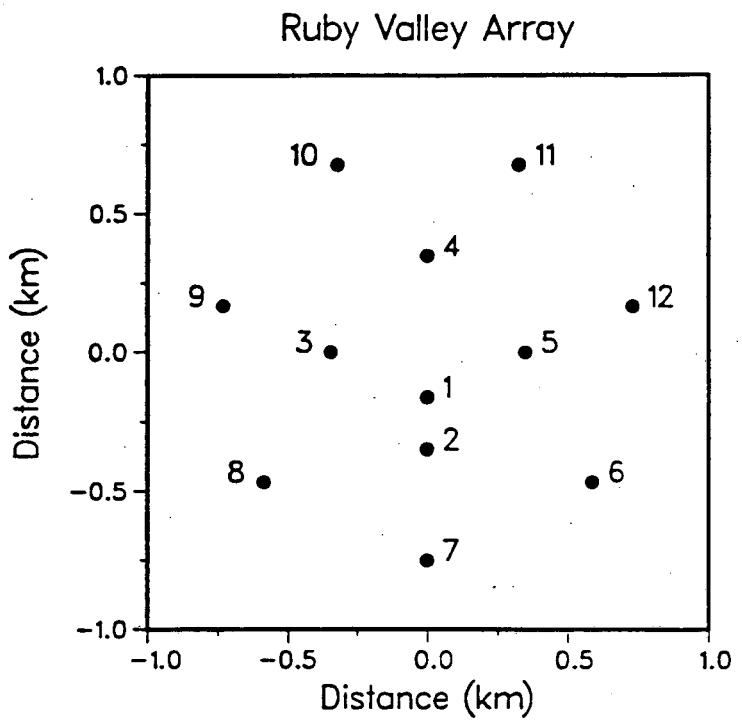

FIG. 2.17 Configuration of the Ruby Valley array. Station numbers are indicated.

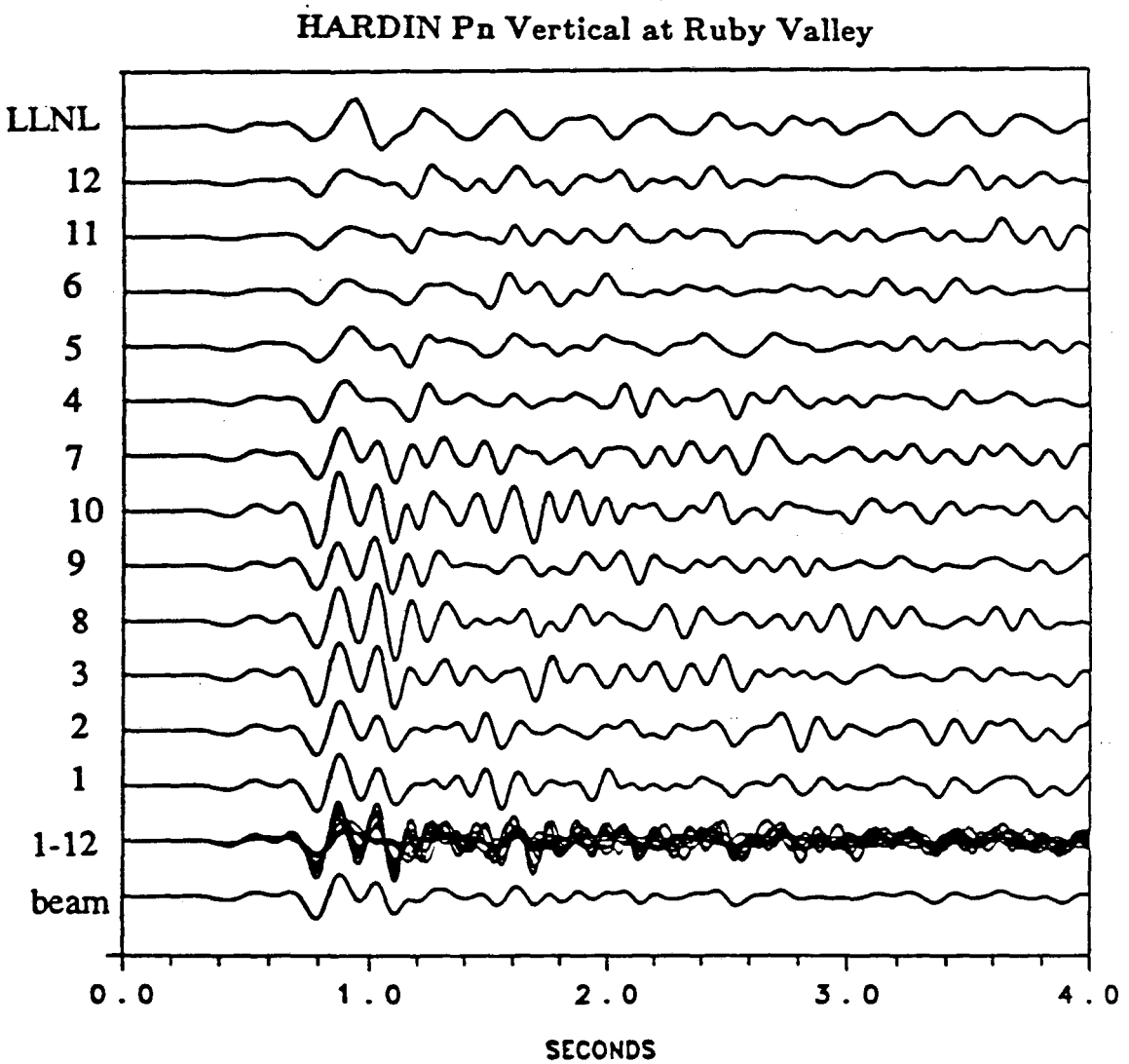

FIG. 2.18a Vertical component Pn recordings of HARDIN to four seconds. Waveforms recorded at each station of the Ruby Valley array are shown, with the station number to the left of each trace. The traces are aligned on the early Pn arrival and are plotted with correct relative amplitudes. The superposition of the array recordings on this Pn alignment is also shown, as is the resulting Pn beam. At the top of the figure is the corresponding portion of the LLNL recording in FIG. 2.15 scaled to the early Pn amplitude at the array.

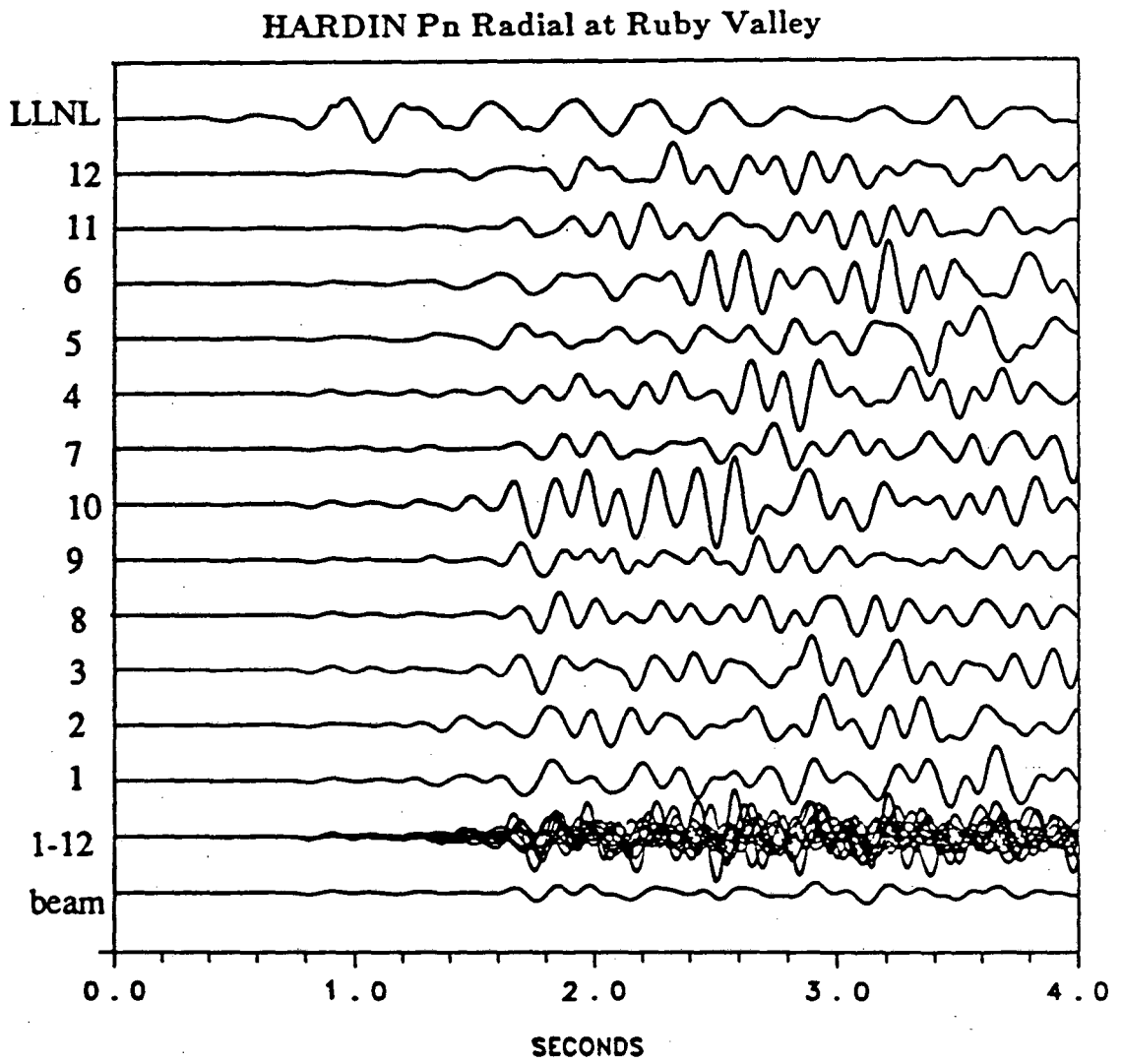

FIG. 2.18b Same as FIG. 18a, but for the radial component.

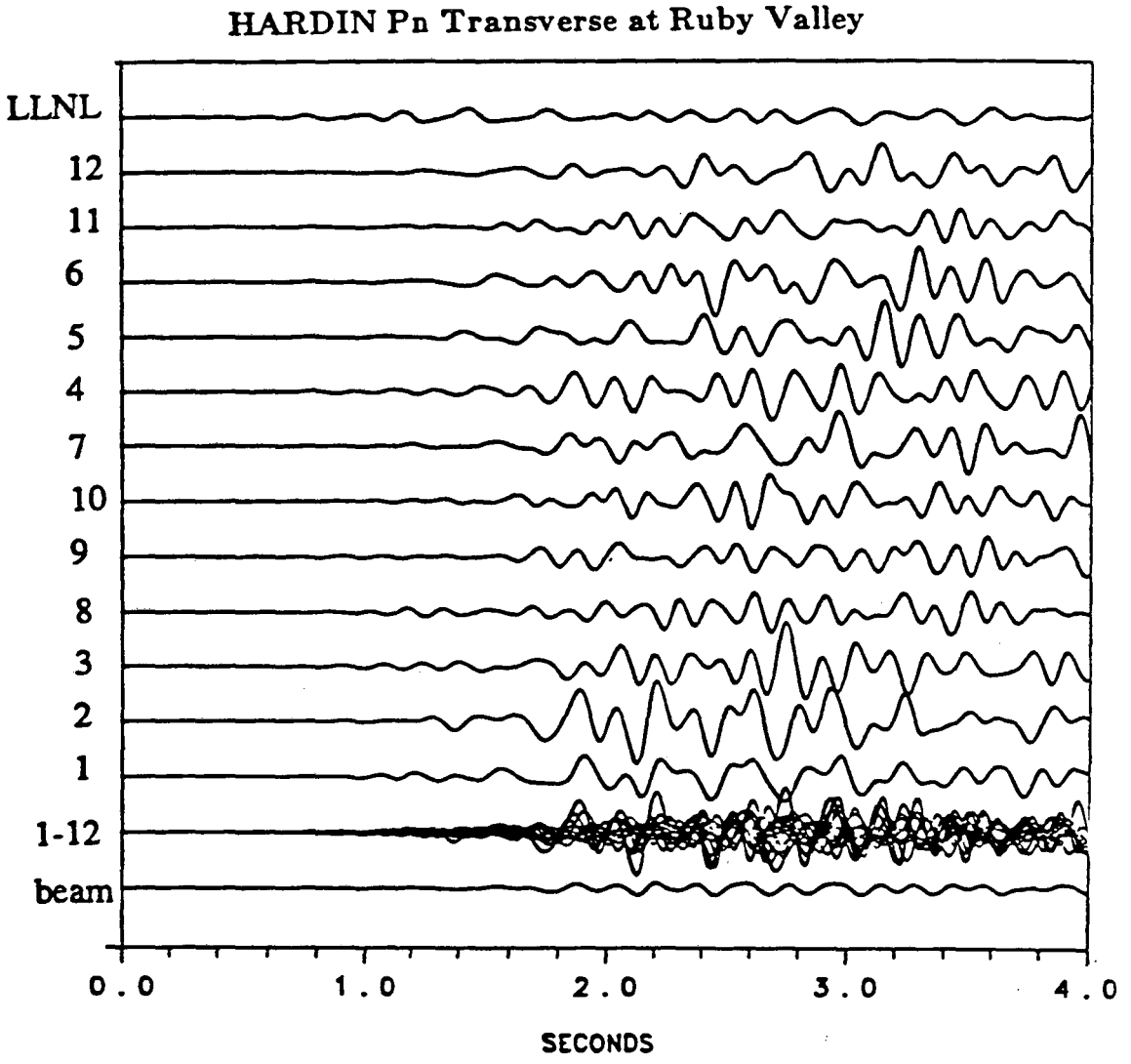

FIG. 2.18c Same as FIG. 2.18a, but for the transverse component.

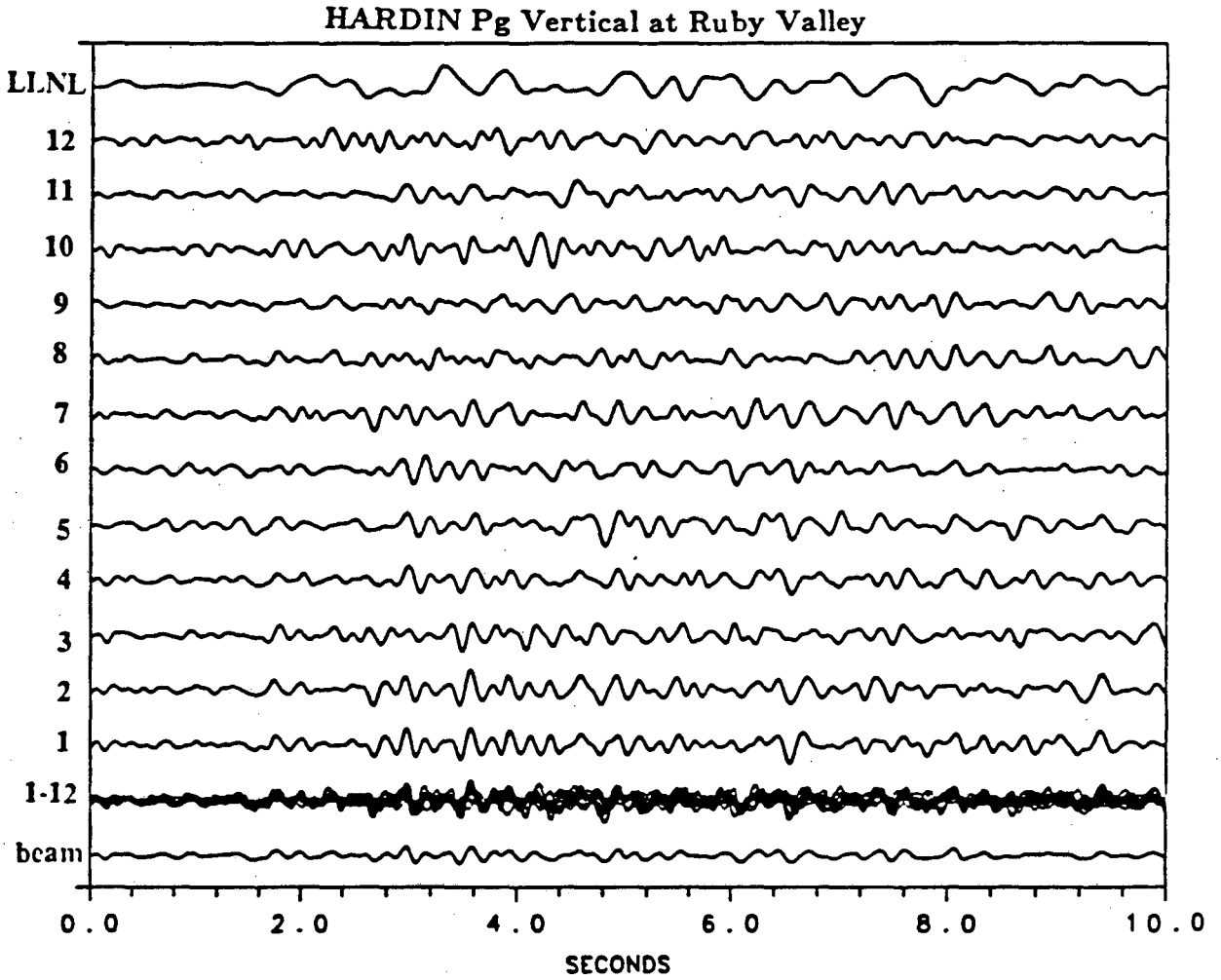

FIG. 2.19a Vertical component Pg recordings of HARDIN. The time window displayed corresponds to the 10 to 20 second time window in FIG. 2.16. Waveforms recorded at each station of the Ruby Valley array are shown, with the station number to the left of each trace. The traces are aligned based on the known source azimuth and a phase velocity of 6 km/sec. The superposition of the array recordings is also shown, as is the resulting Pg beam. At the top of the figure is the corresponding portion of the LLNL recording in FIG. 2.15 scaled to the Pg amplitude at the array.

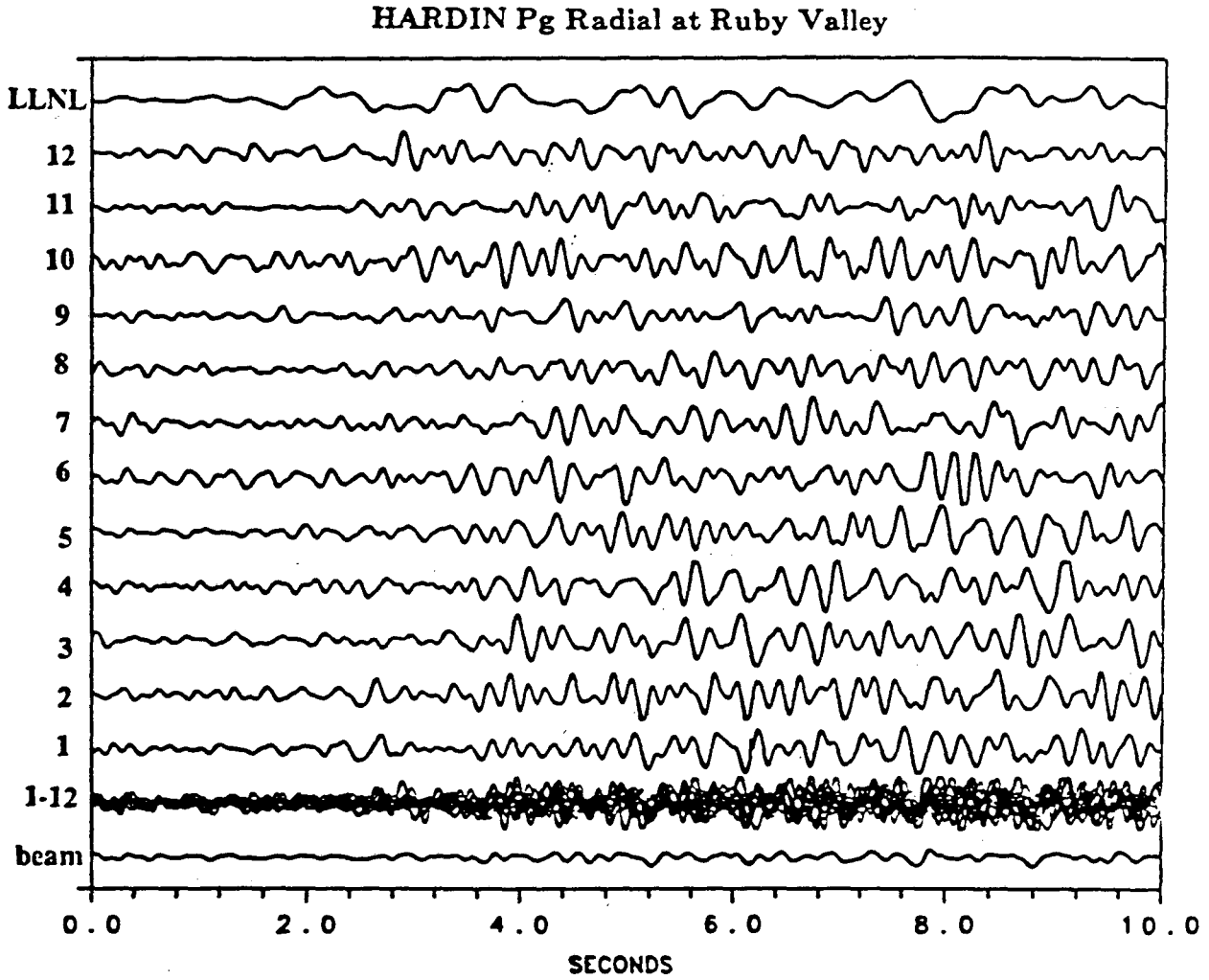

FIG. 2.19b Same as FIG. 2.19a, but for the radial component.

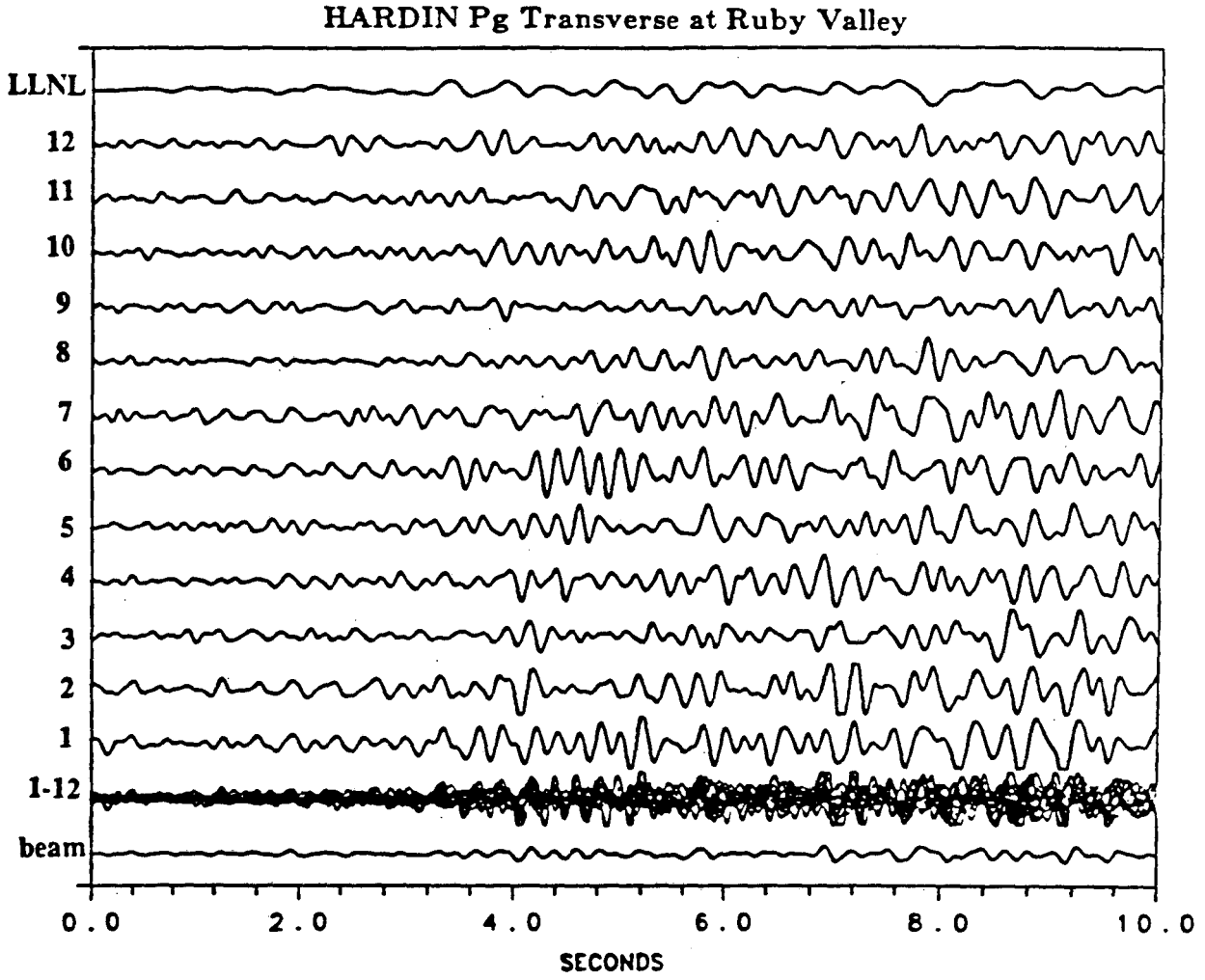

FIG. 2.19c Same as FIG. 2.19a, but for the transverse component.

Chapter 3

Spectral Amplitude Characteristics

3.1 Introduction

In this chapter we will study the spectral amplitude characteristics of the regional data sets described in the previous chapter. There are a number of reasons for doing this. First of all, because we are concerned with high-frequency monitoring, we need to know the frequency limit of the signal. Secondly, to the extent that Pn and Pg can be useful for discrimination and yield estimation, it is important to be aware of the variation in spectral amplitude levels over small distances in receiver location which result from the effects of small-scale variations in geologic structure. Knowledge of these stochastic variations is particularly important for a prospective single-station site which may not otherwise be aware of the spectral uncertainty caused by small-scale spatial variations. We will therefore examine variations in spectral amplitude over the aperture of each of our three arrays. Also, using spectral ratios for a fixed source, we will look briefly at how seismic energy is partitioned between Pn and Pg and how sensitive this partitioning is to slight changes in propagation path. Finally, because we have recorded at both the Savahia Mountain and Rice Valley arrays two explosions with nearby source locations, we are in a position to remove the major path effects using spectral ratios and examine how SALUT and VILLE source characteristics compare with a simple explosion source model.

All spectral plots which follow were computed from the waveforms as displayed in the figures in Chapter 2. The spectra were computed using the first five 3π tapers in the multiple-taper spectral estimation method with adaptive weighting (Thomson, 1982). The principal advantage of this method is its ability to form relatively low-bias, low-variance estimates. A description and examples of this method are given in Appendix A. For consistency with the HARDIN data set, the SALUT and VILLE waveforms were resampled at 200 samples per

second. The Pn and Pg spectral time windows begin near the onset of each phase and extend for 2.6 seconds (512 data points). The sampling in frequency is therefore 0.39 Hz. The Pn and Pg spectra which follow represent instrument-corrected displacement amplitude spectra with no correction for path effects.

3.2 Spectra at Savahia Mountain and Rice Valley

3.2.1 Pn

The spectra of the SALUT Pn wavefield at Savahia Mountain and Rice Valley are shown in Figure 3.1. Spectra from each of the 145 waveforms in Figure 2.6 at Savahia and the 47 waveforms in Figure 2.8 at Rice are plotted. Though the number of spectra shown for each array site differs, recall that the maximum sensor separation is approximately the same, about 4 km. Over this distance, spectral levels vary up to an order of magnitude or greater at both array sites. As a measure of the variation in spectral amplitude the coefficient of variation at each frequency is shown beneath the spectra. This is given by σ/μ, the ratio of the standard deviation of the amplitude spectra, σ, to the mean value of the spectra, μ. We will be interested to see how σ/μ depends on frequency, wavetype, array site, and seismic source. The coefficient of variation in Figure 3.1 is somewhat greater at Savahia, though at the lower frequencies it behaves similarly at both array sites, with local minimum in variation near 1 Hz and 6 Hz. By about 30 Hz, σ/μ has reached a value of one at both array sites. At higher frequencies, σ/μ reaches a peak value of 4.5 near 60 Hz at Savahia, while at Rice, σ/μ remains below 1.3 up to 100 Hz. The means of these spectra, computed assuming a log-normal distribution, are shown in Figure 3.2. Also shown is the the mean pre-event noise and same plot of spectral variation. At Savahia, we see, not surprisingly, that the sharp increase in variation occurs right where the signal runs into the noise, at about 25 Hz. This is also the case at Rice, though the increase is not as dramatic. Beyond 25 Hz, the signal and noise spectra, though each widely variable, have regressed to nearly identical mean values. Refer ahead to Figure 3.5a which superimposes the mean SALUT Pn spectra from Savahia and Rice. Beyond 6 Hz

the two mean signal spectra are very similar both in amplitude level and spectral decay, and both have similar corner frequencies near 6 and 12 Hz. From 1 to 6 Hz, however, the Pn wavefield at Rice is greatly depleted in energy relative to Savahia, indicating significant differences in site response between these locations within this frequency band. Recall we saw this difference in frequency content in the waveform plots of Figure 2.7

The spectra of the VILLE Pn wavefield at Savahia and Rice are shown in Figure 3.3. In Figure 3.3a, spectra from each of the 145 waveforms in Figure 2.9 at Savahia are shown. In Figure 3.3b, only the spectra from 47 of the 94 waveforms in Figure 2.10 at Rice are plotted. The recording stations omitted are the same ones that failed to properly record the SALUT explosion - this is to provide consistency with all of the other spectral plots, which show spectra from waveforms that are separated by no more than approximately 4 km. At Savahia the spectral time window begins about 2.5 seconds into the Pn wavefield since, as shown in Figure 2.9, the instruments did not start recording until this time. The mean spectral plots in Figure 3.4 show the signal to noise ratio to be much less for VILLE, the signal and noise merging near 13 Hz at both array sites. (Recall that the pre-event noise at Savahia is not available; instead, as an approximation, the mean noise spectrum at Savahia for SALUT is plotted.) Given the similarity of propagation path, we would expect, at a given array site, that the spectral variation measured for VILLE to be similar to that measured for SALUT. This is in fact the case at both arrays except below about 2 Hz where, because of a lower signal-to-noise ratio, σ/μ for VILLE has increased. Also, as we observed for SALUT, the spectral variation is somewhat larger at the Savahia array site. In Figure 3.5b the Savahia and Rice Pn spectra are overlaid for VILLE. As was the case for SALUT, the Savahia and Rice spectra are nearly identical beyond about 6 Hz up until where the signal and noise merge, though the structure of high-frequency is different from that for SALUT. Again, below about 6 Hz, the Rice Valley wavefield is depleted in low-frequency energy.

3.2.2 Pg

SALUT Pg spectral plots from the waveforms recorded at Savahia (see Fig. 2.11) and at Rice (see Fig. 2.12) are shown in Figure 3.6. Again the spectral variation is somewhat greater at Savahia. Also at Savahia, the SALUT Pg coefficient of variation is nearly identical to that for the corresponding Pn wavefield, while at Rice Valley σ/μ for Pg is consistently less than that for Pn up to about 20 Hz. The mean spectra are shown in Figure 3.7 along with the pre-event noise, which for both array sites merges with the signal near 20 Hz. Referring ahead to Figure 3.10a, we see that, like for Pn, these two mean spectra merge near 6 Hz and remain nearly identical with increasing frequency. We again see corner frequencies near 6 and 12 Hz, though here the rate of decay between 6 and 12 Hz is greater than it was for Pn. Also similar to Pn, the mean Pg spectrum at Rice is relatively deficient at low frequencies.

VILLE Pg spectral plots from the 148 recordings at Savahia (see Fig. 2.13) and the first 47 of the 96 recordings at Rice (see Fig. 2.14) are shown in Figure 3.8. The corresponding spectral means are displayed in Figure 3.9. The signal and noise merge near 13 Hz at both array sites. There is only a small difference in the Pg coefficient of variation between the array sites. The mean VILLE Pg spectra are superimposed in Figure 3.10b. We again see the lack of energy below 6 Hz at Rice and an overlapping of the spectra beyond. The high-frequency decay shows the same scalloping near 6 and 8 Hz that we saw for Pn. The fact that we do not see this scalloping for SALUT suggests it is due to a VILLE source effect.

Contrasting the spectral variation between Pn and Pg for VILLE, at Savahia the Pg variation remains noticeably less than that for Pn up to about 5 Hz, beyond which the two are almost identical. At Rice there is no significant difference in variation between Pn and Pg beyond 2 Hz, which is about where the VILLE Pn signal climbs out of the noise. Contrasting the two sources SALUT and VILLE, the Pg spectral variations at Savahia are essentially identical except between about 1 and 4 Hz, where the variation is up to twice as great for SALUT. At Rice the Pg variation for SALUT is slightly less than that for VILLE up to about 10 Hz, beyond which the difference is small.

The characteristics of the coefficient of variation can be summarized as follows:

(1) The spectral variations computed are frequency dependent, varying up to a factor of two over the signal bandwidth. The variation increases where the signal-to-noise ratio is small. The least amount of variation occurs typically between 1 and 2 Hz, though comparably low values often exist at higher frequencies.

(2) Contrasting the two explosions SALUT and VILLE for a fixed recording site (Savahia or Rice) and a fixed arrival type (Pn or Pg), σ/μ is generally only slightly larger for VILLE up to from 5 to 10 Hz, beyond which σ/μ is about the same for the two explosions. The difference may be due primarily to the much lower signal-to-noise ratio for VILLE.

(3) Contrasting Pn and Pg for a fixed explosion and fixed recording site, the spectral variation of Pg is typically either equal to or somewhat less than the spectral variation of Pn. Part of the difference here may be due to the lower signal-to-noise ratio for Pn.

(4) Contrasting recording sites for a fixed explosion (SALUT or VILLE) and a fixed arrival type (Pn or Pg), σ/μ is consistently larger at the Savahia Mountain site over almost all of the signal bandwidth. This suggests that decorrelating effects, such as scattering, are more severe at the Savahia site.

3.3 Spectra at Ruby Valley

The Ruby Valley spectra shown below were computed in the same manner as the Savahia and Rice spectra shown above. That is, the first five 3π tapers from the multi-taper estimation procedure with adaptive weighting were used to estimate the spectra from a 2.6 second window of data near the beginning of the Pn and Pg waveforms, as displayed in the figures in Chapter 2. As before, instrument-corrected displacement amplitude spectra are plotted and the sampling in frequency is 0.39 Hz.

3.3.1 Pn

The three-component Pn spectra at Ruby Valley are shown in Figure 3.11. The vertical-component spectral estimates come from the 2.6 second window beginning near 0.2 seconds in Figure 2.18a. The radial and transverse spectral estimates come from 2.6 second windows beginning near 1.4 seconds in Figures 2.18b and 2.18c. This later window is used because of the lack of energy earlier in the horizontal ground motion. For each component, the maximum difference in spectral amplitude among the twelve spectra is about a factor of four, or about 12 db. The coefficient of variation is typically about a factor of two lower on the vertical component as compared to the horizontal components up to about 5 or 6 Hz. At higher frequencies the horizontal variation is generally equal to or slightly less than the vertical variation. The difference in variation between the two horizontal components is not great, though it is the radial component which typically has the lower variation. Contrasting the vertical-component Pn coefficient of variation here with those shown earlier for the larger Savahia Mountain and Rice Valley array sites, we would expect the variation here to be smaller because of the smaller array aperture, 1.5 km as opposed to 4 km. This is in fact the case, but only up to about 7 Hz, beyond which the variation is about the same. It therefore appears that at the higher frequencies the variation in spectral amplitude is less sensitive to increases in sensor separation than at the lower frequencies. The horizontal spectral variation at Ruby Valley is comparable to the vertical-component variation of the Savahia and Rice recordings.

The mean Pn spectrum for each component are superimposed in Figure 3.11d. The noise spectrum shown is that due only to the array site recording system. Pre-event noise was not available due to the insufficient dynamic range of the recording system. The differences between the components are not great. The horizontal spectra merge with the system noise just beyond 20 Hz, while the vertical component is richer in high-frequency energy, merging with the noise near 30 Hz. The spectral notch near 4 Hz may be a consequence of resonance behavior within the valley sediments. Refer ahead to Figure 3.13a where the three-component Pn spectra at the nearby LLNL ELKO station for HARDIN are plotted up to the Nyquist

frequency of 10 Hz. Here, unlike at the array site, the transverse spectrum is generally a good deal lower than the vertical and radial spectra. As a comparison, in Figure 3.14a the LLNL radial Pn spectra is plotted with the mean radial Pn spectra at the array site. With the exception of the 3-5 Hz frequency band, the array spectrum is richer in energy up to about 10 Hz, no doubt due to amplification by lower density sediments underlying the array. The differences between the spectra between 1 and 3 Hz can be reduced somewhat if a higher resolution taper is used; this is shown in Figure A9 of Appendix A.

3.3.2 Pg Spectra

The three-component Pg spectra at Ruby Valley are shown in Figure 3.12. These spectral estimates all come from the 2.6 second windows beginning near 2.9 seconds in Figure 2.19. The range of spectral levels is again about 12 db, and the coefficient of variation here is almost identical to that for Pn on each of the components. The only notable exception is below 2 Hz on the radial component where the Pg variation is about a factor of two less than that for Pn. The vertical-component variation here is again somewhat less than that observed at the Savahia and Rice arrays, but as for Pn, less so with increasing frequency.

The mean Pg spectra for the three components are shown in Figure 3.12d, along with the recording system noise level. Notice that compared to Pn there is much less structure to these spectra. Below about 4 Hz the radial-component spectrum has slightly larger values, though in general the three spectra are very similar and can be characterized simply by a low-frequency slope of about -2.5 up to 5 Hz, then dropping sharply to about a -8 slope at higher frequencies. The signal merges with the noise near 20 Hz. The corresponding Pg spectra at the LLNL station are shown in Figure 3.13b. Again the transverse component is deficient in energy only at the lower frequencies. In Figure 3.14b the LLNL radial Pg spectra is plotted with the mean radial Pg spectra at the array site. Here, the principal difference is the more gradual low-frequency spectral slope of -1 at the LLNL site. Any array site amplification effects are confined to frequencies below 1 Hz, and between 1 and 5 Hz the ELKO site actually recorded

more Pg energy. The two Pg spectra merge between 5 and 10 Hz. Contrasting the spectral differences between the LLNL station and the array for Pn and Pg, it is clear that the site responses are very dependent on the wavetype.

In Figure 3.15 is a summary plot of all the mean Pn and Pg spectra from the two $m_b = 5.5$ explosions. In general, we find the smallest differences occur at the higher frequencies. Pn at the two Mojave arrays produced almost identical mean spectra beyond about 6 Hz. The mean HARDIN Pn spectrum, derived from a very different propagation path, merges with these two Pn spectra near 12 Hz. The mean Pg spectra from all three array sites are nearly equivalent beyond about 6 Hz. If we contrast Pn and Pg at each array site we find much greater differences in spectral amplitude at low frequencies. The high-frequency decay rate of these two wavetypes is the same beyond about 10 Hz at the Mojave arrays and beyond about 7 Hz at the Ruby Valley array. The similarity of Pn and Pg high-frequency decay rates is also seen at the NORESS array (e.g., Baumgardt and Young, 1990). By about 12 Hz the difference among all six Pn and Pg spectra become minimal and they come to share a common high-frequency slope of about -8.

3.4 Pg/Pn Spectral Ratios

Here we will use the mean Pn and Pg amplitude spectra shown above to briefly examine the relative energy content between the Pn and Pg wavefields. We will do this by computing the Pg/Pn power (or energy) spectral ratios for a given source-receiver pair. Combinations of these pairs will tell us the extent to which the energy partitioning between Pn and Pg is maintained over the separation distance of the two array sites on the receiver side, and over the comparable separation distance of the two explosions on the source side.

These spectral ratios can be equivalently thought of as ratios of propagation effects. In general, once a wavefield reaches a distant recording site, the source displacement spectrum, $|S(f)|$, has been modified by propagation, which includes the effects of geometric spreading, attenuation, scattering, and station site response. This can be expressed in terms of an earth

transfer function $G(f,d,\theta)$ for the source, where d is the epicentral distance and θ is the source-to-receiver azimuth. If we also include the signal distortion due to the recording instrument, $I(f)$, and the ambient noise, $N(f)$, which we'll assume to be uncorrelated with the signal, then the measured energy spectrum is given by

$$|A(f)|^2 = |S(f)\ G(f,d,\theta)\ I(f)|^2 + |N(f)\ I(f)|^2 \tag{3.1}$$

So if we have two spectra with the same source spectrum and instrument response, then, after subtracting out the noise energy, the ratio of the measured spectra will be equivalent to a ratio of earth transfer functions. Therefore, Pg/Pn spectral ratios derived from a single source and single recording site display the relative differences in propagation effects between the two phases.

3.4.1 Savahia Mountain and Rice Valley

The Pg/Pn energy spectral ratios from the SALUT and VILLE wavefields are shown in Figure 3.16 over the frequency band for which there was appreciable signal for both phases. The ratios are based on the mean spectra shown earlier. On the average, at both array sites, as frequency increases the power of Pg relative to Pn decreases until finally, between 12 to 13 Hz, Pn actually becomes the more powerful signal, though its strength relative to Pg levels off with increasing frequency. For a given explosion, the sensitivity of the division of energy to the 35 km difference in receiver location is reflected in the differences between the two ratios for that explosion. In Figure 3.16a the Rice energy ratio is consistently greater than that for Savahia below 6 Hz, by as much as a factor of 40. Referring back to Figure 3.15, this is due to the fact that the overall drop in signal amplitude at Rice relative to Savahia is much more significant for Pn than for Pg. The energy balance between Pn and Pg is therefore not maintained for SALUT at the lower frequencies. This is presumably due to the fact that the relationship between the Pn and Pg site responses differs between array sites. Beyond 6 Hz, the differences between the two array sites are much less. For VILLE in Figure 16b, the Rice ratio is again greater at low frequencies but here the greatest differences are confined between

3 and 4 Hz and are no greater than about a factor of ten. The fact that the ratio discrepancies between array sites differ so much between slightly different source locations reflects an azimuthal dependence of low-frequency site effects.

For a given recording site, the sensitivity of the energy ratio to the 40 km difference in source location is also reflected in the differences between the two ratios for that recording site. At Rice the SALUT Pg/Pn ratio is noticeably greater than for VILLE up to about 6 Hz. This is also true at Savahia between about 2 and 6 Hz. This again may reflect an azimuthal dependence. Another possibility are source-related differences, such as SALUT being a more effective generator of Pg energy (independent of its larger yield) due to a difference in properties surrounding the two sources. However it is not clear what these differences in source properties would be.

In general, over the frequency range examined, the division of energy between Pn and Pg is most sensitive to slight changes in path at frequencies between approximately 1 and 5 Hz. Similar to the findings on absolute spectral amplitudes, the spectral energy ratios become less variable at higher frequencies. Appendix B provides an example of how Pn and Pg, as well as Lg, compare in the time domain within various bandpasses.

3.4.2 Ruby Valley

The Pg/Pn energy spectral ratios from the explosion HARDIN are plotted in Figure 3.17. Ratios from all three components of ground motion at both the array site and the LLNL ELKO station are shown. The LLNL ratio values fluctuate more widely and differ more between components. This is perhaps due to stochastic variation at the higher frequencies, which has been reduced at the array site due to spectral averaging. The overall behavior of the ratios at the two sites is similar. The exception is near 2 Hz, however as mentioned earlier, the discrepancy here can be reduced with a higher-resolution data taper. Contrasting the HARDIN spectral ratios with those shown earlier for SALUT and VILLE, notice that while the general structure is similar, that is decreasing ratio values with increasing frequency, the magnitude of

the ratio values is typically much less. Whereas Pn dominates Pg in spectral amplitude beginning near 6 Hz for the NTS-to-Ruby Valley path, Pn does not exceed Pg until near 12 Hz for the NTS-to-Mojave Desert path. These differences reflect the differences in P-wave attenuation properties between these northern and southern portions of the Basin and Range.

3.5 VILLE/SALUT Spectral Ratios

In this section, we will examine source properties from Pn and Pg energy spectral ratios. Spectral models of the explosive source have been described in a number of studies. These include, for example, work by Sharpe (1942), Haskell (1967), Mueller & Murphy (1971), von Seggern & Blandford (1972), and Helberger & Hadley (1981). Evernden *et al.*, (1986) find that the Sharpe model approximates observed explosive source spectra from NTS reasonably well. In this model, if we approximate the source time function by a step-function in pressure, then the displacement amplitude spectrum at the source, $|S(f)|$, of an explosion of yield Y can be parameterized in terms of a low-frequency asymptote $a\,Y$, a corner frequency f_c, and a high-frequency decay having a constant log-log slope of -2 . The relationship can be expressed as

$$|S(f)| = \frac{a\,Y}{1 + \left(\frac{f}{f_c}\right)^2} \tag{3.2}$$

where the constant a is a function of the material properties surrounding the explosion.

If we have two energy spectra $|A_1(f)|^2$ and $|A_2(f)|^2$ with the same earth and instrument transfer functions, then, after subtracting out the noise energy, the ratio of the measured spectra will be equivalent to a ratio of source spectra. For the spectral model above we can predict what this is. If we assume that the corner frequency can be related to yield through

$$f_c = b\,Y^{1/3} \tag{3.3}$$

(e.g., Evernden *et al.*, 1986), where b is a constant which depends on material properties, then the ratio of energy spectra of two explosions having yields Y_1 and Y_2 is given by

$$\frac{|A_2(f)|^2}{|A_1(f)|^2} = \left(\frac{Y_2}{Y_1}\right)^2 \left[\frac{1 + \left(\frac{f}{f_{c1}}\right)^2}{1 + \left(\frac{Y_2}{Y_1}\right)^{2/3} \cdot \left(\frac{f}{f_{c1}}\right)^2}\right]^2 , \tag{3.4}$$

where f_{c1} is the corner frequency corresponding to $A_1(f)$.

Though not identical, the propagation paths for the SALUT and VILLE explosions in this study are similar enough to warrant a brief investigation of source spectral ratios. Specifically, we can compute VILLE/SALUT energy spectral ratios at a fixed array site for both the Pn and Pg wavefields, contrast these with the Sharpe model ratios, and speculate on the causes of any differences. The mean amplitude spectra used to compute the observed energy spectral ratios are shown again in Figures 3.18 and 3.19 for the Pn and Pg wavefields, respectively. The noise corrected ratios are shown in Figures 3.20a and 3.20b. In each figure the VILLE to SALUT energy spectral ratio is shown for both the Rice Valley and Savahia Mountain array sites over the frequency band for which there was appreciable signal. Also shown are the theoretical curves of spectral ratio generated from Equation (3.4) above; adjacent curves are separated by a factor of ten difference in yield ratio. Spectral ratios for other explosive source models such as those mentioned earlier, would display similar behavior, namely a constant value at low frequencies, a transition to larger values around the corner frequency, and finally leveling off at higher frequencies. The corner frequency f_{c1} in (3.4) is taken to be 1 Hz for SALUT, which is about that expected for m_b = 5.5 explosions at Pahute Mesa (Murphy *et al.*, 1989).

The differences between the observed spectral ratios and those predicted by the Sharpe model are considerable. Based on magnitude-yield relations for NTS (Evernden,1987), the actual VILLE/SALUT yield ratio should be about 0.03. Except for the Pg ratio at Savahia near 1 Hz, the observed ratios fall well below the 0.03 contour. In fact, rather than displaying ratio values which monotonically increase with increasing frequency, the observed ratios increase only up to at most a bit past 2 Hz. Beyond this, the ratios in general decrease with

increasing frequency, reaching minimal values between about 2 and 4 orders of magnitude less than those predicted, depending on the array site and wave type. The difference between the two Pn ratios, as well as the two Pg ratios, is most likely due to the small difference in propagation path arising from the 35 km separation of the two array sites. The differences between the Pg and Pn ratios, for example the somewhat greater Pn ratio values between about 2 and 6 Hz, are most likely due to propagation differences between Pn and Pg. For a given array site, these are differences in earth transfer function ratio G_2 / G_1, which, recall, are not entirely canceled out due to the 40 km separation of the two sources.

Now let's examine possible explanations for the basic observation that, for each of the four computed ratios, relative to the Sharpe model predictions, the VILLE wavefield appears deficient in spectral energy, and increasingly so above 1 to 3 Hz, depending on the array site and wave type. For our data set, discrepancies between the predicted ratios and those observed should arise principally for two reasons: (1) source-to-receiver propagation path differences due to the 40 km separation of the two sources and (2) source depth effects. The fact that the differences between the spectral ratios arising from the 35 km separation of recording sites are relatively small argues against major discrepancies with the model due to propagation path differences arising from the 40 km separation of the two sources. With regard to source depth effects, the model does not account for the effects of spall, amplitude-dependent attenuation, and differences in medium properties between the two shot points. The effect of spall is to act as a delayed secondary source which will add energy to the signal spectrum. Consequently, low spectral ratios values could result over the bandwidth where the SALUT spall effect is more pronounced than the VILLE spall effect. However, for an explosion the size and depth of SALUT, the addition of significant spall energy is restricted primarily to frequencies below about 1 Hz (Taylor and Randall, 1989). Therefore, at best, it appears than spall can account for the low spectral ratio values only near 1 Hz in Figures 3.20a and 3.20b. At higher frequencies, attenuation effects arising from the 311 m separation in source depth may be responsible, as described below.

In the region surrounding an explosion where large strains result in a non-linear behavior of the wavefield, the attenuation may be modeled as a linear function of strain, ε,

$$Q^{-1}(f,\varepsilon) = Q_0^{-1}(f) + \gamma\,\varepsilon \tag{3.5}$$

(e.g., Mavko, 1979, Minster and Day, 1986). The sensitivity to strain is determined by the constant γ, which is a function of rock type, microstructure (crack density, porosity, grain size), confining pressure, and volatile content, and can range in value from near 1 to 1000 (Bonner *et al.*, 1989). The question here is whether $Q^{-1}(f,\varepsilon)$ surrounding the VILLE source is sufficiently larger than that surrounding the SALUT source such that by the time the wavefields leave the source area, the VILLE wavefield is depleted in 1 to 20 Hz energy more so than SALUT.

While the strain amplitude, ε, is certainly greater for the the larger explosion SALUT, and would therefore contribute to greater attenuation, this may be over compensated by other attenuation effects. For instance, due to the lower confining pressure at shallower depth, the strain-independent attenuation $Q_0(f)^{-1}$ experienced by the downgoing VILLE wavefield above the depth of SALUT should be greater than that experienced the downgoing SALUT wavefield. In addition, the strain sensitivity γ is larger for shallower, relatively higher attenuating, lower modulus materials, but can be decreased greatly with increased confining pressure. Also, being above the water table, the source coupling is less for VILLE than for SALUT, which was below the water table. Therefore, in addition to a larger $Q_0(f)$ for the VILLE explosion we should also expect that γ surrounding the VILLE explosion to be significantly greater than that surrounding the deeper SALUT explosion. While these parameters are difficult to quantify, it seems likely that the values of $Q_0(f)$, γ, and ε should have resulted in a greater net attenuation for VILLE, which could explain much of the anomalous spectral ratio behavior. The indication here is that source depth appears to have a significant effect on the emitted wavefield and that discriminates based on the spectral characteristics of explosions must bear in mind attenuation effects which may be strongly depth, as well as yield, dependent.

3.6 Summary Discussion

In this chapter we have examined a number of spectral characteristics of regional Pn and Pg wavefields recorded outside the Nevada Test Site. The principal findings are listed below.

Signal Bandwidth

For the m_b = 5.5 explosions, SALUT and HARDIN, we find the vertical component Pn signal recorded above the noise to approximately 30 Hz. The Pn horizontal components at the Ruby Valley array merge with the noise closer to 20 Hz. The Pg high-frequency spectral amplitude levels are somewhat less than for Pn. The SALUT Pg wavefield and all three components of the HARDIN Pg wavefield reach the noise near 20 Hz. For the smaller m_b = 4.4 VILLE explosion both the Pn and Pg signals reach the noise near only 13 Hz. In the context of a low-yield test ban treaty, effective high-frequency monitoring of small-magnitude events, smaller still than VILLE, will require good signal to noise ratios - the 13 Hz signal limit for VILLE suggests that we may have to depend on low-noise borehole instruments to increase the signal bandwidths for small events.

Spatial Variation in Spectral Amplitude

Over the 4 km aperture of the Rice Valley and Savahia Mountain arrays, spectral amplitude levels vary by as much as 30 db. However, it is significant that at high frequencies the mean of these widely varying spectra regress to very similar means between array sites (Figure 3.15). This underscores the usefulness of spatial averaging for reliable estimates of regional spectra. Over the 1.5 km aperture of the Ruby Valley array the maximum difference in spectral levels drops to about 12 db for each of the three components. The means of the three-component spectra are almost identical.

The coefficient of variation was found to be most consistently dependent on recording site characteristics rather than on wavetype or source properties. The spectral variation is greater over the larger aperture arrays, but only up to about 7 Hz, beyond which there is little

difference in variation between the 1.5 km and 4 km arrays. The greatest variation exists at the Savahia Mountain array site. At the Ruby Valley site, the spectral variation of the horizontal components becomes as low or lower than the vertical variation as the frequency increases beyond about 5 Hz.

If we consider the spectral variation over the much larger distance between array sites, we find much greater variation below 6 Hz. Beyond 6 Hz the differences in spectra between the three array sites becomes very small.

Spectral Energy Ratios

The Pg/Pn ratios we examined display the common feature that the amount of Pg energy relative to Pn decreases, on the average, with increasing frequency. Pn eventually becomes the dominant signal. The magnitude of the ratio values is strongly dependent on the source-array site combination with the greatest differences taking place at the lower frequencies. Finally, the anomalous behavior of the VILLE/SALUT spectral ratios indicates that depth-dependent attenuation effects on these regional wavefields is significant.

An important point to make from this chapter is that variations in mean spectral amplitude and energy ratios due to array-site separation appear more stable at the higher frequencies. This observation is somewhat reassuring given that it is the high-frequency spectral characteristics which are particularly important in low-yield seismic monitoring.

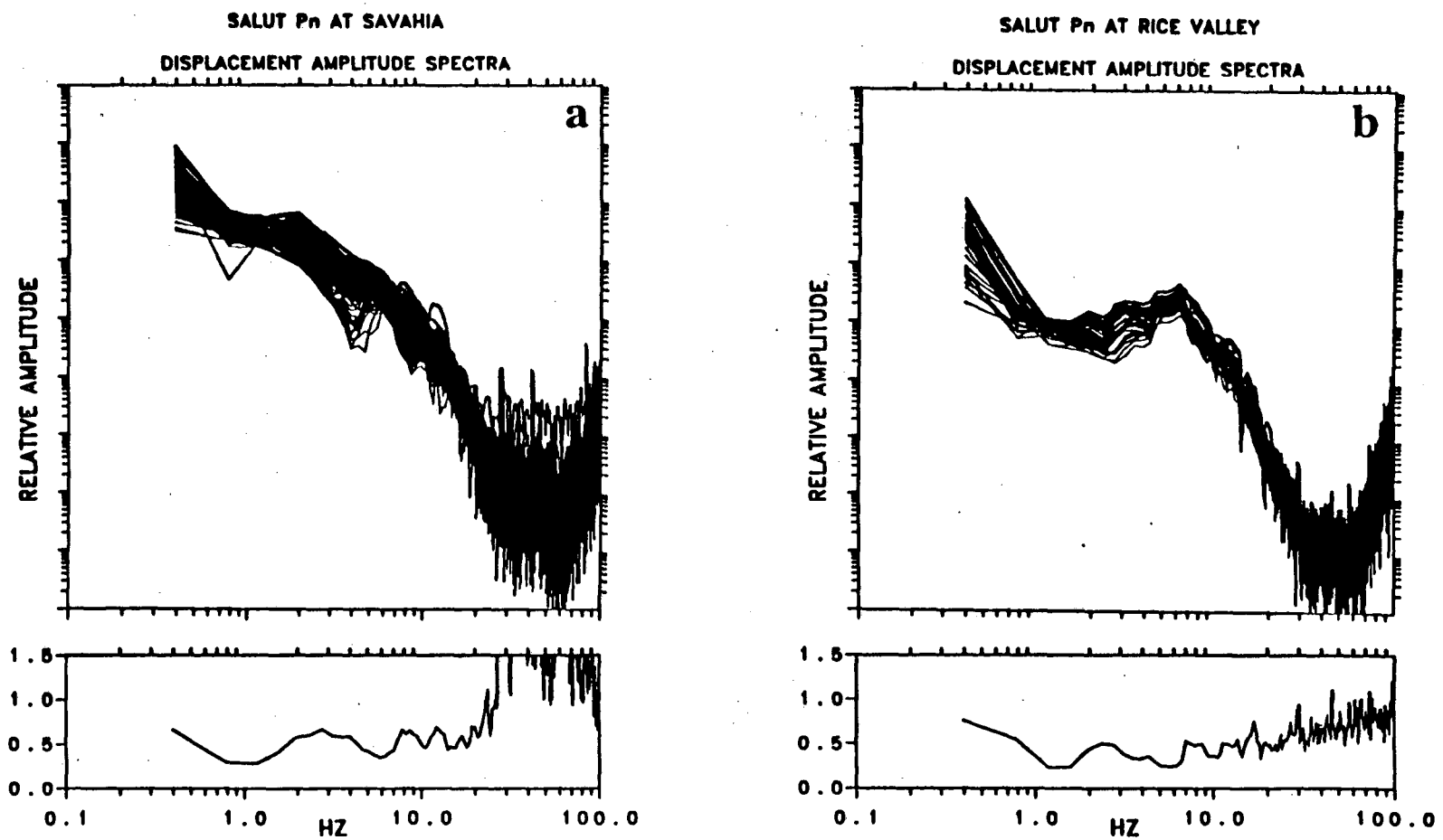

FIG. 3.1 Instrument-corrected Pn displacement amplitude spectral estimates for SALUT at the Savahia Mountain and Rice Valley arrays. (a) For Savahia, spectra from the 145 waveforms in FIG. 2.6 are plotted. (b) For Rice, spectra from the 47 waveforms in FIG. 2.8 are plotted. Each spectrum is computed from the first 2.6 seconds following the onset of Pn. The spectral estimates are made using the multiple 3π tapering described in Appendix A. The maximum sensor separation for both groups of spectra is approximately 4 km. Also shown is the coefficient of variation for each group of spectra.

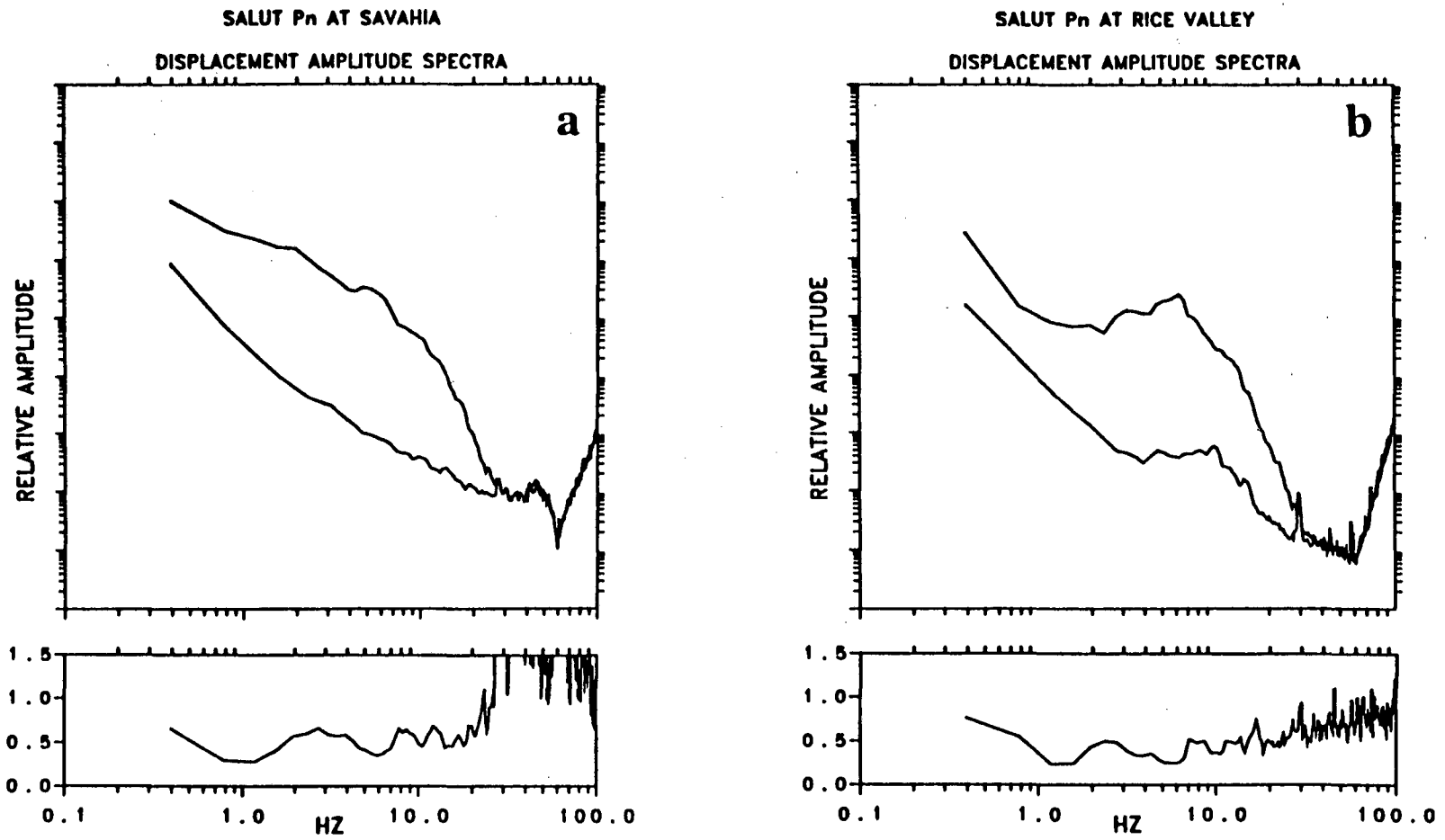

FIG. 3.2 Mean Pn displacement amplitude spectra from Figure 3.1 and the mean pre-event noise averaged over noise estimates from each station. Also shown is the coefficient of variation of the Pn spectra, as in Figure 3.1

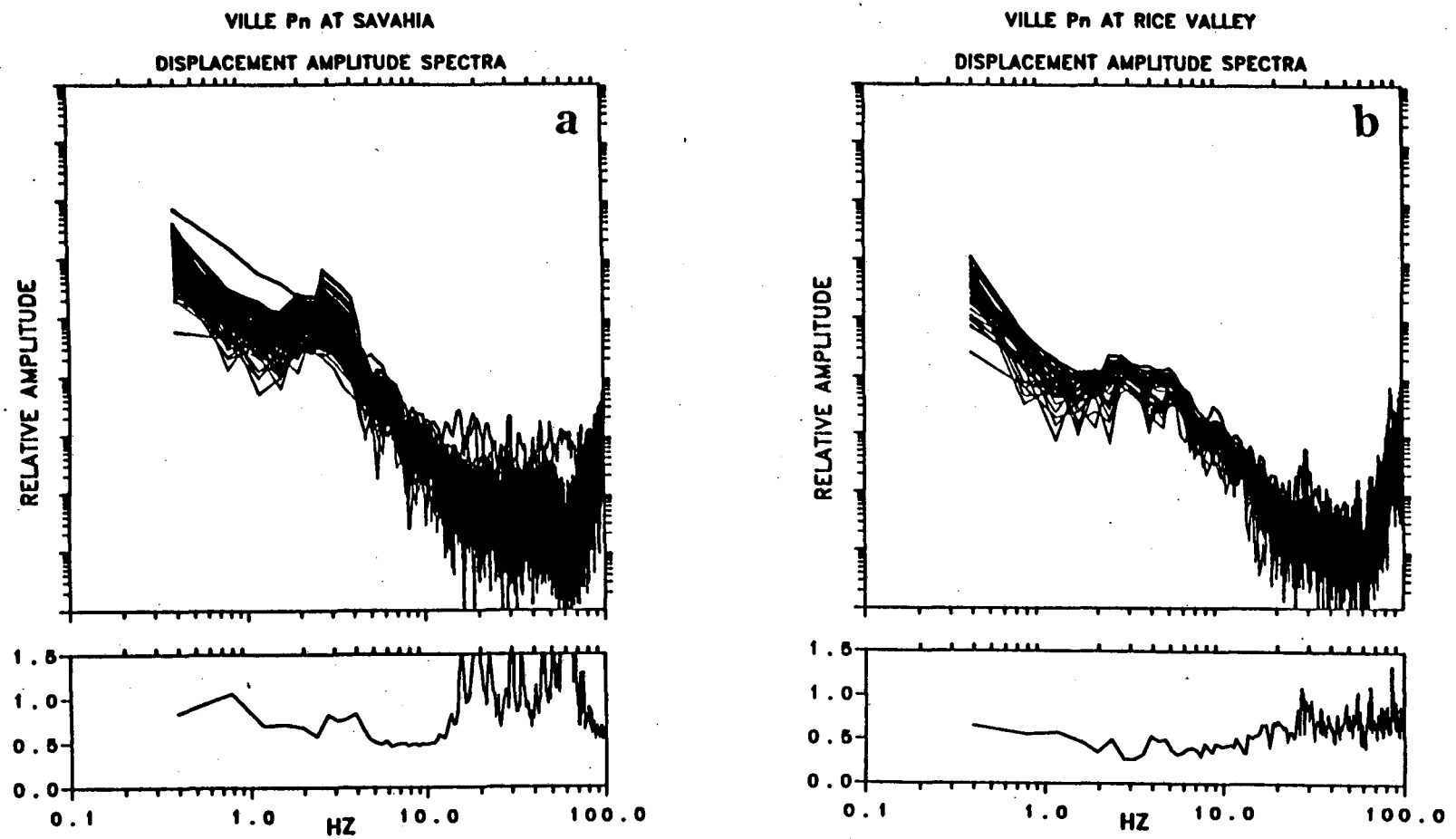

FIG. 3.3 Instrument-corrected Pn displacement amplitude spectral estimates for VILLE at the Savahia Mountain and Rice Valley arrays. (a) For Savahia, spectra from the 145 waveforms in FIG. 2.9 are plotted. (b) For Rice, spectra from the 47 waveforms in FIG. 2.10 are plotted. Each spectrum is computed from the first 2.6 seconds following the onset of Pn. The spectral estimates are made using the multiple 3π tapering described in Appendix A. The maximum sensor separation for both groups of spectra is approximately 4 km. Also shown in the figure is the coefficient of variation of the spectra.

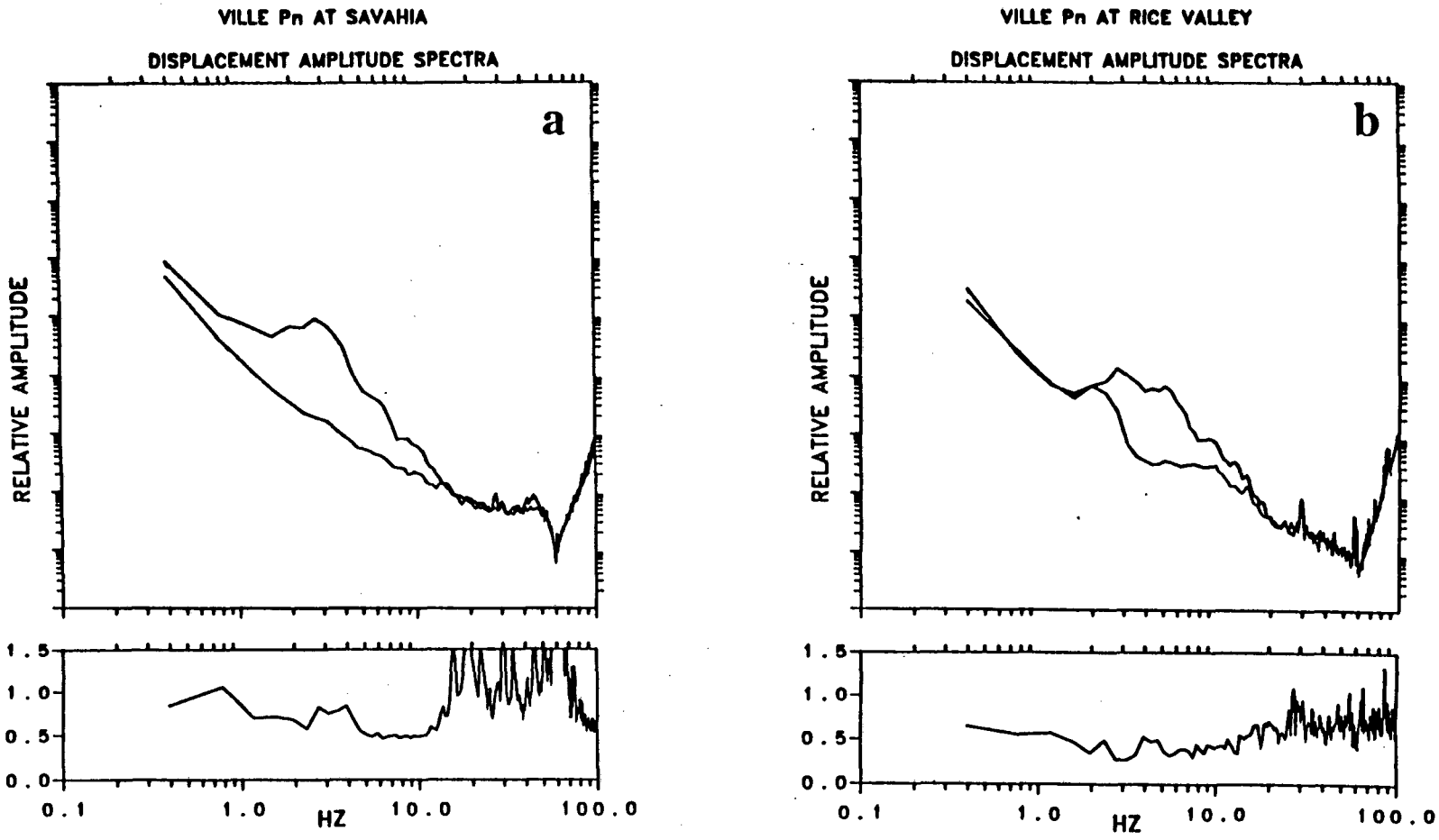

FIG. 3.4 Mean Pn displacement amplitude spectrum from Figure 3.3 and the mean pre-event noise averaged over noise estimates from each station. Also shown is the coefficient of variation of the Pn spectra, as in Figure 3.3.

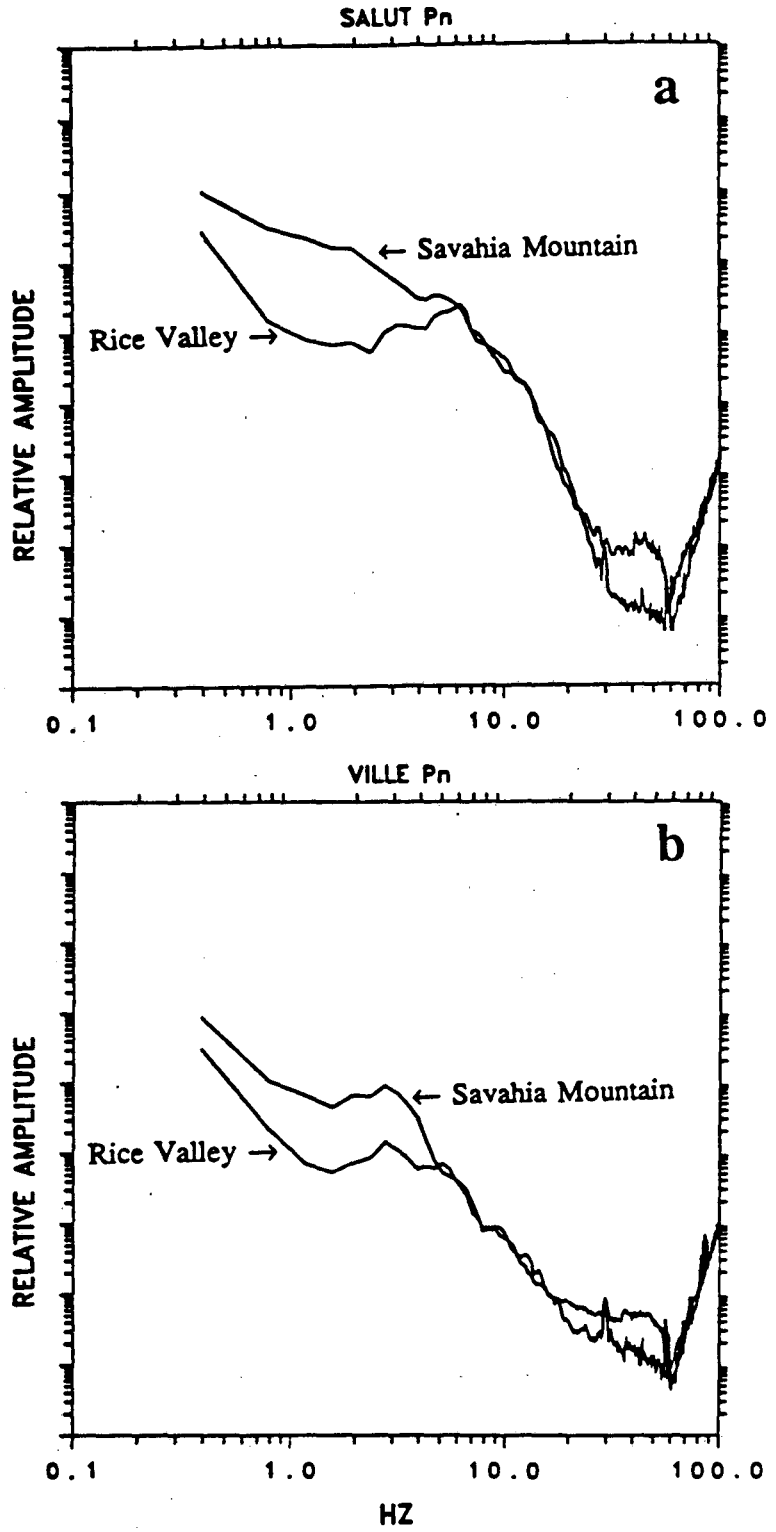

FIG. 3.5 Superimposed mean instrument-corrected Pn displacement amplitude spectra (replotted from Figures 3.2 and 3.4).

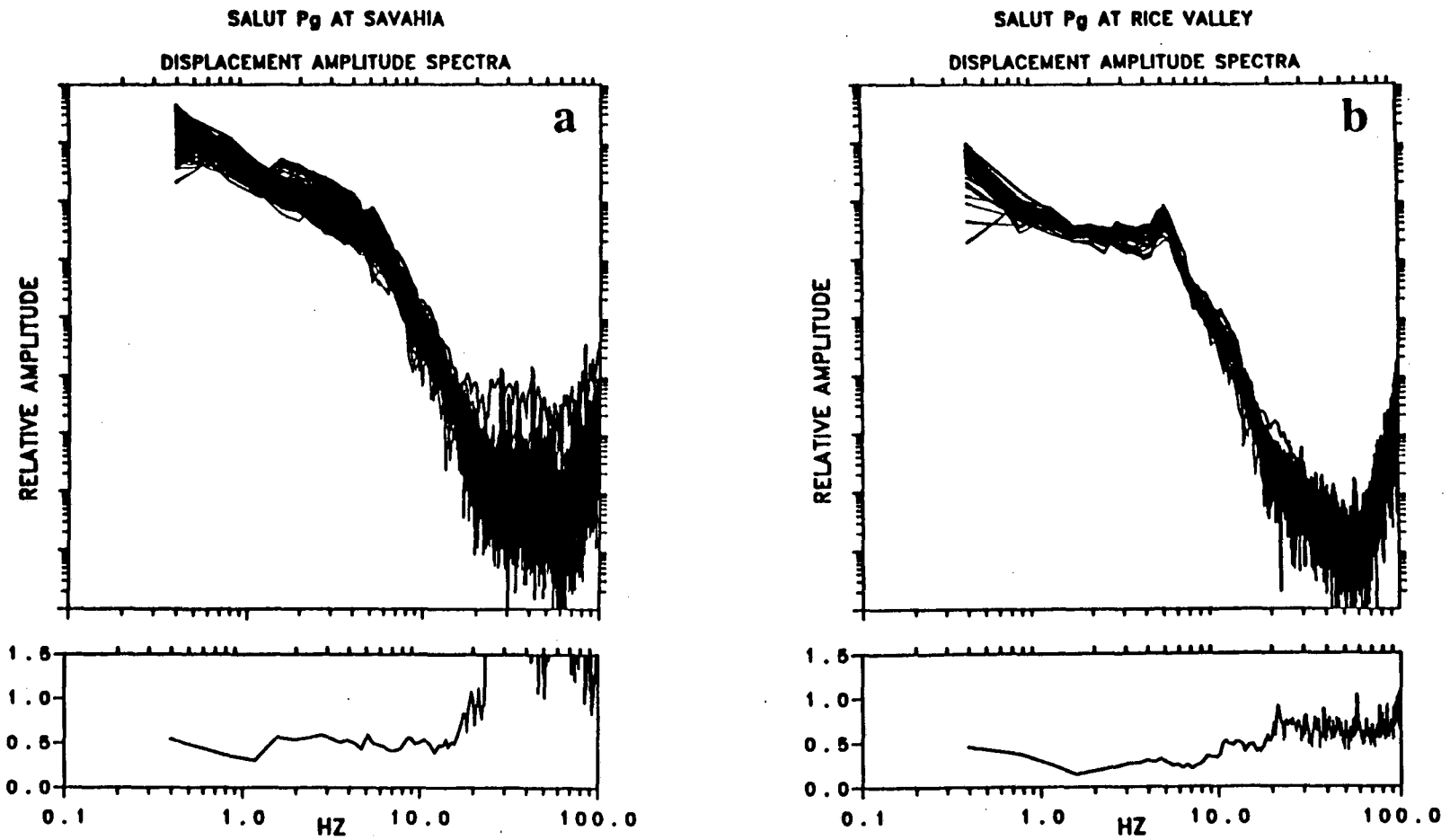

FIG. 3.6 Same as Figure 3.1, but for Pg.

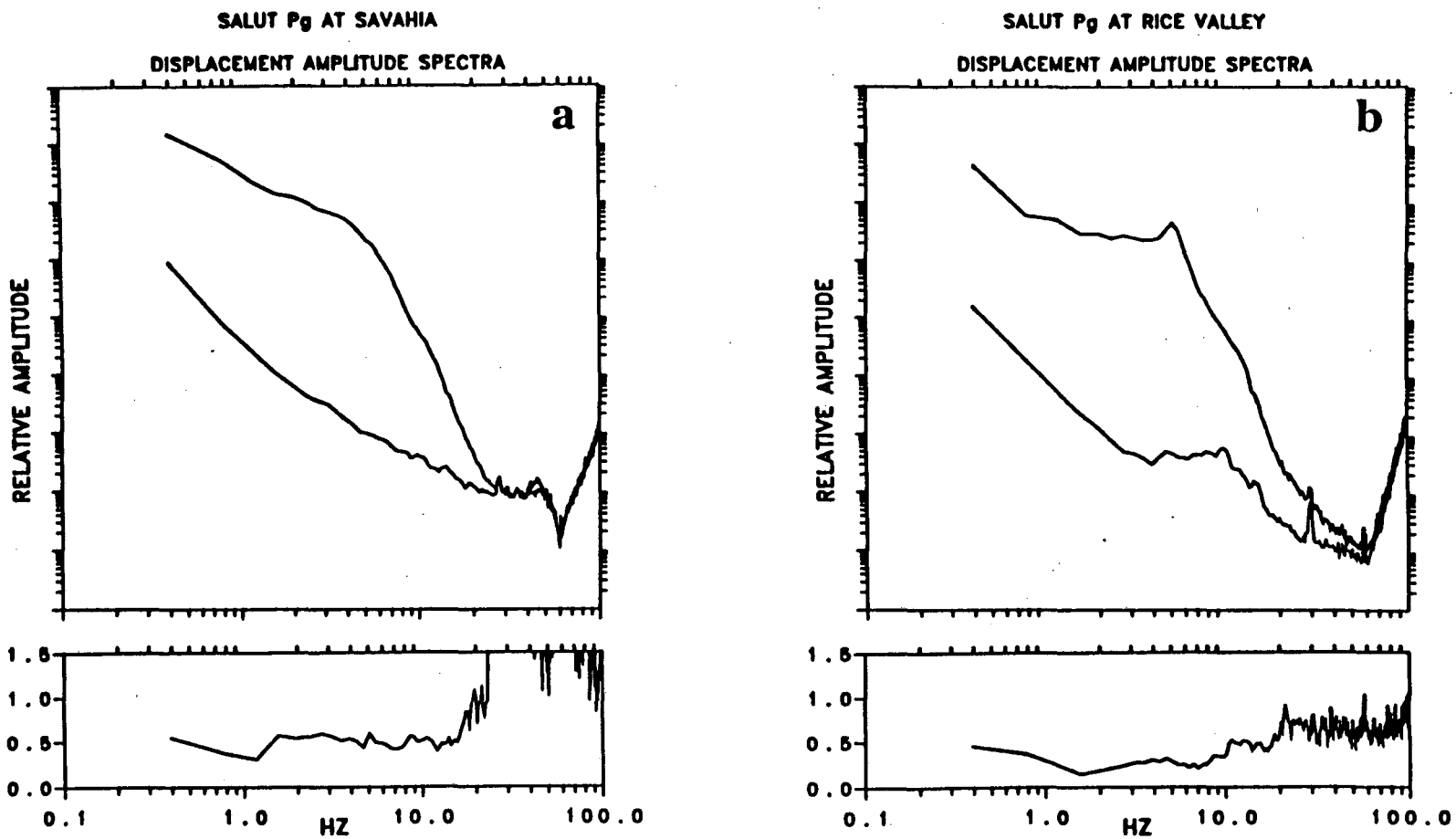

FIG. 3.7 Mean Pg displacement amplitude spectra from Figure 3.6 and the mean pre-event noise averaged over noise estimates from each station. Also shown is the coefficient of variation of the Pg spectra, as in Figure 3.6.

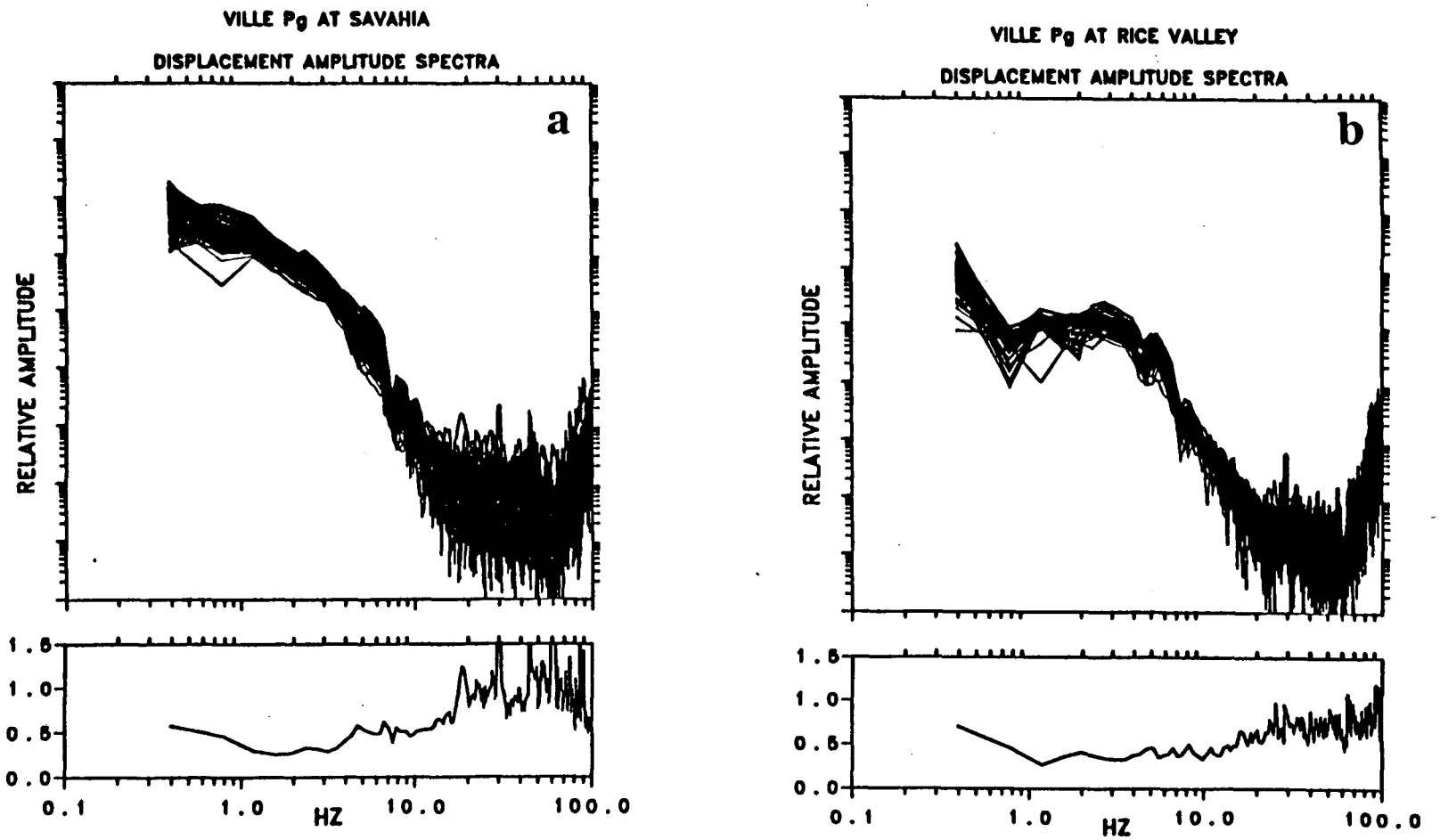

FIG. 3.8 Same as Figure 3.3, but for Pg.

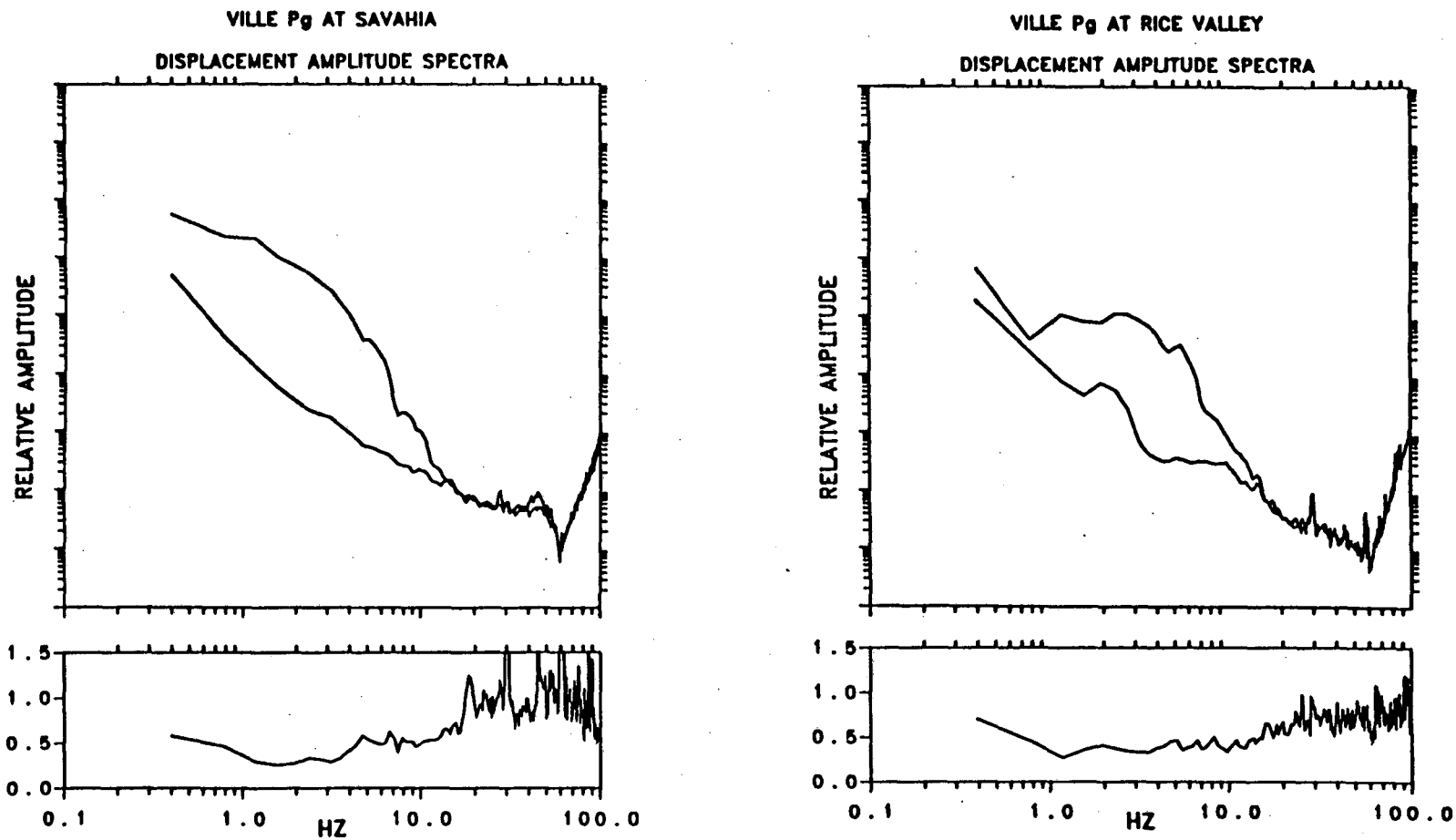

FIG. 3.9 Mean Pg displacement amplitude spectrum from Figure 3.8 and the mean pre-event noise averaged over noise estimates from each station. Also shown is the coefficient of variation of the Pg spectra, as in Figure 3.8.

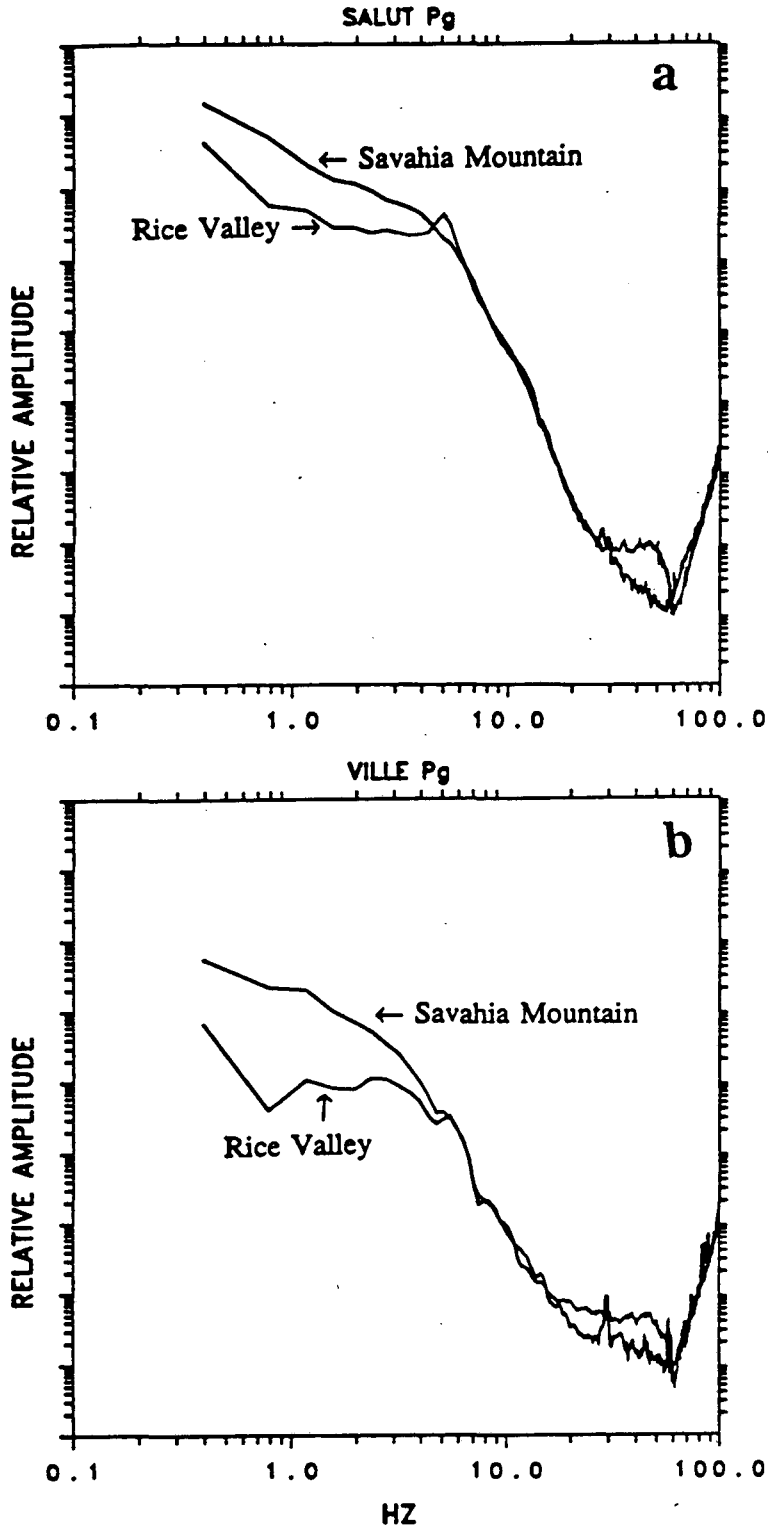

FIG. 3.10 Superimposed mean instrument-corrected Pg displacement amplitude spectra (replotted from Figures 3.7 and 3.9).

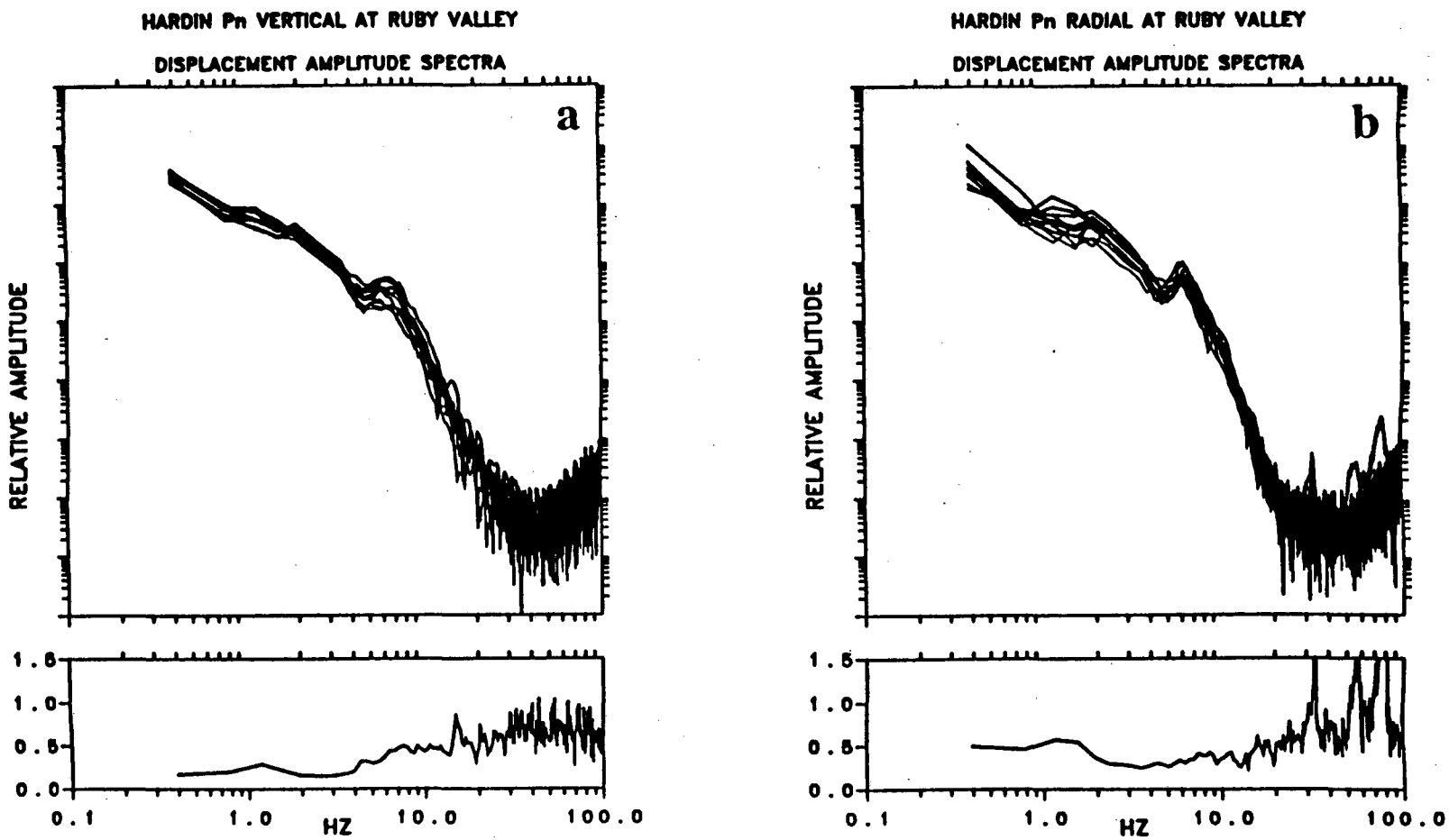

FIG. 3.11 Instrument-corrected Pn displacement amplitude spectral estimates for HARDIN at the Ruby Valley array. Spectra from the 3-component waveforms in Figures 2.18 are plotted. For (a) the vertical component, the spectra are computed from the first 2.6 seconds following the onset of Pn. For (b) the radial and (c) transverse components, because so much of the initial Pn energy is delayed, the spectra are computed from the 2.6 second window occurring 1.2 seconds beyond the Pn onset. The spectral means are superimposed in (d), which also shows the system noise spectrum. The spectral estimates are made using the multiple 3π tapering described in Appendix A. The maximum sensor separation for this array is approximately 1.5 km. Also shown in the figures are the coefficient of variations of the spectra.

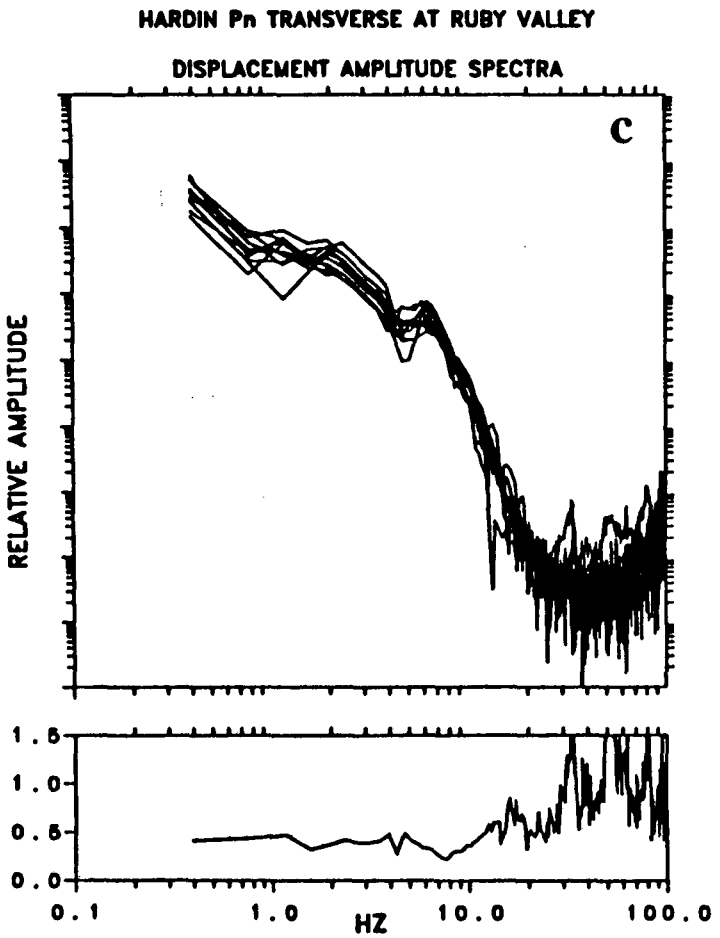

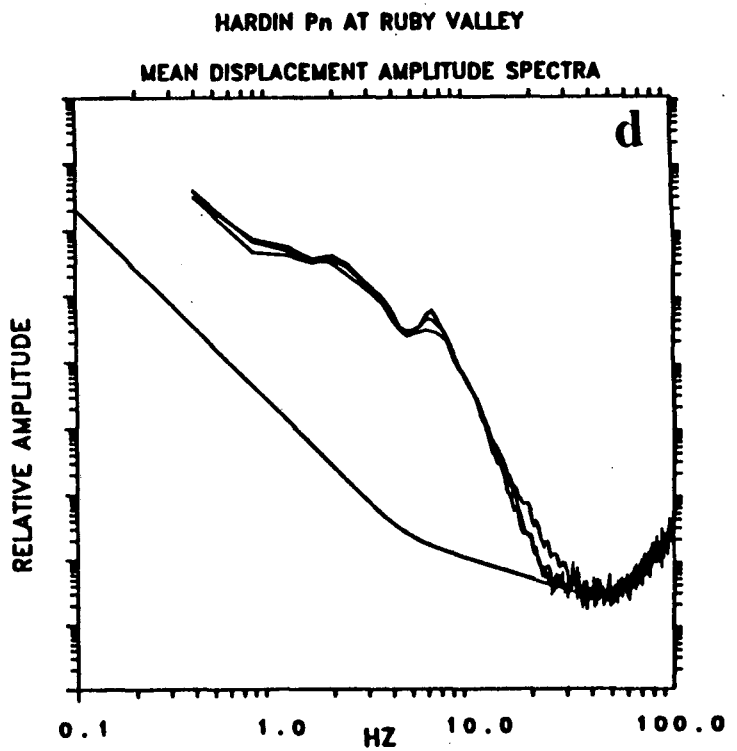

FIG. 3.11 continued

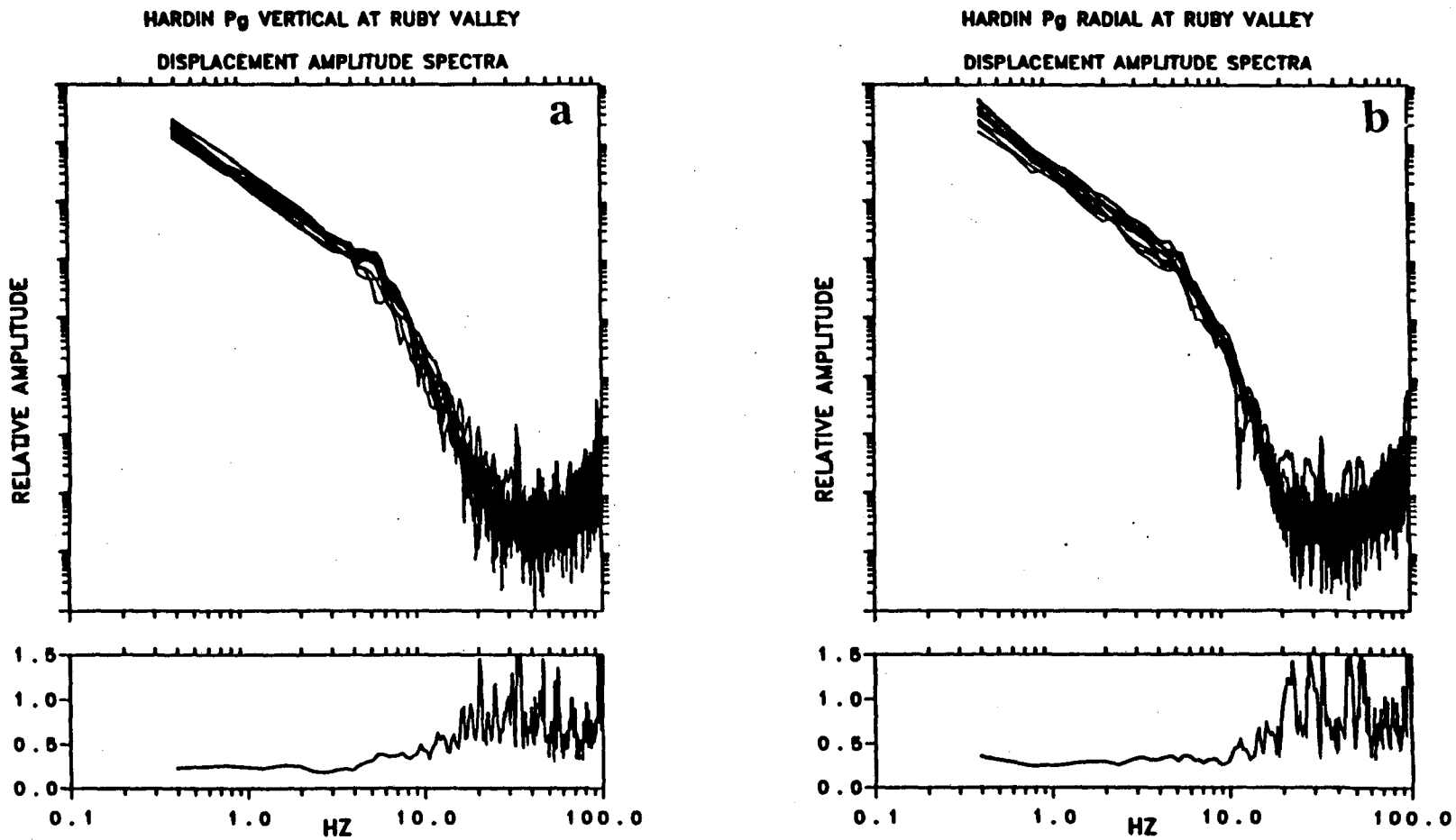

FIG. 3.12 Instrument-corrected Pg displacement amplitude spectral estimates for HARDIN at the Ruby Valley array. For all three components, the spectra are computed from the 2.6 second window beginning at 2.9 seconds in Figure 2.19. The spectral means are superimposed in (d), which also shows the system noise spectrum. The spectral estimates are made using the multiple 3π tapering described in Appendix A. The maximum sensor separation for this array is approximately 1.5 km. Also shown in the figure is the coefficient of variation of the spectra.

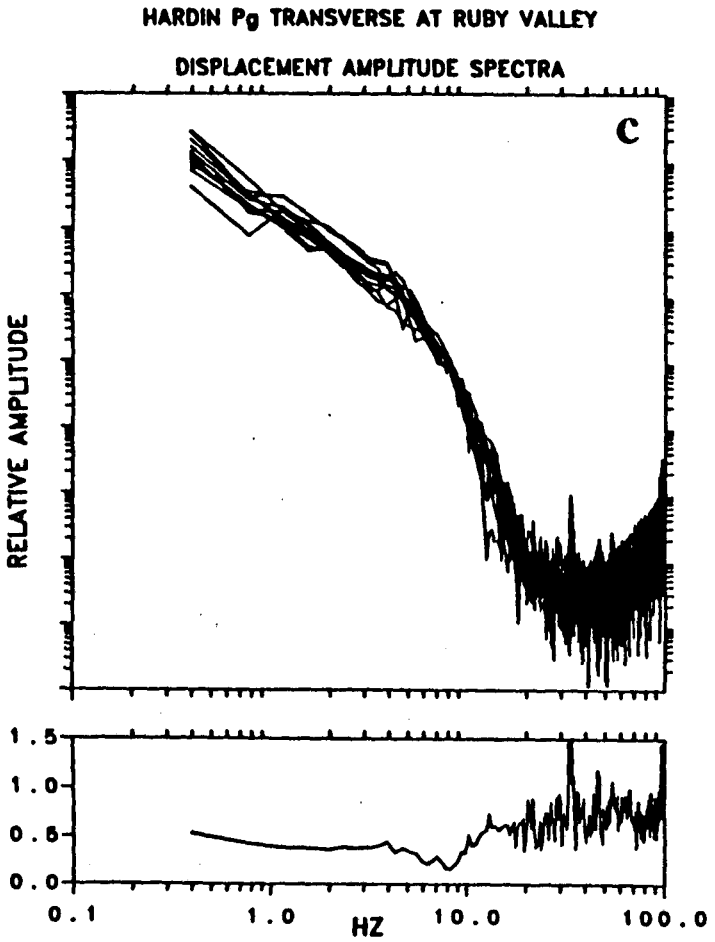

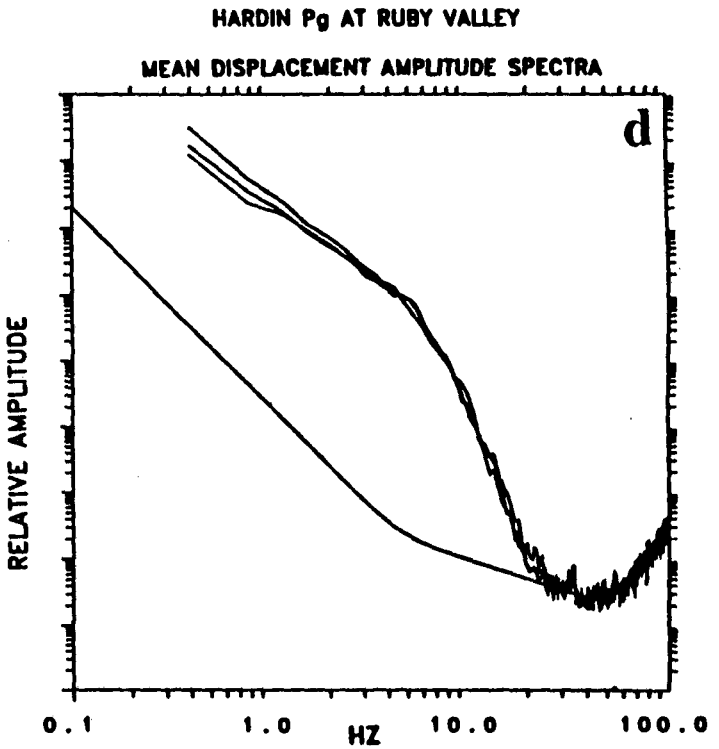

FIG. 3.12 continued

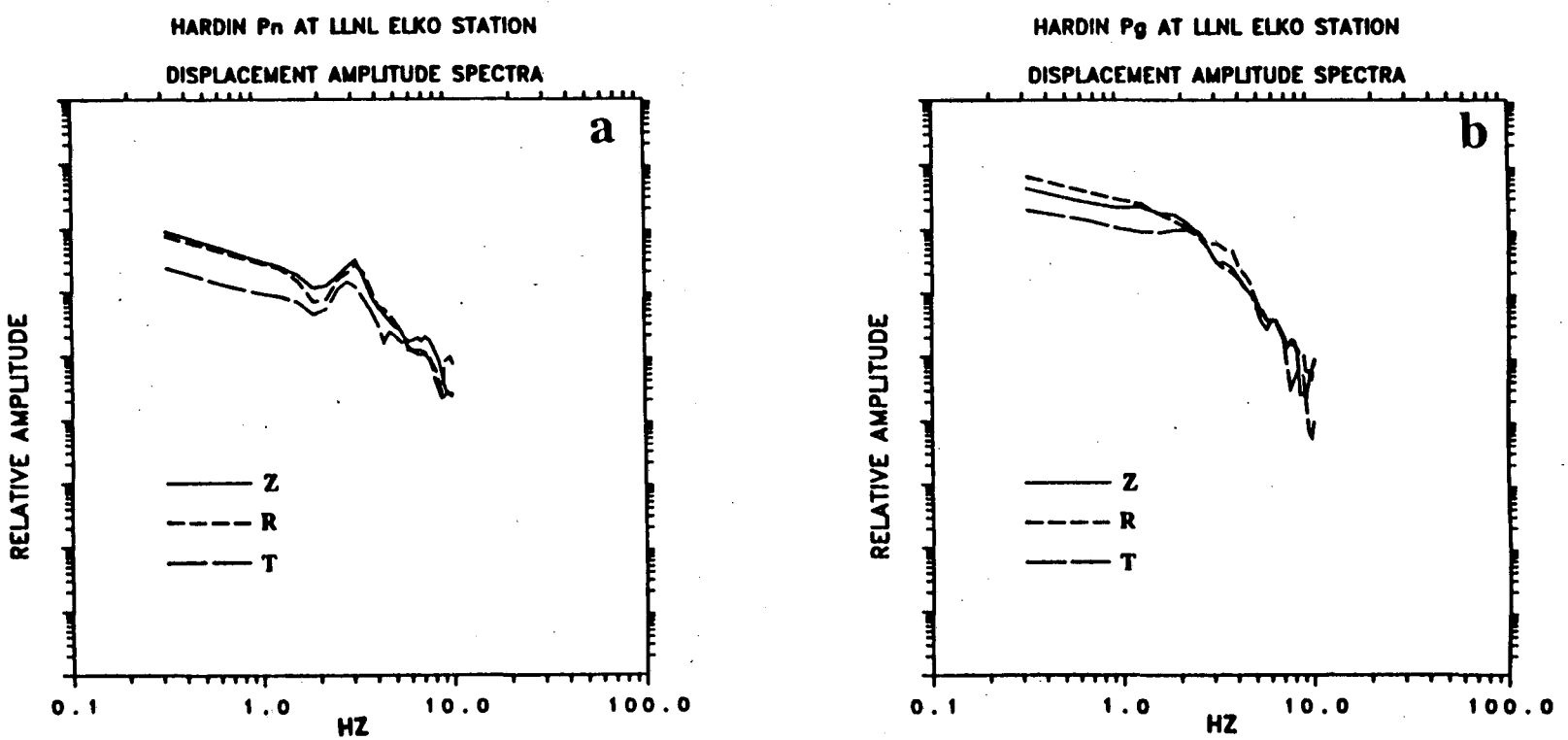

FIG. 3.13 (a) Pn and (b) Pg three-component amplitude spectra for HARDIN at the LLNL ELKO station, located 15 km away from the Ruby Valley array site. The spectra are instrument corrected and remain well above the noise up to the 10 Hz Nyquist frequency.

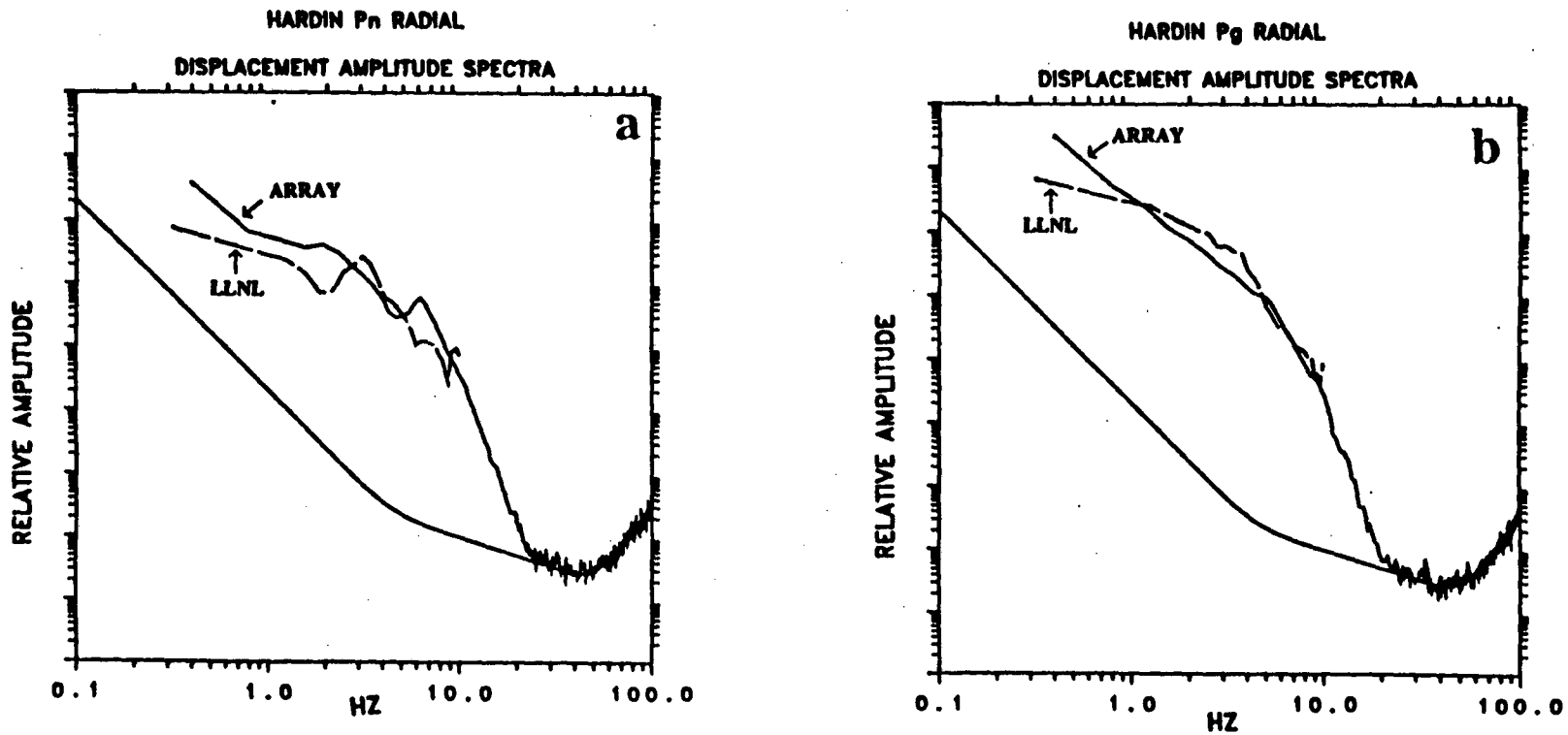

FIG. 3.14 Mean radial amplitude spectra for HARDIN at the Ruby Valley array displayed with the corresponding radial amplitude spectra at the LLNL station from Figure 3.13 for (a) Pn and (b) Pg.

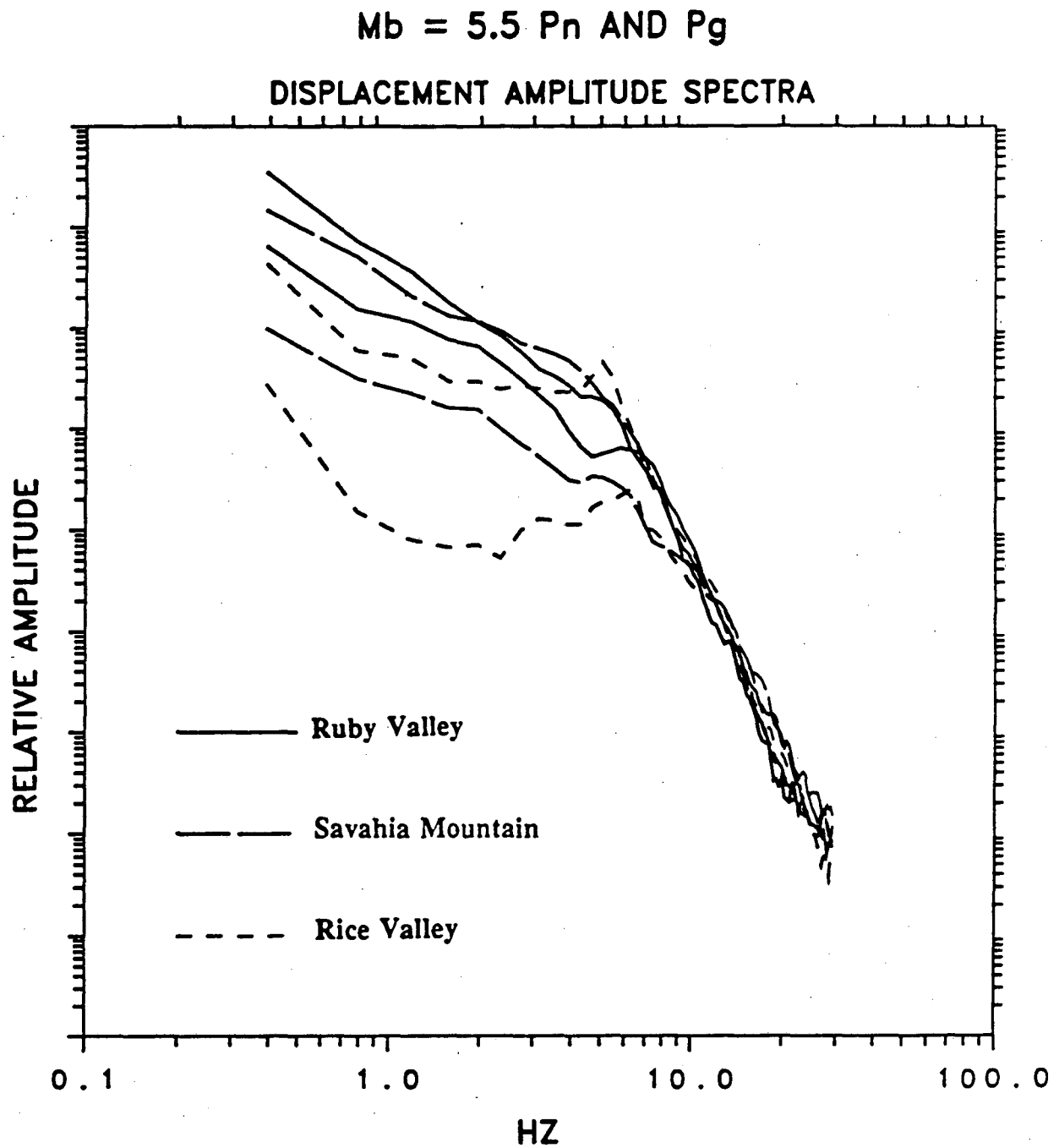

FIG. 3.15 Mean m_b = 5.5 Pn and Pg spectra recorded at the Savahia Mountain and Rice Valley arrays (explosion SALUT) and at the Ruby Valley array (explosion HARDIN). Each Pg spectrum can be distinguished from its corresponding Pn spectrum by its larger low-frequency amplitudes. Note the similarity of high-frequency decay among the six spectra.

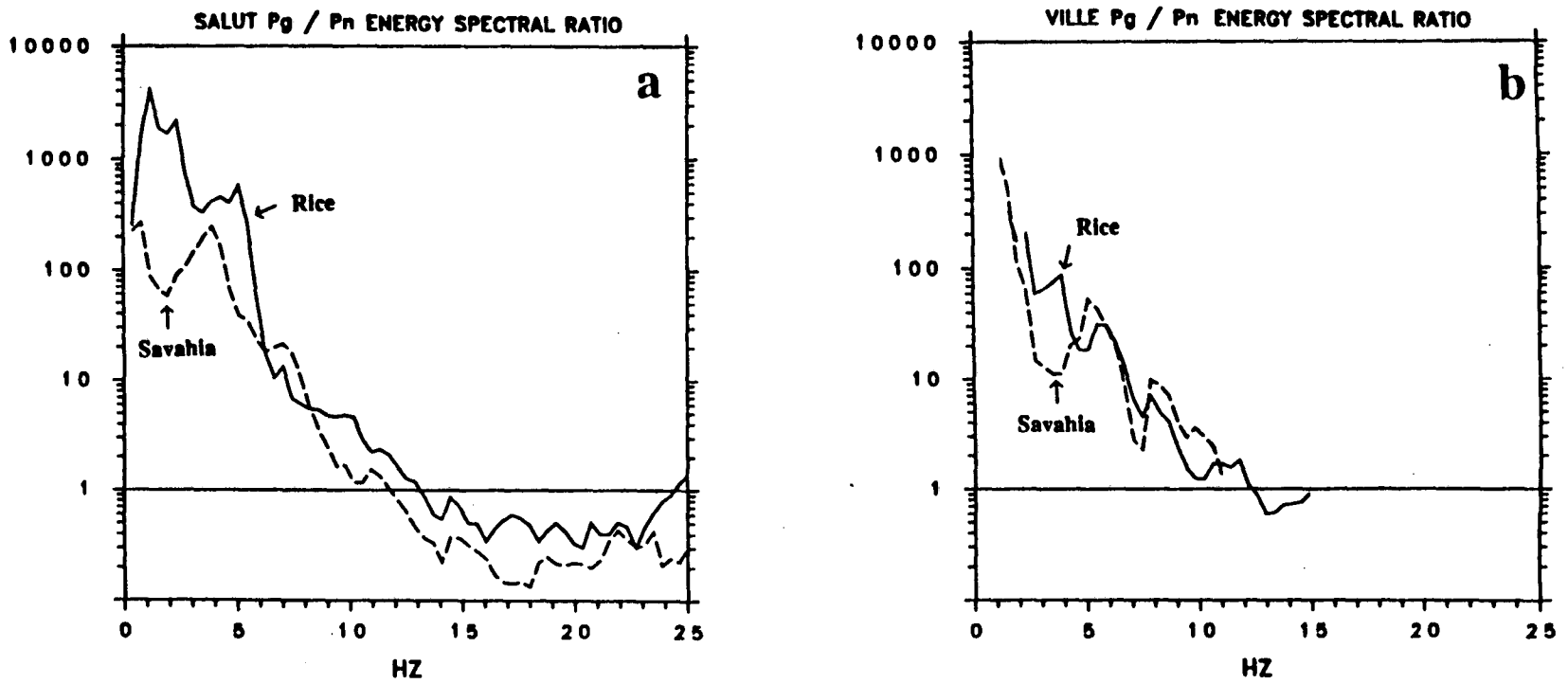

FIG. 3.16 Ratio of the Pg spectral energy to the Pn spectral energy at Rice Valley and Savahia Mountain for the explosions (a) SALUT and (b) VILLE. The ratios were computed from the mean spectral amplitudes shown earlier, and are plotted over the frequency range for which the signal energy is above the noise energy.

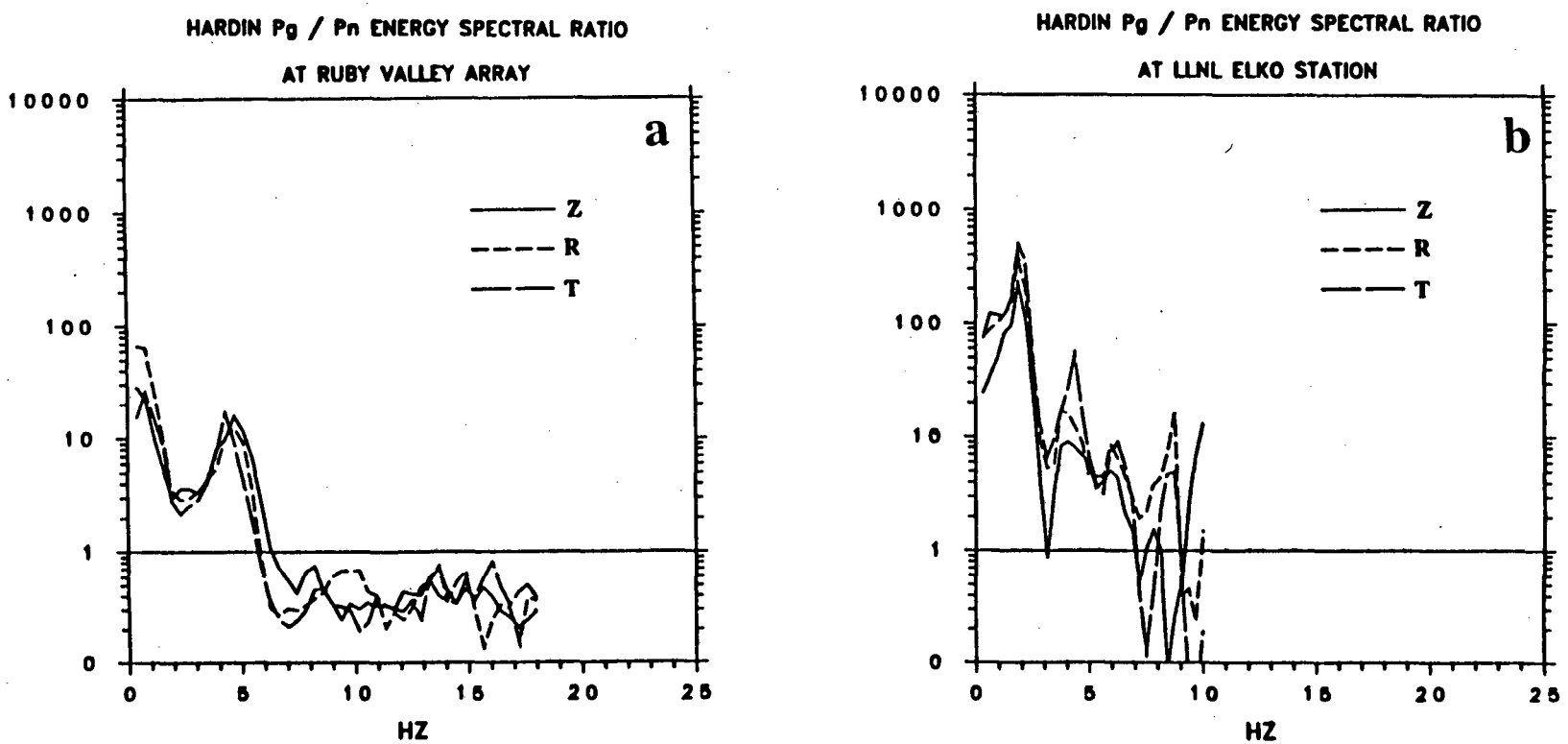

FIG. 3.17 Ratio of the Pg spectral energy to the Pn spectral energy at Ruby valley for the explosion HARDIN. The ratios were computed from the mean spectral amplitudes shown earlier, and are plotted over the frequency range for which the signal power is above the noise power.

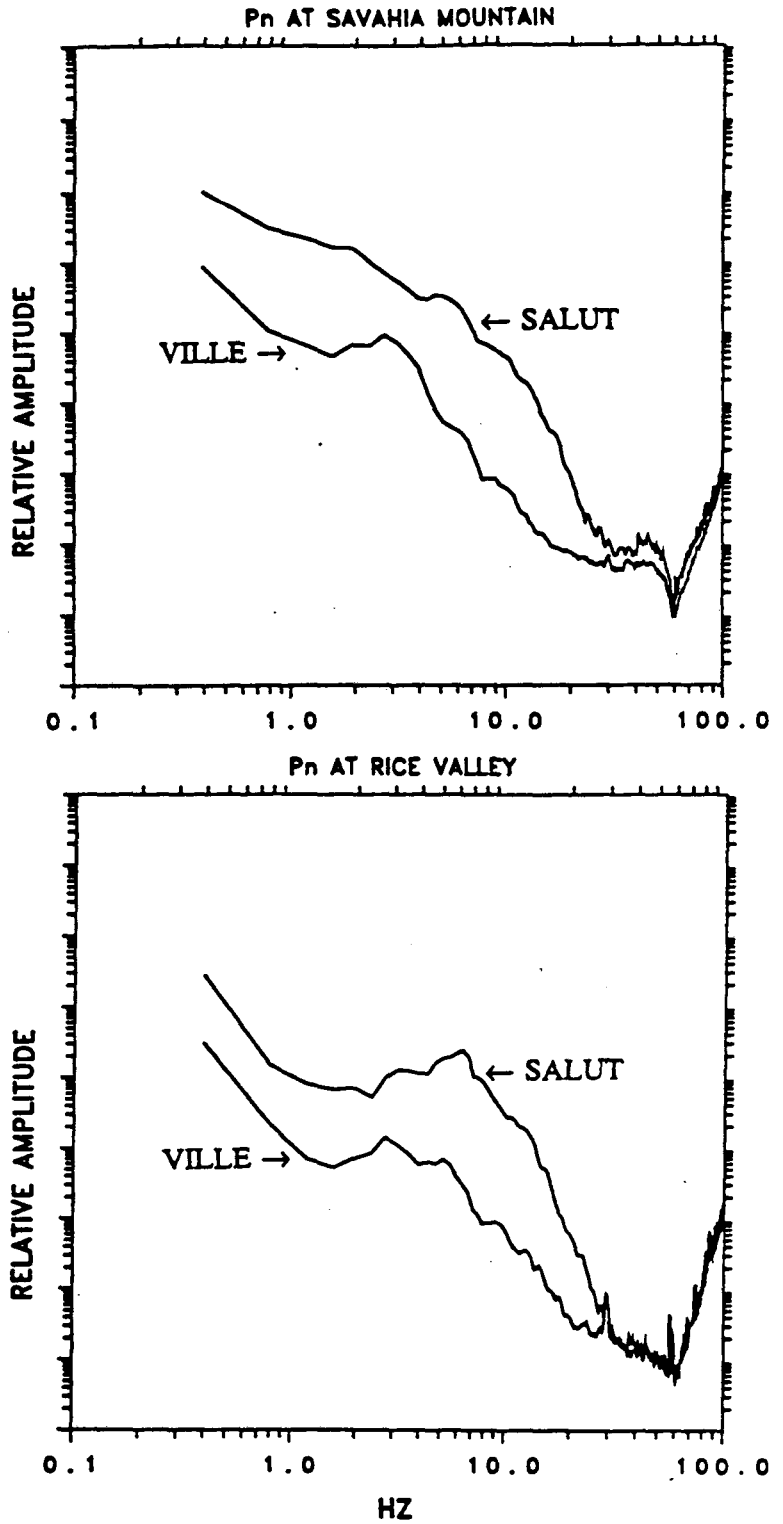

FIG. 3.18 Superimposed mean SALUT and VILLE Pn displacement amplitude spectra (replotted from Figures 3.2 and 3.4).

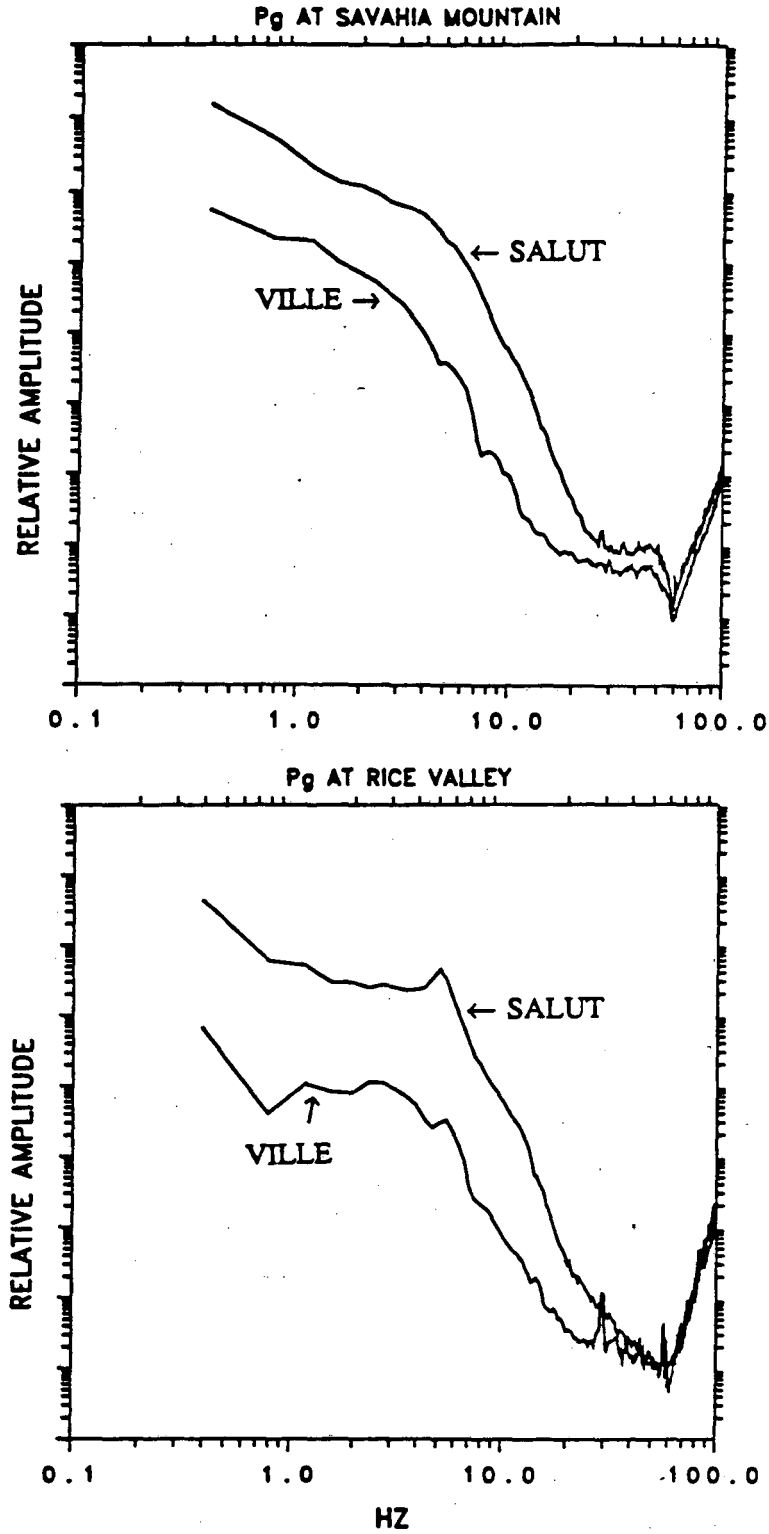

FIG. 3.19 Superimposed mean SALUT and VILLE Pn displacement amplitude spectra (replotted from Figures 3.7 and 3.9).

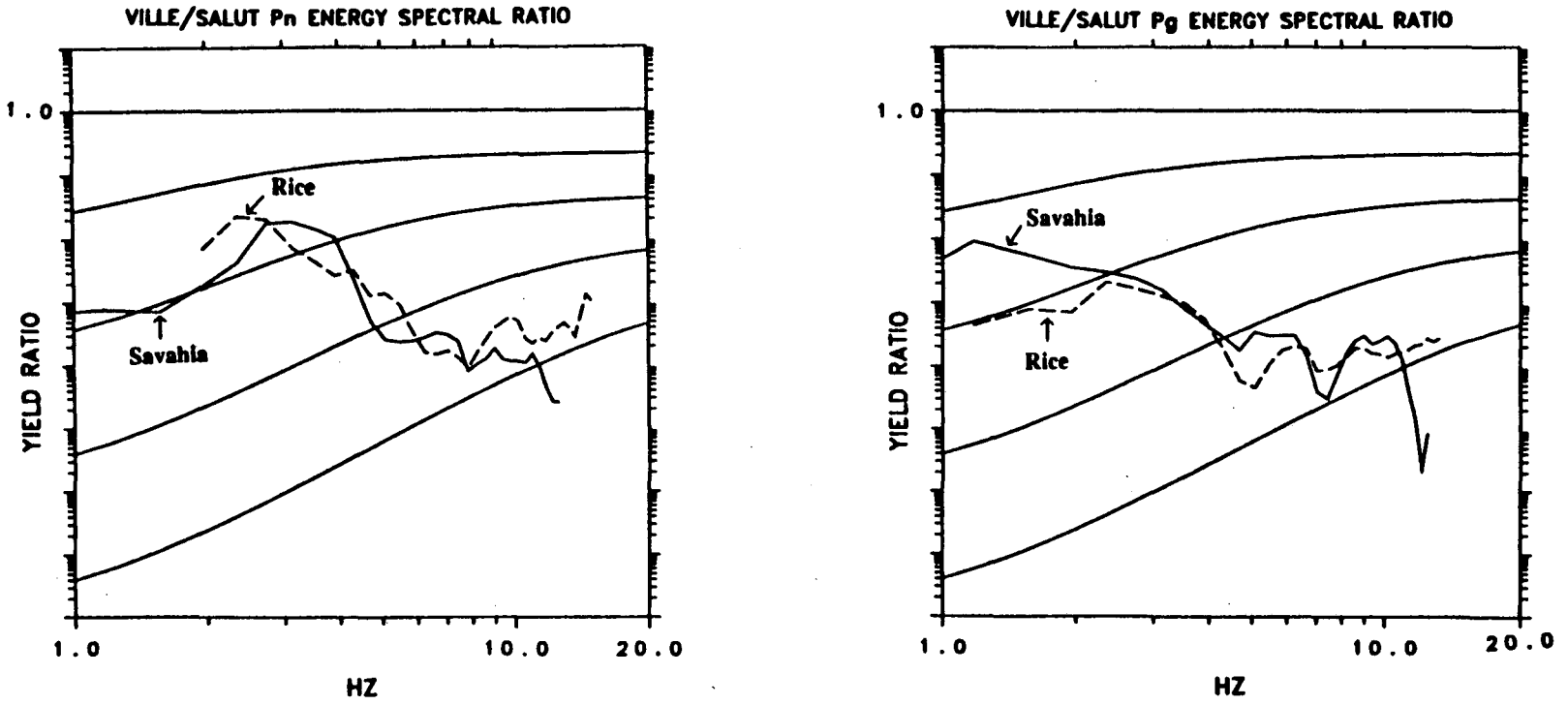

FIG. 3.20 VILLE/SALUT spectral energy ratios for (a) Pn and (b) Pg at Rice Valley and Savahia Mountain. The ratios were computed from the mean spectral amplitudes shown earlier, and are plotted over the frequency range for which the signal power is above the noise power. Also shown are curves of spectral ratio for factor of ten decreases in the power ratio as predicted by the ω^{-2} source model.

Chapter 4

Pn and Pg Propagation Characteristics at the Ruby Valley Array

4.1 Introduction

The purpose of this chapter is to study the propagation characteristics of the Hardin Pn and Pg wavefields recorded at the Ruby Valley array. Recall that a major aim of array processing is to use the redundancy of the recordings to raise the signal to noise ratio of the wavefield. This can be extremely important for detecting small-amplitude signals. Additionally, the relative phase delays of the wavefield as it propagates across the array can be used to estimate phase velocity and source azimuth. The wavetype can be identified by its phase velocity and, if the locations of weapons testing sites are known, the azimuth can aid in discrimination. However it is well known that a wavefield undergoes some amount of decorrelation as it propagates through the earth. This is particularly true of regional wavefields, which propagate largely through the crust and are subjected to all its structural complexities. Scattering, multipathing, warping, dispersion, and attenuation of the wavefield due to geologic structure can result in amplitude and phase fluctuations across the array. Wavefield distortions of this kind will degrade the performance of an array. In this chapter we will we use frequency-wavenumber array processing to examine the array processing performance of Pn and Pg in terms of array gain, coherence, phase velocity, and source azimuth, paying particular attention to the extent and manner in which these performance measures are affected by wavefield distortions. Knowledge and anticipation of the array processing capabilities of the Pn and Pg wavefields bear upon the design and siting of regional arrays.

Also of interest is the frequency limit to which useful array processing can be done. While signal amplitude may extend up to 30 Hz and beyond, viable array processing is dependent on the wavefield being spatially coherent over the aperture of the array. As frequency

increases, the wavefield will lose spatial coherence over a given distance as heterogeneities are sampled over more wavelengths. At the Noress array Claassen (1985) found that significant signal enhancement is possible up to 20 Hz for Pn and up to 10 Hz for Pg. It is not surprising that Pg loses signal correlation at lower frequencies than Pn because Pg spends much more of its time in the crust. The frequency limit for source-azimuth estimation at NORESS is about 16 Hz for Pn (Bame *et al.*, 1990) and about 8 Hz for Pg (Claassen, 1985). However, a stable geologic shield, upon which NORESS is sited, is one of the best environments for signal propagation. In the more tectonically active Basin and Range we should expect lower frequency limits for these wavefields. It is worth noting that Bame *et al.*, (1990) found that the sub-configuration of the NORESS array that provides the best regional azimuth estimates is the 13-station, 1.5 km aperture combination of its center element A_0 and rings B and C. This sub-configuration is very similar to the 12-station, 1.5 km aperture configuration of the Ruby Valley array.

We are also concerned with the utility of deploying three-component sensors. While a three-component sensor alone may not perform as well as a single-component array, for example in terms of velocity and azimuthal estimates (e.g., Harris, 1990), there can be advantages to forming a three-component multi-sensor array if the horizontal ground motion is sufficiently coherent (e.g., Jurkevic, 1988; Jepsen and Kennet, 1990). Therefore, we will also be examining the frequency-wavenumber spectra of the radial and transverse components of ground motion recorded at the array.

Before presenting results, we will begin with a description of the computational methods used.

4.2 Array Power Estimation

The basic array processing tool we will use here is the so-called "conventional" estimate of the array power spectrum. A description of this estimate more detailed than given here can be found in Abrahamson and Bolt (1987). The array power is based upon cross-spectral

estimates for all station pairs at an N-station array. If we denote the frequency domain representation of a time series recording at the jth station by $u_j(f)$, then the cross-spectra form an NxN matrix S(f), with its elements given by

$$S_{jk}(f) = E\,[u_j(f)\; u_k(f)^*]\;, \tag{4.1}$$

where E is the expectation operator and * denotes the complex conjugate. The estimate of the cross-spectral matrix will be computed from a weighted average of cross-spectra over nearby frequencies. If we assume that the cross-spectral values at each frequency within the averaging bandwidth are statistically independent and identically distributed, then the error of the estimate should decrease as the averaging bandwidth is widened. The validity of this assumption degrades if there are significant variations in cross-spectral amplitude and phase, as would likely be the case with large averaging bandwidths.

The conventional estimate of the frequency-wavenumber array power spectrum is given by

$$P(f, \mathbf{k}) = \frac{1}{N^2}\, \bar{\mathbf{b}}(\mathbf{k})\; S(f)\; \mathbf{b}(\mathbf{k}) \tag{4.2}$$

where the overbar denotes the conjugate transpose. The vector $\mathbf{b}(\mathbf{k})$ is called the beamsteering vector and represents the spatial phase delays which steer the cross-spectra into the wavenumber vector $\mathbf{k}$, i.e., $b_j = e^{i\mathbf{k}\cdot\mathbf{x}_j}$. In computing $P(f,\mathbf{k})$ over a range of $\mathbf{k}$, we are essentially searching for that value of $\mathbf{k}$ which represents the best plane-wave fit to the wavefield, as characterized by a maximum in the power spectrum. The value of $\mathbf{k}$ at the maximum tells us both the phase velocity and azimuth of propagation.

Theoretically, the amplitude of the maximum array power should be greater than the power level of any of the individual recordings. A measure of this is the array signal gain which is proportional to the maximum of the total power in the array beam divided by the average power of the individual recordings,

$$G(f) = \frac{1}{N^2}\; \frac{\max\,[\bar{\mathbf{b}}(\mathbf{k})\; S(f)\; \mathbf{b}(\mathbf{k})]}{\dfrac{\mathrm{tr}\; S(f)}{N}} \tag{4.3}$$

where tr denotes the trace of the matrix. The gain is normalized so that its maximum value is 1.0. Zero correlation between all stations produces a gain of 1/N; lower values are possible if stations pairs are negatively correlated. Values of $G(f) < 1$ result from anomalous variations in both amplitude and phase. We can isolate the effects of phase alone by normalizing the cross-spectral matrix. It then becomes a matrix of intersensor phase differences and $\mathrm{tr}\, S(f) = N$. When normalized in this way equation (4.3) effectively becomes a coherence estimate. We will refer to this as the array coherence C(f). Its range of values for positive correlation is also $1/N \leq C(f) \leq 1$. Other methods of measuring signal enhancement based on signal-to-noise ratios exist which we cannot examine here because our instruments lacked the dynamic range to record the pre-event noise field. These methods take advantage of the correlation structure of the noise and use station-weighting schemes to improve the detection performance of an array (e.g., Mykkeltveit *et al.*, 1983; Ingat *et al.*, 1985; Der *et al.*, 1988; and Kværna, 1989). Because we are without the advantages of a recorded noise field, the analysis here represents a lower bound on array performance.

An important aspect of the frequency-wavenumber spectrum is that it is shaped by the array response, or beam pattern, which is determined by the array geometry. This is simply the power spectral response to perfectly correlated input and describes the resolution and spatial aliasing characteristics of the array. The Ruby Valley array response is shown in Figure 4.1. The resolution is characterized by the central peak width, which is a function of the array aperture. The resolution improves (a narrower peak) as the aperture increases. Spatial aliasing is a function of the intersensor spacing within the array. The aliasing effect decreases (a greater bandwith up to the Nyquist wavenumber) as the average intersensor spacing decreases. Because the Ruby Valley array is two-dimensional the Nyquist wavenumber varies with azimuth, but is typically near about 3 cycles/km. Our ability to resolve low apparent velocity wavefronts, resulting perhaps from multipathing or coherent local scattering, is limited to the lower frequencies. At higher frequencies, low velocity energy becomes aliased. For example, for this array a 3 km/sec wavefront becomes aliased above about 9 Hz. Higher velocities will

have higher frequency limits. A Pn wavefront traveling at 7 km/sec can be array processed without aliasing up to about 20 Hz. In general, the tradeoff to constructing a large aperture, many-sensor array is that the signal becomes increasingly decorrelated as the aperture increases and the noise becomes increasingly correlated as the intersensor spacing is decreased with the addition of more sensors.

In the analysis of the Pn and Pg wavefields below, we will be obtaining estimates of array power, coherence, phase velocity, and source azimuth, all as a function of frequency. The power spectra, upon which all depend, are calculated as follows. First, to reduce the bias due to spectral leakage, the time series are pre-whitened. The cross-spectral estimates are computed using multi-taper cross-spectral averaging (Thomson, 1982). This method of cross-spectral estimation and its advantages are discussed in Appendix C. Here we use the five lowest-order 4π tapers applied over the first adjacent frequency to either side of each discrete frequency f_n, for a total of 15 cross-spectra in the average. For the T=1.3 second time windows we will be considering below this corresponds to an averaging bandwidth of about 1.6 Hz ($f_n \pm 1/T$). For simplicity, the spectra are computed in the frequency-slowness (f,s) domain rather than the frequency-wavenumber (f,**k**) domain. The two are simply related by **k**=fs. Power spectra are first computed on the raw data to produce a preliminary estimate of the slowness propagation vector. Then, in attempt to remove the propagation effects, the slowness propagation vector is used to realign the waveforms to near infinite velocity and the power spectra are then recomputed. Aligning the waveforms removes extraneous noise and uncorrelated signal and it generally results in greater beam power. Typically, after this temporal alignment, slight propagation effects remain for some frequencies, i.e., the initial alignment is not optimal because the revised spectral peak does not lie precisely at zero slowness. Appropriate phase corrections are made in the frequency domain to each cross-spectrum and the power spectrum is recalculated. The process is repeated until the spectral peak converges to zero slowness, usually requiring only one or two iterations. The net slowness vector is simply the sum of the initial slowness vector with which the waveforms were aligned plus the subsequent

adjustments. An iterative approach very similar to this is described by Wang and Kaveh (1985). A boxcar weighting function for cross-spectral averaging is used on the aligned waveforms. In all calculations, the spectra are computed over a slowness grid sampled in increments of 0.0025 sec/km. Finally, because phase velocity and azimuth are essentially based upon cross-spectral phase information, the cross-spectra from which they are determined are normalized prior to computing the array power spectrum to remove the effects of amplitude variation. This normalization takes place both before and after the frequency averaging process.

4.3 Pn Wavefield

Since our concern is achieving high signal gain and reliable estimates of slowness, we will concentrate on just the first few seconds of the Pn and Pg wavefields, avoiding the later-arriving coda. As we will see below, the coherence quickly degrades in later time windows. The 3-component Pn waveforms we'll examine are displayed in Figure 4.2 and ordered from bottom to top in order of increasing epicentral distance from the NTS explosion. As we noted in Chapter 2, the earliest ground motion is essentially vertical, indicating a high near-surface velocity gradient. Significant horizontal ground motion is delayed and does not begin until about 1.3 seconds. This delay, combined with the large transverse amplitudes, suggests an onset of scattered and/or multi-pathed energy beyond 1.3 seconds. To examine this further we will divide the waveforms into two sequential T=1.3 second (256 point) time windows, denoted W1 between 0 and 1.3 seconds and W2 between 1.3 and 2.6 seconds. Note that even in the earlier time window, we can see anomalies in amplitude and phase. For example, looking at the vertical-component in window 1, in addition to the eastern amplitude attenuation we noted in Chapter 2 (stations 4, 5, 6, 11, and 12), those station pairs which lie at identical epicentral distances and should therefore have no relative time delays (i.e., stations 6&8, 3&5, 9&12, and 10&11) appear to have delays up to a tenth of a second or so. These anomalies will further reveal themselves in the analysis of power spectra below.

4.3.1 Signal Correlation

We will first examine the signal correlation of Pn in terms of the maximum array power and array gain. The results for windows W1 and W2 are shown in Figure 4.3. No instrument correction has been applied to the power. Recall that the array power is influenced by signal strength and signal correlation, and that high power does not necessarily translate into high array gain. Array gain is a measure of the ability of the array to pull a signal further above the background noise level, and is theoretically independent of overall signal strength. In practice however, array gain can can be degraded by a low signal to noise ratio. Within window 1, the horizontal power levels fall typically at least two orders of magnitude below the vertical. In contrast, in W2 the horizontal power levels are up to an order of magnitude greater than the vertical at low frequencies. However beyond 8 Hz there is very little difference in power among the three components in W2. Looking at the array gain, in window W1 the vertical-component reaches the 0.32 mean gain level for white noise near 10 Hz. This general drop in gain with increasing frequency is as expected for a scattering media since inhomogeneities become sampled over more wavelengths. The gain of the horizontals is significantly less than the vertical, no doubt largely due to the much lower signal to noise ratio. By window 2 the vertical gain has dropped dramatically, falling below the noise level by 5 Hz. The horizontal gains fall near or below the noise level over the entire bandwidth, indicating that the increase in horizontal array power is due to signal strength and not signal correlation. This increase in horizontal energy combined with a drop in array gain relative to W1 is consistent with an onset of increased scattering within this delayed time window.

The array coherence estimates for the two windows are shown in Figure 4.4. In general, we should expect these values to be somewhat larger than for array gain since we are ignoring the effects of amplitude variation. Here, the mean coherence value for white noise is approximately 0.43. Within W1, as was the case with array gain, the array coherence is greatest on the vertical and least on the transverse at the lower frequencies. The vertical and radial coherence values are much higher than the gain values below 5 Hz. However beyond 5 Hz there is

a rapid transition to low coherence values. The vertical gain in W2 is much lower and decays more rapidly than in W1. The coherence on both W2 horizontal components has dropped to extremely low values. Overall, we see a drop in coherence moving out of window W1 and into W2, again consistent with increased scattering in W2. As we see below, this will have an effect on Pn phase velocity and source azimuth estimates.

4.3.2 Phase Velocity and Source Azimuth

The Pn phase velocity and source azimuth estimates we will focus on here are based only on the most coherent component of ground motion, i.e., the vertical. They are determined from the slowness location of the peak in the power spectra, computed with cross-spectral normalization. The amplitude of the peak is given by the magnitude of the coherence in Figure 4.4. The results are shown in Figure 4.5 for both time windows. In W1 the phase velocity increases smoothly with frequency up to 12 Hz, increasing from 5 to 7 km/sec. In W2 the velocity ranges between 5 and 6 km/sec up to 6 Hz, beyond which the coherence is very low and the velocities are for the most part aliased. The W1 azimuth estimates display a systematic variation, ranging from about 140 degrees at the low frequencies to within about 5 degrees of the true azimuth of 180 degrees between 8 and 12 Hz. Azimuthal estimates from W2 also fall east of the true azimuth but due to the extremely low coherence beyond 4 Hz, we cannot see similar variations at higher frequencies. An analysis of the latter 0.65 seconds of W1 alone did not reveal velocities or azimuths significantly different from the first 0.65 seconds of W1. This suggests that the onset of energy in this latter half is due to pPn and not Moho scattering as discussed in section 2.3.1.

The strong variation of azimuth with frequency in W1 is obviously not consistent with a non-dispersive, plane-propagating wavefront. Also, the estimates of Pn phase velocity are well below the 7.6-7.8 km/sec Pn velocities typical for this region of Basin and Range (Hearn *et al.*, 1990). To examine this further, Figure 4.6 shows linearly interpolated travel-time contours based on picks of vertical Pn arrival times at each recording station. These contours

represent an approximation of how the onset of the Pn wavefront propagated with time. The contours show a counter-clockwise warping of the wavefield. The uniformity of surface properties at the array site and the magnitude of the relative time delays between stations of equal epicentral distance argue against the warping being due to variations in shallow soil response. The source of the warping, if it is a local one, extends at least a few kilometers beneath the array.

The back-azimuthal direction of the contours gradually increases from about 140 degrees on the eastern side of the array to near 180 degrees on the westernmost side of the array. This is the same range of W1 azimuths we saw in Figure 4.5. Note that the greatest amount of counter-clockwise rotation takes place among the attenuated stations to the east. The strong azimuthal variation with frequency arises from the fact that, in addition to there being an east-west transition in signal amplitude, there is also a transition in coherence across the array. An example of this can be seen in Figure 4.7 which contrasts two-station coherence for station pairs 7 & 8, both located on the western side of the array, 6 & 12, both located on the eastern side, and 6 & 7, which overlaps the two sides (refer back to Figure 2.17 for the array configuration). The station separation in all cases is 650 meters. The mean coherence level for white noise is approximately 0.33. The details of two-station coherence estimation are discussed in the next chapter and in Appendix C. This example shows that when both stations are located on the same side of the array the coherence remains fairly high up to about 10 Hz. However when the two sides are taken together the coherence drops significantly with increasing frequency, up to about 7 Hz in this example, with some recovery at higher frequencies. The net result over the entire array is that as frequency increases, the array power spectra become increasingly weighted by the greater number of higher-amplitude stations to the west. Because the wavefield becomes less warped towards the west, the accuracy of the source azimuth steadily improves. This variation of coherence also explains the increase in velocities with frequency. Looking back at Figure 4.6 we can see that the distance between contours generally increases, i.e., velocity increases, moving west across the array.

One explanation for the generally low values on Pn phase velocity could be the effect of a local northward-sloping dip in the basement of the valley sediments. For example, a dip of ten degrees with the velocity increasing from 2 km/sec above the dip to 3 km/sec below would drop the apparent velocity from 8 km/sec to about 6.5 km/sec. However we do not know if such a dip exits. The warping of the wavefield can perhaps be explained by a focusing effect caused by the three-dimensional structure of the valley. Similar effects of phase velocity reduction and wavefield rotation were seen by Chiou (1991) who modeled the effects of a three-dimensional basin located beneath a small-aperture array. Focusing might also explain the relatively larger amplitudes on the western side of the array. A more complete understanding of the true nature of the wavefield distortion and an anticipation of its effects would compensate to some extent for the degraded source-azimuth and phase-velocity estimation performance at this array site.

4.3.3 Slowness Stacking

A further examination of the wavefield can be made by displaying the complete power spectrum in the slowness plane. Rather than show the spectrum at each frequency, we will sum, or stack, the power spectra over frequency in the slowness plane to produce an average spectrum. This is referred to as slowness stacking. Note that an ideal non-dispersive propagating plane wave will display a power peak at the same location in the slowness plane as a function of frequency. Therefore if spectra from such a wave are summed, or stacked, in the slowness plane, spectral peaks will sum constructively, while spectral sidelobes, which vary in their location with frequency, and random noise will sum destructively. A more peaked response will result. A slowness stack should provide a more reliable estimate of source azimuth and phase velocity, and remove spurious peaks in the spectrum. Any decorrelation or dispersive qualities of the wavefield will show up as a broadening or smearing of the peak in the stack.

Two frequency bands will be used in the stacks: a low-frequency band of 1.6-5.5 Hz and a broadband of 1.6-10.2 Hz. The low-frequency band encompasses those frequencies where we find the greatest coherence values. The broadband encompasses higher frequencies with low coherence, which nevertheless might sum constructively. For comparison with the data results, Figures 4.8a and 4.8b show, in both two- and three-dimensional perspectives, the response of a perfectly correlated plane wave and the response of a random wavefield stacked over these frequency bands. Note that provided the signals are well correlated, the spectral resolution improves with frequency. Given what we've learned about the Pn wavefield, the best estimates of source azimuth and phase velocity would come from a high-frequency stack, or a broadband stack which downweights the eastern stations. Nevertheless we will display simple low-band and broad-band stacks to display the effects of the wavefield distortion. The Pn low-frequency stacks from W1 are shown in Figure 4.9; all three components are included. The spectra are plotted at slowness increments of 0.01 sec/km. The stacks are based on normalized cross-spectra and so are somewhat more peaked than they would be if amplitude decorrelation were included. The maximum power possible when normalized like this is 1.0.

Within window W1, the vertical and radial low-frequency stacks result in similar estimates of velocity and source azimuth, however the vertical component displays a somewhat more peaked response. The azimuthal estimates are in error by about 25 degrees, and the phase velocity is more typical of Pg than Pn. A power peak also shows up on the transverse component though its amplitude is very low and its azimuth differs from the other components by about 10 degrees. The peak power levels within W2 (Figure 4.10) are all less than those for W1. The vertical-component azimuth is comparable to that in W1, however the transverse power is very low and displays no coherent energy in the direction of the source. There is also a greater difference between vertical and radial phase velocities and azimuths. Isolated peaks representing coherent scattering or multipathing are difficult to identify within either time window. This suggests that the onset of horizontal ground motion and corresponding drop in correlation is primarily due to near-receiver random scattering.

The broadband stacks for W1 and W2 are shown in Figures 4.11 and 4.12, respectively. Within W1 all peak power levels have dropped relative to the low-band stacks. The vertical-component peak, however, is much closer to the true source azimuth of 180 degrees, though a good deal of energy is still spread to the east. The velocity of the peak has also increased from 6.1 km/sec to 6.7 km/sec. The horizontal stacks, lacking high-frequency coherence, display no improvement in azimuth. The vertical stack within W2 displays a similar eastward spread, but its peak is in error by about 45 degrees, has a much lower amplitude, and a velocity of only 5.3 km/sec. Both horizontal power levels within W2 are near the noise level and may not be significant. In general, energy away from the source direction within both time windows is spread throughout the slowness plane and of low amplitude. It therefore appears that local scattering is not only strong, i.e., large signal amplitude, but is also quite random. As we will now see below, the situation is similar for Pg.

4.4 Pg Wavefield

Here again we will restrict the analysis to the early portion of the wavefield. Figure 4.13 displays the first 2.6 seconds for all three components. Unlike Pn, with its lack of early horizontal ground motion, the Pg wavefield arrives essentially isotropic. There is comparable ground motion on all three components, with an increase in overall amplitude in the latter half of the 2.6 window. Given the horizontal nature of Pg propagation, we would expect a good deal of initial radial motion. However the initial transverse energy indicates an earlier presence of scattering than for Pn, some of which derives from the Pn coda. We do not see for Pg the eastward attenuation we saw for Pn. This is presumably because by virtue of their different mode of propagation, the local sites effects between the two wave types differ. As before, we will divide the waveforms into two sequential 1.3 second time windows, again denoted W1 and W2. The computational parameters for power spectra will be identical to those used for Pn.

4.4.1 Signal Correlation

The array power and array gain for the two time windows are shown in Figure 4.14. The power is plotted with the same relative scale as for Pn in Figure 4.3. Within W1 the three-component power levels are fairly similar, in contrast to W1 power levels for Pn. The greatest variation in the power is below 5 Hz, where the vertical power is up to about three times greater than the horizontals. Within W2 the power levels are somewhat greater than in W1 and the greatest power is still in the vertical component at the low frequencies. The Pg array gain in W1, like Pn, is greatest on the vertical, but is lower in magnitude and drops to the noise level by 6 Hz. The horizontal gains fall below the noise level over the entire bandwidth. The vertical array gain in W2 also drops to the noise level near 6 Hz, however the gain values are less in this later time window, though the decrease from W1 is not as dramatic as that for Pn. The horizontal gain levels remain below the noise.

The Pg array coherence estimates are shown in Figure 4.15. The vertical coherence within window 1 is as high as it was for Pn at the lowest frequencies, but falls off more rapidly with increasing frequency. The vertical coherence drops in W2. There is no significant horizontal coherence in either of the two time windows. In later time windows signal correlation drops even further - within about two seconds beyond W2, the vertical coherence falls to the mean noise level over the entire bandwidth. The principal difference between the Pn and Pg array gains and coherence are the much lower Pg values in W1, particularly on the horizontal components. The gain and coherence in window 2 of Pn and Pg are comparably low on all three components. In terms of overall signal correlation, Pn and Pg share two basic characteristics, namely (1) in the presence of scattering the vertical component remains much more coherent than the horizontal components and (2) the decorrelating effect of scattered waves is greater in later time windows. We'll now see how they compare in terms of phase velocity and source azimuth.

4.4.2 Phase Velocity and Source Azimuth

The estimates of Pg phase velocity and source azimuth are shown in Figure 4.16. As for Pn, these estimates are based on vertical-component normalized cross-spectra. The velocities in W1 range between 5 and 6 km/sec up to about 6 Hz and display an overall increase with frequency, similar to the W1 Pn velocity estimates. In contrast to Pn, the maximum phase velocities of close to 6 km/sec are quite reasonable. Beyond 6 Hz, where the coherence is low, the velocity becomes aliased. Though the velocities in W2 appear stable over a wider frequency band, this may not be significant given the low coherence values beginning near 5 Hz. Below 5 Hz, these velocities range between about 5.0 and 5.5 km/sec and also increase with frequency. The W1 azimuthal estimates display a low-frequency variation similar to Pn, i.e., they generally increase with frequency, increasing from 150 to 160 degrees. Beyond 6 Hz the estimates are very erratic due to the low coherence and aliased velocities. The open triangles denote azimuths that fall off the scale of the plot. In contrast to W1, the W2 azimuths fall within only a few degrees of the true azimuth below 3 Hz. Beyond 3 Hz the azimuthal error increases with frequency, but again, at 5 Hz and beyond the coherence is not significant.

Because of its different mode of propagation, we would not have necessarily expected the same behavior in Pg estimates of velocity and azimuth that we found for Pn. Nonetheless the behavior is similar within the onset of Pg at low frequencies where the coherence is high. However in the later time window, though the velocity remains similar, the azimuthal estimates are very different and in fact improved, falling to within a few degrees of the true azimuth at low frequencies. It therefore appears that the onset of the Pn and Pg wavefields are subject to similar site effects. However in the later high-amplitude Pg time window, by virtue of a slightly different path of propagation, the site effect has changed such that relatively little azimuthal bias takes place at low frequencies.

4.4.3 Slowness Stacking

The low-frequency Pg stacks for windows 1 and 2 are shown in Figures 4.17 and 4.18. Within W1, only the vertical component displays a significant source-directed spectral peak. The azimuthal estimate of 156 degrees is identical to that for Pn in W1. The Pg phase velocity estimate is 5.6 km/sec. The horizontal stacks have very low amplitude but nevertheless fall above the 0.19 noise level. If significant, the low velocities and large azimuthal errors may be indicative of locally generated P to Lg or Rg scattered energy. Scattering of this kind is also suggested for some regional events recorded at the Scandanavian arrays (Dainty and Toskoz, 1990). Within W2 the vertical peak power levels have dropped somewhat but the phase velocity and azimuth have changed very little. Both horizontal components have very low power and resemble the random wavefield spectra. Contrasting these low-frequency Pg stacks with those for Pn we find for Pg lower power levels and a lack of source-directed horizontal energy. There is a similar eastward bias of the vertical-component azimuthal estimates, however this can be removed for Pg by restricting the stacking in W2 to frequencies under 3 Hz. The Pg phase velocities are less than Pn, but not by much. For example, the vertical-component Pg velocity in W1 of 5.6 km/sec is very close to the corresponding Pn velocity in W1 of 6.1 km/sec.

The Pg broadband stacks are shown in Figures 4.19 and 4.20. Within W1, the vertical-component spectrum shows no improvement in estimates of velocity and azimuth and the power is now quite low. The horizontals resemble the broadband random stack in Figure 4.8b. The situation is W2 is similar, with the vertical-component azimuthal error increasing to 43 degrees. The horizontal spectra again appear random. Contrasting the broadband and low-frequency stacks for Pn and Pg, we find that adding the higher frequency spectra generally degrades estimates of phase velocity and azimuth due to the low coherence. The exception is the earliest time window of Pn, where broadband stacking improved the source azimuth estimate and resulted in a greater velocity contrast between Pn and Pg, 5.6 vs. 6.7 km/sec.

4.5 Summary Discussion

In this chapter we have examined and contrasted the array processing characteristics of the three-component Pn and Pg wavefields recorded at the Ruby Valley array. The principal findings are summarized and discussed below.

Scattering Effects

The analysis has focussed on only the first few seconds of these wavefields because we find that the array processing performance is degraded at later times due to more severe decorrelation effects. In just a little over a second into the Pn wavefield there is an abrupt onset of horizontal ground motion and a sharp drop in signal correlation. Frequency-wavenumber analysis within this later time window was quite random and did not reveal any coherent sources of scattering. Pg differs from Pn in that it *arrives* at the array with incoherent, high-amplitude horizontal ground motion. There is however significant vertical signal correlation which, like Pn, drops in the later time window. The fact that vertical correlation is sustained and horizontal correlation is lost indicates that the wavefields are being complicated more by horizontal structural irregularities in the crust than by vertical ones. Given the horizontal nature of Pg propagation, it is not surprising it arrives at the array with poor signal correlation. An additional decorrelating effect for Pg is that is superimposed on random Pn coda.

The onset and persistence of incoherent ground motion are likely due to local effects such as reverberations and wavetype conversions in and around Ruby Valley. The strong effect of the valley was seen clearly in Chapter 2 in a comparison of the array recordings, located near the center of the valley, with the LLNL recording, located 14 km to the north and away from the interior of the valley (see Figures 2.15 and 2.16). High-amplitude ground motion is sustained for a much longer period of time within the valley. These random effects are in contrast to more systematic peculiarities which may be related to local site effects.

Site Effects

In this analysis we have come upon irregularities in phase velocity and source azimuth which may be related to local site effects, though we have made no attempt to model these effects. Within the onset of Pn, over the bandwidth where the array gain and coherence are sufficiently high, the azimuth varies systematically from eastward-biased azimuths 40 degrees in error at the low frequencies, to estimates within a few degrees of the true source azimuth at higher frequencies. The Pn phase velocity also displays variation, increasing slightly with frequency. Still, at its maximum it reaches only 7.0 km/sec, well below the expected 7.6-7.8 km/sec range. The behavior in the later time window is similar at the lower, coherent frequencies. Estimates of average phase velocity and source azimuth from slowness stacking are complicated by this frequency dependence of the power spectra. This obviously poses a problem for velocity-based phase identification and azimuth-based source discrimination. These irregularities in azimuth and velocity may be due to a wavefield distortion effect caused by the three-dimensional structure of Ruby Valley.

The onset of Pg appears to be subject to a site effect similar to that for Pn. However in the later time window below 3 Hz the azimuthal bias drops greatly, with estimates falling just a few degrees shy of the true source azimuth. This improvement in source azimuth is good to see, however it is perplexing and reflects the almost capricious nature of these regional wavefields.

Array Processing Capability

The array processing capability is of course degraded by the random scattering and site effects discussed above. In terms of signal correlation, the array gain and coherence are greatest at the onset of the Pn and Pg wavefields, and approach the mean noise level near 5 or 6 Hz. This is significantly less than the frequency limits for signal enhancement reported at Noress where, for example, Claassen (1985) reports a Pn array coherence of nearly 0.9 at 8 Hz. The performance at the Ruby Valley site can be improved to some extent with more

sophisticated signal enhancement methods which take advantage of noise correlation properties and use station weighting schemes.

In terms of source azimuth and phase velocity, azimuthal estimates in error by 20 to 30 degrees and Pn phase velocities only slightly higher than Pg velocities were not uncommon. Nevertheless there were isolated segments of both the Pn and Pg wavefields which produced azimuthal estimates only a few degrees in error, though this was within isolated bandwidths. In particular we had to rely on the very low, yet still significant, coherence of the Pn onset beyond 5 Hz. For later portions of the Pn wavefield and all of the Pg wavefield, velocity and azimuth estimates are not significant above 5 or 6 Hz. It is clear that effective routine azimuthal-based source discrimination and velocity-based phase identification at this site would require the further experimental operation of an array so as to come to a better understanding of the local Pn and Pg azimuthal and velocity bias effects.

Three-component Processing

The extent of random wave propagation within Ruby Valley severely limits the utility of three-component processing. Only within the onset of the Pn wavefield is the horizontal array gain and coherence significantly above the noise level. These results indicate that three-component signal processing schemes may be viable for Pn at this array site. However, due to low coherence levels, this would have to be limited to frequencies below about 5 Hz and probably to only the very early portion of the Pn wavefield.

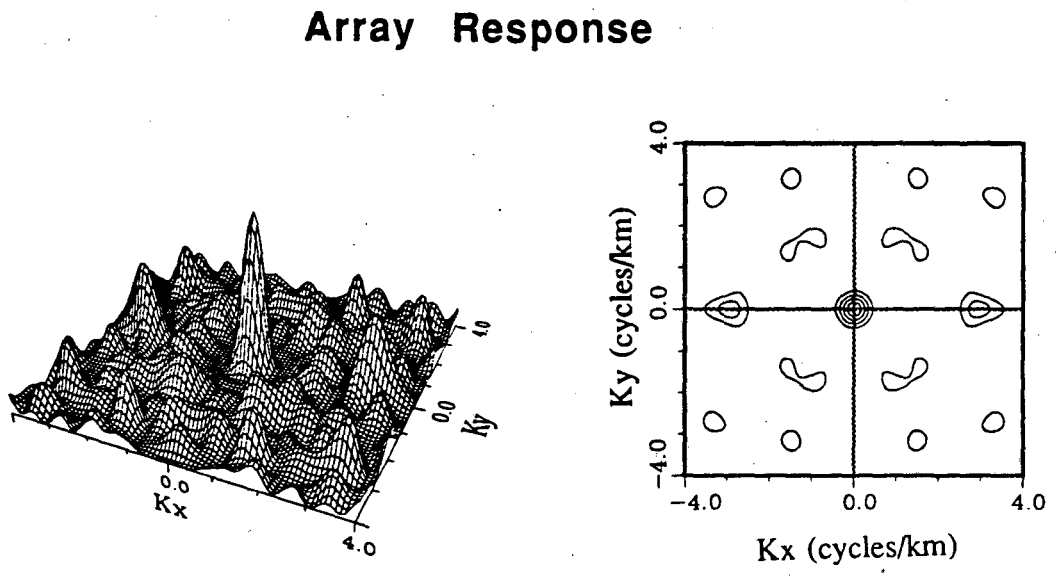

FIG. 4.1 Array response of the Ruby Valley array in two- and three-dimensional perspectives. The power contours are in linear 10% intervals of the maximum power.

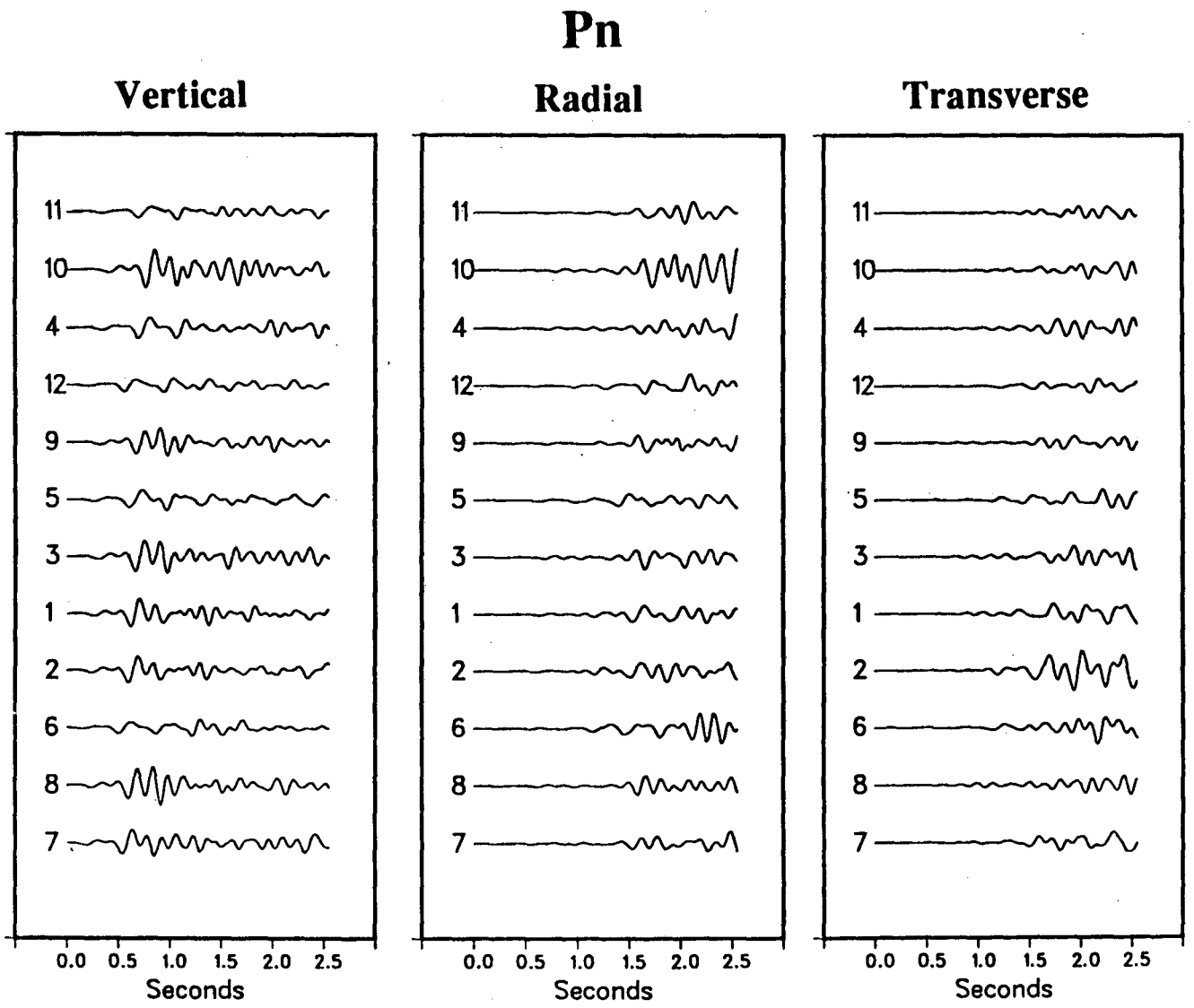

FIG. 4.2 3-component Pn waveforms used in the analysis. The waveforms are ordered from bottom to top in order of increasing epicentral distance from the NTS explosion. The station numbers are indicated to the left of the waveforms. Two time windows are examined: Window 1: 0 to 1.3 seconds and Window 2: 1.3 to 2.6 seconds. These windows are abbreviated as W1 and W2 in the text.

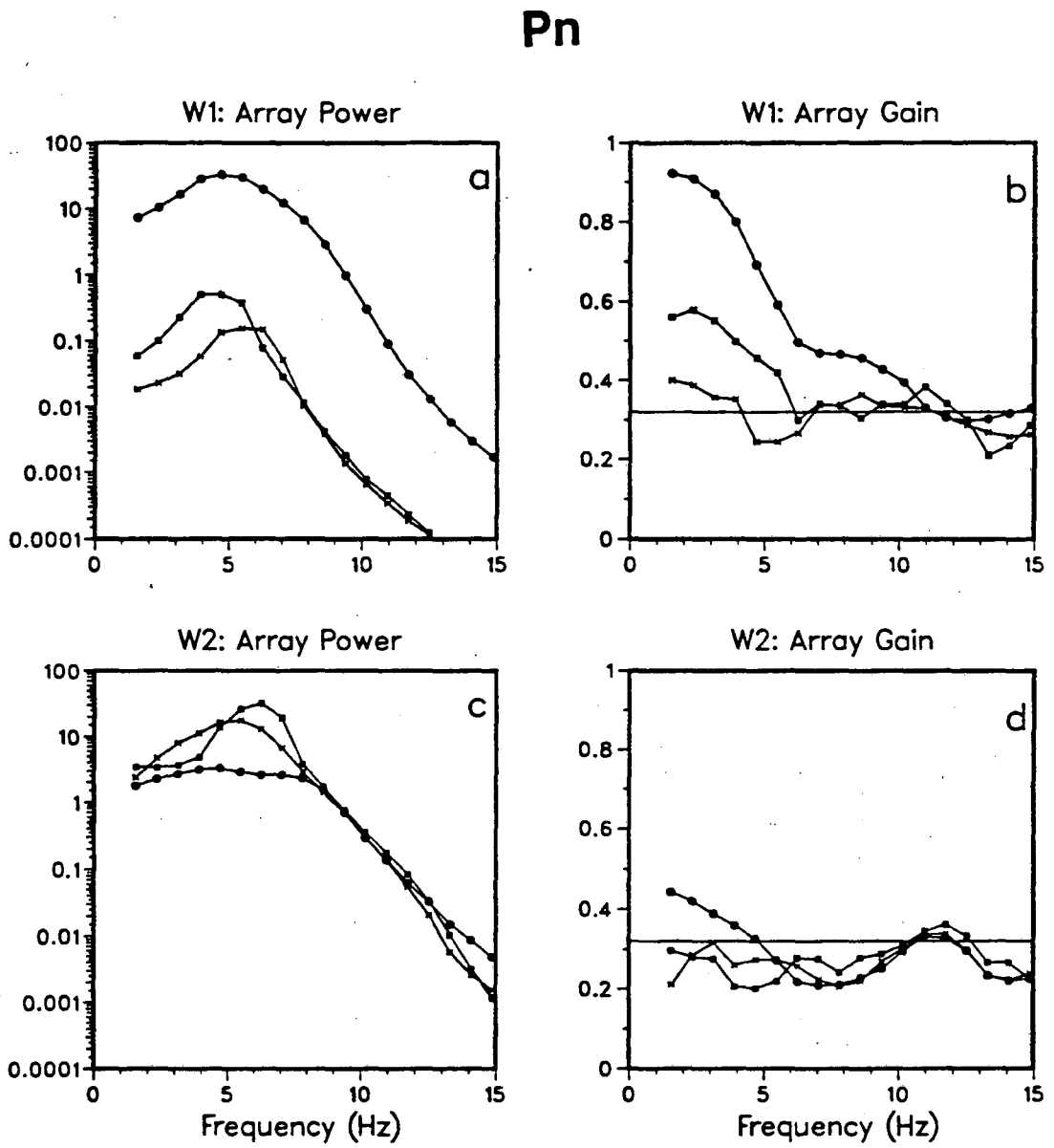

FIG. 4.3 3-component Pn array power and array gain for Window 1 and Window 2. The vertical component is denoted by solid circles, the radial by solid squares, and the transverse by crosses. The instrument response has not been removed from the power. The mean array gain level for white noise is approximately 0.32.

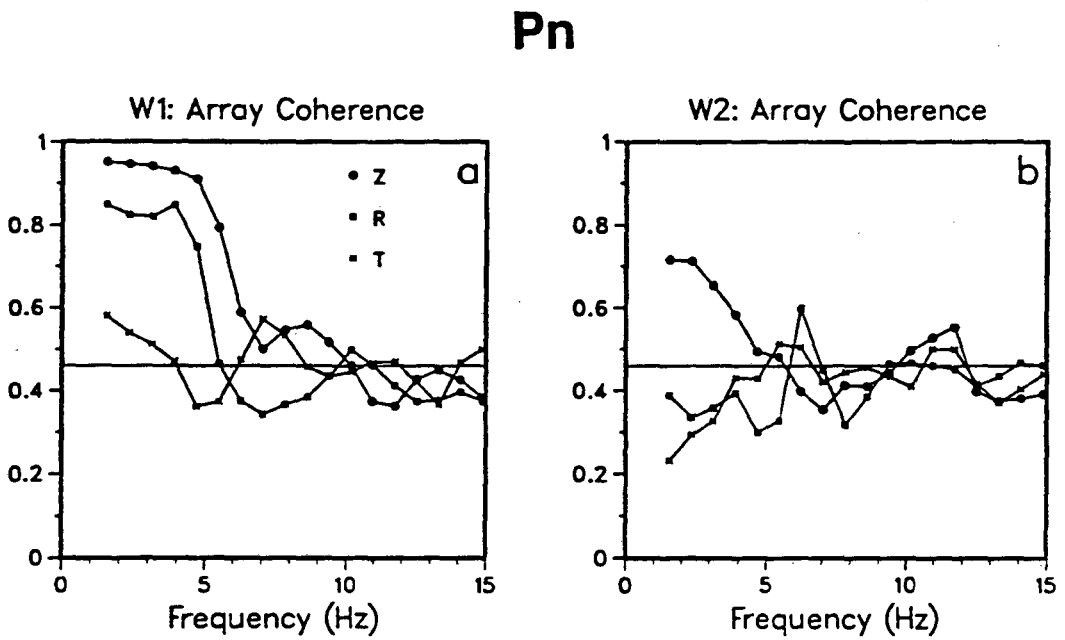

FIG. 4.4 3-component Pn array coherence for Windows 1 and 2. The vertical component is denoted by solid circles, the radial by solid squares, and the transverse by crosses. The mean coherence level for white noise is approximately 0.43.

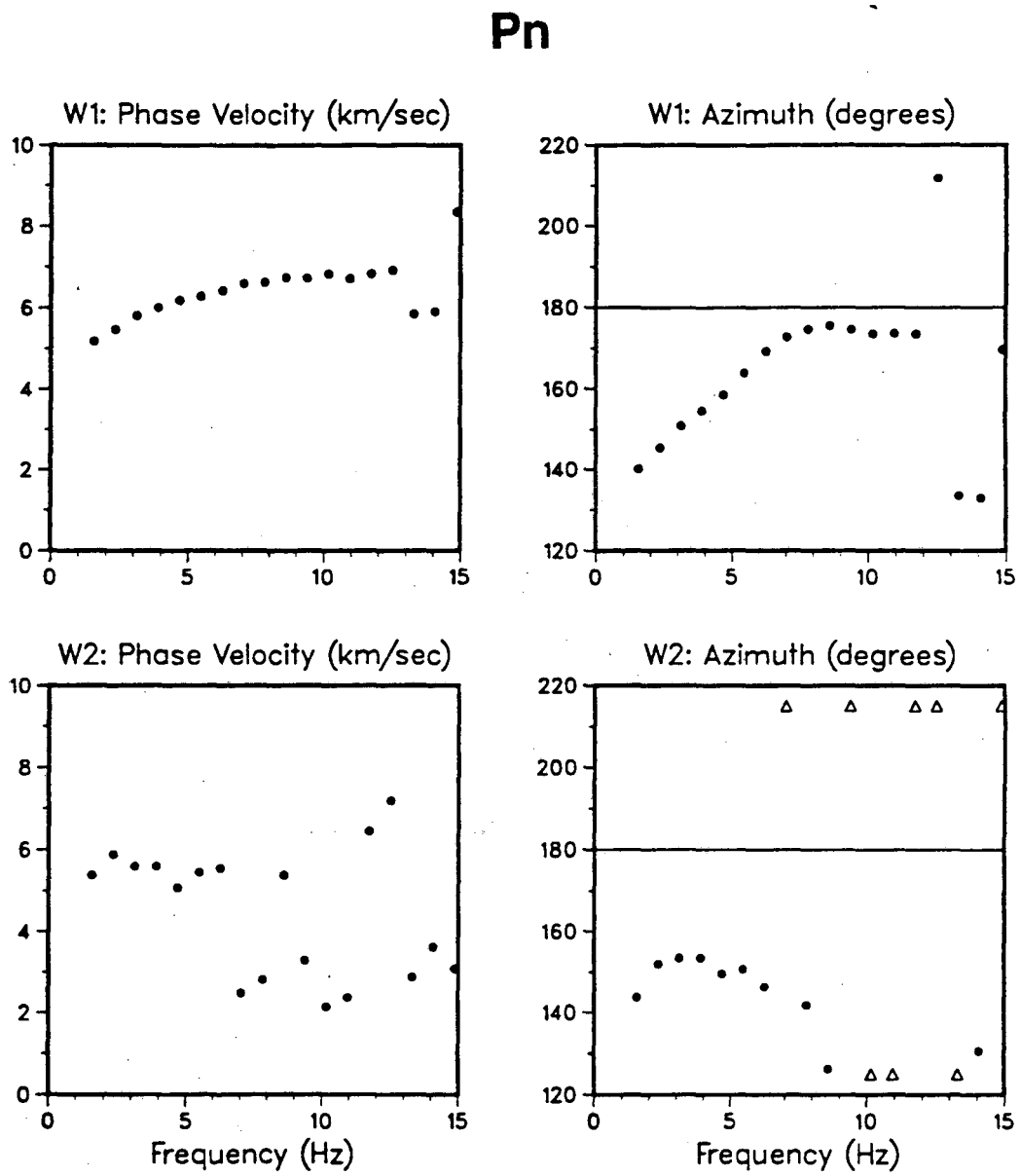

FIG. 4.5 Estimates of Pn phase velocity and wavefront azimuth, determined from the locations of vertical-component power spectral peaks in the slowness plane. Azimuth refers to the azimuth to the source. The true source azimuth is 180 degrees.

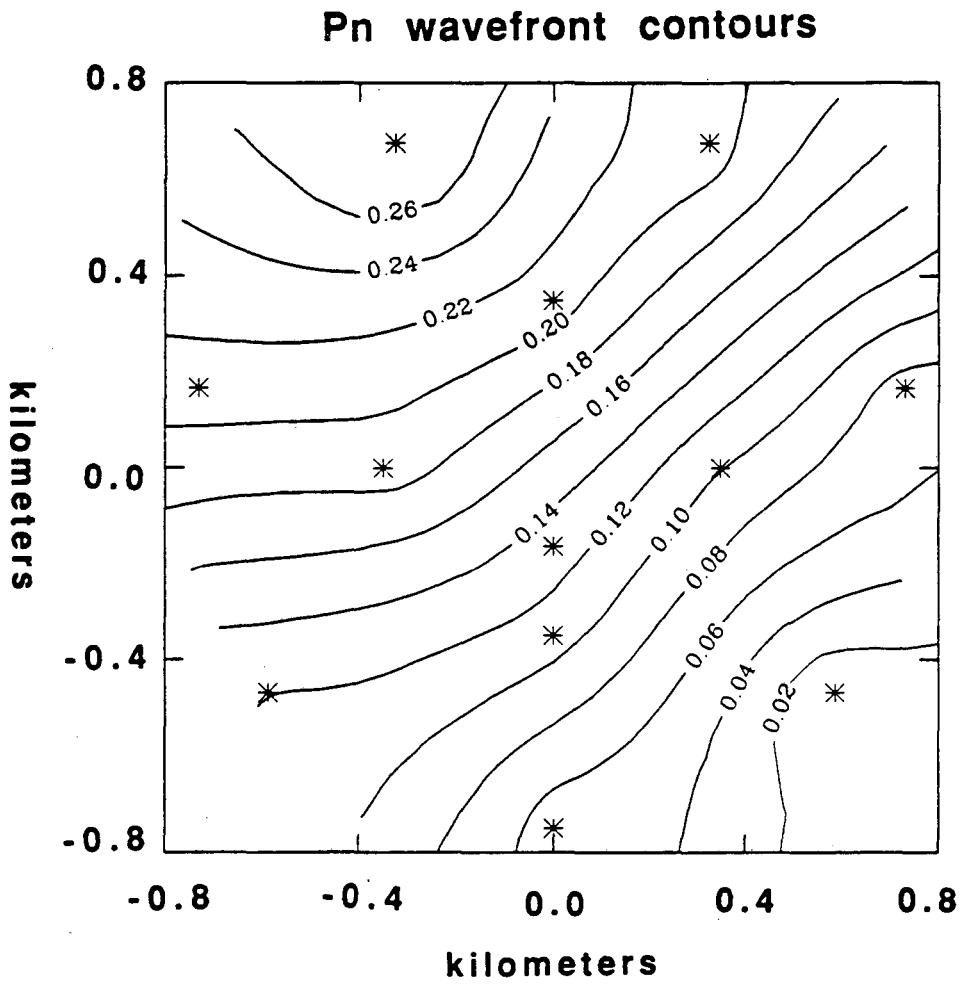

FIG. 4.6 Pn arrival time contours interpolated from manual picks of first motion on the vertical component. The absolute contour values are times relative to the earliest time of arrival at the array. The contour interval is 0.02 seconds. Each element of the array is denoted by an asterisk.

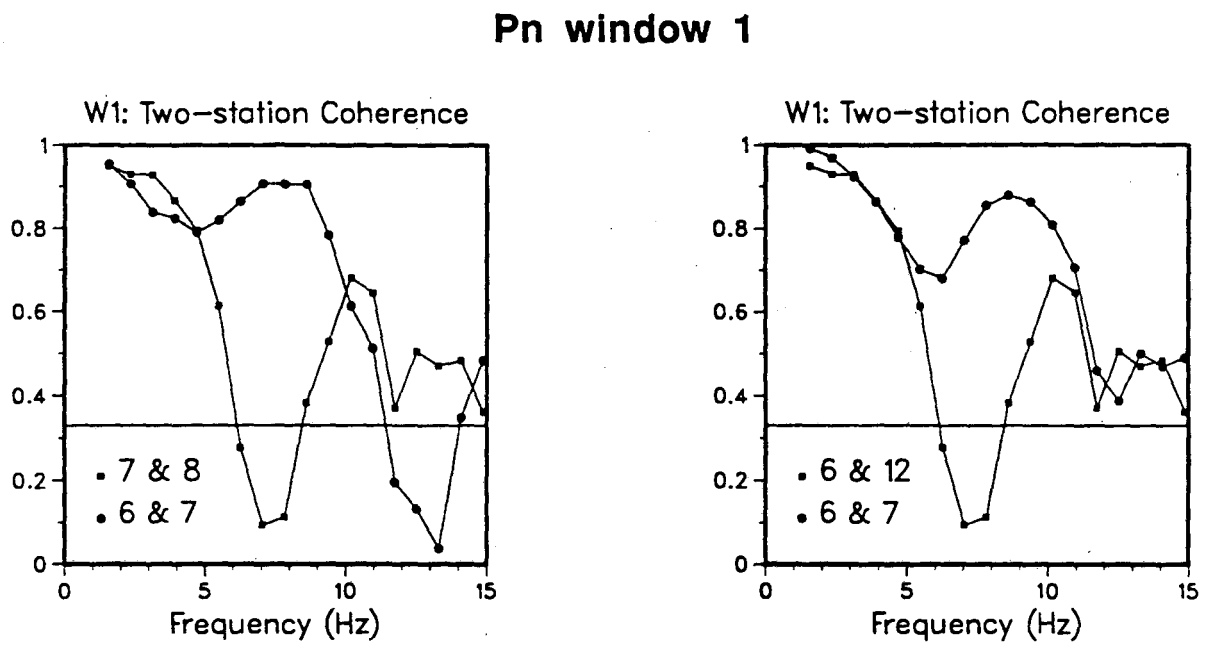

FIG. 4.7 Two-station Pn coherence from window 1 for station pairs 7 & 8, both located on the western side of the array, 6 & 12, both located on the eastern side, and 6 & 7, one from each side. The station separation is 650 meters in all cases.

Perfect Correlation

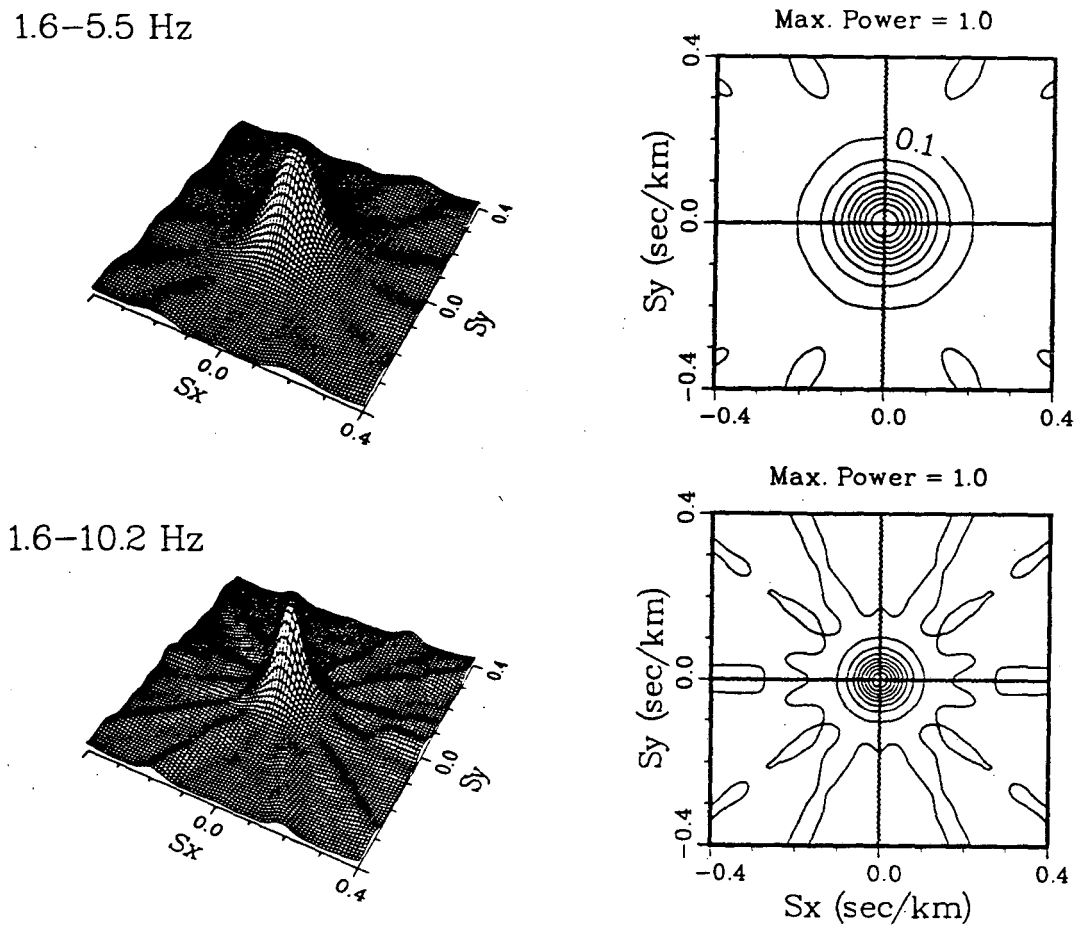

FIG. 4.8a Slowness stacks over the frequency range 1.6 to 5.5 Hz and 1.6 to 10.2 Hz for a perfectly correlated planer wavefront. The spectrum is centered at zero slowness. The power contours are in linear intervals of 0.1.

Random Wavefield

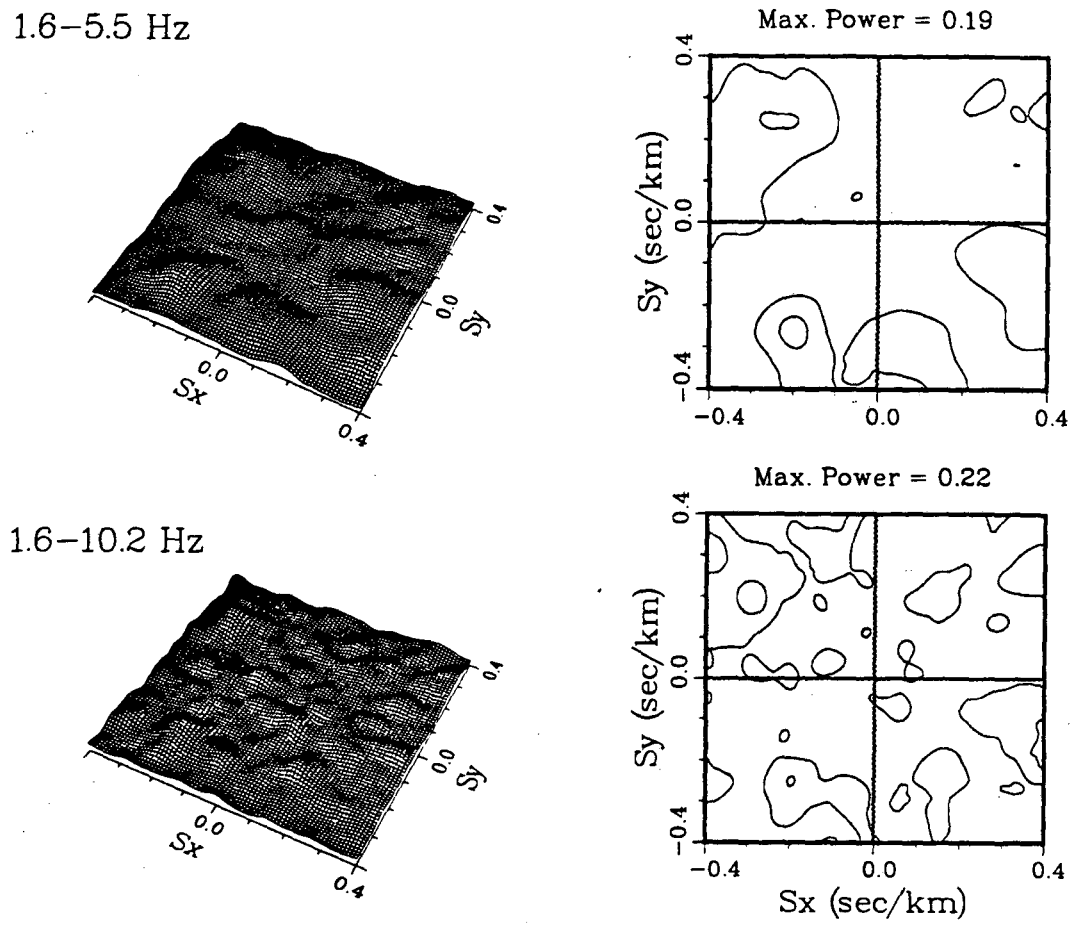

FIG. 4.8b Frequency-slowness spectral stacks over the frequency range 1.6 to 5.5 Hz and 1.6 to 10.2 Hz for a random wavefield. The power contours are in linear intervals of 0.1.

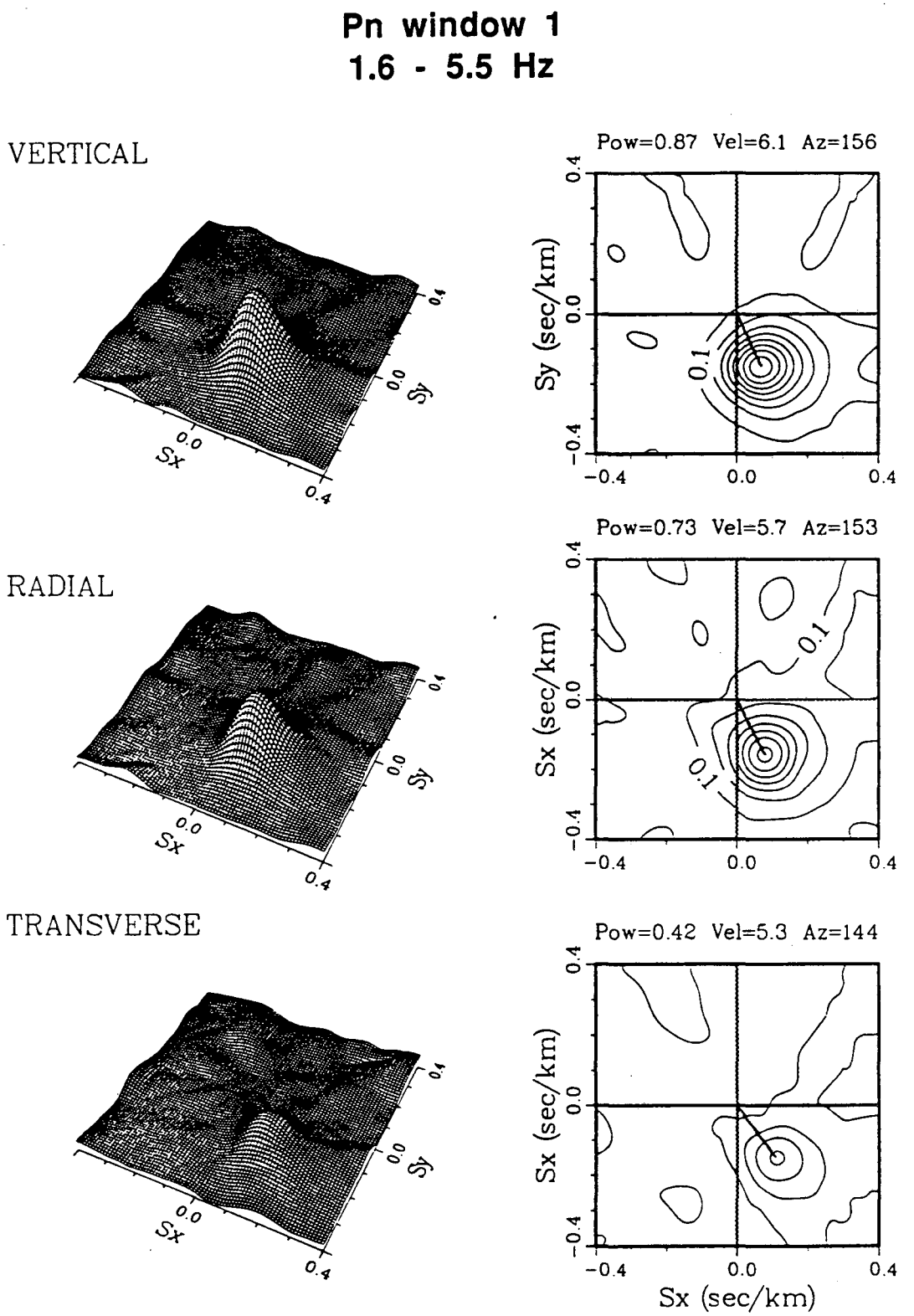

FIG. 4.9 Observed Pn 3-component slowness stacks over the frequency range 1.6 to 5.5 Hz for Window 1. The peak power levels and corresponding estimates of phase velocity and azimuth are indicated above the two-dimensional plots.

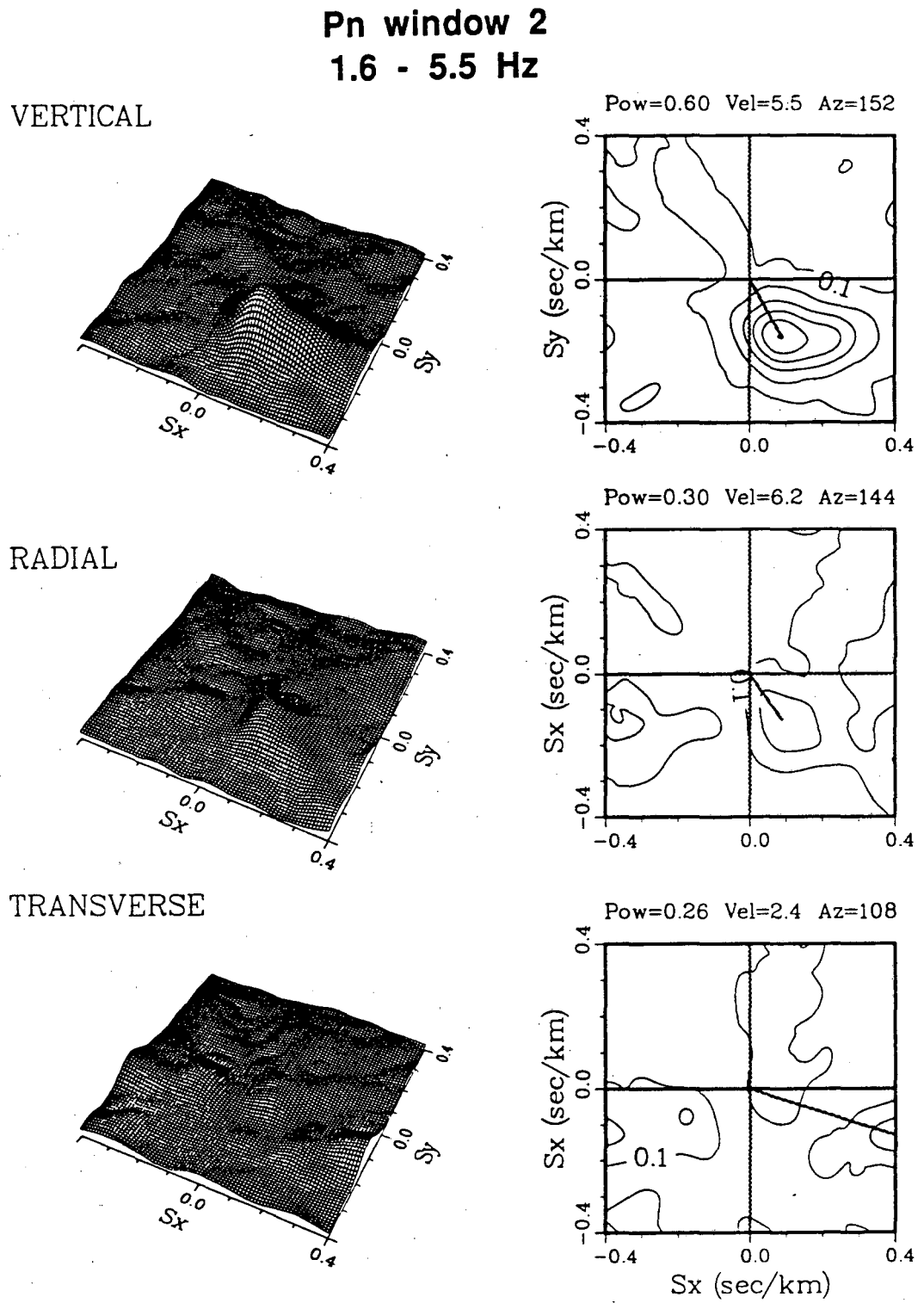

FIG. 4.10 Same as Figure 9 but for Window 2.

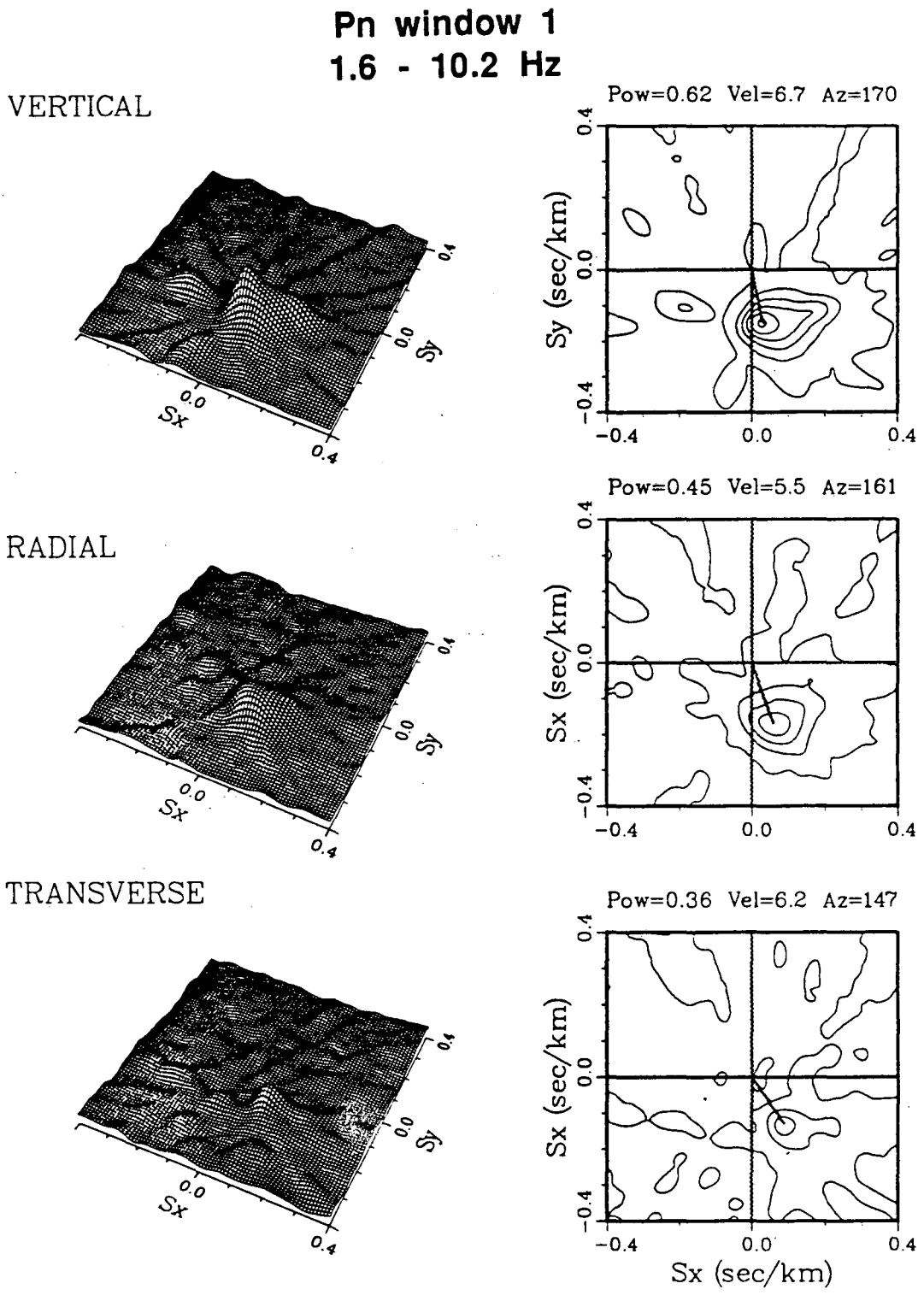

FIG. 4.11 Same as Figure 9 with stacking over the frequency range 1.6 to 10.2 Hz.

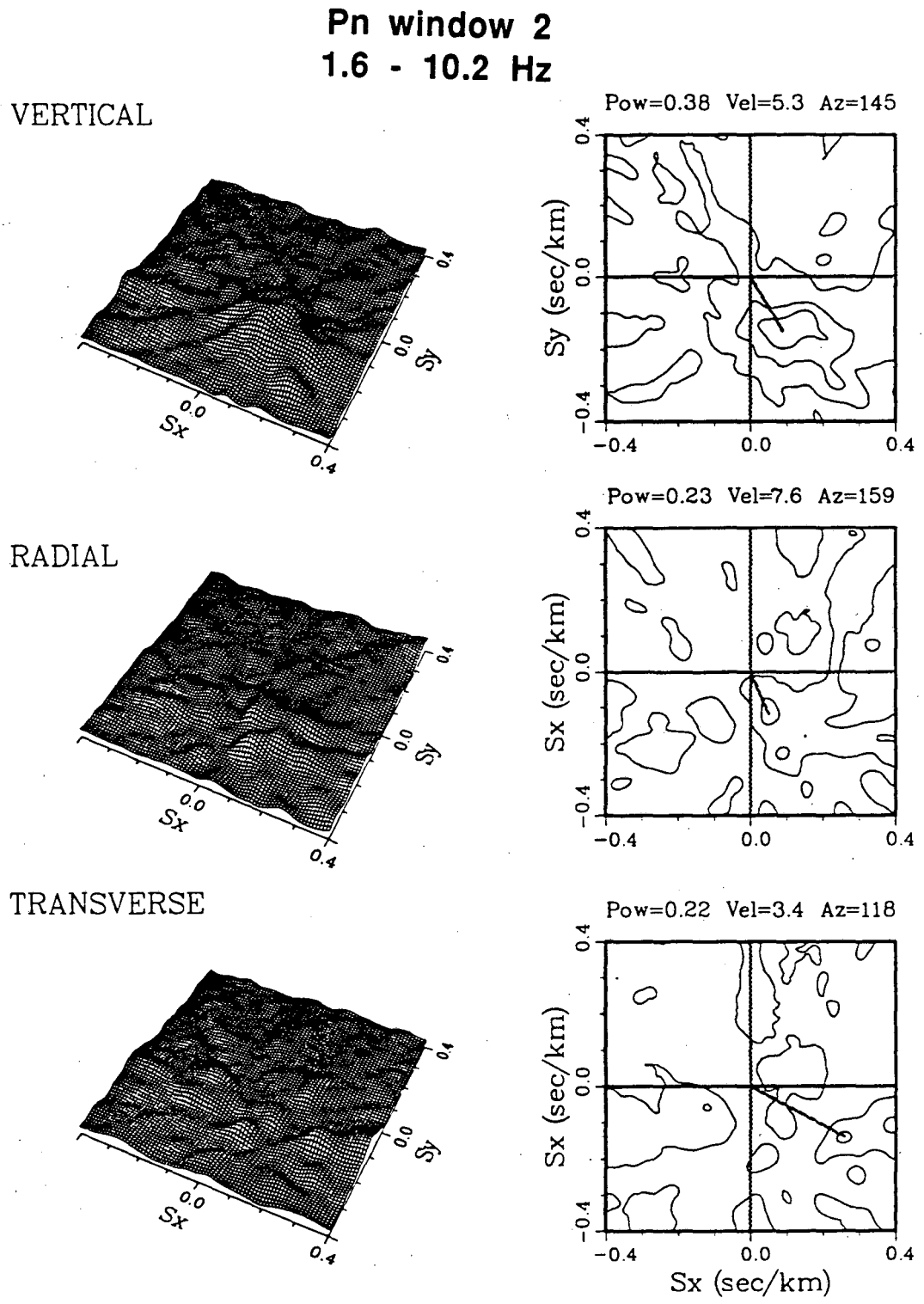

FIG. 4.12 Same as Figure 11 with stacking over the frequency range 1.6 to 10.2 Hz.

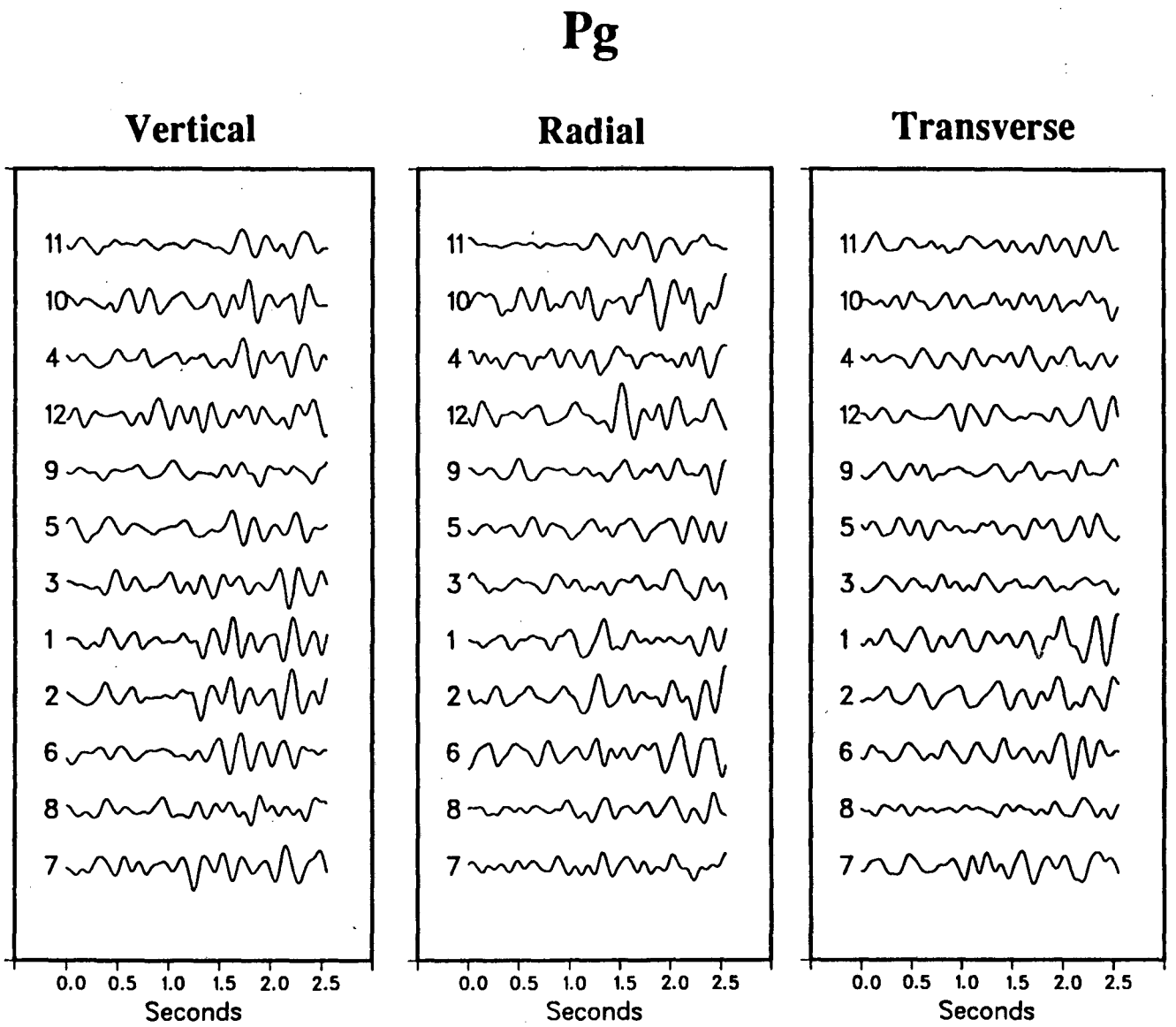

FIG. 4.13 3-component Pg waveforms used in the analysis. The waveforms are ordered from bottom to top in order of increasing epicentral distance from the NTS explosion. The station numbers are indicated to the left of the waveforms. As for Pn, two time windows are examined: Window 1: 0 to 1.3 seconds and Window 2: 1.3 to 2.6 seconds.

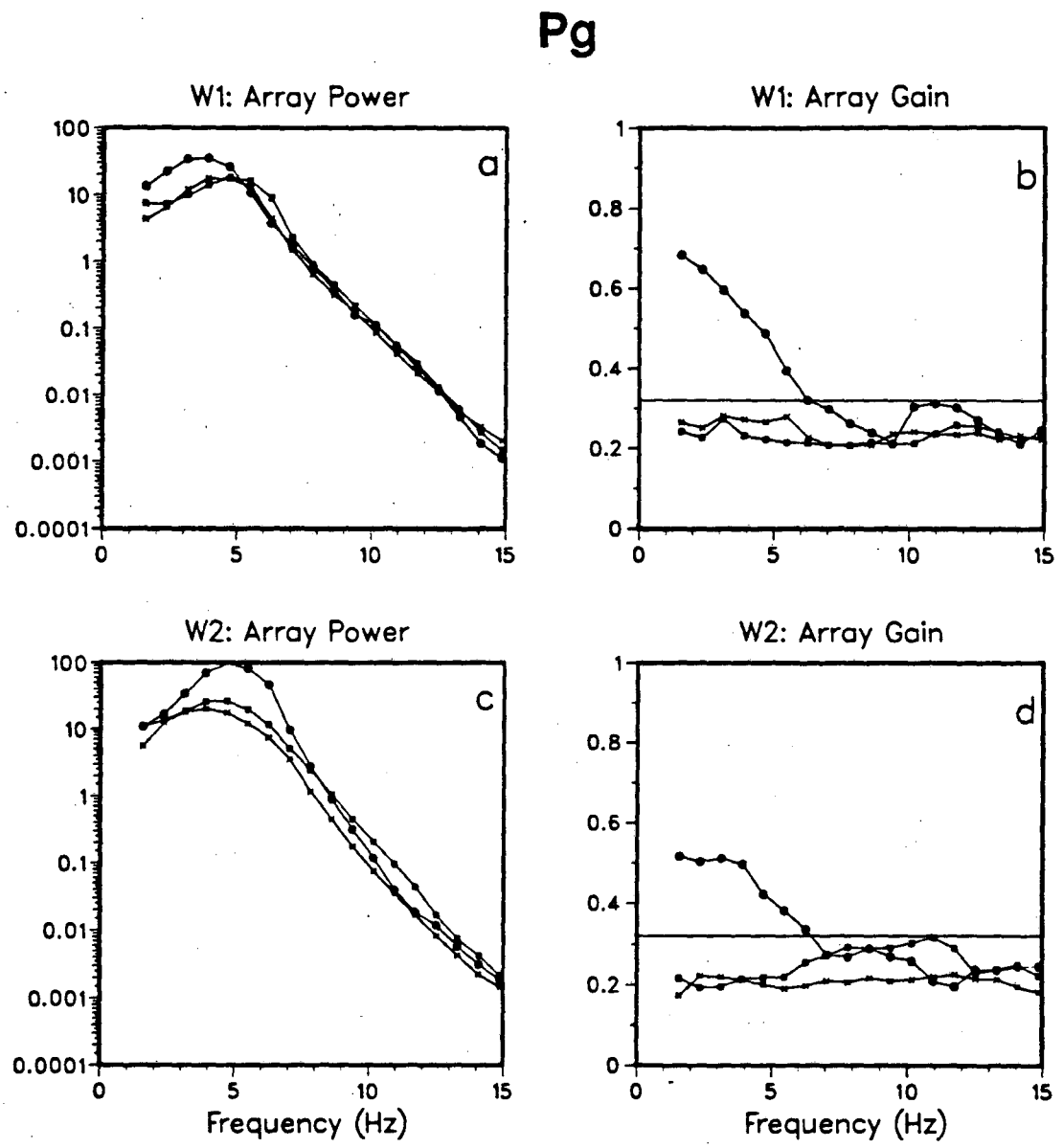

FIG. 4.14 3-component Pg array power and array gain for Window 1 and Window 2. The vertical component is denoted by solid circles, the radial by solid squares, and the transverse by crosses. The instrument response has not been removed from the power. The mean array gain level for white noise is approximately 0.32.

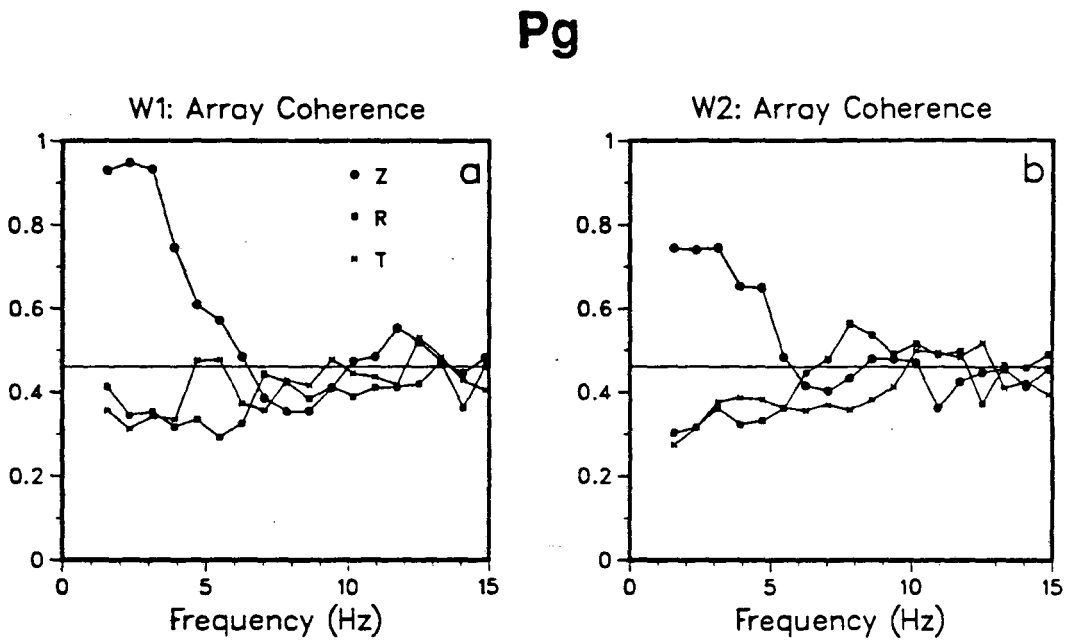

FIG. 4.15 3-component Pg array coherence for Windows 1 and 2. The vertical component is denoted by solid circles, the radial by solid squares, and the transverse by crosses. The mean coherence level for white noise is approximately 0.43.

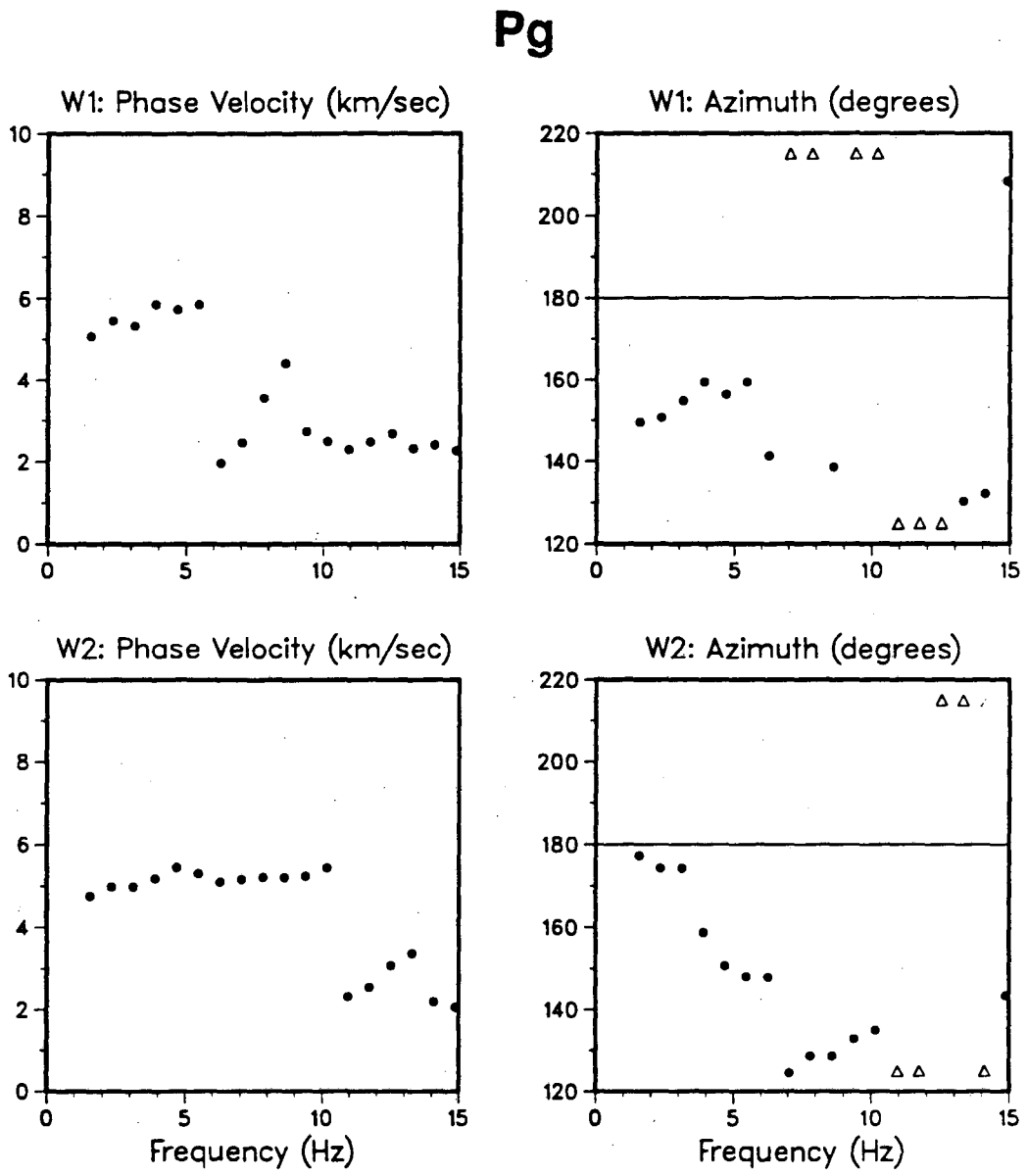

FIG. 4.16 Estimates of Pg phase velocity and azimuth, determined from the locations of vertical-component power spectral peaks in the slowness plane. The true source azimuth is 180 degrees.

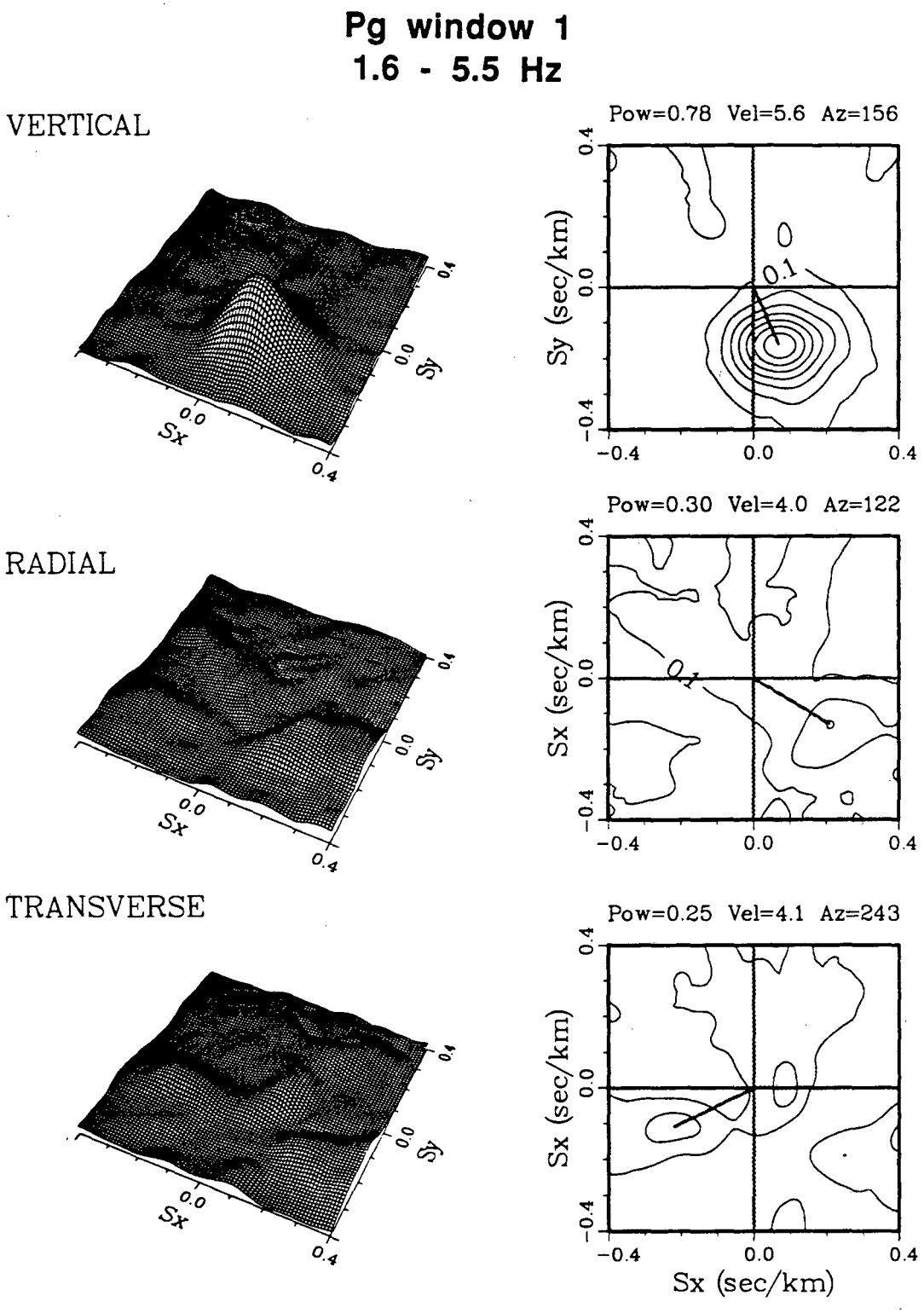

FIG. 4.17 Observed Pg 3-component slowness stacks over the frequency range 1.6 to 5.5 Hz for Window 1.

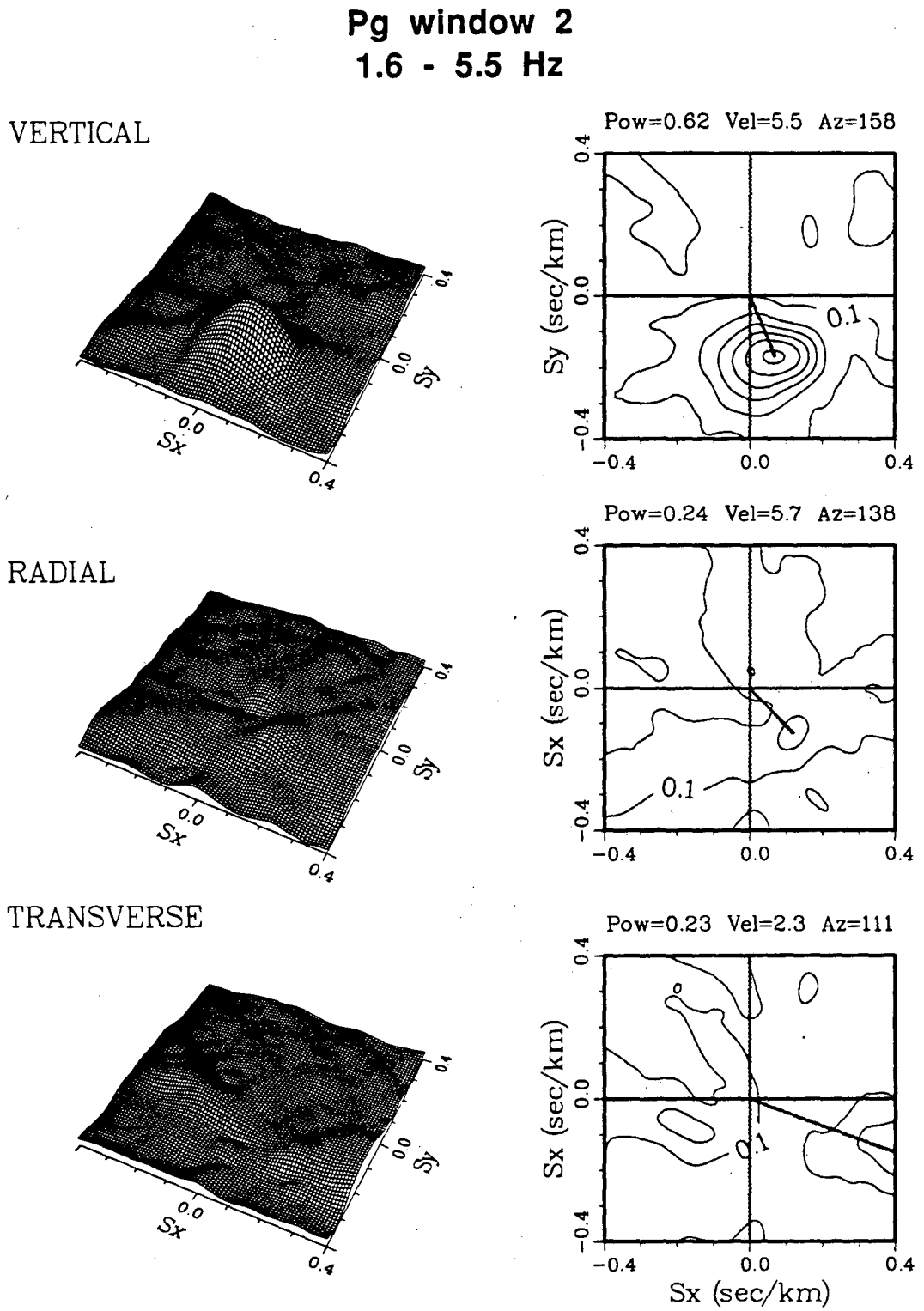

FIG. 4.18 Same as Figure 17 but for Window 2.

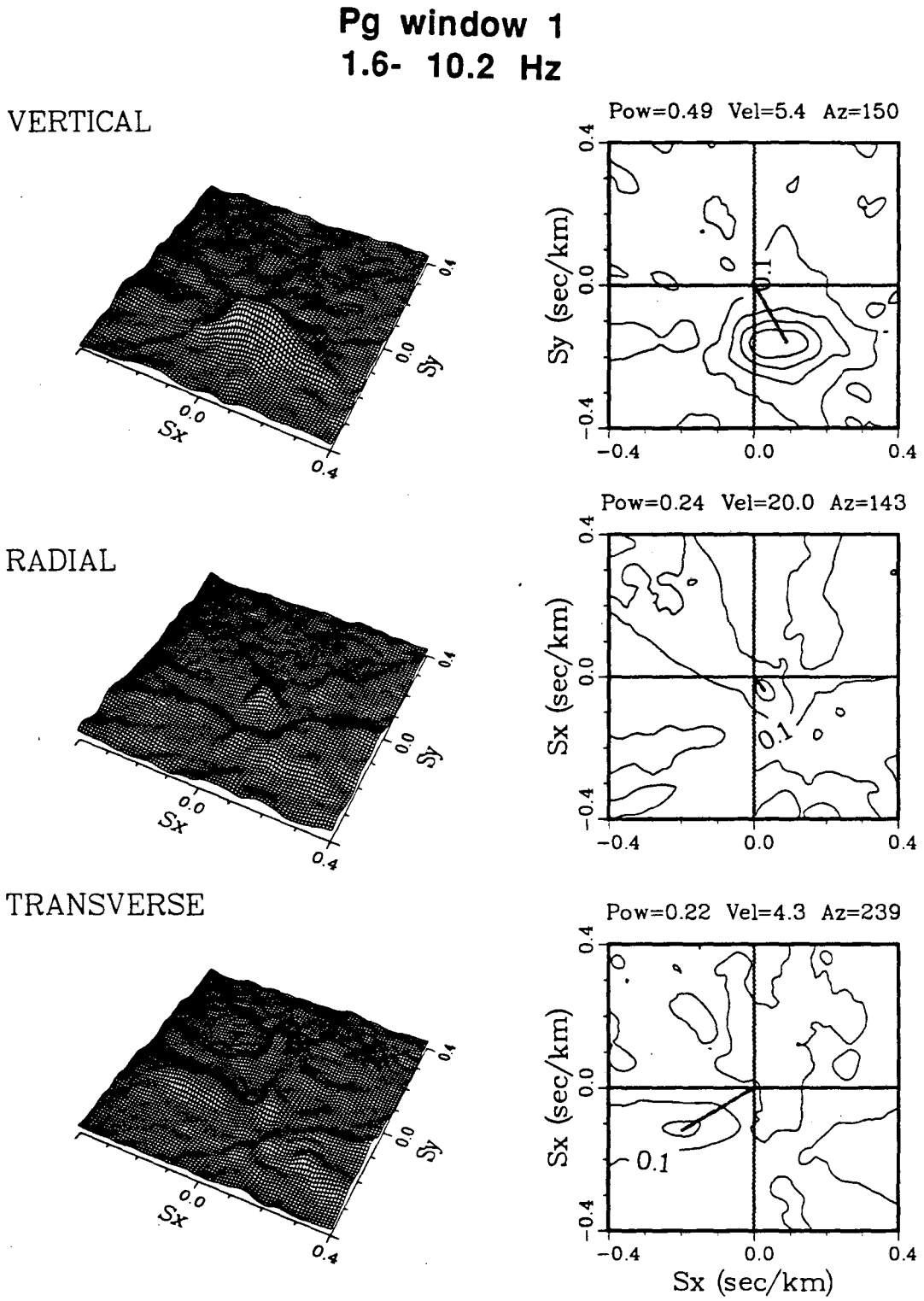

FIG. 4.19 Same as Figure 17 with stacking over the frequency range 1.6 to 10.2 Hz.

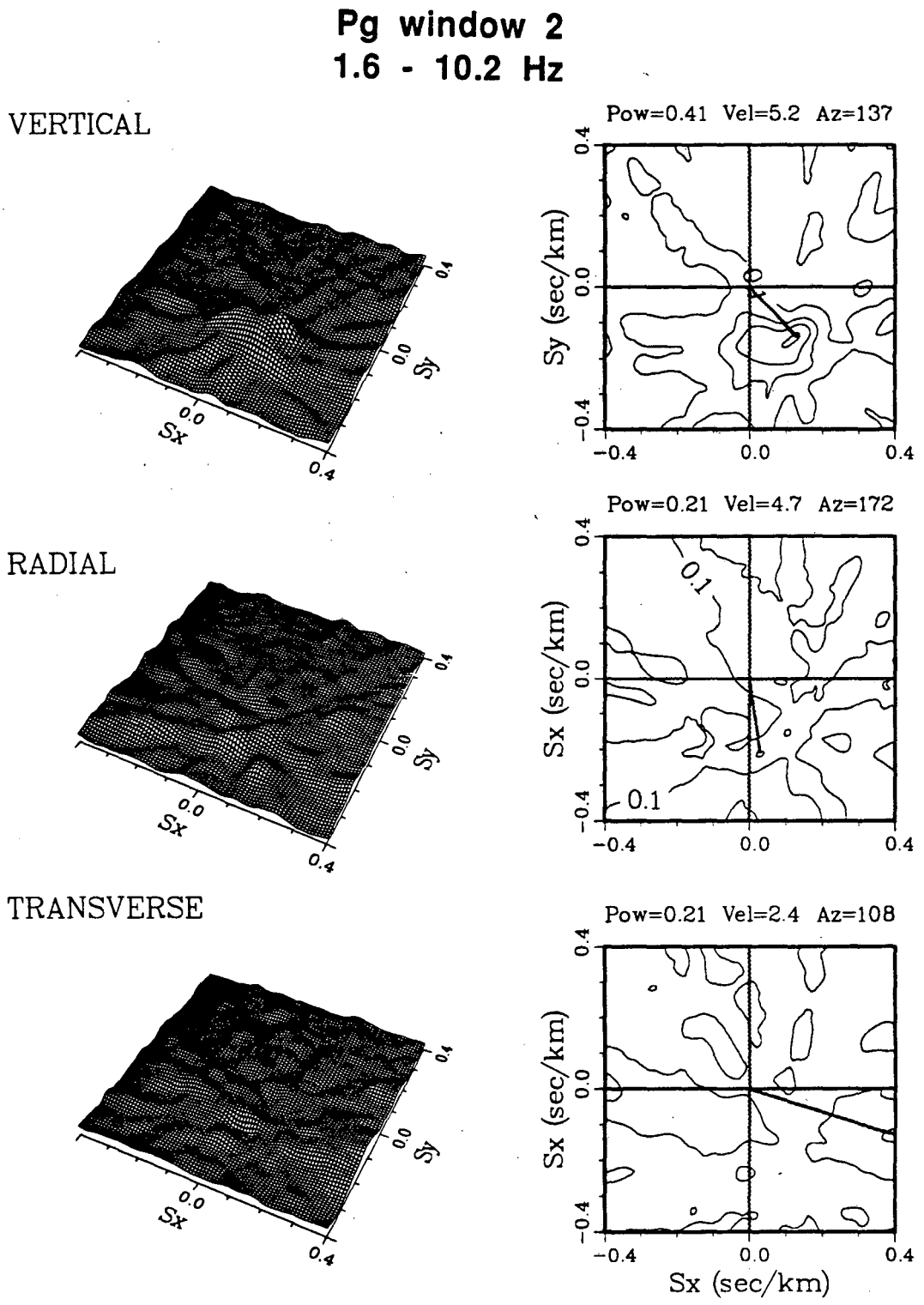

FIG. 4.20 Same as Figure 18 with stacking over the frequency range 1.6 to 10.2 Hz.

Chapter 5

Coherence Analysis

5.1 Introduction

In this chapter we will study the spatial correlation properties of the Pn and Pg wavefields at the Ruby Valley, Rice Valley, and Savahia Mountain array sites. It is spatial correlation which primarily determines the effectiveness of array processing schemes and hence the suitability of a location as a potential array monitoring site for NTS explosions. Correlation structure of course affects array design directly. Recording stations placed too far apart will have too little correlation. Stations placed very close together, though having high signal coherence, may also have high noise coherence. The final design of the NORESSS array, for example, was preceded by a reconnaissance array which studied signal and noise correlation properties (Mykkeltveit *et al.*, 1983). This chapter will assess the relative effectiveness of the three array locations as potential monitoring sites in terms of signal correlation and in doing so provide a means of constructing signal correlation models which can be used to simulate array processing characteristics.

The approach here is to first construct reliable estimates of coherence as a measure of signal correlation. We then parameterize these estimates in terms of spatially continuous models using a least squares inversion. Using these models we can specify a common geometry for the three array sites and directly contrast their array processing capability. The data come from the explosion HARDIN recorded at the Ruby Valley array and the explosion SALUT recorded at the Rice Valley and Savahia Mountain arrays. The smaller explosion VILLE is not included because of its low signal to noise ratio. In the process of the inversions we will be assessing the relative efficacy of six different models of coherence. The relative performance of each array will be quantified in terms of array signal gain, though additional

measures are possible.

The high station density at Rice Valley and Savahia Mountain will allow us to obtain very statistically significant estimates of signal decorrelation properties. A particular aspect of decorrelation which will be examined at all array sites is directionality. Studies by Mrazek *et al.* (1980) and Der *et al.* (1984) on regional wavefield correlation at large-aperture arrays find the Lg phase to decorrelate more along the wavefront (transversely) as compared to along the direction of propagation (longitudinally). Longitudinal decorrelation of Lg is expected because of dispersion. However the more significant transverse decorrelation indicates that inhomogeneous effects are more significant, such as scattering and multipathing, which causes a spread in the direction of arrivals and so decorrelate the wavefield transversely. Claassen (1985), studying a regional event at NORESS, finds transverse decorrelation to be more severe for all the regional phase he examined, Pn, Pg, Sn, and Lg. As we will see, our ability to resolve directional differences of Pn and Pg will be largely dependent on array geometry. We will precede the discussion of the coherence inversion results with a section describing the methods of coherence estimation and model parameterization.

5.2 Coherence Estimation and Modeling Procedure

The measure of signal correlation we will examine is the magnitude of the complex coherence spectrum. For a pair of time series the complex coherence is defined by

$$\gamma_{jk}(f) = \frac{S_{jk}(f)}{[S_{jj}(f)\, S_{kk}(f)]^{1/2}} \quad , \tag{5.1}$$

where the cross-spectrum $S_{jk}(f)$ is defined as in Equation 4.3. In effect, given that the complex spectral estimates have zero mean, the coherence is the correlation coefficient between $u_j(f)$ and $u_k(f)^*$. Its absolute value $|\gamma_{jk}|$ is commonly used as a measure of similarity, reflecting the extent to which two time series are linearly related. $|\gamma_{jk}|$ ranges in value from 0 to 1. Values of $|\gamma_{jk}| < 1$ suggest any combination of the following:

(1) decorrelation of the wavefield due to scattering from heterogeneities within the earth

(2) improper alignment of the two time series; the relative time delays from an impulsive propagating plane wave should be removed to isolate the pulse and concentrate its energy within the time segment being analyzed

(3) the presence of uncorrelated noise, including recording system noise and background earth noise

(4) dispersion

As evident in (5.1), the coherence estimates require a procedure for estimating cross- and auto-spectra of two time series. Here again we use the multiple-taper spectral estimation procedure of Thompson (1982). As in chapter 4 with the frequency-wavenumber analysis, we use the five lowest-order 4π tapers averaged over the first adjacent frequency to either side of the center frequency. The details and advantages of using multiple-taper estimation are discussed in Appendix C. The statistical properties of $|\gamma_{jk}|$ are rather complex. In particular, $|\gamma_{jk}|$ is not normally distributed and it has a variance which depends on the magnitude of its value. However, a transformation to $\tanh^{-1}|\gamma_{jk}|$ produces a distribution that is approximately normal, has a constant variance, and a constant bias which can be removed (Enochson and Goodman, 1965). For these reasons, a least squares fitting procedure is more appropriate for $\tanh^{-1}|\gamma_{jk}|$ rather than $|\gamma_{jk}|$. The $\tanh^{-1}|\gamma_{jk}|$ distribution becomes a poor approximation for small values of $|\gamma_{jk}|$. A more detailed discussion of the $\tanh^{-1}|\gamma_{jk}|$ transformation and the corresponding statistics is given in Appendix C. The standard deviation of the $\tanh^{-1}|\gamma_{jk}|$ estimates, based on our cross-spectral estimation procedure, is 0.26 (Equation C6 in Appendix C).

We will consider three types of correlation models: exponential, gaussian, and self-similar. Random scattering phenomena described in terms of exponential and gaussian models have been used, for example, by Chernov (1960), Aki (1973), Frankel and Clayton (1986), and Flatte' and Wu (1988). Frankel and Clayton (1986) also examined a self-similar model. These studies used these models to characterize the correlation properties of the earth's crust.

Here, functions of these types will be used to characterize the random nature of the ground motion itself. For each of the three models, we will fit one-dimensional (isotropic) and two-dimensional (directional) models. The isotropic models depend on the absolute separation between sensors and are characterized by a correlation distance a. The directional models depend on sensor separation in the longitudinal and transverse directions and are characterized by orthogonal correlation distances a_L and a_T, respectively. The functional forms of the $|\gamma|$ models are given in Table 1. The self-similar model is derived from the zeroth order Bessel function $K_0(r)$. Because K_0 equals infinity at $r = 0$, this function is used to model $\tanh^{-1}|\gamma|$ directly.

The three isotropic coherence models are shown in Figure 5.1a for $a = 1$. Below $r = a$, the exponential model exhibits the greatest decay rate, while beyond $r = a$, it is the gaussian model which decays most rapidly. The self-similar model is a compromise between these two models, behaving most like the gaussian model below $r = a$, and most like the exponential model beyond $r = a$. If we assume unit amplitude of the wavefield the complex coherence in Equation (5.1) becomes equivalent to the cross-spectrum and we can use Equation (4.3) to compute the corresponding wavenumber power spectrum for each model. These are plotted in Figures 5.1b and 5.1c to display the differences in decay rate and in Figure 5.2a to display the full three-dimensional perspective. Were there no decorrelation of the wavefield the power spectrum would simply be a spike located at the wavenumber of propagation. However, effects such as scattering produce a continuum of propagation velocities and directions resulting in a bandpass of power in **k** space centered at the dominant wavenumber. The bandpass of the one-dimensional models is isotropic in **k** space, i.e., decorrelation effects are uniform in all directions. The two-dimensional models allow for non-uniform decorrelation about the central wavenumber. In terms of array processing, transverse decorrelation will tend to degrade azimuthal estimates while longitudinal decorrelation will tend to degrade estimates of phase velocity. Examples of the directional coherence models are shown in Figures 5.2b for equal decay constants and in Figure 5.2c for decay constants differing by a factor of two. Note that

the isotropic exponential and self-similar models are not equivalent to the corresponding directional models with equal decay constants, while the gaussian model is.

The inversion for the model parameters from $\tanh^{-1}|\gamma|$ is a non-linear one and here we a Levenberg-Marquart inversion procedure (e.g. Lawson and Hanson, 1974). The inversion requires an initial estimate of the decay constants, which for the exponential and gaussian models we can get by performing a linear inversion with values of $\ln(|\gamma|)$. By taking the natural logarithm the exponential and gaussian models become linear in $1/a$ and $1/a^2$, respectively. The initial gaussian decay constants are also used as starting values for the self-similar inversion, which proved sufficient in synthetic tests. The non-linear inversions are iterated until no further significant improvement in fit can be obtained.

Synthetic random noise values of $\tanh^{-1}|\gamma_{jk}|$ at each array are shown in Figure 5.3. The values are plotted as a function of absolute station-pair separation and the best-fitting isotropic model is superimposed. The number of station pairs at each array site is 66 at Ruby Valley, 1081 at Rice Valley, and 10440 at Savahia Mountain. The 90% significance level for $\tanh^{-1}|\gamma_{jk}|$ noise, as derived in Appendix C, is approximately 0.7, which appears consistent with the random simulations. The noise will have its greatest effect on inversions for low values of decay constant, tending to return values with a positive bias. An additional biasing effect is that at low coherence the $\tanh^{-1}|\gamma_{jk}|$ transformation becomes one-sided as it nears its lower limit of zero. One course of action is to omit from the inversion, or downweight, $\tanh^{-1}|\gamma_{jk}|$ values at distances beyond which they fall almost exclusively below the noise level. However, the choice of a cutoff distance is not necessarily an obvious one, as we will see. In the inversions here we will simply weight the $\tanh^{-1}|\gamma_{jk}|$ values equally over the full aperture of the arrays, and keep the biasing effects in mind when we make use of the resulting models later on.

The ability of the $\tanh^{-1}|\gamma|$ data to reliably estimate the model parameters is largely dependent on the distribution of the independent variables, i.e., the spatial separations. Note in Figure 5.3 that differences in the best-fitting isotropic decay rates arise out of differences in

station distribution. In general, estimates of the decay constant improve as the number and range of the spatial separations increase. In Figures 5.4, 5.5, and 5.6 we examine the distribution of spatial separations at each array site. The distribution of the intersensor separations at the Ruby Valley array shown in Figure 5.4 is based on a 160 degree back-azimuth to the HARDIN event. For each of the 66 station pairs Figure 5.4a displays the longitudinal and transverse components of intersensor separation. In Figure 5.4b is a histogram of the number of station pairs vs. the absolute separation between them. The histogram interval is 0.2 km. Histograms are also shown in Figures 5.4c and 5.4d for the components of longitudinal and transverse separation; the similarity of the distributions indicates that the two directional decay constants will be estimated with about equal uncertainty. Similar distribution plots for Rice Valley array are shown in Figure 5.5 based on the known back-azimuth to SALUT. Here the range of longitudinal separation is almost a factor of four less than the range of transverse separations and so we would expect greater uncertainty in the estimate of the longitudinal decay constant. At Savahia Mountain in Figure 5.6 the span of longitudinal separation is again greater than the span of transverse separation, though the difference is not as great as at Rice Valley.

The effect of station distribution on the ability to resolve two-dimensional model parameters is shown in Figures 5.7, 5.8, 5.9, which display predicted values of $\tanh^{-1}|\gamma_{jk}|$ at each array site based on a two-dimensional exponential model with decay constants differing from between a factor of 2 and 15. In anticipation of the results below we have set $a_L > a_T$ at Ruby Valley and Savahia Mountain and $a_L < a_T$ at Rice Valley. The propagation directions used are the same as those used in the inversions. Best-fitting isotropic exponential models are also shown. We see that as the decay constant ratio increases so does the spread of $\tanh^{-1}|\gamma_{jk}|$ values. The spread would change very little had we chosen larger values of a_L and a_T with the same ratio. The important point to make here is that for small decay constant ratios the variation in $\tanh^{-1}|\gamma_{jk}|$ values away from a one-dimensional model may be within the standard deviation of the data, in which case it may not be possible to resolve the true directionality of the

wavefield correlation. This is particularly true for Savahia Mountain where the spread of values is almost imperceptible even with a factor of 15 difference in the two decay constants. This is a result of the narrowness of the intersensor distribution in Figure 5.6a. These points about the effects of station distribution, as well as the bias effects caused by noise, must be kept in mind when interpreting the inversion results below.

5.3 Pn Coherence

As we saw in Chapter 4, the choice of time window can have a strong effect on signal correlation. If the window is too long the coherence can be greatly reduced. But a very short window will result in poor frequency resolution. To reduce the contaminating effects of delayed scattering, and as an acceptable degree of frequency resolution, we will (as we did in Chapter 4) restrict the Pn window length to the first 1.3 seconds ($\Delta f = 0.78$ Hz) following the onset of Pn at each of the three array sites. The recordings are aligned prior to windowing.

The $\tanh^{-1}|\gamma_{jk}|$ estimates used in the inversions are displayed in Figures D1, D2, and D3 in Appendix D for each array site at frequencies ranging from 1.6 to 14.9 Hz; the best-fitting isotropic models are also plotted. In general, by 15 Hz there appears to no significant coherence beyond a station separation of about 500 meters. Vernon and Fletcher (1990), in a coherence study of local earthquakes at Pinon Flats, California also find P waves to be incoherent beyond about 15 Hz for station separations over 500 meters. We will make relative comparisons of the data in Appendix D through the model parameters discussed below.

We'll preface the examination of the the model parameters by referring to Table 5.2 which describes the relative goodness of fit for each of the six models. This is listed at each frequency in terms of the F statistic, which provides a relative comparison of the ability of the models to fit the data. The F statistic is simply the ratio of the variance of fit of each model to the variance of fit to the best-fitting model. Larger F statistics represent poorer fits to the model. The best fitting models are indicated by an asterisk *; in some cases two models fit the data equally well. At all three array sites it is generally the exponential models which provide

the best, or near-best, fit to the data. At Ruby Valley the variance of the directional exponential model is about a factor of two smaller than the isotropic variance at low frequencies, but as frequency increases the difference in fit between the two models becomes insignificant. We see similar behavior in the self-similar and gaussian models at Ruby Valley. At Rice Valley the difference in fit between the isotropic and directional exponential models is very small over the entire frequency band. This is also the case at Savahia Mountain. Some of the poorest model fits occur at Savahia from the self-similar and gaussian models. The actual standard deviations of fit for the best-fitting models are shown in Figure 5.10, and typically fall between about 0.3 and 0.5 $\tanh^{-1}|\gamma_{jk}|$ units.

With this background in mind, we can now turn to Table 5.3 which lists the Pn decay constants obtained at the three array sites for each of the six models. Because of their superiority of fit, we will focus the discussion primarily on the exponential models. It is extremely unlikely that the larger decay constants, up to 59 km for the isotropic model at Ruby Valley, can be extrapolated to such great distances. We can only assert that they are appropriate over the aperture of the array from which they are derived. In general, we should expect the decay constants to decrease with increasing frequency since a higher frequency wave traverses subsurface heterogeneities over more wavelengths. Referring to Figure 5.11a, which plots the exponential isotropic decay constants for each array site, we see that this is generally the case. However, there are pronounced local maxima in decay constant values near 4 Hz at Rice Valley and near 10 Hz at Ruby Valley, which are probably due to complex site effects. The increase near 10 Hz at Rice Valley and Savahia Mountain is due to noise bias mentioned earlier (see Figures D.2 and D.3 in Appendix D).

An alternative parameterization of isotropic coherence is an exponential one used by Menke (1990), which has the advantage of also incorporating frequency. This model is given by $|\gamma|=e^{-dfr}$, where d is a constant. Equating this to our $|\gamma|=e^{-r/a}$ model, and using the fact that $f = v/\lambda$ where v is velocity and λ is wavelength, implies that our decay constant a is a linear function of wavelength and that the quantity a*f is a constant. To examine the extent to which

such a model would be applicable to the data set here, Figure 5.11b displays a*f for Pn at each array site. The strong variation over frequency at each array site indicates that the relationship between the decay constants and wavelength is more complicated that a linear one and is site dependent. It is interesting to note that beyond 5 Hz the behavior of a*f is almost identical between Rice Valley and Savahia Mountain, though they differ by a factor of two.

The two-dimensional exponential decay constants are more closely examined in Figure 5.12. For each frequency the ratio of the two decay constants is plotted such that the result is greater than one. So if $a_L < a_T$ the ratio a_T/a_L is plotted (the cross-hatched bars in the figure) and if $a_L > a_T$, a_L/a_T is plotted (the blank bars). The ratios therefore indicate the factor by which the two decay constants differ. For random noise the ratio is within a factor of two. At Ruby Valley the difference in decay constants is large, with a_L between about 9 to 18 times greater than a_T (i.e., much greater decorrelation along the wavefront). The difference in the two decay constants eventually decreases with increasing frequency, as we would expect as we gradually fall into the noise. Beyond 9 Hz the ratios lie just above a value of one and the isotropic model fits the data just as well.

At Rice Valley, the differences between decay constants is probably not significant. With the exception of the 2-5 Hz range, the ratio values correspond to two-dimensional $\tanh^{-1}|\gamma_{jk}|$ spreads that are within the standard deviation of the data (see Figure 5.8). The large ratio values between 2 and 5 Hz correspond to inversions where a_L was unable to converge to a positive value. This is obviously non-physical since it implies that signal correlation improves with increasing sensor separation. The decay constant at these frequencies is given the value of infinity in Table 5.2. The cause of this could be the disparity in sensor separation range. Less constraint is placed on a_L because the maximum sensor separation in this direction is four times smaller than in the a_T direction. The F statistics in Table 5.3, obtained by setting $a_L = \infty$ actually represent relatively good fits to the data, however F statistics only 10% greater can be obtained by setting $a_L = a_T$, indicating little sensitivity of a_L to the data. In any case, over the entire bandwidth the isotropic model fits the data about equally well.

There is also little indication of directionality at Savahia Mountain. Below 5 Hz the ratio values are very small and inconsistent in their inequality. At higher frequencies, a_L again failed to converge to positive values. As at Rice Valley, the quality of fit is little affected by changes in a_L. And here again, the fit of the directional model is no better than the isotropic. However, because of the insufficient array geometry we cannot exclude the possibility of directional correlation at these two array sites. However at Ruby Valley the large differences in decay constants and the consistency of their sense of inequality with frequency indicates that directionality is significant.

5.4 Pg Coherence

As was the case for Pn, the Pg waveforms are aligned and windowed beginning at the onset of the phase. At Ruby Valley the time window is 1.3 seconds long, like Pn. At Rice Valley and Savahia Mountain the Pg window length is 2.6 seconds long. A longer window length is used here since it does not significantly degrade the signal correlation and provides greater frequency resolution (Δf = 0.39 Hz). The Pg $\tanh^{-1}|\gamma_{jk}|$ values used in the inversions are displayed in Figures D4, D5, and D6 of Appendix D.

The F statistics for Pg are given in Table 5.4. At Ruby Valley and Savahia Mountain the exponential models again provide the best fits. This is true also at Rice Valley beyond 6 Hz, however below 6 Hz the self-similar models are superior. The standard deviations of the best model fits is shown in Figure 5.13. The notable improvement in high-frequency fit of Pg relative to Pn at Ruby Valley is not significant. Figure D4 shows the Pg data to be near or below the noise level at high frequencies over the entire distance range. The standard deviations at Rice and Savahia are comparable to those for Pn.

The Pg decay constants are listed in Table 5.5. Looking back to Figure 5.11c, the exponential isotropic decay constants are plotted for each array site. Rice Valley consistently has the greatest decay constants. The decay constants at Ruby Valley and Savahia Mountain are very similar, with the exception of the 6-9 Hz bandwith where the Savahia values are

notably larger. The a*f values in Figure 5.11d again show a good deal of variation, though at Ruby Valley the values are much closer, relative to Pn, to the constant values predicted by the linear $a=p\lambda$ relationship (p a constant). In general however, it does not appear that incorporating this simple linear relationship into the exponential isotropic model would be appropriate for our data set.

The two-dimensional exponential decay constant ratios are plotted in Figure 5.14. At Ruby Valley a_L is again consistently greater than a_T, however the ratios are about five times smaller than for Pn. Though the ratios are relatively low, their consistency of magnitude and sense of inequality suggests the directionality is significant below 7 Hz, where the fit is also slightly superior to the isotropic model. At Rice Valley, the ratios are again probably not significant, as suggested by the very erratic ratio values. Below about 8 Hz, the three directional models often inconsistent in their sense of inequality, unlike Pg at Ruby Valley where the directionality appears robust enough to produce consistent inequalities across the three model types. The larger Rice Valley ratios beyond 10 Hz are also suspect given that so much of the data used in the inversion falls below the noise level. Also, the fit of isotropic models, the self-similar above 6 Hz and the exponential below 6 Hz, is comparable to the directional models. At Savahia Mountain we have the same problem as we had for Pn. The directional exponential model is again a poorly constrained model, with a_L converging to negative values. Restricting the inversion to station separations of 1.5 km or less, thus omitting low-amplitude, possibly noise-contaminated $\tanh^{-1}|\gamma_{jk}|$ values, does not improve the convergence. And again, the isotropic model provides as good a fit over the entire width.

Overall we cannot conclude significant directional properties in signal correlation at the Rice Valley and Savahia Mountain array sites for either Pn or Pg. This is not to say that directional characteristics do not exist. They might still be revealed with more spatially uniform distributions of stations. It does appear, however, that directional properties exist at the Ruby Valley array site. Specifically, at frequencies below 10 Hz for Pn and below about 7 Hz for Pg, the wavefields decorrelate more rapidly with distance along the transverse direction.

The directional sense of decorrelation agrees with the studies referenced earlier. We will now put our correlation results to the task of constructing models for array gain.

5.5 Modeling Array Gain

The objective here is to use our spatial measurements of $|\gamma_{jk}|$ to construct continuous models for the cross-spectrum, which can then be used in array processing simulations. We will form the cross-spectrum using

$$S(f,\mathbf{r}) = |\gamma(f,\mathbf{r})|\, e^{i\theta(f,\mathbf{r})}, \tag{5.2}$$

where $\mathbf{r}$ is the relative displacement vector between sensor-pair locations. This relation is a simplification of (5.1) in that it assumes unit amplitude of the cross-spectrum. The phase term is modeled from a propagating plane wave having wavenumber vector $\mathbf{k}$, and so is given by $\theta(f,\mathbf{r}) = \mathbf{k} \cdot \mathbf{r}$. The model cross-spectra are constructed by inserting the parameterized coherence models into (5.2). We will use these models to construct predictions of array signal gain. Recall from Chapter 4 that array gain reflects the overall signal correlation at an array and is a measure of how well the detectability of a phase can be improved through array processing. From Equations (4.3) and (5.2) we have the gain expressed as

$$G(f) = \frac{1}{N^2} \frac{\max\,[\bar{\mathbf{b}}(\mathbf{k})\, S(f)\, \mathbf{b}(\mathbf{k})]}{\frac{\mathrm{tr}\, S(f)}{N}} = \frac{1}{N^2} \sum_{j,k=1}^{N} |\gamma_{jk}(f)|. \tag{5.3}$$

5.5.1 Pn Array Gain

Before performing array processing simulations with the coherence models we'll first examine how modeled array gain compares with observed array gain, and use this information to make any necessary adjustments to the models. Beginning at Ruby Valley, Figure 5.15a shows the Pn model gain (5.2) based on the decay constants in Table 5.2. The directional exponential model is used up to 9 Hz. Beyond 9 Hz, where there is much less suggestion of directionality, the exponential isotropic model is used. The observed array gain computed

directly from the cross-spectra of the data is also shown; this gain is equivalent to the array gain of Chapter 4 (see Equation 4.3 and Figure 4.3). The two are close in agreement up to about 5 Hz. At higher frequencies the data gain drops to much lower values than the model gain. Figures 5.15b and 5.15c explain this behavior. In Figure 5.15b the model is compared to the magnitude coherence gain of the data, i.e., observed values of $|\gamma_{jk}(f)|$ are used in (5.3). These gain values are in good agreement with the model gain values over the entire bandwidth. In Figure 5.13c the model values are contrasted with the complex coherence gain, i.e., we simply include the cross-spectral phase term and compute the gain using $G = \frac{1}{N^2}\sum|\gamma_{jk}|e^{i\theta_{jk}}$. We see that when we add the phase term the gain values falls to much lower levels beyond 5 Hz. The reason for this is that at higher frequencies the phase becomes increasingly more variable, which has the effect of scaling down the gain. At lower frequencies the cross-spectral phase is consistently near zero and so has little effect on the gain. The array signal gain in Figure 5.15a is almost identical to the complex coherence gain, the slight differences owing to the fact that for the coherence gain cross-spectral normalization takes place before the matrix multiplication with the beamsteering vectors and for the signal gain it takes place after. The model gain and the observed signal gain in Figure 5.15a can be brought into agreement with the model correction factors in Figure 5.15d. These factors, when multiplied by the model gain values, produce the observed array signal gain. Below 5 Hz the correction factors are near unity. They become more significant with increasing frequency. These model correction factors will be used to scale down the model gains that we simulate in the following section.

A similar analysis is done for Pn at Rice Valley in Figure 5.16. Here, rather that examine the entire 4 km aperture of the array, the array is subdivided into all possible 1.5 aperture sub-arrays. This allows us to compare the results with those from the 1.5 km aperture Ruby Valley array, and it will give the model correction factors less statistical uncertainty. In all, there are 32 sub-arrays with between 15 and 17 elements each. The observed signal gain from each array is plotted in Figure 5.16a; there is a great deal of variation above 5 Hz. The model gains for each sub-array are plotted in Figure 5.16b. Because the existence of directional

decorrelation properties at Rice Valley is not conclusive, the exponential isotropic model parameters are used for the model gains. Plotted with these gains at each frequency are the sub-array magnitude coherence gain values which, like for Ruby Valley in Figure 5.15b, should be close to the model values. The differences however are greater here. This is due primarily to the variation in decorrelation properties among the sub-arrays and the fact that the model parameters represent an average of these properties over the entire 4 km aperture. The sub-array data values do, however, fall within the range of model gains. There is a relative offset of the model gains at higher frequencies. This is due to a noise effect mentioned earlier, i.e., the inversion for these small decay constants receives a positive bias by the noise values at distances beyond 1.5 km (see Figure D2c in Appendix D). These high-frequency model gains can be brought to the mean of the sub-array values if the inversion is restricted to station separations of within 1.5 km. The model correction factors are plotted in Figure 5.16c. There is a value at each frequency for every sub-array which brings the model gains in Figure 5.16b into agreement with the observed gains in Figure 5.16a. The mean of the correction factors, which is also plotted, becomes more significant (i.e., lower values) with increasing frequency. It is this mean of the model correction factors which will be used in the later array gain simulations. The mean of the model gains in Figure 5.16b, when scaled by the mean correction factors, produces the mean sub-array gain shown in Figure 5.16d. This mean gain can of course also be computed from an average of the observed gain in Figure 5.16a. Note that our overestimation of high-frequency decay constants due to noise contamination is compensated by lower model correction values.

The same sequence of plots for Pn at Savahia Mountain is shown in Figure 5.17. Here there are a total of 97 1.5 km aperture sub-arrays, having between 52 and 63 elements each. The sub-array gains are in general less than at Rice Valley. Again, because directionality is not conclusive, the model gains are based on the isotropic exponential model parameters listed in Table 5.3. The model correction factors are more significant here than at Rice Valley and the mean Pn gain in Figure 5.16d is consistently about 0.2 gain units less than the Rice Valley

Pn gain.

We should not expect that the model correction factors derived here for a 1.5 km aperture to be applicable to other array aperture dimensions. For example, a larger aperture array will have station pairs with greater decorrelation and more erratic cross-spectral phases, resulting in more significant model correction factors. 3 km aperture arrays are examined in Figures 5.18 and 5.19. At Rice Valley there are 15 sub-arrays with this aperture, having 33 or 34 elements each. The variation in sub-array gain (Figure 5.18a) is greatly reduced relative to the 1.5 km gains. The mean gain levels are also reduced. Notice that there is generally better agreement between the model gains and the sub-array gains in Figure 5.18b. This is because the 3 km aperture over which the sub-array gains were computed is much closer to the 4 km over which the model decay constants were derived. As expected, the model correction factors have also become more significant, particularly beyond 8 Hz. Similar results for the 45 3 km arrays at Savahia Mountain (111 to 113 elements each) are displayed for Pn in Figure 5.19. The disparity of coherence gain values in Figure 5.19b beyond 7 Hz is due to the large number of $\tanh^{-1}|\gamma_{jk}|$ values falling below the noise level but above the fit of the model. Recall that at these low decay constant values, $\tanh^{-1}|\gamma_{jk}|$ is bounded very nearby by zero; the distribution is no longer normal and values of $\tanh^{-1}|\gamma_{jk}|$ get "piled up". These low decay constant models decay so rapidly with distance that they necessarily underestimate the noise gain over an aperture of this size. (see Figure D3 in Appendix D).

5.5.2 Pg Array Gain

An examination of Pg array gain at the three array sites paralleling that for Pn is displayed in Figures 5.20 to 5.24. The Pg model gain at Ruby Valley in Figure 5.20a is computed using the directional exponential model up to 7 Hz. At higher frequencies, where there is little evidence for directionality, the isotropic exponential model is used. The difference between the model and data increases greatly beyond 5 Hz, as it did for Pn. The relatively low values of the model relative to the coherence gain beyond 5 Hz in Figure 5.20b is again

due to the small decay constants and the larger number of $\tanh^{-1}|\gamma_{jk}|$ values falling below the noise level at these higher frequencies (see Figure D4 in Appendix D). The Pg correction factors are a bit more significant relative to Pn, but the behavior with frequency is very similar.

The Pg gains at the 1.5 km sub-arrays at Rice Valley are shown in Figure 5.21. Like Pn, there is a wide range of signal gain. The model gains are computed using the best-fitting isotropic models. These are the self-similar model below 6 Hz and the exponential model above. The disparity between the model and coherence gains beyond 6 Hz can again be remedied by restricting the inversions to sensor separations to within 1.5 km. The model correction factors are a bit more significant than for Pn and the mean sub-array gain is about 0.1 units less than for Pn. At Savahia Mountain in Figure 5.22 the sub-array gains also span a wide range of values. The mean Pg signal gain falls between about 0.1 and 0.2 gain units below Pn and about 0.3 gain units below the Pg gain at Rice Valley. The correction factors are comparable to Pn, except between 5 and 10 Hz where the Pg values are up to 0.2 units lower. For the 3 km aperture sub-arrays in Figures 5.23 and 5.24 we find, as we do for Pn, that with respect to the 1.5 km sub-arrays there is (a) less variation in signal gain, (b) decreased mean signal gain, and (c) more significant model correction factors.

The Pn and Pg gain calculations above, performed as a check on the applicability of our model parameters, have been invaluable. We find that due primarily to stochastic fluctuations in cross-spectral phase away from that predicted by the best-fitting planar wavefront, our model parameters consistently overestimate the array signal gains. Correction factors had to be derived to bring the models into agreement with the data. We also find extreme variation in signal gain from the 1.5 km sub-arrays even though they are themselves confined within a 4 km aperture. This again underscores the stochastic nature of these wavefields and the need to approach them in a statistical fashion, as we have done here by matching average gains for a given aperture. Now, with our revised models in hand, we are ready to proceed to simulations of arrays gain.

5.5.3 Array Gain Simulations

As discussed at the outset, a principal reason for parameterizing the coherence was to use the results to construct spatially continuous models of the cross-spectral matrix (see Equation 5.2). This allows us to simulate array processing characteristics for an arbitrary array configuration and wavefield propagation direction. Here we will use this fact to reference our array gains, which are based on three very different array configurations, to a single array geometry. This will remove differences in gain due to differences in the arrangement of sensors and, if significant, azimuthally-dependent differences arising from directional correlation properties. The array design we will use is that used for the NORESS array. The configuration is shown in Figure 5.25 and is very similar to ARCESS, FINESA, and GRESS, the other recently deployed regional arrays mentioned in Chapter 1. The NORESS stations are laid out in four concentric rings A, B, C, and D, with one station A_0 located at the center. We'll use two geometries: (1) rings A, B, and C with A_0 (1.5 km aperture), and (2) rings A, B, C, and D with A_0 (3.0 km aperture). The basic difference between the two arrays is that the larger has greater resolving power in frequency-wavenumber space. This advantage can be negated, however, if the signal looses significant coherence over the larger intersensor separations. The Pn and Pg array gains for these two array geometries are shown in Figure 5.26. The model parameters used are the same as those used above in Figures 5.15 to 5.24. The gains have been scaled by the model correction factors appropriate for the indicated aperture. The mean correction factors are used for the Rice Valley and Savahia Mountain gains.

For the 1.5 km array the gain is typically the greatest at Rice Valley; Ruby Valley is only slightly greater below 4 Hz. The lowest Pn gain is consistently at Savahia Mountain. Rice Valley also maintains the greatest Pg gain, by an even greater margin than for Pn. The Ruby Valley Pg gain is notably greater than Savahia below 5 Hz, but the two become indistinguishably low at higher frequencies. At all array sites the Pn gain is greater than the Pg gain. Analogous 3 km gains are shown in Figure 5.26c and 5.26d. The model correction factors used for Ruby Valley correspond to its 1.5 km aperture, and so probably overestimate the 3

km gain simulations - the correction factors for Rice Valley and Savahia Mountain are typically more significant for the 3 km sub-arrays. A better representation might be to reduce the 1.5 km correction factors by the average of the amount that these factors were reduced at the two other array sites. The 3 km gain is in all cases lower the the 1.5 km gain. The Pg gain has fallen extremely low, with the most dramatic drop taking place at Rice Valley.

As a final example, we will use the fact that we can simulate the array gain from an arrival having an arbitrary azimuth to examine the effects of directional decorrelation on array gain. Figure 5.27 shows Pn gain based on Ruby Valley exponential decay constants and the 1.5 km NORESS configuration. Three gain curves are plotted. One is based on the isotropic decay constants and so is independent of wavefront propagation direction. The others are based on the directional decay constants up to 9 Hz, (and again isotropic beyond) with two orthogonal directions of propagation, one propagating due north (0 degrees) and the other propagating due west (90 degrees). We see that even though the directional decay constants differ by up to a factor of 18, the orthogonal gains are practically identical and only slightly lower than the isotropic gain below 9 Hz. This similarity is a positive attribute of the NORESS array configuration, which samples longitudinal and transverse station separations about equivalently, independent of propagation direction. Were the configuration a linear one similar to those of Rice Valley and Savahia Mountain, we would see a more significant azimuthal dependence with these values of directional decay constants. Array simulations of this kind can be an aid to effective array design once one has established signal correlation models for a potential array site of interest.

5.6 Summary Discussion

The aim of this chapter was to contrast the signal correlation properties at our three regional array sites and in doing so provide a means of constructing signal correlation models that could be used to simulate array processing characteristics. Below we summarize and discuss the principal results.

Modeling Procedure

Several notable aspects of the modeling procedure are worth summarizing. One is the use of multiple-taper spectral estimation techniques, which improved the frequency resolution of the estimates by decreasing the amount of frequency-averaging needed to obtain acceptable statistics (see Appendix C). Another is the $\tanh^{-1}|\gamma|$ transformation, which produced a more nearly normal distribution of data, making a least squares inversion more appropriate. In addition, because we have no way of knowing *a priori* how the spatial coherence behaves, we were careful to examine a range of correlation models. No doubt, even somewhat better parameterizations than those used here can be found, however the ability of the models to match the magnitude coherence gain indicates that the model fits are adequate. One obvious refinement to the modeling procedure is to restrict the inversion to sensor separations to within the array aperture being simulated. This would further reduce model misfit and avoid much of the noise bias that comes at high frequencies and large sensor separations. Although the configurations of the Rice Valley and Savahia Mountain array geometries precluded an understanding of directional correlation properties, we were nevertheless very fortunate to have such a high density of stations. The large number of recordings at these sites allowed us to obtain very statistically significant estimates of isotropic decay constants and mean array gain.

Modeling Results

The exponential models typically provided the best fits to the $\tanh^{-1}|\gamma_{jk}|$ data. The self-similar model gave the best fit in a few cases and the gaussian model usually gave the worst fit of all. We can argue for the directionality of decay constants only at Ruby Valley, where we find for Pn, and to a lesser extent Pg, that the wavefield decorrelates more severely transverse to the direction of propagation. This larger transverse decorrelation reflects the significant spread in propagation directions that we found in Chapter 4 for Pn and Pg at Ruby Valley (see Figures 4.5 and 4.16). Again, we cannot exclude the possibly that directionality also exits at the Rice Valley and Savahia Mountain sites. The greatest correlation of the Pn and Pg

wavefields, measured in terms of the magnitude of the isotropic decay constants, exits at the Rice Valley site. This could be due to the combined effects of less significant subsurface heterogeneity and topographic scattering effects.

Simulations

The array gain simulations were performed so that geometry- and azimuth-independent comparisons could be made between the array sites. They also serve as an example of the kinds of simulations which can be performed as an aid to the design of an array at a potential recording site, or to enhance understanding of wavefield properties at an existing array site. However, the mechanics of array gain simulations were not as straight forward as initially thought. The stochastic behavior of the cross-spectral phase at Ruby Valley required that adjustments be made to the parameterized models, our model correction factors. Then, even more randomness was revealed in the wide range of sub-array gains at Rice Valley and Savahia Mountain. Mean correction factors were computed which were themselves found to depend on array aperture. These stochastic manifestations of Pn and Pg underscore the fact that study of these wavefields requires good statistical sampling.

The analysis of simulated array gains showed that effective array processing of Pn much beyond a few Hz, and of Pg perhaps at any frequency much above 1 Hz, may not be possible for an array dimension as large as 3 km. We also find that though differences in directional decay constants will result in differences in the ability to resolve phase velocity and propagation azimuth, they do not result in a strong azimuth-dependency of array gain as long as there is a fairly uniform two-dimensional distribution of recording stations.

We have obviously not exhausted all possible array processing simulations. Any computations involving the cross-spectral matrix can be explored. This includes frequency-wavenumber power spectra, as in Figures 5.1 and 5.2, and other measures of signal enhancement which incorporate the correlation structure of noise. Additionally, the ability to simulate correlation characteristics can facilitate the determination of complex station weighting parameters aimed at optimizing array processing capability.

Coherence Models		
$\lvert\gamma\rvert$ model	isotropic	directional
Exponential	$e^{-r/a}$	$e^{-x/a_T}\, e^{-y/a_L}$
Gaussian	e^{-r^2/a^2}	$e^{-x^2/a_T^2}\, e^{-y^2/a_L^2}$
Self-similar	$\tanh(K_0(r/a))$	$\tanh(K_0(x/a_T))\, \tanh(K_0(y/a_L))$

Table 5.1 Coherence models considered in this study. For the directional models a_L is the decay constant in the longitudinal direction (i.e., in the direction of propagation) and a_T is the decay constant in the transverse direction (i.e., perpendicular to the direction of propagation). For statistical reasons the inversion for decay constants takes place after performing inverse hyperbolic tangent transformations on the coherence data and the models.

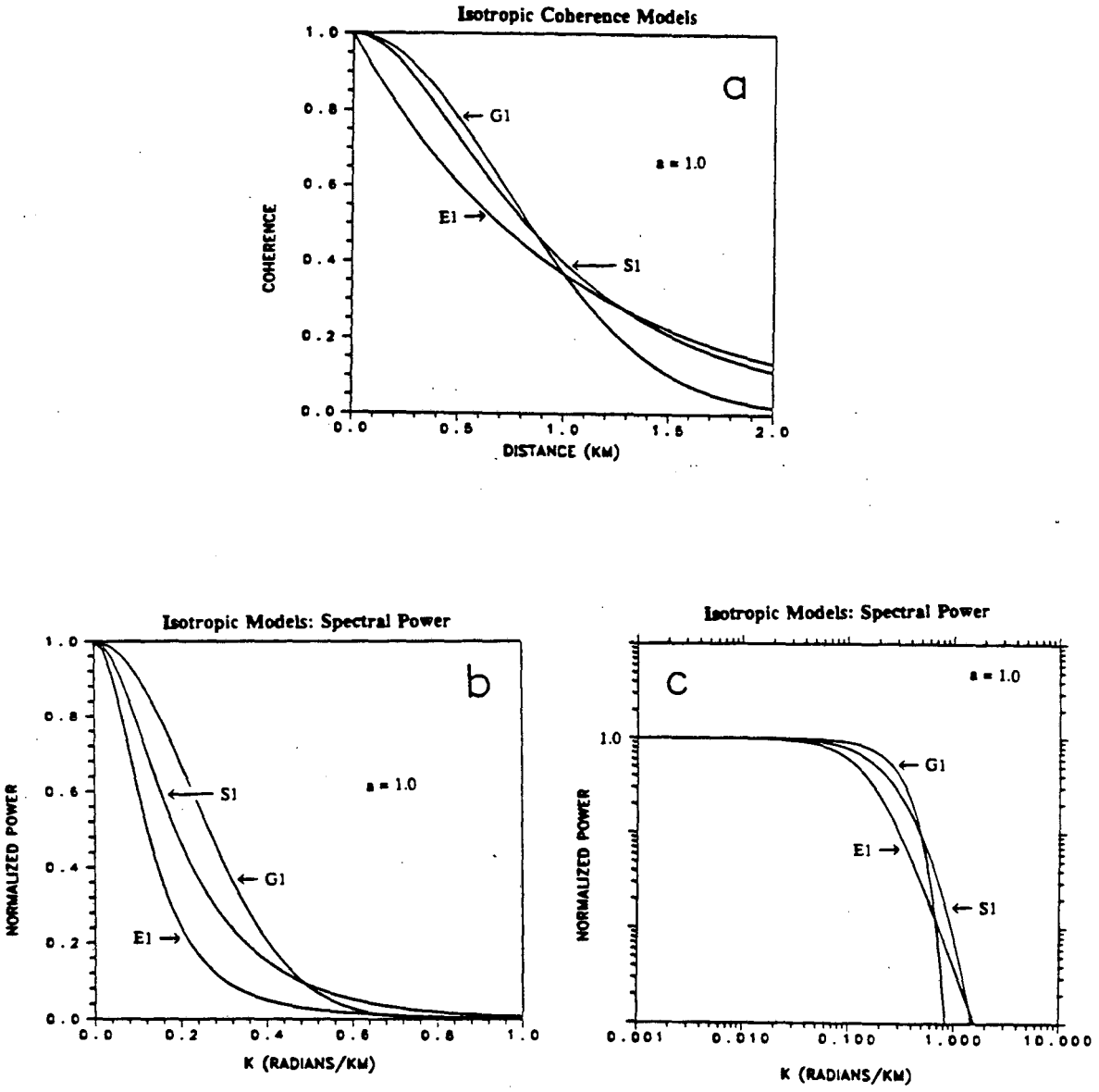

FIG. 5.1 (a) Examples of the three isotropic coherence models used. (b) and (c) The corresponding spectral power in linear and log plots. The decay constant here is 1.0 for all three models. The power for each model is normalized to a value of one. (E1 = Exponential, G1 = Gaussian, and S1 = Self Similar)

a = 1

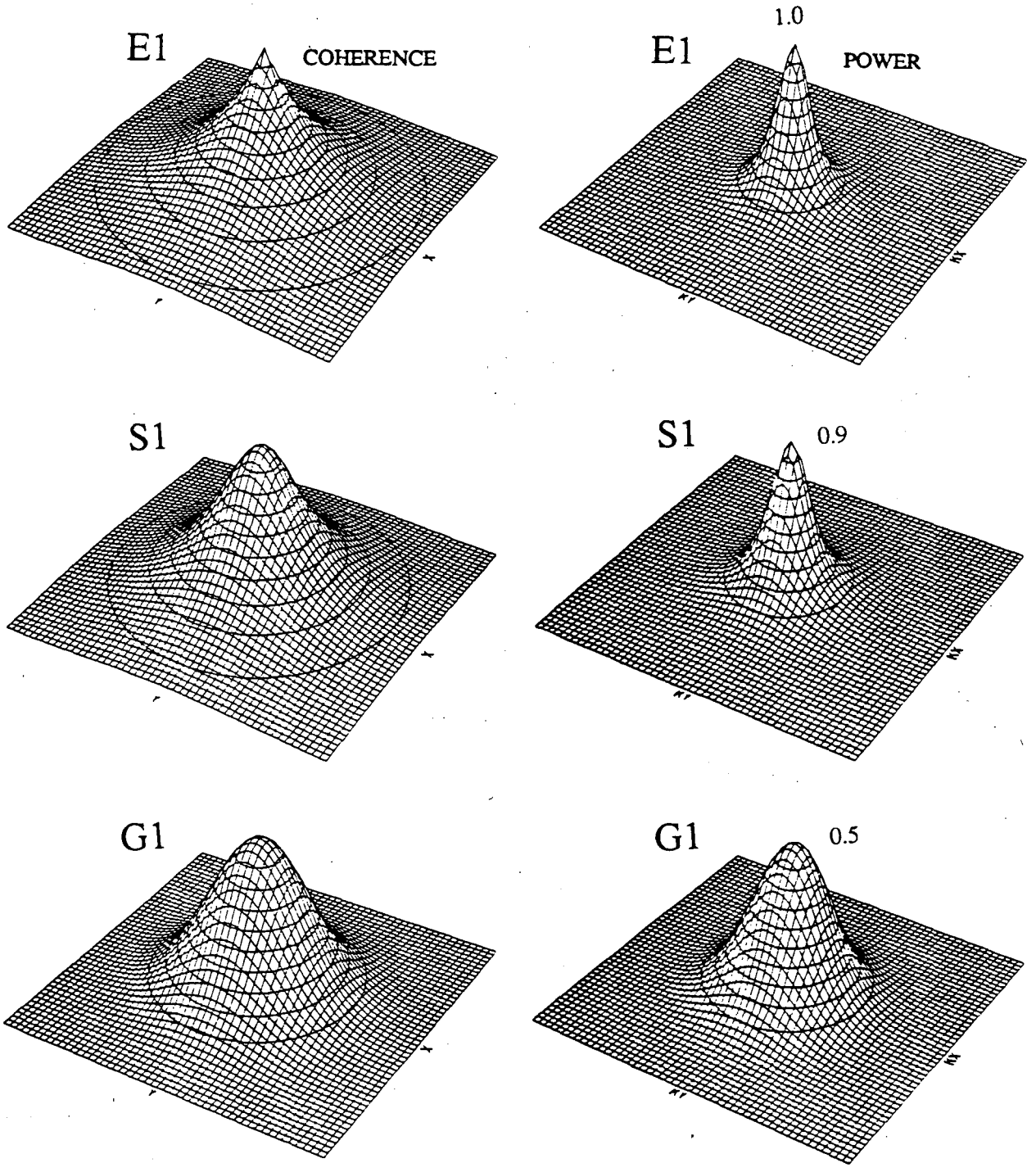

FIG. 5.2a Examples of the three isotropic coherence models and the corresponding wavenumber power spectra in three-dimensional perspective. The decay constant is 1.0 for all three models. The power spectra are normalized with the actual peak amplitude indicated.

$$a_L = a_T = 1$$

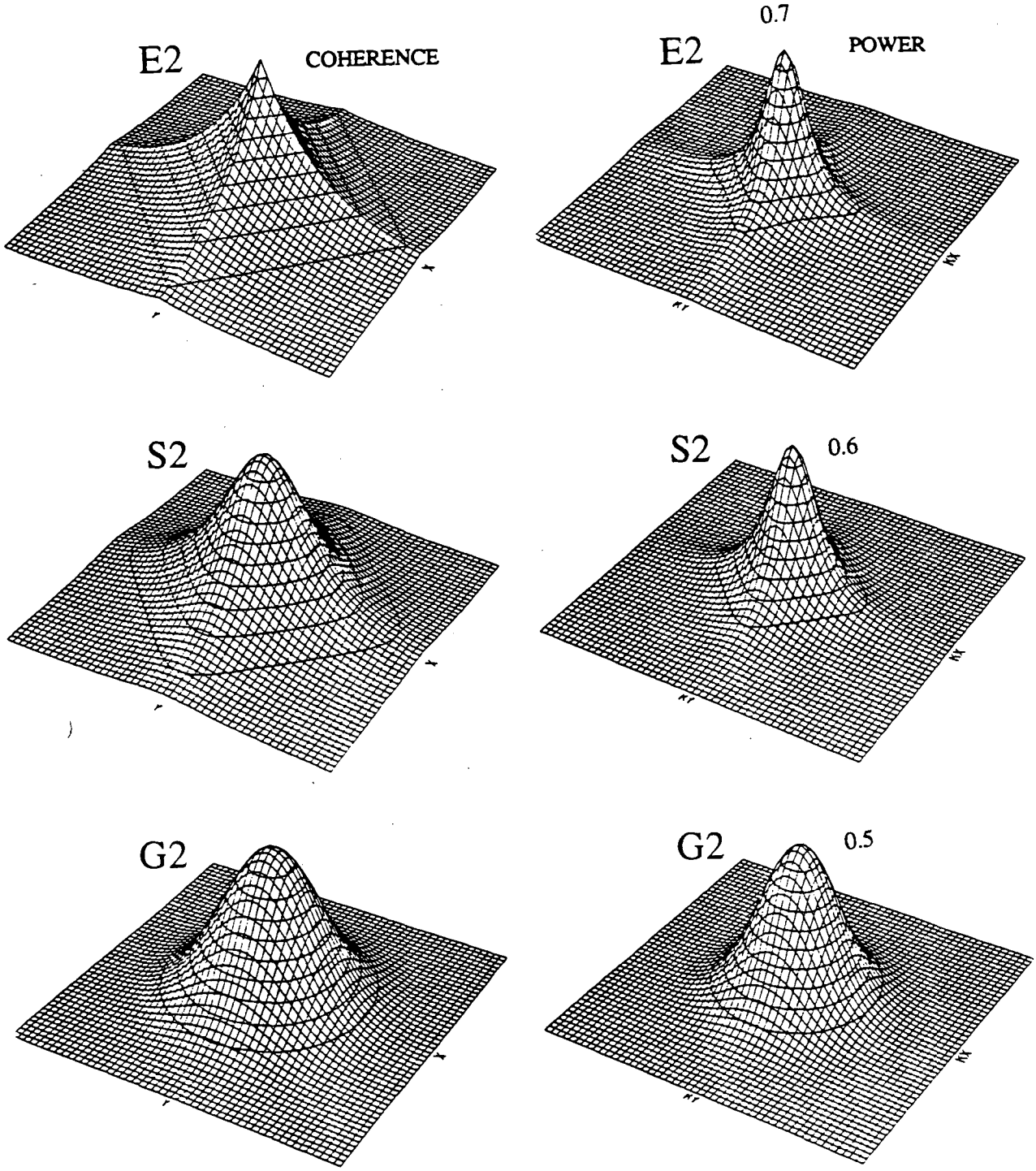

FIG. 5.2b Examples of the three directional coherence models and the corresponding wavenumber power spectra with equal decay constants, $a_L = a_T$. The power spectra are normalized with the actual peak amplitude indicated.

$$a_L = 2\ a_T = 1$$

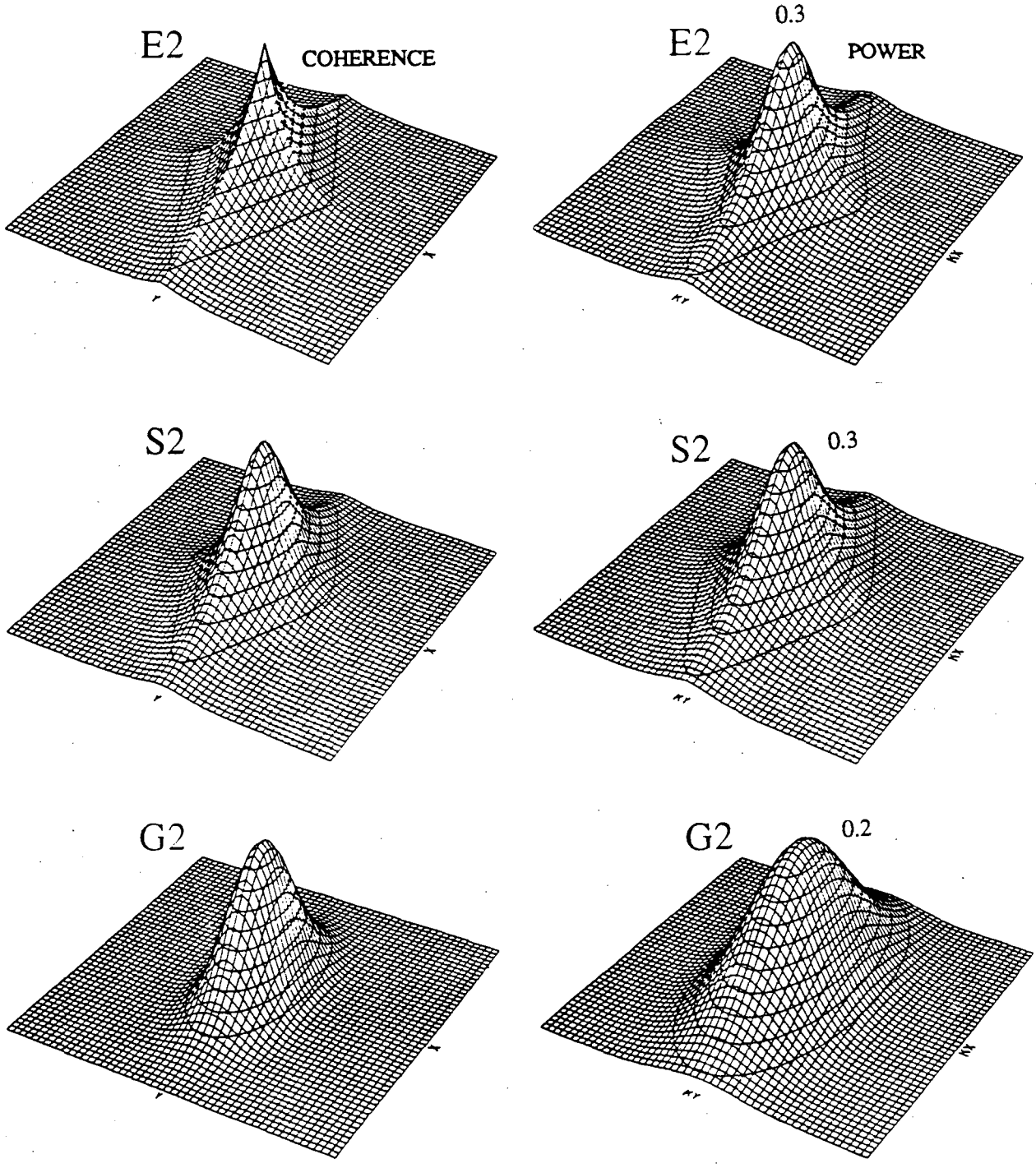

FIG. 5.2c Same as Figure 5.2b with decay constants differing by a factor of two, $a_L = 2a_T$.

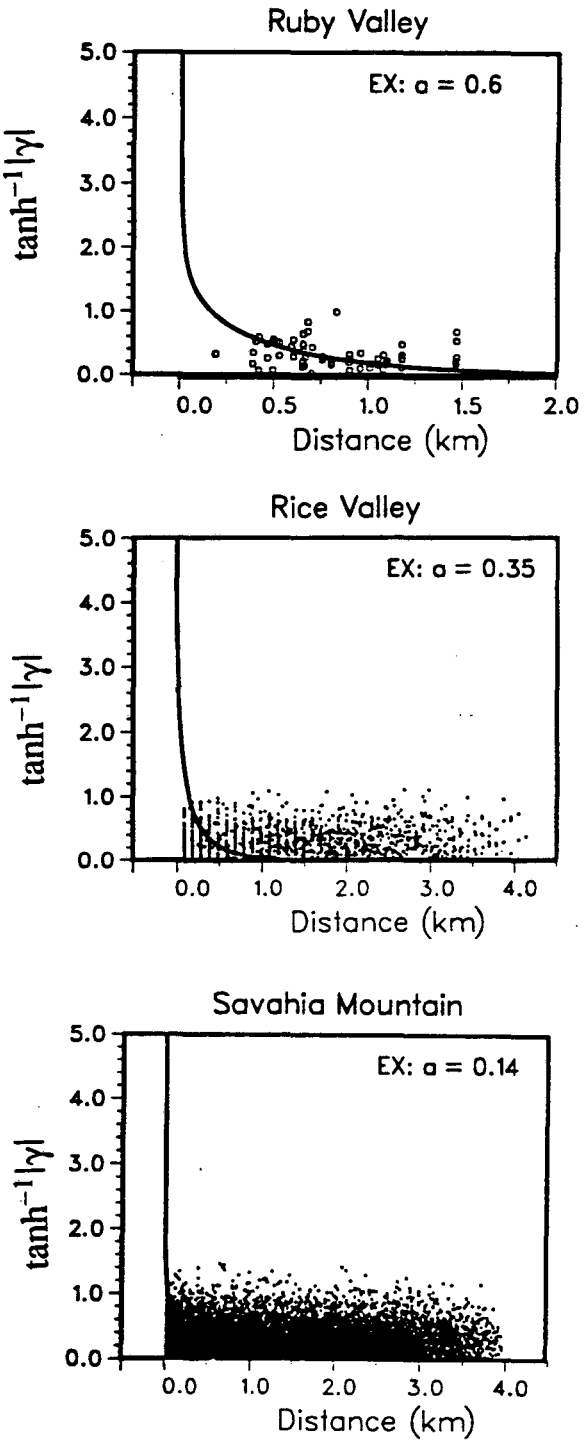

FIG. 5.3 Random noise $\tanh^{-1}|\gamma|$ values for all station pairs at each array site. The $\tanh^{-1}|\gamma|$ 90% significance level for noise is approximately 0.7. The best-fitting isotropic model is also plotted; the decay constant and model type are indicated (EX = Exponential).

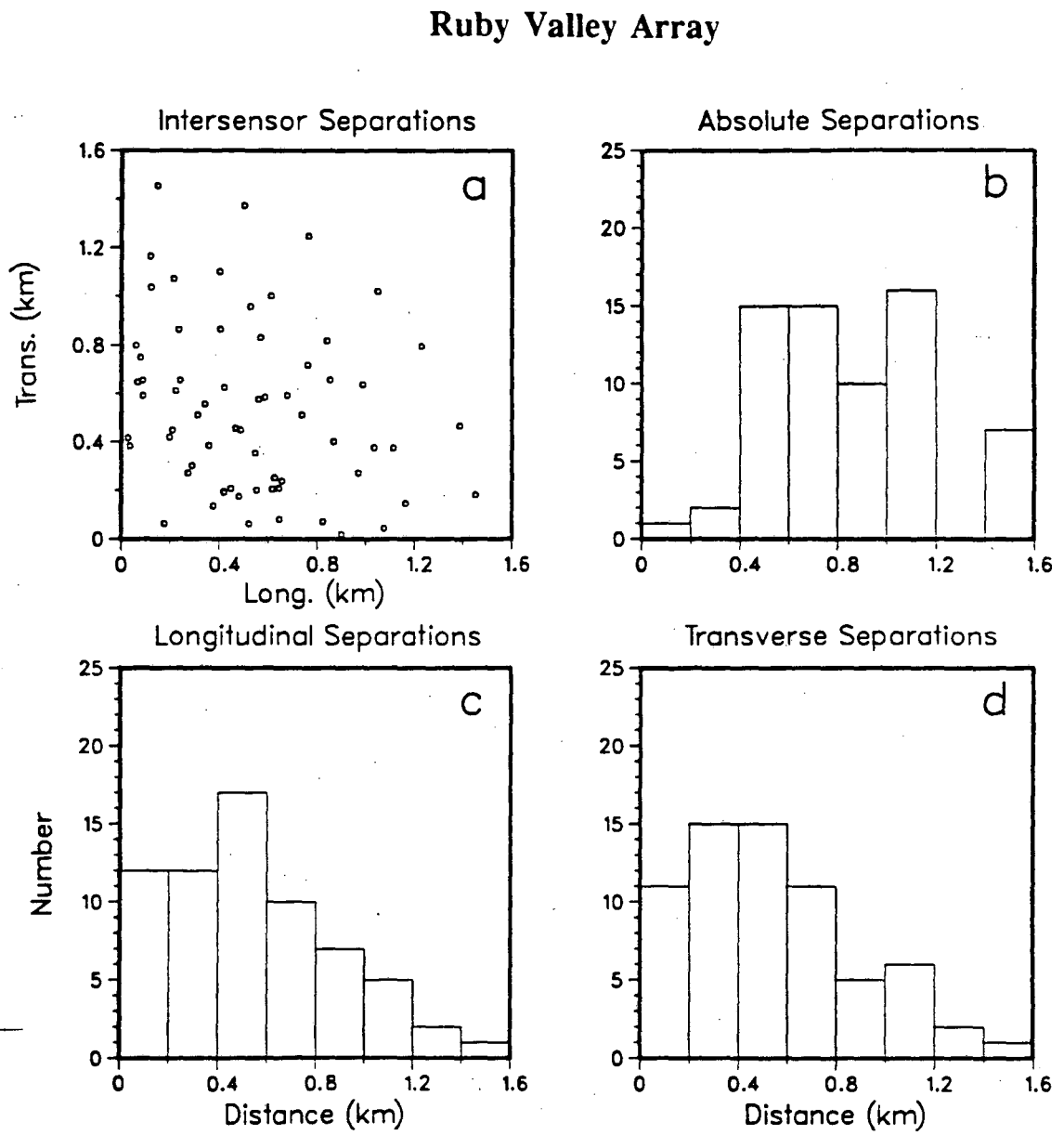

FIG. 5.4 (a) Distribution of the longitudinal and transverse components of inter-sensor separations for all 66 station pairs at the Ruby Valley array. (b) Histogram of absolute intersensor separations, summed in 0.2 km intervals. (c) Histogram of the longitudinal-component separations. (d) Histogram of the transverse-component separations.

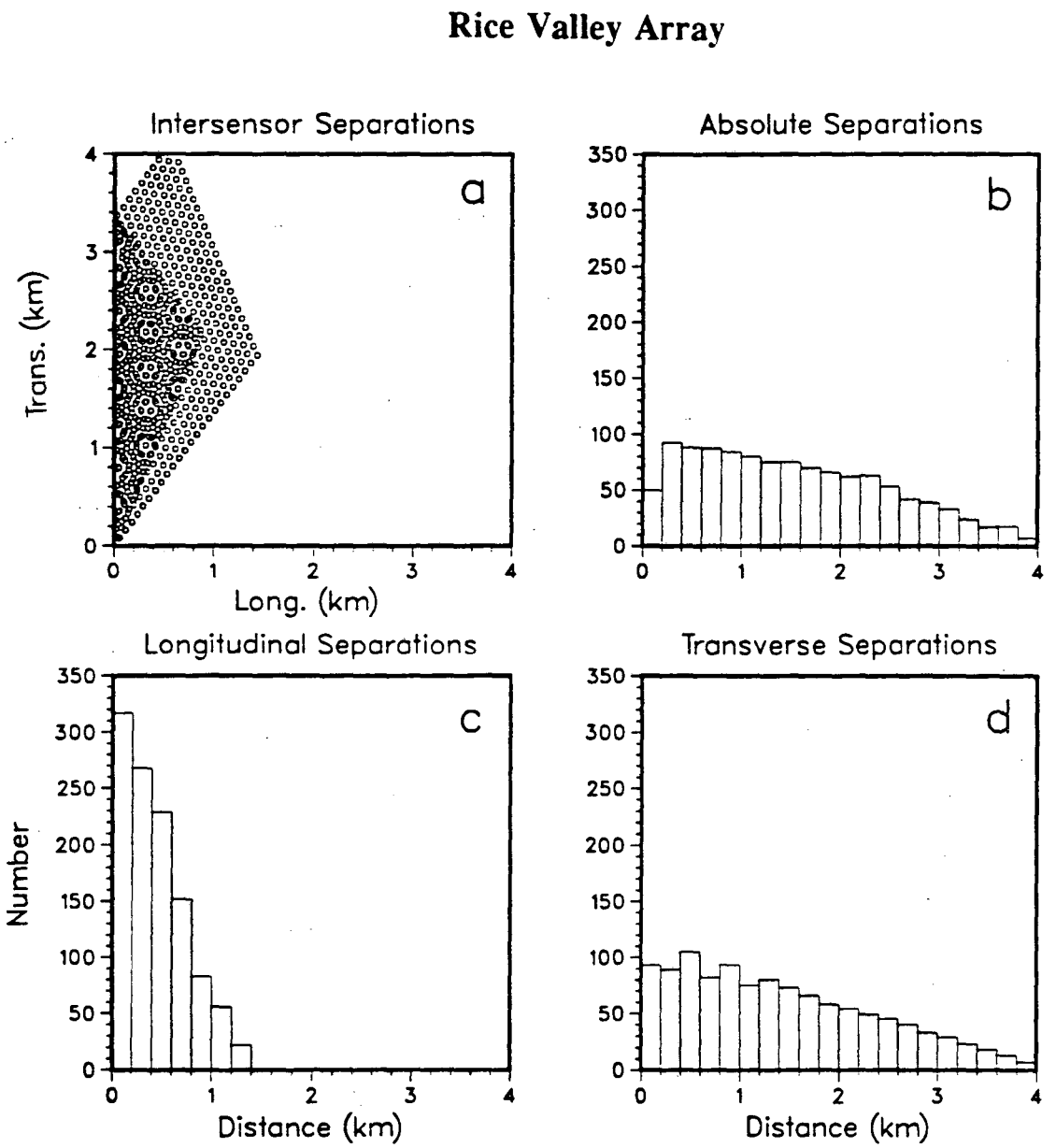

FIG. 5.5 Same as FIG. 5.4 but for the 47 stations at the Rice Valley array that recorded the explosion SALUT.

Savahia Mountain Array

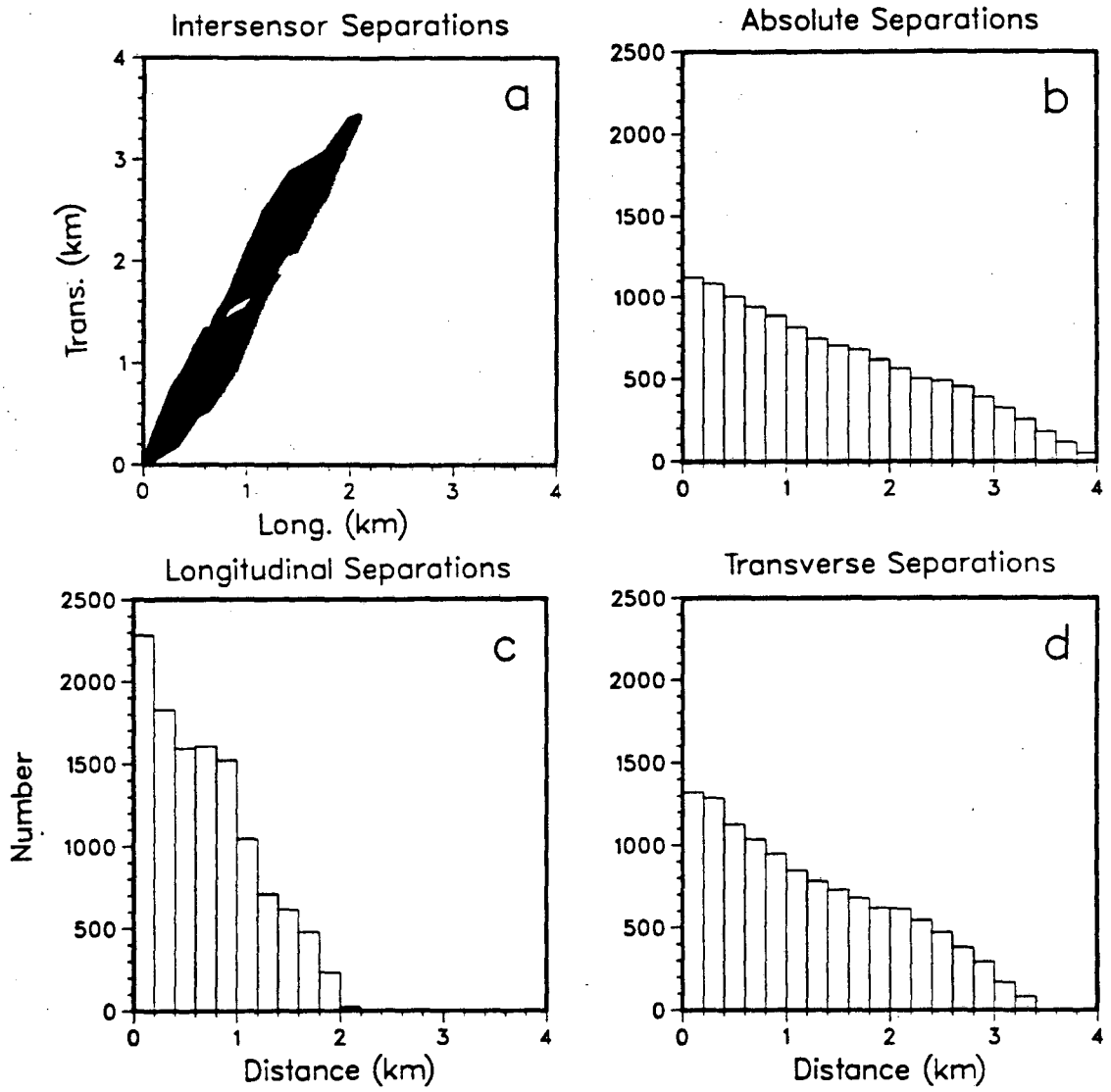

FIG. 5.6 Same as for FIG. 5.4 but for the 145 stations at the Savahia Mountain array that recorded the explosion SALUT.

2-D Exponential Model at Ruby Valley

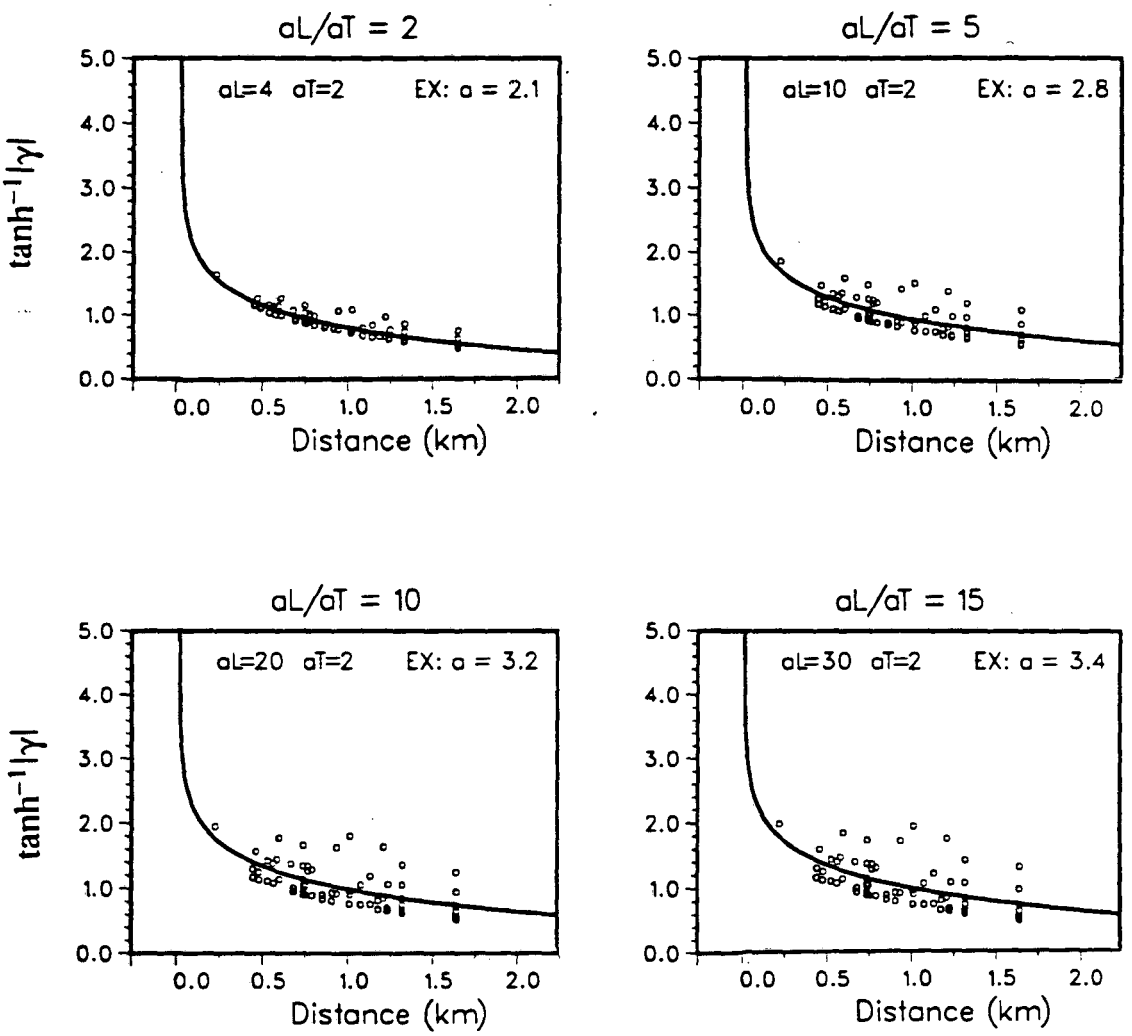

FIG. 5.7 Predicted $\tanh^{-1}|\gamma|$ values at Ruby Valley based on the directional exponential model with the indicated values of decay constant ratios. The best-fitting isotropic exponential model is also plotted.

2-D Exponential Model at Rice Valley

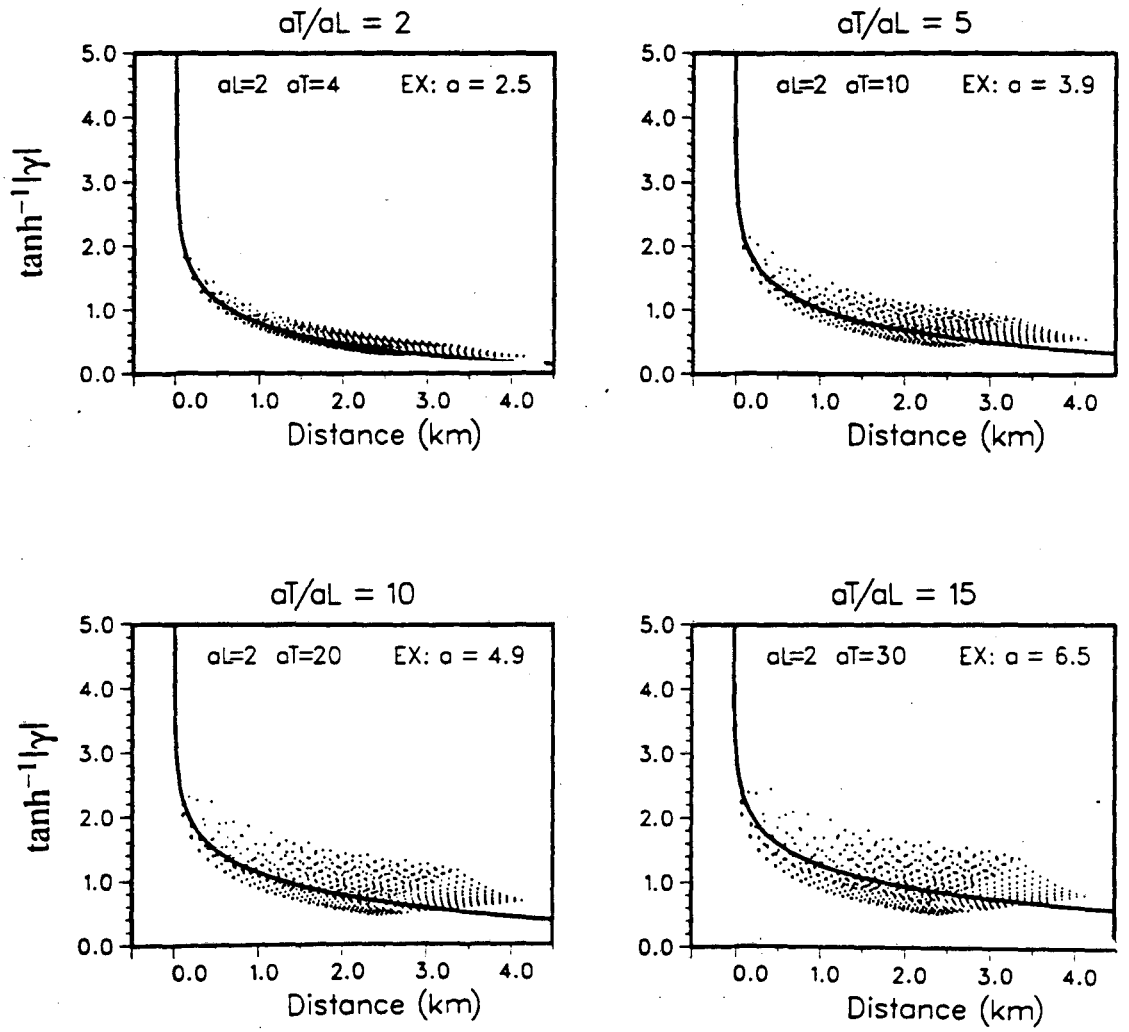

FIG. 5.8 Same as FIG. 5.7 but for Rice Valley.

2-D Exponential Model at Savahia Mountain

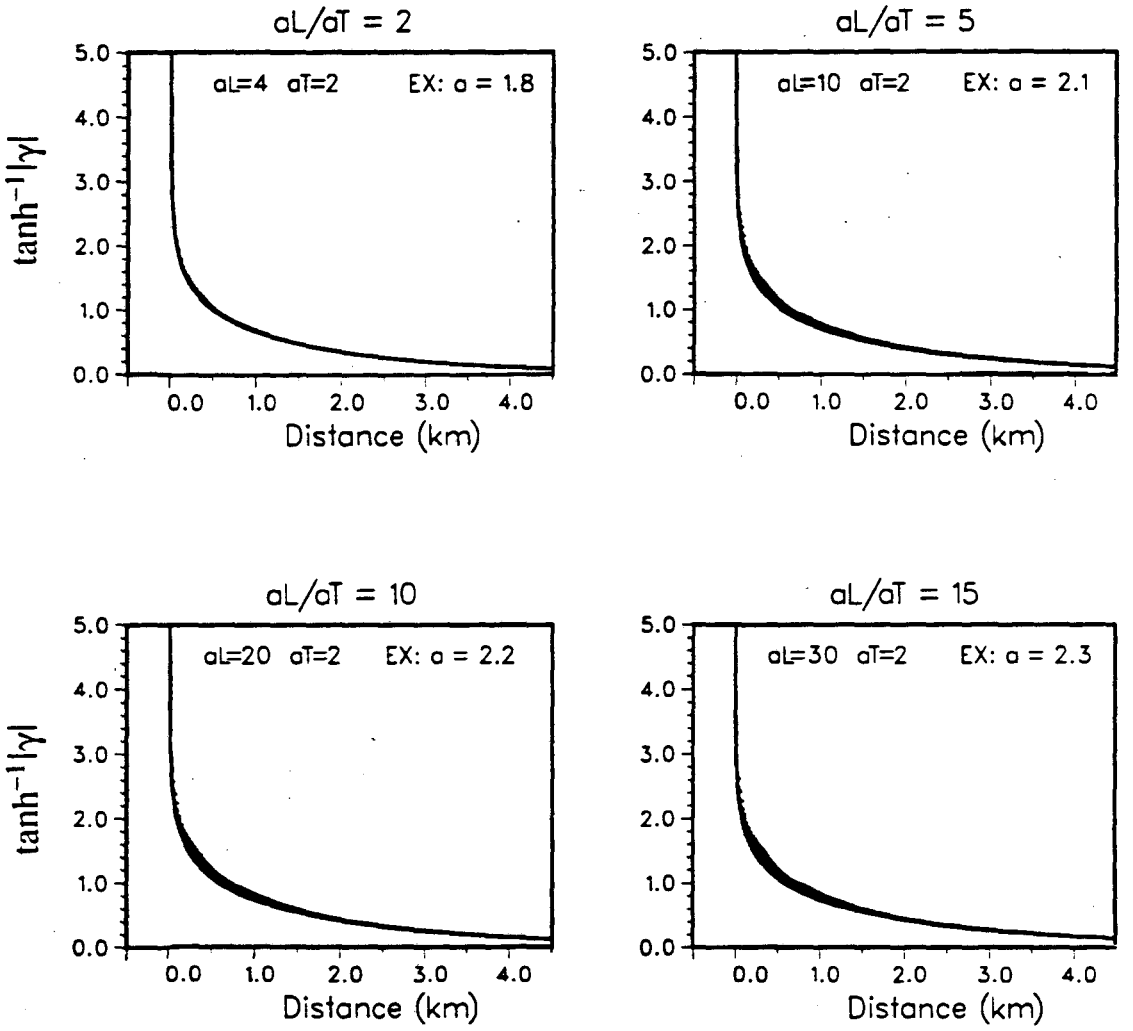

FIG. 5.9 Same as FIG. 5.7 but for Savahia Mountain.

F Statistics for Pn at Ruby Valley

Hz	E1	E2	S1	S2	G1	G2
1.6	1.8	*	2.3	1.6	2.4	1.6
2.3	1.8	*	2.6	1.8	2.6	1.8
3.1	2.1	*	2.3	1.2	2.4	1.3
3.9	1.8	*	1.9	*	2.0	1.1
4.7	1.9	1.1	1.8	*	1.9	*
5.5	1.8	1.1	1.7	*	1.7	*
6.3	1.5	1.2	1.4	*	1.5	*
7.0	1.2	1.1	1.3	*	1.3	1.1
7.8	1.2	*	1.3	*	1.5	1.1
8.6	1.2	*	1.2	1.1	1.3	1.3
9.4	*	*	1.2	1.1	1.3	1.3
10.2	*	*	1.3	1.3	1.5	1.5
11.0	*	*	1.3	1.3	1.4	1.4
11.7	*	*	1.2	1.2	1.4	1.3
12.5	*	*	1.2	1.2	1.5	1.4
13.3	*	*	1.2	1.2	1.5	1.4
14.1	*	*	1.2	1.2	1.4	1.4
14.9	*	*	1.2	1.2	1.5	1.5

F Statistics for Pn at Rice Valley

Hz	E1	E2	S1	S2	G1	G2
1.6	1.2	1.2	1.4	*	1.5	*
2.3	1.1	1.4	*	*	1.1	1.1
3.1	*	1.1	1.1	1.1	1.2	1.2
3.9	*	1.2	1.2	1.2	1.3	1.3
4.7	*	*	1.1	*	1.3	1.1
5.5	1.1	*	1.6	1.1	2.1	1.3
6.3	1.1	*	1.7	1.2	2.1	1.4
7.0	1.1	*	1.7	1.2	2.2	1.5
7.8	1.1	*	1.5	1.2	2.1	1.5
8.6	1.1	*	1.3	1.1	1.7	1.4
9.4	1.1	*	1.4	1.2	1.8	1.5
10.2	1.1	*	1.5	1.3	1.9	1.6
11.0	1.1	*	1.7	1.4	2.1	1.8
11.7	1.1	*	1.8	1.6	2.3	2.0
12.5	1.1	*	1.8	1.7	2.3	2.1
13.3	1.1	*	1.9	1.8	2.5	2.2
14.1	*	*	1.8	1.8	2.3	2.2
14.9	*	*	1.8	1.8	2.3	2.1

F Statistics for Pn at Savahia Mountain

Hz	E1	E2	S1	S2	G1	G2
1.6	*	*	2.6	2.7	3.1	3.1
2.3	*	*	2.4	2.6	3.0	2.9
3.1	*	*	2.6	2.7	3.1	3.0
3.9	*	*	2.7	2.8	3.3	3.3
4.7	*	*	2.6	2.7	3.3	3.3
5.5	*	*	2.3	2.4	2.9	2.9
6.3	*	*	2.5	2.5	3.1	3.1
7.0	*	1.5	2.2	2.1	2.8	2.7
7.8	*	1.1	2.1	2.1	2.7	2.6
8.6	*	*	2.1	2.1	2.7	2.6
9.4	*	*	1.9	1.9	2.3	2.2
10.2	*	*	1.8	1.7	2.0	2.1
11.0	*	*	1.7	1.7	2.0	1.9
11.7	*	*	1.6	1.6	1.9	1.8
12.5	*	*	1.5	1.5	1.8	1.8
13.3	*	*	1.5	1.5	1.8	1.7
14.1	*	*	1.7	1.7	1.9	1.9
14.9	*	*	1.6	1.6	1.8	1.8

Table 5.2 F statistics for Pn $\tanh^{-1}|\gamma|$ model fits for all six models as a function of frequency. The best-fitting models are indicated by *. In some cases two models fit the data equally well. Larger F statistics represent poorer model fits. (E1 = 1-D Exponential, E2 = 2-D Exponential, S1 = 1-D Self Similar, S2 = 2-D Self Similar, G1 = 1-D Gaussian, G2 = 2-D Gaussian)

Standard Deviations of Best Fitting Models

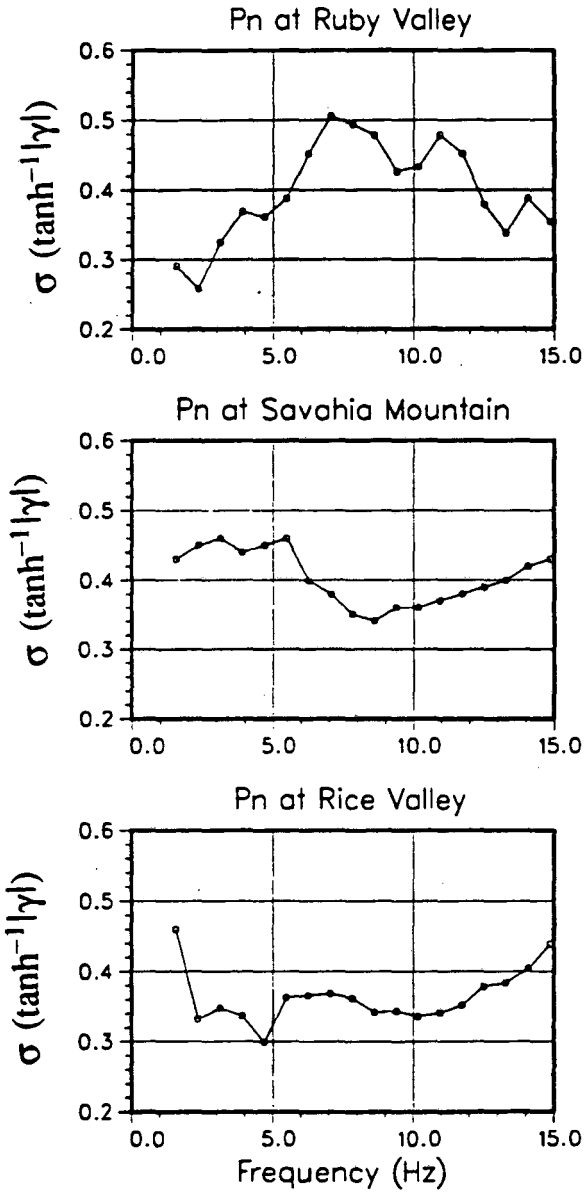

FIG 5.10 Standard deviations of the best Pn $\tanh^{-1}|\gamma|$ model fits at each of the array sites.

Decay Constants for Pn at Ruby Valley

Hz	E1	a_L E2	a_T	S1	a_L S2	a_T	G1	a_L G2	a_T
1.6	59.4	303.7	38.8	2.3	13.6	6.1	6.8	10.8	4.9
2.3	35.1	152.0	23.8	6.4	9.8	4.8	5.2	7.8	3.9
3.1	13.5	139.9	7.9	3.9	8.4	2.5	3.2	6.5	2.1
3.9	7.0	68.8	4.1	2.8	6.2	1.8	2.3	4.8	1.5
4.7	3.9	32.7	2.4	2.0	4.4	1.3	1.7	3.4	1.2
5.5	2.7	23.4	1.6	1.6	3.7	1.0	1.4	2.8	0.9
6.3	2.0	17.2	1.2	1.3	3.1	0.8	1.2	2.3	0.8
7.0	2.0	14.1	1.2	1.3	2.7	0.9	1.2	2.1	0.8
7.8	2.0	11.5	1.3	1.3	2.5	0.9	1.2	2.0	0.9
8.6	2.2	8.2	1.6	1.4	2.3	1.0	1.3	1.8	1.0
9.4	2.8	5.3	2.7	1.6	2.0	1.4	1.5	1.7	1.3
10.2	3.4	5.3	2.7	1.8	1.7	2.0	1.6	1.7	1.3
11.0	2.5	2.7	4.0	1.5	1.3	1.8	1.4	1.2	1.5
11.7	1.8	1.8	2.8	1.2	1.1	1.4	1.1	1.0	1.3
12.5	1.4	1.4	2.4	1.0	0.9	1.3	1.0	0.8	1.1
13.3	1.2	1.1	2.1	0.9	0.8	1.2	0.9	0.7	1.1
14.1	1.1	1.3	1.6	0.9	0.9	1.0	0.9	0.8	0.9
14.9	1.2	1.6	1.3	0.9	1.0	0.9	0.9	0.9	0.8

Decay Constants for Pn at Rice Valley

Hz	E1	a_L E2	a_T	S1	a_L S2	a_T	G1	a_L G2	a_T
1.6	31.4	31.0	44.3	7.2	3.3	11.5	5.9	2.7	9.3
2.3	19.2	∞	12.1	5.5	4.6	5.8	4.6	3.2	5.1
3.1	44.0	∞	29.6	8.6	7.3	9.0	7.0	5.5	7.5
3.9	45.8	∞	28.5	8.7	16.4	8.2	7.2	8.9	6.9
4.7	18.4	∞	16.3	5.3	3.3	6.6	4.5	2.6	5.6
5.5	6.2	5.5	9.3	2.7	1.2	5.2	2.5	1.1	4.4
6.3	5.1	4.2	8.1	2.4	1.1	4.9	2.2	0.9	4.1
7.0	4.1	3.2	6.6	2.0	0.9	4.4	1.9	0.8	3.8
7.8	3.0	2.4	4.9	1.6	0.7	3.7	1.5	0.6	3.3
8.6	2.0	1.6	3.3	1.1	0.5	2.7	1.0	0.5	2.7
9.4	1.8	1.4	3.1	1.0	0.5	2.4	0.9	0.4	2.3
10.2	1.7	1.3	3.1	1.0	0.5	2.4	0.8	0.4	2.3
11.0	1.8	1.2	3.6	1.0	0.5	2.8	0.8	0.4	2.6
11.7	2.0	1.3	4.0	1.0	0.5	3.1	0.9	0.4	2.9
12.5	2.1	1.5	3.7	1.1	0.5	3.0	0.9	0.4	2.7
13.3	2.3	1.8	3.8	1.1	0.5	3.1	1.0	0.5	2.7
14.1	2.3	2.1	3.5	1.1	0.5	2.9	1.0	0.4	2.6
14.9	2.4	1.9	4.0	1.1	0.5	3.1	0.9	0.5	2.7

Table 5.3 Pn decay constants in kilometers for each of the six models at each array site.

Decay Constants for Pn at Savahia Mountain

Hz	E1	a_L E2	a_T	S1	a_L S2	a_T	G1	a_L G2	a_T
1.6	5.4	14.7	5.7	2.1	44.4	1.6	2.0	1.9	2.1
2.3	5.0	5.1	8.5	2.0	4.6	1.8	1.9	1.5	2.3
3.1	5.5	4.8	11.0	2.1	2.0	2.4	2.0	1.4	2.6
3.9	4.5	4.8	7.4	1.8	176.9	1.5	1.8	1.3	2.1
4.7	4.1	7.4	4.9	1.7	7.5	1.3	1.6	1.2	1.7
5.5	3.1	∞	2.6	1.3	6.4	1.1	1.2	1.3	1.2
6.3	2.4	∞	2.3	1.1	4.3	0.9	1.0	2.3	0.8
7.0	1.8	∞	0.7	0.8	11.0	0.6	0.8	3.3	0.6
7.8	1.4	∞	0.8	0.7	3.8	0.5	0.6	2.2	0.5
8.6	1.3	∞	1.1	0.6	5.4	0.4	0.5	1.6	0.4
9.4	1.2	∞	1.0	0.5	53.7	0.4	0.4	2.4	0.4
10.2	1.0	∞	0.9	0.4	2.7	0.3	0.4	1.4	0.3
11.0	0.9	∞	0.8	0.4	4.5	0.3	0.3	1.1	0.3
11.7	0.9	14.9	0.8	0.4	7.8	0.3	0.3	1.2	0.3
12.5	1.0	3.2	0.9	0.4	2.1	0.3	0.3	1.0	0.3
13.3	1.0	1.9	1.1	0.4	18.3	0.3	0.3	0.7	0.3
14.1	1.21	1.7	1.6	0.42	1.8	0.3	0.4	0.6	0.3
14.9	1.1	1.9	1.4	0.4	2.4	0.3	0.3	0.6	0.3

Table 5.3 continued

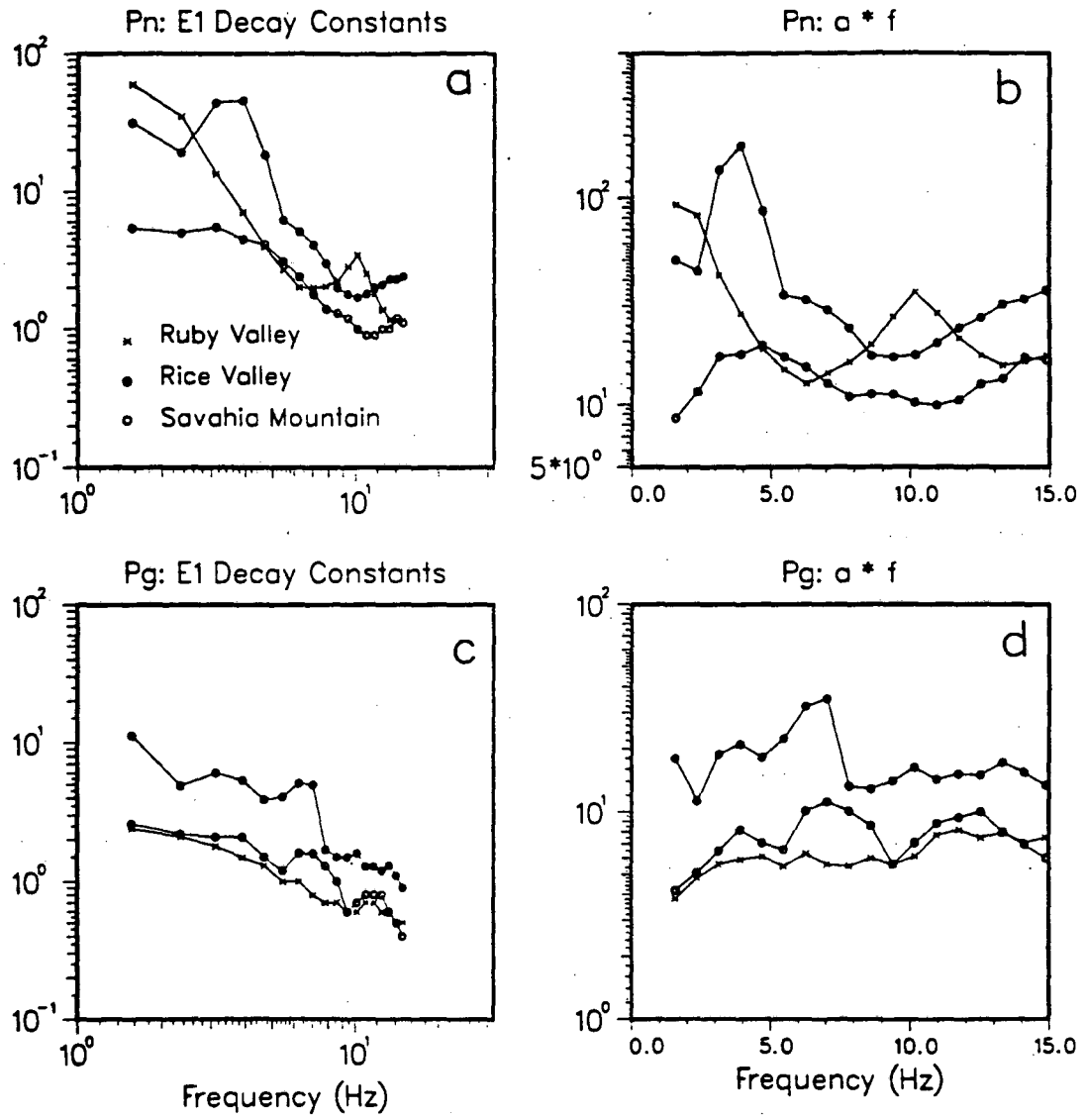

FIG. 5.11 (a) Isotropic exponential decay constants for Pn at each array site. See also Table 5.3. (b) Product of the 1-D exponential decay constants and frequency. A constant value of a*f over frequency would indicate that the decay constant is a linear function of wavelength. (c) and (d) Same as (a) and (b) but for Pg.

Exponential 2-D Decay Constant Ratios

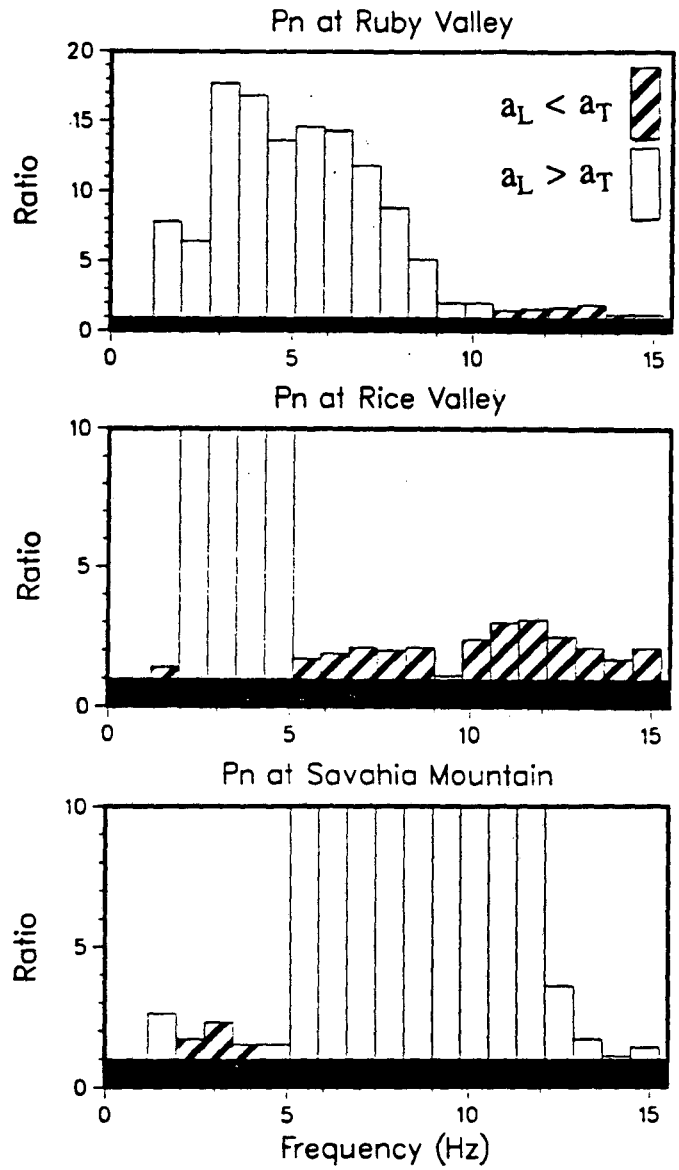

FIG. 5.12 Two-dimensional exponential decay constant ratios for Pn at each array site. The cross-hatched bars represent values of a_T/a_L and the blank bars values of a_L/a_T. Except for the 11.7 Hz value at Savahia, ratios for Rice Valley and Savahia that reach a value of 10 actually extend to infinity and are insignificant (see text).

F Statistics for Pg at Ruby Valley

Hz	E1	E2	S1	S2	G1	G2
1.6	1.1	*	1.2	1.1	1.4	1.3
2.3	1.1	*	1.3	1.2	1.5	1.3
3.1	1.2	*	1.4	1.3	1.7	1.5
3.9	1.2	*	1.4	1.3	1.7	1.5
4.7	1.2	*	1.5	1.3	1.9	1.6
5.5	1.2	*	1.4	1.3	1.9	1.6
6.3	1.3	*	1.7	1.5	2.2	1.9
7.0	1.1	*	1.4	1.4	1.9	1.9
7.8	1.1	*	1.3	1.3	1.8	1.8
8.6	*	*	1.1	1.2	1.5	1.5
9.4	*	*	1.1	1.2	1.5	1.5
10.2	*	*	1.2	1.2	1.6	1.6
11.0	*	*	1.2	1.2	1.5	1.5
11.7	*	*	1.2	1.2	1.5	1.5
12.5	*	*	1.2	1.2	1.5	1.5
13.3	*	*	1.2	1.3	1.6	1.6
14.1	*	*	1.2	1.3	1.6	1.5
14.9	*	*	1.2	1.3	1.5	1.5

F Statistics for Pg at Rice Valley

Hz	E1	E2	S1	S2	G1	G2
1.6	3.3	5.6	*	*	1.1	1.1
2.3	1.6	1.7	*	*	1.1	1.1
3.1	*	1.3	*	*	1.3	1.3
3.9	1.2	1.5	1.1	*	1.3	1.1
4.7	1.5	2.1	1.2	*	1.4	*
5.5	1.4	1.4	1.3	*	1.6	1.1
6.3	1.3	1.1	1.7	*	2.5	1.2
7.0	*	*	1.5	1.6	2.0	1.9
7.8	*	*	1.2	1.2	1.6	1.5
8.6	*	*	1.3	1.4	1.5	1.5
9.4	*	*	1.3	1.4	1.6	1.6
10.2	1.1	*	1.7	1.5	2.1	1.9
11.0	1.1	*	1.6	1.5	1.9	1.9
11.7	1.1	*	1.5	1.6	1.7	1.8
12.5	1.1	*	1.5	1.6	1.8	1.9
13.3	1.2	*	1.7	1.6	2.0	2.0
14.1	1.1	*	1.5	1.5	1.8	1.8
14.9	1.2	*	1.5	1.5	1.7	1.7

F Statistics for Pg at Savahia Mountain

Hz	E1	E2	S1	S2	G1	G2
1.6	1.2	*	2.3	2.1	2.4	2.2
2.3	1.1	*	2.4	2.2	2.6	2.3
3.1	1.1	*	2.5	2.3	2.8	2.6
3.9	1.1	*	2.0	1.9	2.6	2.2
4.7	1.1	*	1.8	1.6	2.0	1.9
5.5	*	*	1.7	1.7	2.0	1.9
6.3	*	*	1.7	1.7	2.1	2.0
7.0	*	*	1.7	1.7	2.0	2.0
7.8	*	*	1.7	1.7	2.1	1.9
8.6	*	*	1.7	1.6	1.8	1.8
9.4	*	*	1.7	1.6	1.8	1.8
10.2	*	*	1.4	1.4	1.5	1.5
11.0	*	*	1.3	1.2	1.3	1.3
11.7	*	*	1.1	1.1	1.2	1.2
12.5	*	*	1.1	1.1	1.2	1.2
13.3	*	*	1.1	1.1	1.2	1.2
14.1	*	*	1.1	1.1	1.2	1.2
14.9	*	*	1.1	1.1	1.2	1.2

Table 5.4 Same as Table 5.2 but for Pg.

Standard Deviations of Best Fitting Models

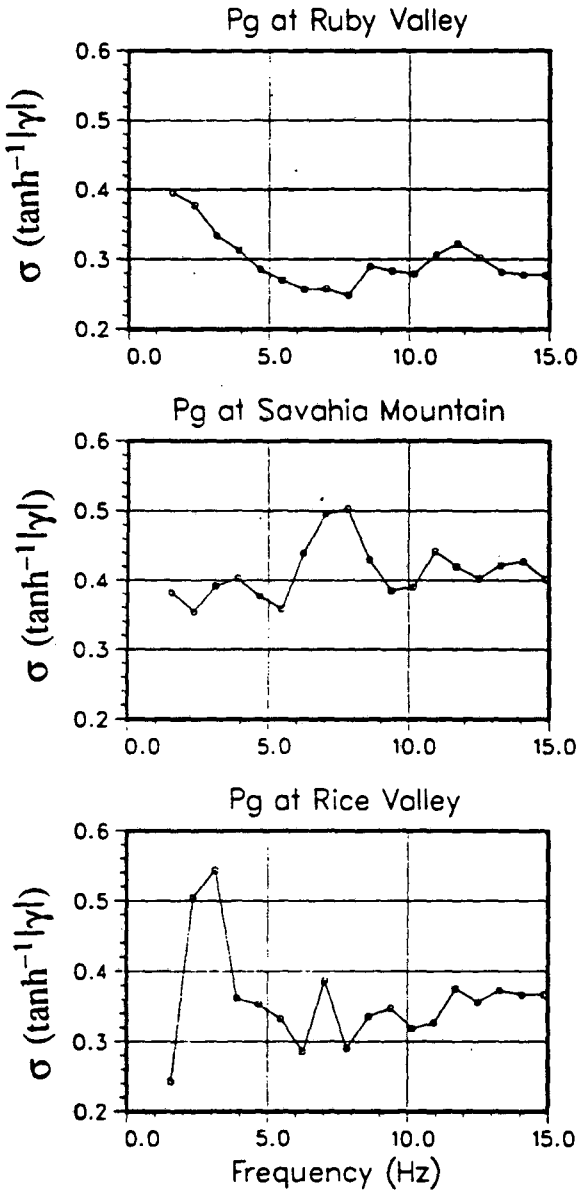

FIG 5.13 Same as Figure 5.10 but for Pg.

Decay Constants for Pg at Ruby Valley

Hz	E1	a_L	E2	a_T	S1	a_L	S2	a_T	G1	a_L	G2	a_T
1.6	2.4	5.3		2.0	1.4	1.9		1.2	1.3	1.6		1.1
2.3	2.1	5.2		1.7	1.3	1.9		1.1	1.2	1.6		1.0
3.1	1.8	4.6		1.4	1.2	1.7		1.0	1.1	1.5		0.9
3.9	1.5	3.7		1.2	1.1	1.5		0.9	1.0	1.3		0.8
4.7	1.3	3.3		1.0	1.0	1.4		0.8	0.9	1.2		0.7
5.5	1.0	2.6		0.8	0.8	1.2		0.7	0.8	1.1		0.6
6.3	1.0	2.6		0.8	0.8	1.2		0.6	0.8	1.1		0.6
7.0	0.8	1.7		0.7	0.6	0.9		0.5	0.7	0.8		0.5
7.8	0.7	1.2		0.7	0.6	0.7		0.5	0.6	0.7		0.5
8.6	0.7	1.1		0.7	0.5	0.7		0.5	0.5	0.6		0.5
9.4	0.6	0.9		0.8	0.5	0.6		0.6	0.5	0.5		0.5
10.2	0.6	0.8		0.8	0.5	0.6		0.6	0.5	0.5		0.6
11.0	0.7	0.9		0.8	0.5	0.6		0.6	0.6	0.5		0.6
11.7	0.7	1.0		0.7	0.6	0.6		0.6	0.6	0.6		0.5
12.5	0.6	0.8		0.7	0.5	0.5		0.5	0.5	0.5		0.5
13.3	0.6	0.8		0.7	0.5	0.5		0.5	0.5	0.5		0.5
14.1	0.5	0.8		0.6	0.5	0.5		0.5	0.5	0.5		0.4
14.9	0.5	0.8		0.6	0.5	0.5		0.5	0.5	0.5		0.4

Decay Constants for Pg at Rice Valley

Hz	E1	a_L	E2	a_T	S1	a_L	S2	a_T	G1	a_L	G2	a_T
1.6	11.3	∞		4.7	4.1	9.6		3.8	3.5	3.4		3.5
2.3	4.9	5.1		6.0	2.5	3.4		2.4	2.2	2.2		2.2
3.1	6.1	1.6		20.9	2.7	8.9		2.3	2.4	1.3		3.4
3.9	5.4	3.5		6.0	2.6	1.6		3.3	2.3	1.4		3.2
4.7	3.9	1.9		3.5	2.1	1.2		3.1	1.9	1.0		2.9
5.5	4.1	5.0		5.3	2.1	1.1		3.5	2.0	0.9		3.3
6.3	5.1	3.6		9.1	2.4	1.1		4.9	2.2	0.9		4.4
7.0	5.0	7.8		6.2	2.3	1.4		3.1	2.1	1.1		3.3
7.8	1.7	1.7		2.5	1.0	0.6		1.7	0.9	0.5		1.4
8.6	1.5	3.0		1.7	0.8	0.6		0.7	0.7	0.6		0.7
9.4	1.5	2.0		1.8	0.8	0.6		0.9	0.7	0.4		0.9
10.2	1.6	1.1		3.2	0.8	0.4		2.3	0.7	0.3		2.1
11.0	1.3	0.8		3.2	0.7	0.3		2.1	0.6	0.3		2.0
11.7	1.3	0.8		2.9	0.6	0.3		1.4	0.5	0.3		1.2
12.5	1.2	0.8		2.7	0.6	0.3		1.7	0.5	0.2		1.3
13.3	1.3	0.7		4.2	0.6	0.3		3.0	0.5	0.2		2.7
14.1	1.1	0.7		2.7	0.5	0.2		2.2	0.4	0.2		2.0
14.9	0.9	0.5		3.7	0.4	0.2		2.7	0.3	0.2		2.5
10.0	10.0	10.0		10.0	10.0	10.0		10.0	10.0	10.0		10.0

Table 5.5 Same as Table 5.3 but for Pg.

Decay Constants for Pg at Savahia Mountain									
Hz	E1	a_L E2	a_T	S1	a_L S2	a_T	G1	a_L G2	a_T
1.6	2.6	∞	2.5	1.4	8.1	1.1	1.3	2.1	1.1
2.3	2.2	∞	2.0	1.1	1.3	1.0	1.1	1.3	1.0
3.1	2.1	5.5	2.2	1.0	6.5	0.7	0.9	0.9	0.9
3.9	2.1	6.2	2.2	0.9	4.5	0.7	0.8	0.9	0.8
4.7	1.5	8.1	1.5	0.7	5.8	0.5	0.6	0.8	0.5
5.5	1.2	∞	1.0	0.5	2.7	0.4	0.5	1.3	0.4
6.3	1.6	∞	1.4	0.6	3.3	0.5	0.6	2.0	0.5
7.0	1.6	∞	1.3	0.6	3.4	0.4	0.5	1.8	0.4
7.8	1.3	∞	1.2	0.4	6.6	0.3	0.3	3.8	0.3
8.6	1.0	4.5	1.0	0.3	3.8	0.2	0.3	0.5	0.2
9.4	0.6	0.5	1.3	0.2	0.1	5.7	0.2	0.1	0.3
10.2	0.7	0.7	1.1	0.2	0.1	1.0	0.2	0.1	0.3
11.0	0.8	1.5	1.0	0.2	1.2	0.2	0.2	0.2	0.2
11.7	0.8	1.7	0.9	0.2	0.3	0.2	0.2	0.3	0.2
12.5	0.8	∞	0.6	0.2	2.3	0.2	0.2	0.4	0.2
13.3	0.6	1.3	0.7	0.2	0.2	0.1	0.2	0.2	0.1
14.1	0.5	0.7	0.7	0.1	1.3	0.1	0.1	0.1	0.1
14.9	0.4	0.4	0.5	0.1	0.3	0.1	0.1	0.1	0.1

Table 5.5 continued

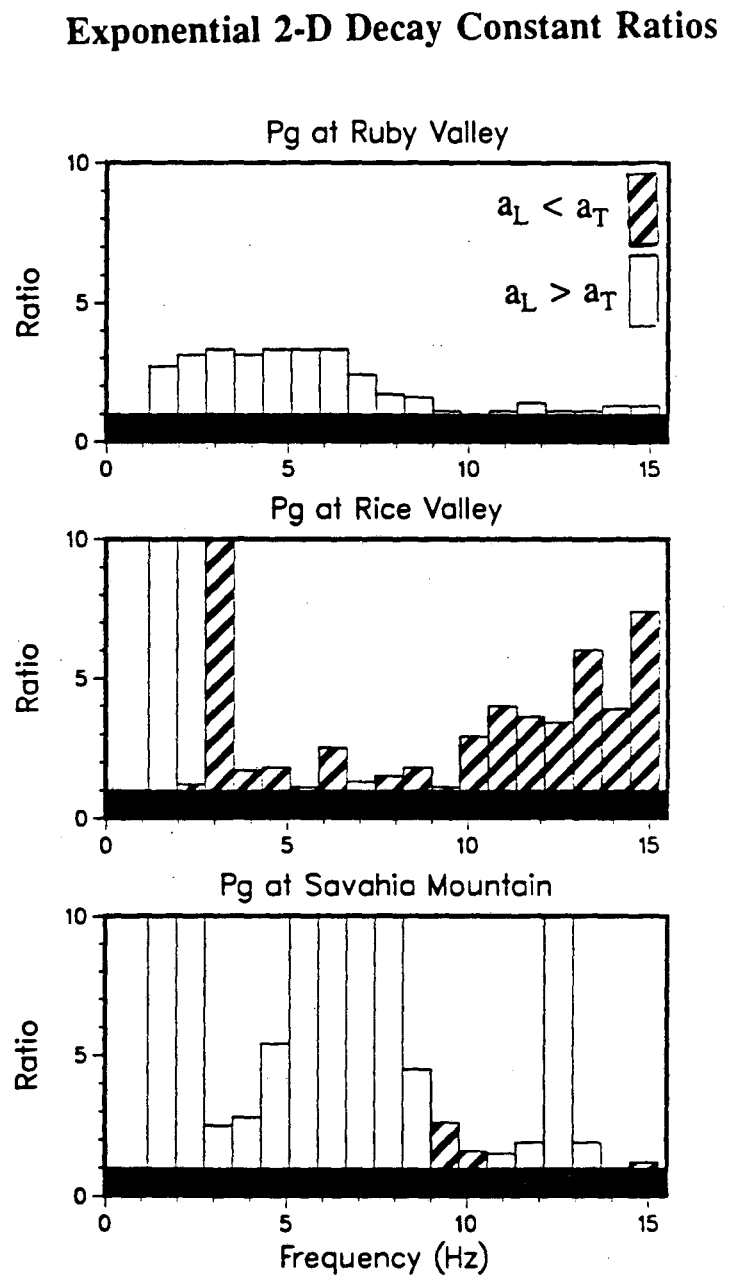

FIG. 5.14 Two-dimensional exponential decay constant ratios for Pg at each array site. Except for the 1.6 Hz value at Rice valley, ratios for Rice Valley and Savahia that reach a value of 10 actually extend to infinity and are insignificant (see text).

Pn: Ruby Valley

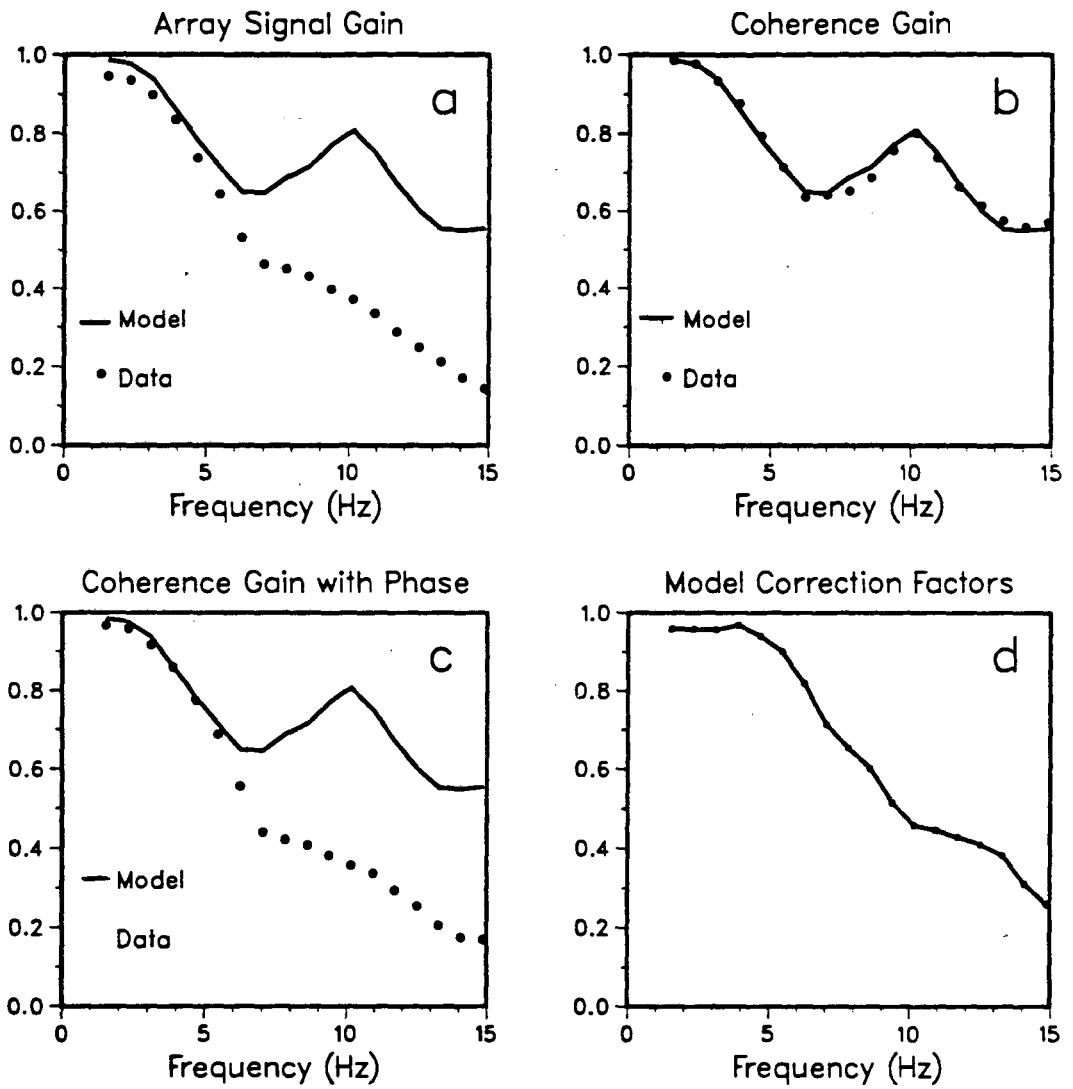

FIG. 5.15 (a) Pn model array gain at Ruby Valley (solid line) and Pn array gain (solid dots) obtained from the cross-spectra of the data $S_{ij}(f)$. (b) Model array gain in (a) and the observed magnitude coherence gain obtained by setting the cross-spectra equal to the observed magnitude coherence, $S_{ij}(f) = |\gamma_{ij}(f)|$. (c) Model array gain in (a) and the observed complex coherence gain obtained by setting the cross-spectra equal to the complex coherence, $S_{ij}(f) = \gamma_{ij}(f)$. (d) Correction factors which when multiplied by the model gain produce the observed array gain in (a).

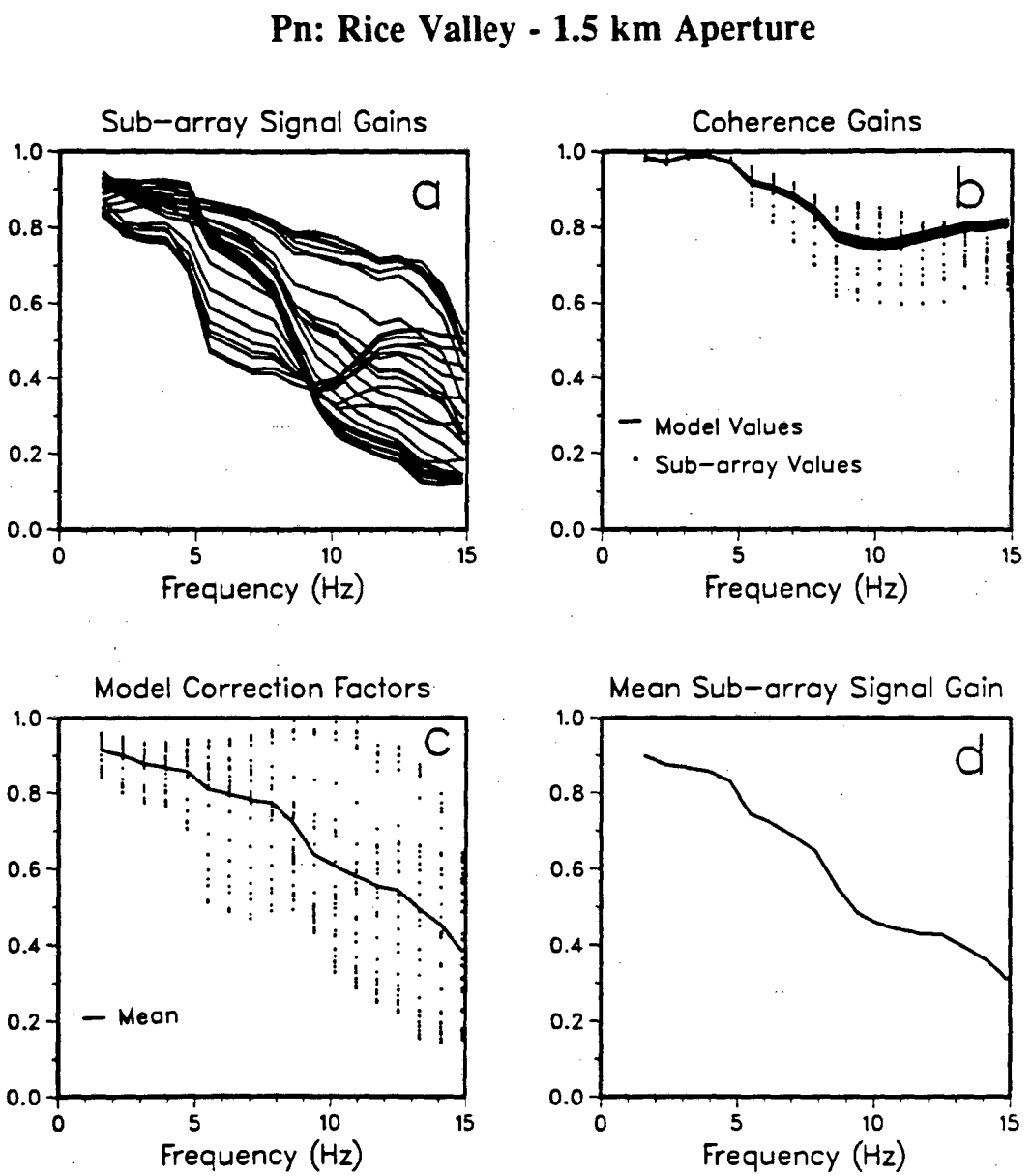

FIG. 5.16 (a) Observed Pn array signal gain from the 32 1.5 km aperture sub-arrays at Rice Valley. (b) Model array gains for each sub-array configuration. Also shown are the observed sub-array magnitude coherence gain values obtained by setting $S_{ij}(f) = |\gamma_{ij}(f)|$. (c) Model correction factors for each sub-array which produce the observed gains in (a). The mean correction factors fall along the solid line. (d) Mean of the sub-array signal gains in (a). This is equivalent to the mean of the model gains in (b) scaled by the mean correction factors in (c).

Pn: Savahia Mountain - 1.5 km Aperture

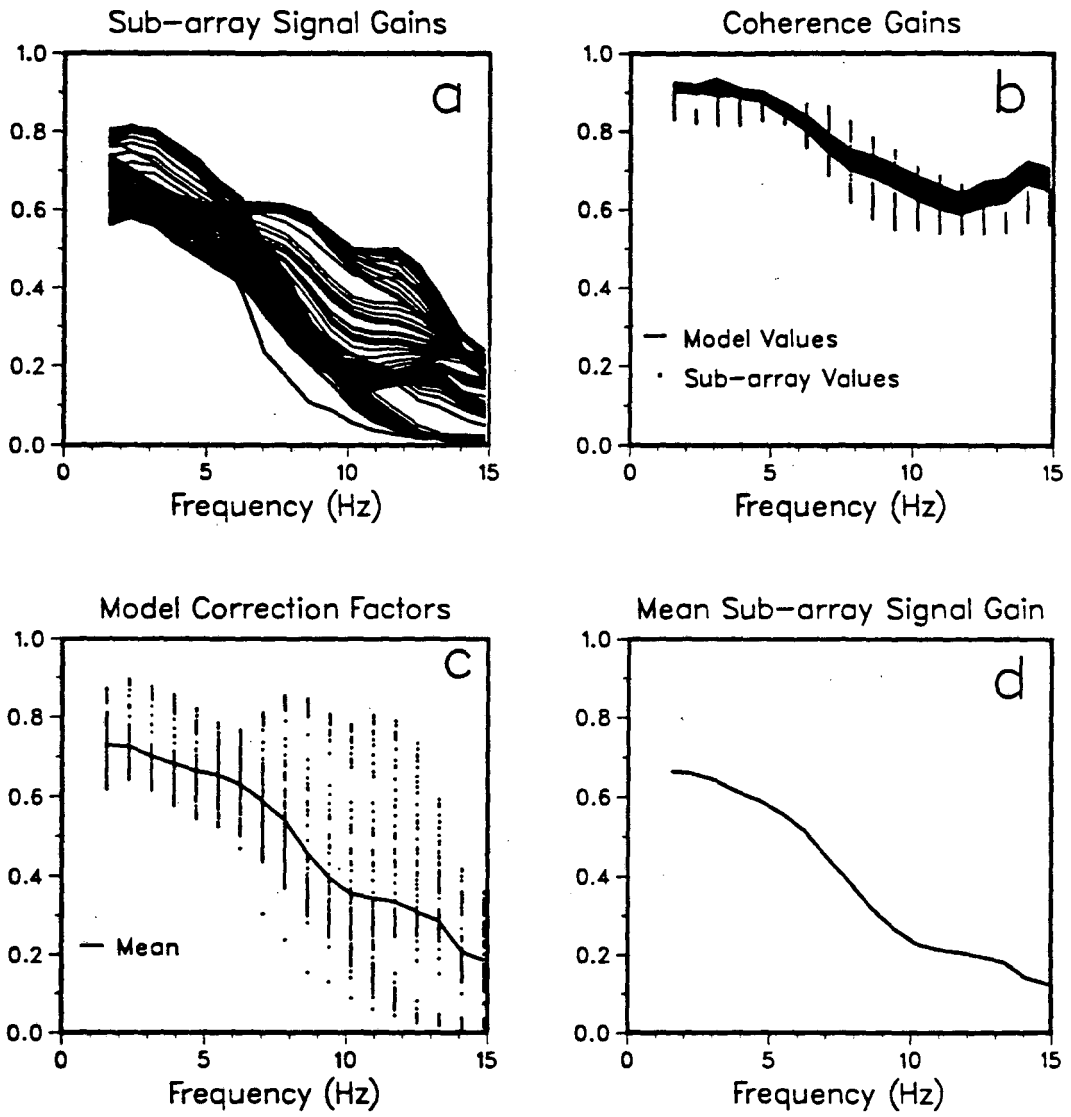

FIG. 5.17 Same as Figure 5.16 but for the 97 1.5 km aperture sub-arrays at Savahia Mountain.

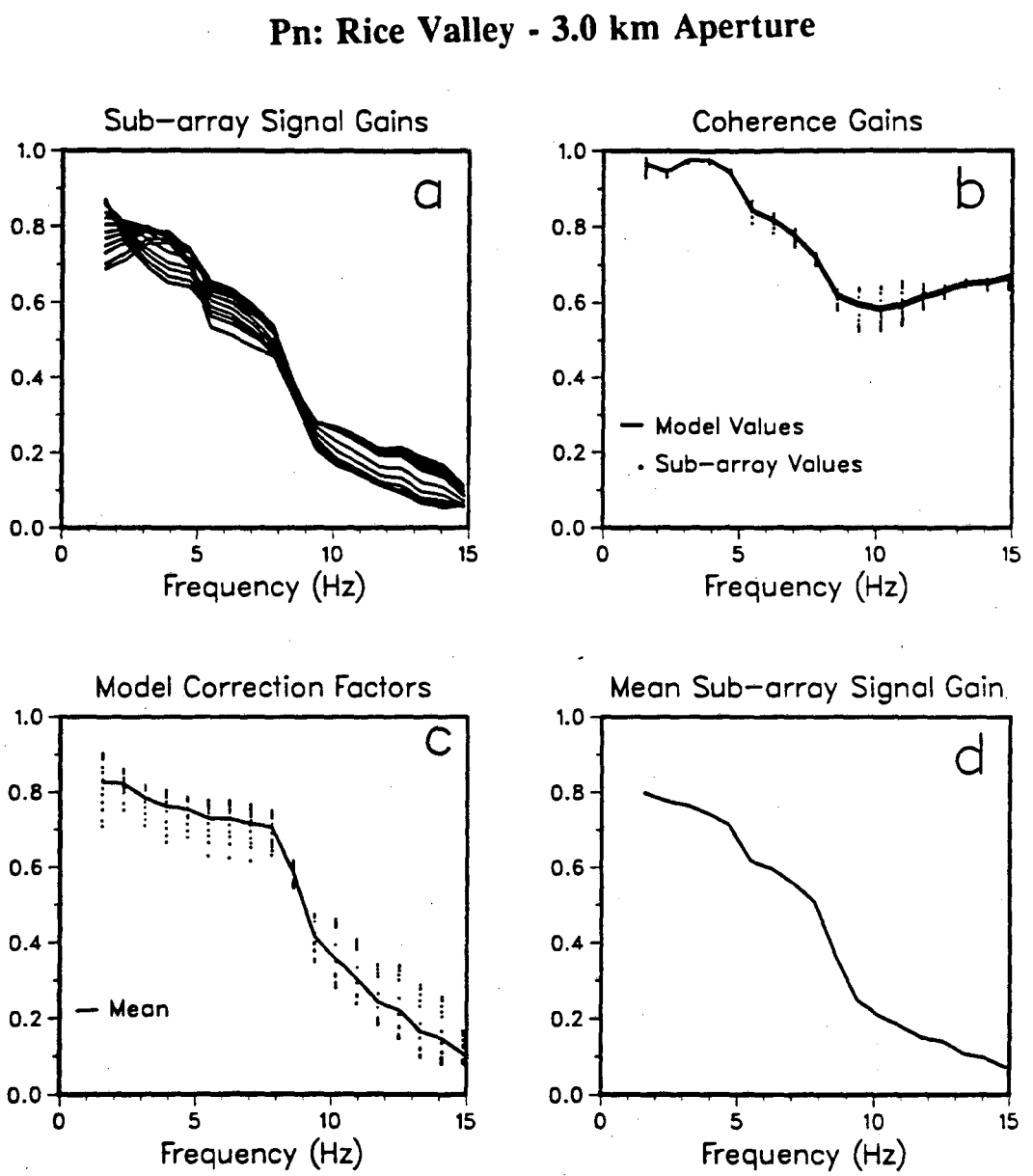

FIG. 5.18 Same as Figure 5.16 but for the 15 3.0 km aperture sub-arrays at Rice Valley.

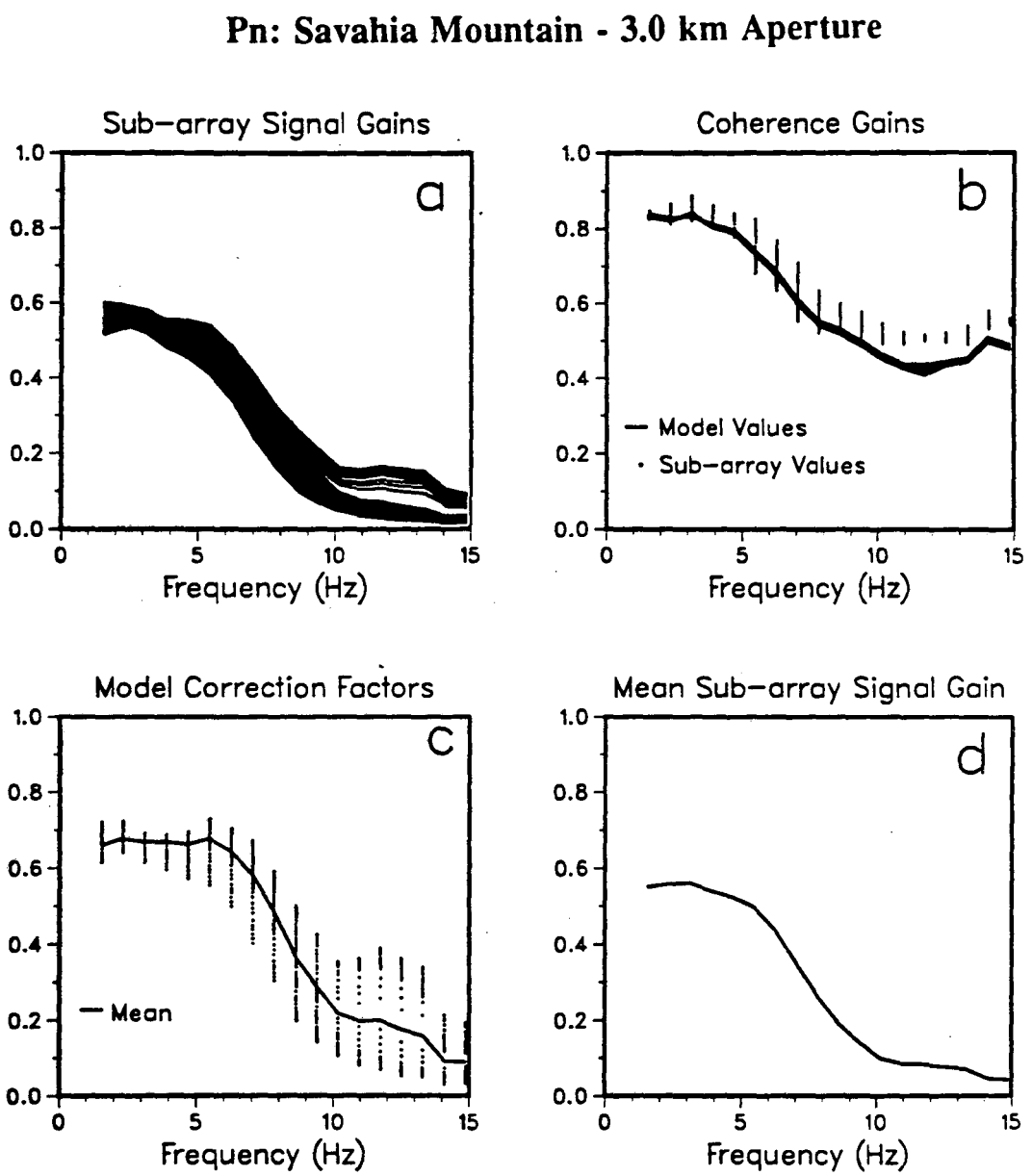

FIG. 5.19 Same as Figure 5.16 but for the 45 3.0 km aperture sub-arrays at Savahia Mountain.

Pg: Ruby Valley

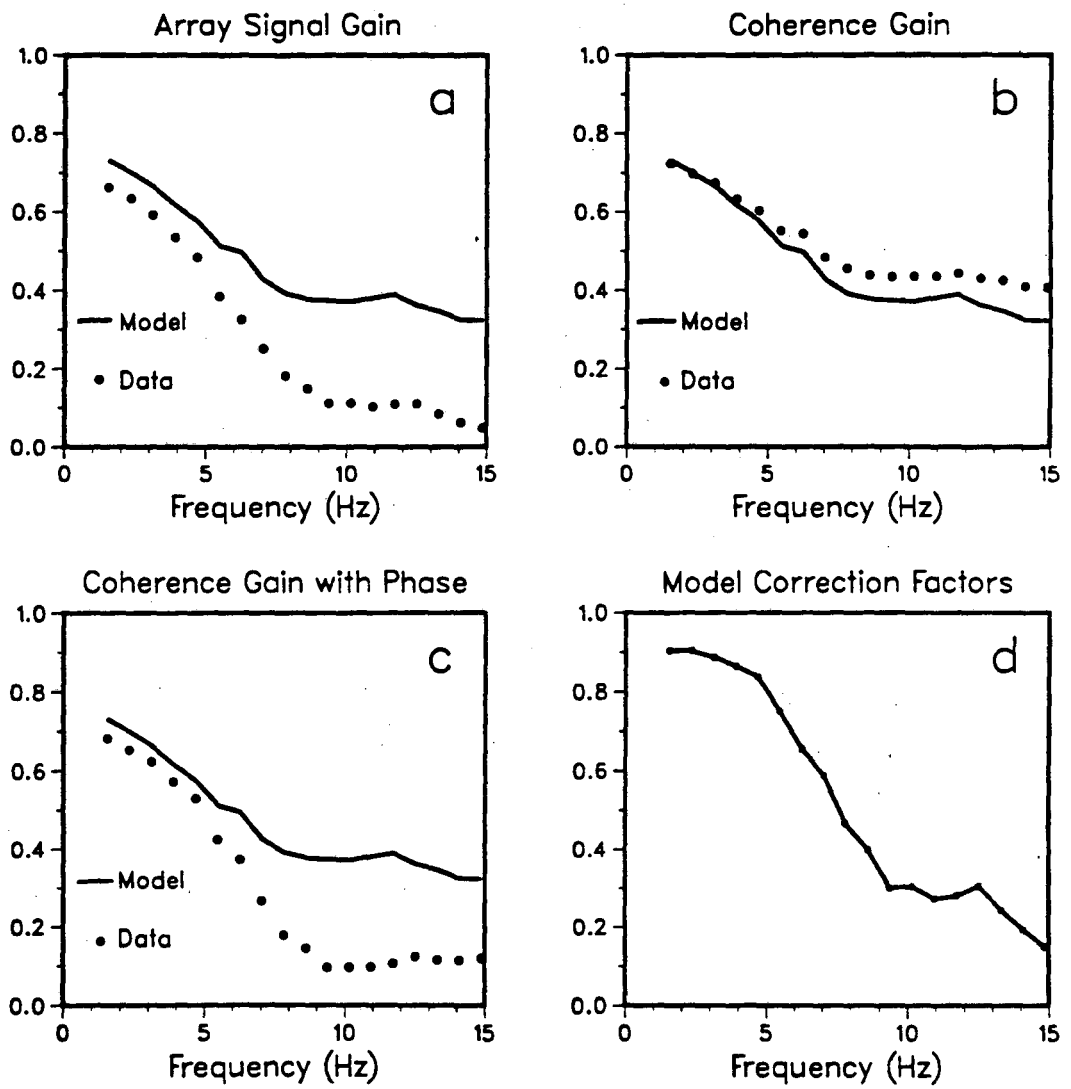

FIG. 5.20 Same as for Figure 5.15 but for Pg.

Pg: Rice Valley - 1.5 km Aperture

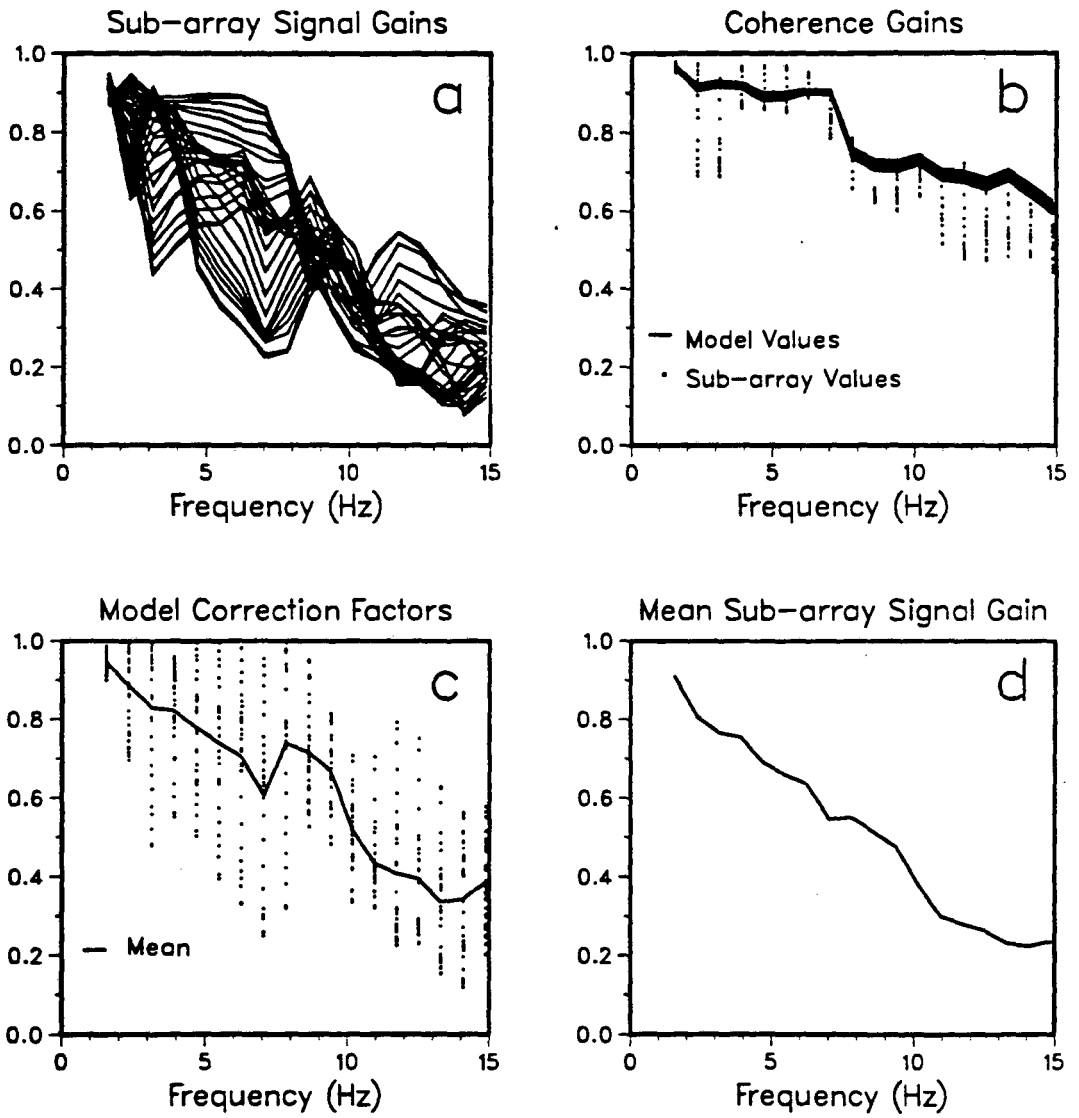

FIG. 5.21 Same as Figure 5.16 but for Pg.

Pg: Savahia Mountain - 1.5 km Aperture

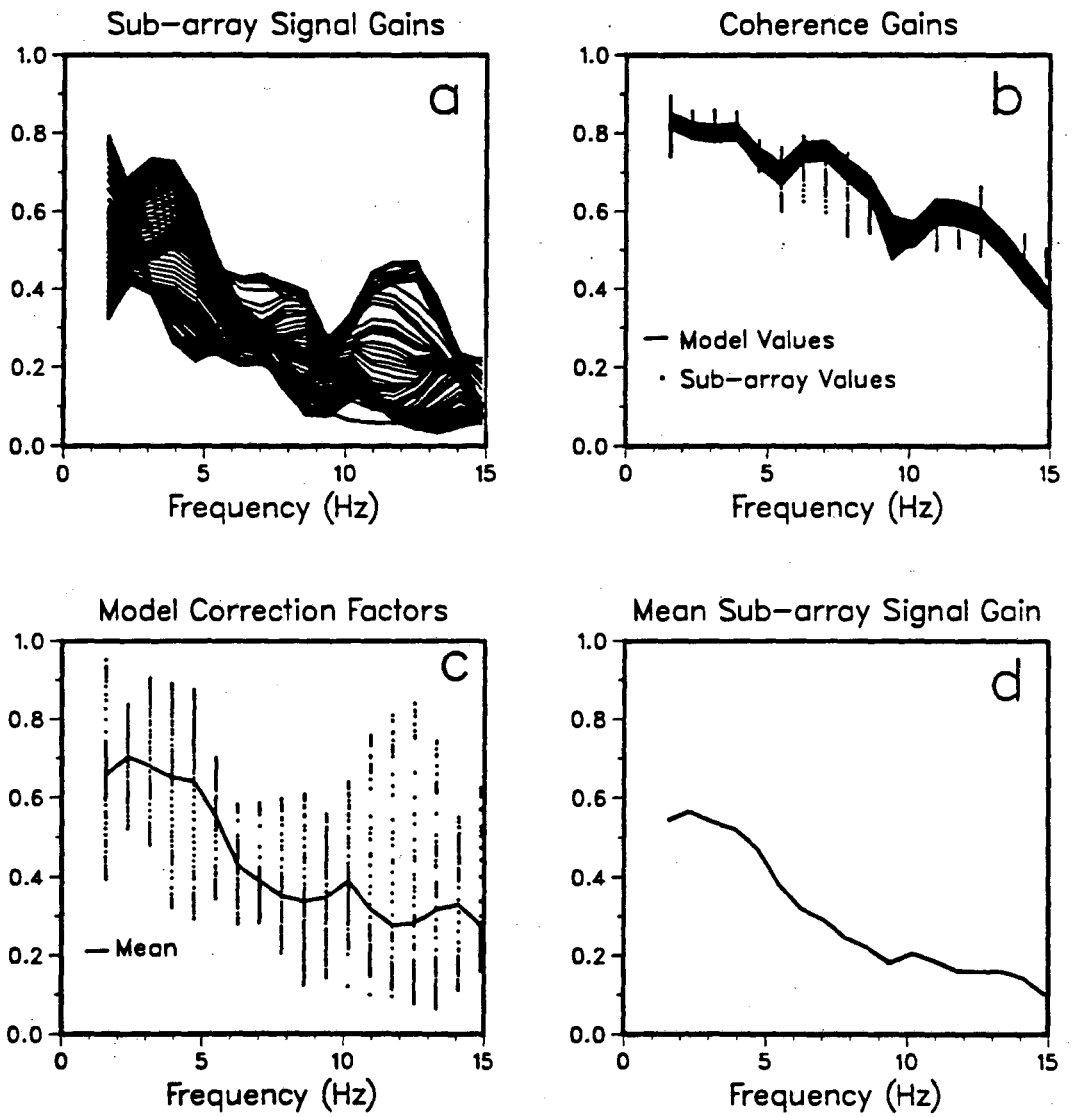

FIG. 5.22 Same as Figure 5.17 but for Pg.

Pg: Rice Valley - 3.0 km Aperture

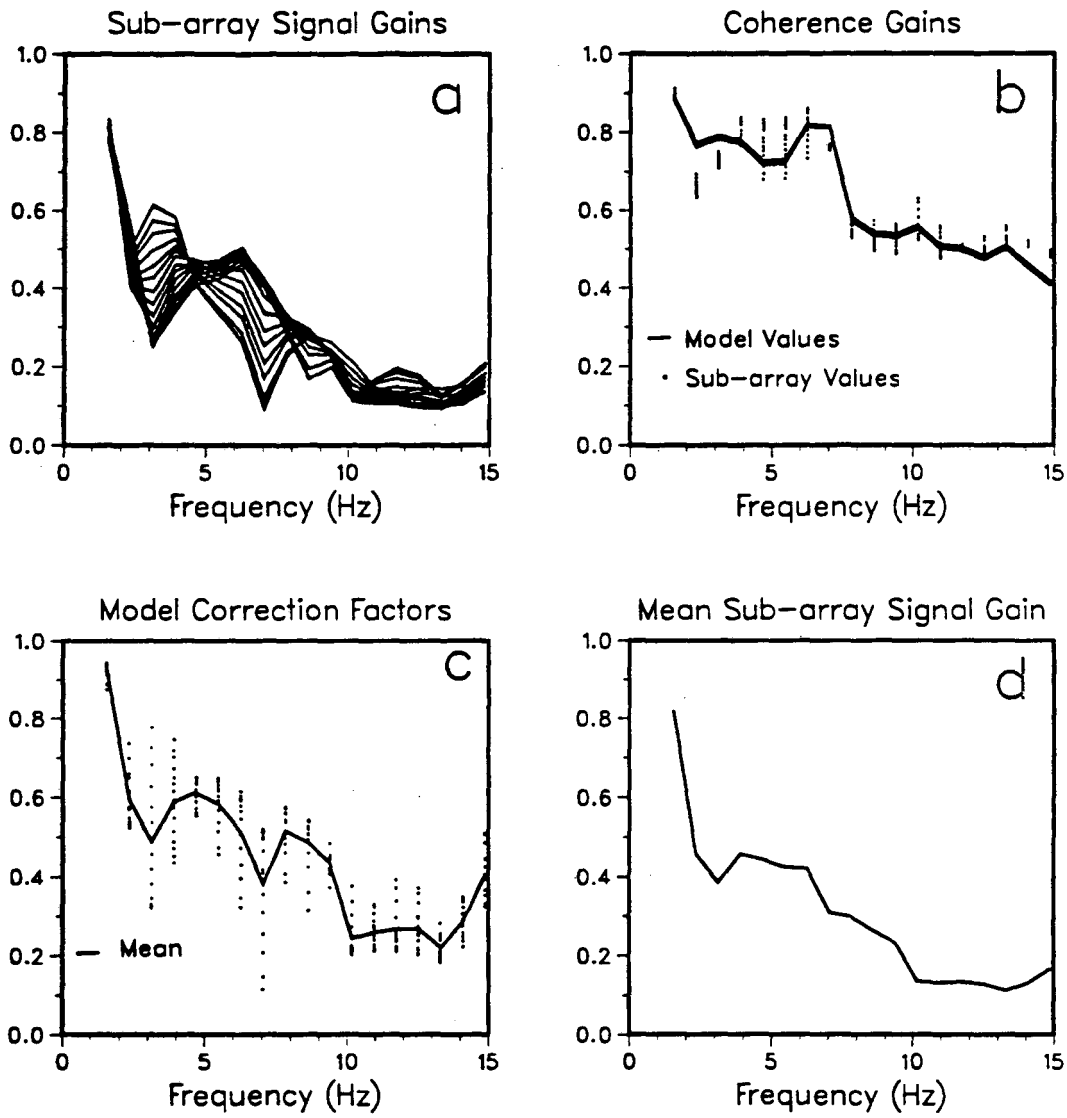

FIG. 5.23 Same as Figure 5.18 but for Pg.

Pg: Savahia Mountain - 3.0 km Aperture

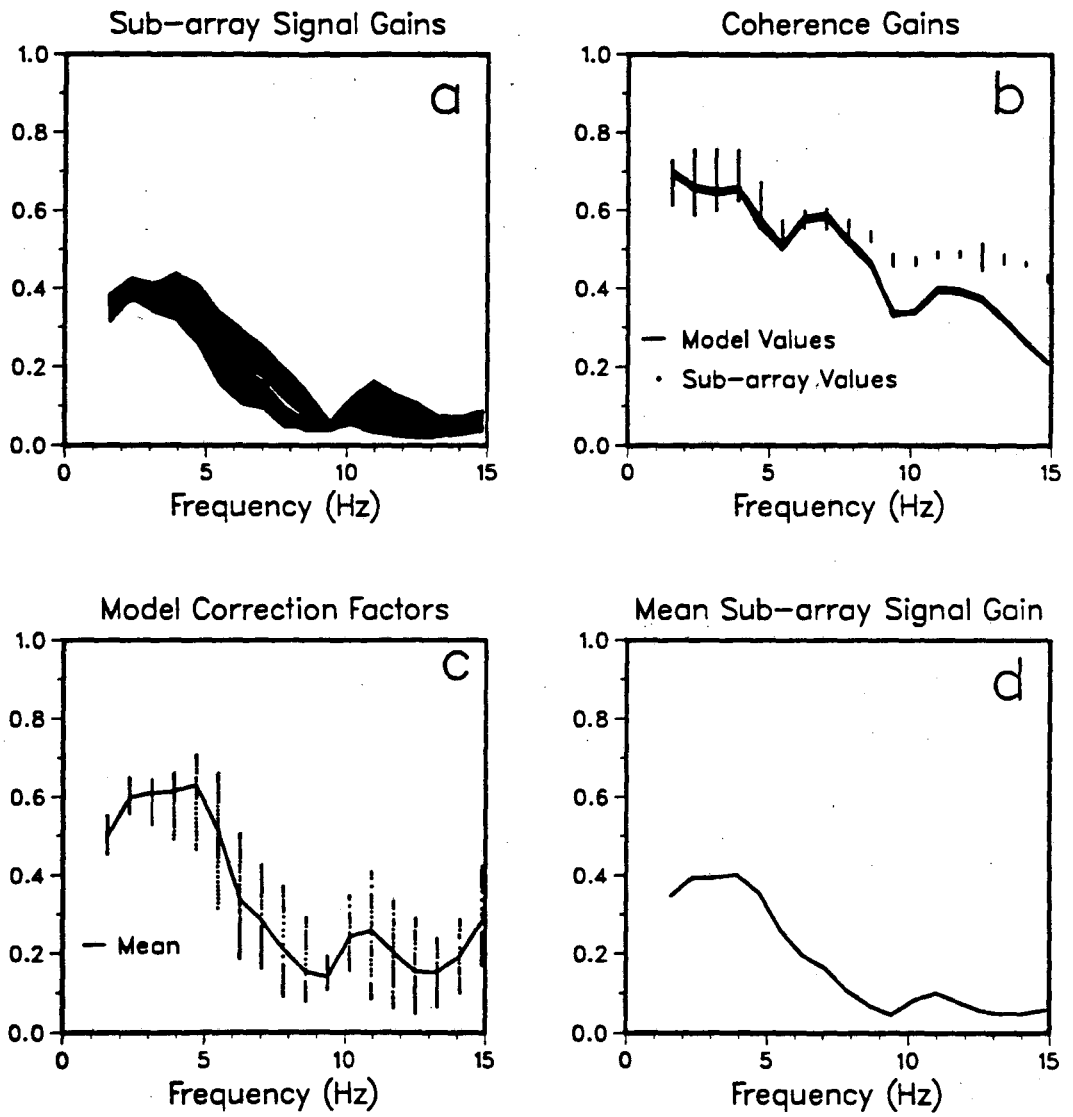

FIG. 5.24 Same as Figure 5.19 but for Pg.

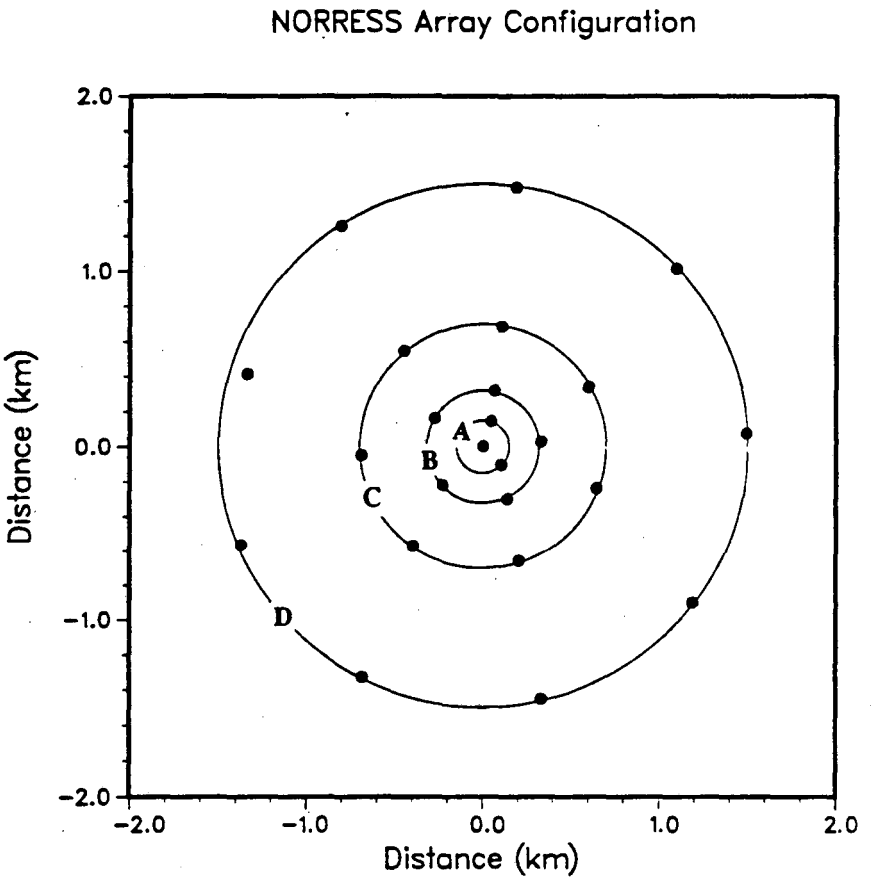

FIG. 5.25 24-element configuration of the NORESS array used in the array gain simulations. The A, B, C, and D rings are indicated.

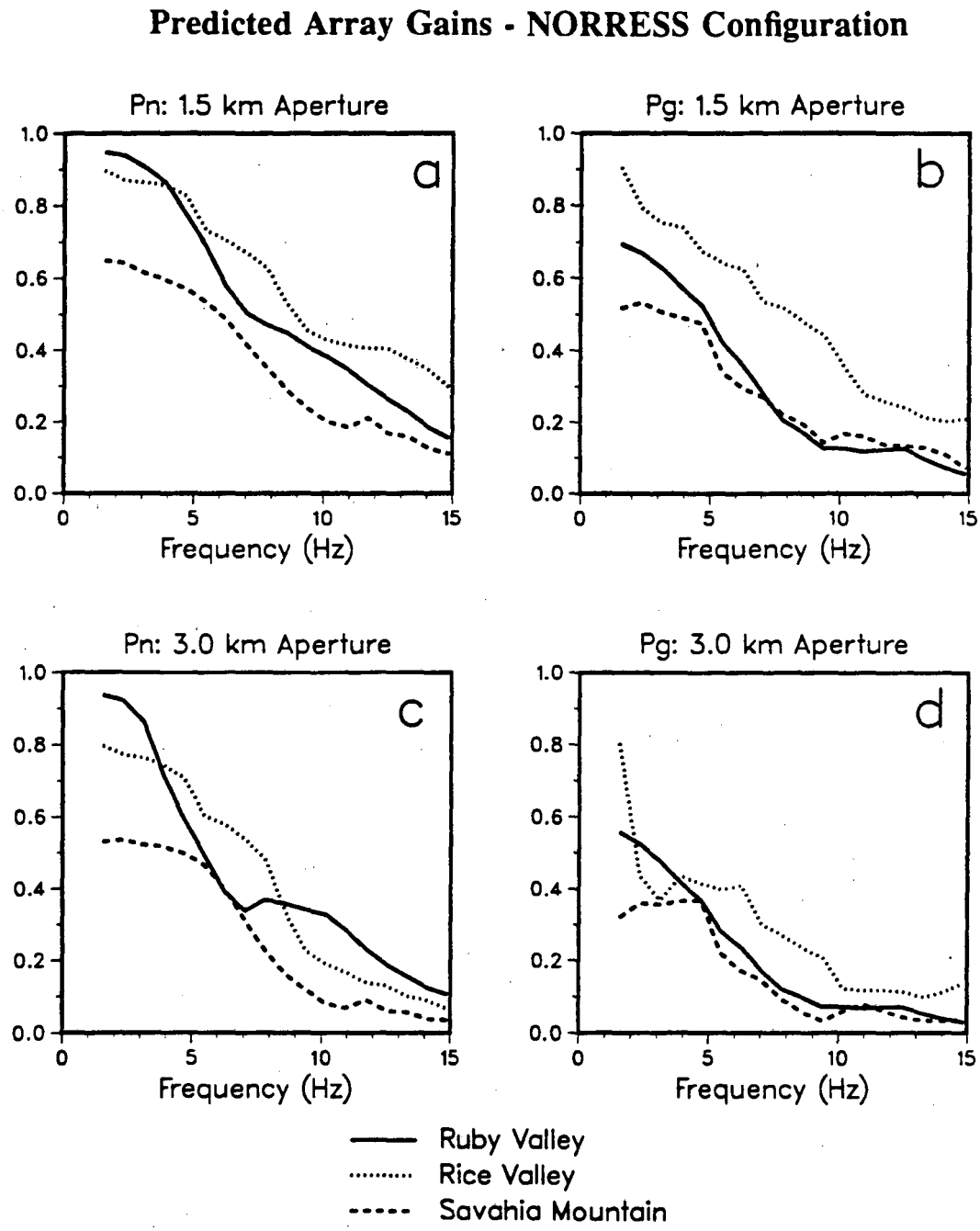

FIG. 5.26 Predicted Pn and Pg array gains based on the NORESS configuration and the coherence models used in the proceeding figures of array gain. The mean model correction factors derived earlier have been applied to obtain the Rice Valley and Savahia Mountain results. The 3.0 km aperture gains for Ruby Valley are derived from the 1.5 km aperture correction factors. The propagation direction is due north in all cases.

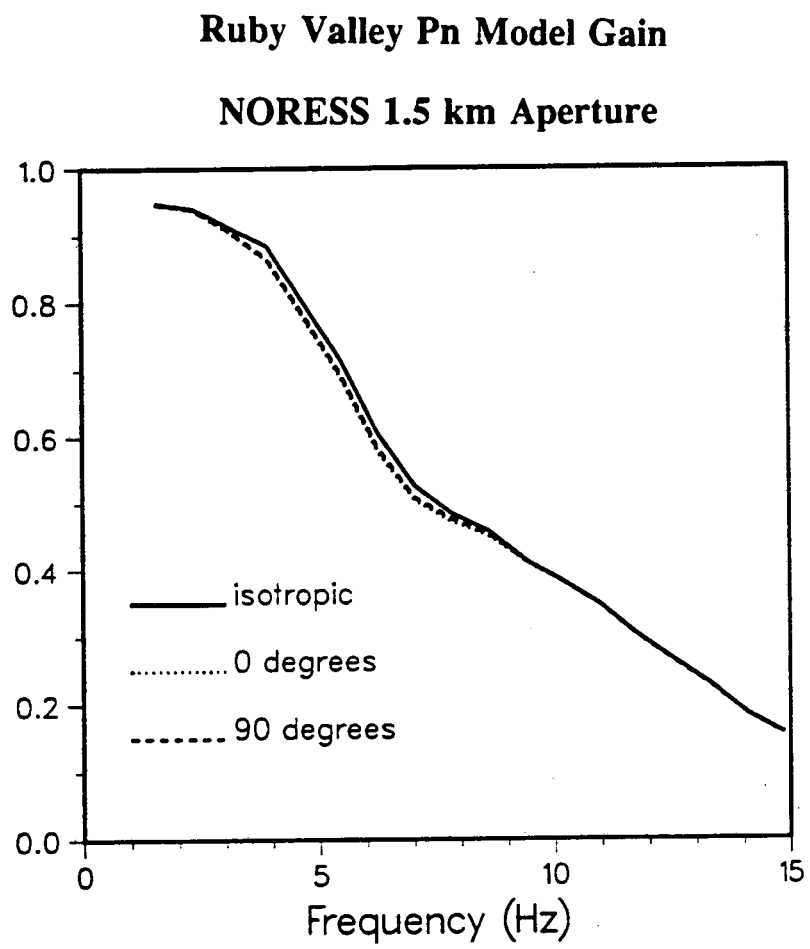

FIG. 5.27 Predicted Pn array gain based on the NORESS 1.5 km configuration and the Ruby Valley exponential models. Plotted is the gain for the isotropic model and gains for the directional model using orthogonal directions of wavefront propagation. The directional model extends only to 9 Hz. The directional gains essentially overlap and are only slightly lower than the isotropic gain.

Chapter 6

Recommendations

Regional seismic arrays in Scandanavia have proven valuable for monitoring small-magnitude events of the kind that would be of concern under the restrictions of a low-yield Threshold Test Ban Treaty. However, their utility in a place like the tectonically active western United States has been less well established. This study was undertaken to begin to assess the regional array monitoring characteristics and potential of high-frequency Pn and Pg wavefields from the Nevada Test Site. The conclusions of the work have been described fully at the end of the preceding chapters. This final chapter offers a number of recommendations on the deployment and processing of regional arrays.

(1) Amplitude Spectra

The advantages of usings arrays over single-station recordings sites was described at length in Chapter 1, however it is worth reiterating the point made regarding the statistical improvement of spectral amplitude estimates. In Chapter 2 we saw very significant variation in spectral amplitude over fairly short distances. A factor of 10 variation at a given frequency over the 4 km aperture arrays at Rice Valley and Savahia Mountain was typical. At the same time we observed very similar mean spectra at high frequencies over the much larger distances separating the array sites themselves. These observations underscore the need for statistical averaging of spectral estimates to improve the reliability of spectral-based discrimination techniques. The recommendation here is that (a) permanent arrays be used to achieve this, and (b) if a single-station monitoring site is used instead that a temporary array be installed around it to estimate the statististical properties of the site.

(2) Array Design

An effective array design is critically dependent on the signal and noise correlation characteristics of the site. These characteristics must be determined before a permanent array is installed. In particular, given the wide variability of signal correlation that we observed in Chapter 5, this should be carried out with a high density of temporary sensors so as to obtain statistically meaningful results. In geologic regions similar to those upon which the arrays of this study were located, it's unlikely that significant advantage can be gained by installing permanent arrays having apertures much beyond 1.5 km. Exceeding this aperture at even the NORESS array, where signal correlation is greater, results in degraded estimates of source azimuth (Bame *et al.*, 1990). The gain simulations in Chapter 5 showed that while a 1.5 km aperture may be appropriate for Pn and Pg at the Rice Valley array and Pn at the Ruby Valley array, it is too large for Pg at Ruby Valley and, even more so, for both Pn and Pg at Savahia Mountain. Decreasing the aperture can of course increase array gain, but then one needs to be concerned about increased noise correlation and degraded resolving power of the array. In these cases it may be better to go in search of more suitable locations. Of the three sites examined in this study, Rice Valley, because of its overall greater Pn and Pg signal correlation shows the most promise as a potential monitoring site. An additional consideration are the array characteristics of Lg, which have not been examined here. Because of the importance of this phase in discrimination and yield estimation, reconaissance siting of regional arrays must also take its properties into account.

(3) Using Noise

Other than compute spectral amplitude levels in Chapter 3, we have done little analysis of noise wavefields. With very small magnitude events, however, the noise field becomes very important and, if possible, knowledge of its correlation structure should be taken advantage of. Der *et al.* (1988), for example, present a general method for using parameterized models of signal and noise cross-spectra to obtain stations weights which optimize signal to noise ratios.

For later arriving phases like Pg and Lg one can model the noise from the coda of the previous arrival.

(4) Identification of Coherent Scattering Sources

An obvious hindrance to processing regional data is its complexity due to scattering. However, in some cases the scattering is coherent and its source may be understood. For example, careful examination of the SALUT wavefields recorded at the Savahia Mountain array site reveals coherent low-velocity wavefronts propagating across the array (see Figures 2.6 and 2.11). The direction and low velocity suggests that these are scattered surface waves from Savahia Mountain. This kind, and other less obvious types, of coherent scattering is amenable to sophisticated frequency-wavenumber methods, such as the multiple signal characterization (or MUSIC) method of Schmidt (1986). The MUSIC method is superior to the conventional method in its ability to detect multiple signals, and its utility should be explored for regional data. Velocity filtering techniques can also be used to isolate (or remove) coherently scattered wavefields. Additional analysis of the Savahia Mountain and Rice Valley data sets for coherent sources of scattering is warranted. Note, however, that without the high density of sensors at Savahia, spatial aliasing of this low velocity scattered wavefield would prevent these analysis methods from being useful. This again stresses the need for the temporary placement of high-density arrays at potential monitoring sites.

(5) Wavefield Simulations

We have seen throughout this study that regional wavefields are significantly affected by very local variations in geologic structure. In some cases the effects are systematic, such as the velocity-azimuth bias at Ruby Valley and the coherent scattering at Savahia Mountain, and in some cases they are random, as characterized by the coherence functions themselves at each array site. Effects like these will no doubt be typical of array monitoring sites in the western United States. This clearly presents problems for routine array monitoring of regional events.

However, given a sufficiently detailed knowledge of the geologic structure surrounding an array site, we can approach this problem through numerical wavefield simulations. The effects of the structure on array processing characteristics can be determined by propagating synthetic regional wavefields through the structure using finite difference methods. Effects such as the biasing of phase velocity and source azimuth could be predicted and therefore compensated. Coherent scattering sources, once identified, can be routinely removed through velocity filtering or simple subtraction in the frequency-wavenumber domain (Gupta *et al.*, 1990). Because detailed subsurface imaging is so costly, a first approach to array site selection is to consider regions which have already undergone extensive crustal imaging. The areas around Rice Valley and Savahia Mountain, and other regions explored by CALCRUST are examples. The effects of random crustal variations on array processing can be also simulated as well, given a distribution of the randomness. Array data itself can be used to estimate these distributions (Flatte′ and Wu, 1988; Wu and Flatte′, 1990).

In general, effective routine use of high-frequency regional monitoring arrays in the western U.S. will require site-specific studies aimed at fully understanding the distortional effects caused by local structural irregularities.

References

Abrahamson, N. A. and B. A. Bolt (1987). Array analysis and synthesis mapping of strong seismic motion, In: Bolt, B. A. (ed.), *Strong Motion Synthetics: Computational Techniques Series*, Academic Press.

Aki, K. (1973). Scattering of P waves under the Montana Lasa, *J. Geophys. Res.*, **78**, 1334-1346.

Bame, D. A., M. C. Walck, and K. L. Hiebert-Dodd (1990). Azimuth estimation capabilities of the NORESS regional seismic array, *Bull. Seis. Soc. Amer.*, **80**, Part B, 1999-2015.

Barker, B. W., Z. A. Der, and C. P. Mrazek (1981). The effect of crustal structure on the regional phases Pg and Lg at the Nevada Test Site, *J. Geophys. Res.*, **86**, 1686-1700.

Baumgardt, D. R. and G. B. Young (1990). Regional seismic waveform discriminants and case-based event identification using regional arrays, *Bull. Seis. Soc. Amer.*, **80**, Part B, 1874-1892.

Bennet, T. J. and J. R. Murphy (1986). Analysis of discrimination capabilities using regional data from western United States events, *Bull. Seis. Soc. Am.*, **76**, 1069-1086.

Bennet, T. J., B. W. Barker, K. L. McLaughlin, and J. R. Murphy (1986). Regional discrimination of quarry blasts, earthquakes, and underground nuclear explosions, Final Report, GL-TR-89-0114, S-Cubed, LaJolla, California.

Berger, J., J. N. Brune, P. A. Bodin, J. S. Gomberg, D. M. Carrel, K. F. Priestley, D. E. Chavez, W. R. Walter, C. B. Archambeau, T. B. Tarassov, and Y. A. Sutelov, (1987). A new U.S.-U.S.S.R. seismological program, *EOS*, **68**, 105.

Bolt, B. A. (1976). Nuclear Explosions and Earthquakes. The Parted Veil, W. H. Freeman and Co., San Francisco.

Bonner, B., B. J. Wanamaker, and S. R. Taylor (1989). Amplitude-dependent attenuation and implications for the seismic source, Proceedings of the DOE/LLNL Symposium on Explosion-Source Phenomenology, Lake Tahoe, Calif., 37-43.

Bouchon, M. (1982). The complete synthesis of seismic crustal phases at regional distances, *J. Geophys. Res.*, **87**, 1735-1741.

Claassen, J. P. (1985). The estimation of seismic spatial coherence and its application to a regional event, SAND85-2093, Sandia National Laboratories, Albuquerque, New Mexico.

Chernov, L. A. (1960). Wave Propagation in a Random Media, McGraw-Hill, New York.

Chiou (1991). Ph.D. Thesis, University of California at Berkeley.

Coward, M. P., Dewey, J. F., and Hancock, P. L. (eds.) (1987). *Continental Extensional Tectonics*, Geologic Society Special Publication No. 28, 299-311.

Dainty, A. M. and M. N. Toskoz (1990). Array analysis of seismic scattering, *Bull. Seis. Soc. Am.*, **80**, Part B, 326-338.

Dahlman, O. and H. Israelson (1977). Monitoring Underground Nuclear Explosions, Elsevier Scientific Publishing Co., Amsterdam.

Davis, G. A., J. L. Anderson, D. L. Martin, D. Krummenacher, E. G. Frost, and R. L. Armstrong (1982). Geologic and geochronological relations in the lower plate of the Whipple detachment fault, Whipples MOuntains, southeastern California: A progress report, in *Mesozoic-Cenozoic Tectonic Evolution of the Colorado River Region, California, Arizona, and Nevada*, edited by E. G. Frost, 409-432, Cordilleran Publishers, San Diego, Calif., 1982.

Davis, G. A. (1988). Rapid upward transport of mid-crustal mylonitic gneisses in the footwall of a Miocene detachment fault, Whipple Mountains, southeastern California, *Geol. Rundsch.*, **77**, 191-209.

Der, Z. A., M. E. Marshall, A. O'Donnell, and T. W. McElfresh (1984). Spatial coherence structure and attenuation of the Lg phase, site effects, and the interpretation of the Lg coda, *Bull. Seis. Soc. Am.*, **74**, 1125-1147.

Der, Z. A., R. A. Shumway, and A. C. Lees (1988). Frequency domain coherent processing of regional seismic signals at small arrays, *Bull. Seis. Soc. Am.*, **78**, 326-338.

Doornbos, D. and T. Kvaerna (1987). A scattering model of regional Pn propagation, NORSAR Scientific Report No. 1-87/88, Semiannual Technical Summary, L.B. Loughran (ed.), 26-34.

Enochson, L. D. and N. R. Goodman (1965). Gaussian approximations to the distribution of sample coherence, Tech. Rep. AFFDL-TR-65-57, Wright-Patterson Air Force Base.

Epstien, W. (1991). *Bull. of Atomic Sci.*, December, 45-47.

Evernden, J. F., C. B. Archambeau, and E. Cranswick (1986). An evaluation of seismic decoupling and underground nuclear test monitoring using high-frequency seismic data, *Rev. Geophys.*, **24**, 143-215.

Evernden, J. F. (1987). Yields of U.S. and Soviet nuclear tests, *Physics Today*, August, 37-44.

Flatte, S. M. and R. S. Wu (1988). Small-scale structure in the lithosphere and asthenosphere deduced from arrival-time and amplitude fluctuations at NORSAR, *J. Geophys. Res.*, **93**, 6601-6614.

Frankel, A. and R. W. Clayton (1986). Finte difference simulations of seismic scattering: implications for the propagation of short-period seismic waves in the crust and models of crustal heterogeneity, *J. Geophys. Res.*, **72**, 2583-2587.

Garbin, H. D. (1986). Decoupling estimate of the Mill Yard event, EOS , **67**, 1092.

Glenn, L. A., M. D. Denny, and J. A. Rial (1987). Sterling revisited: the seismic source for a cavity-decoupled explosion, *Geophys. Res. Lett.*, **14**, 1103-1106.

Hannon, W. J. (1985), Seismic verification of a comprehensive test ban, *Science*, **227**, 251-257.

Hannon, W. J. (1986), Verification, In: Earth Sciences Annual Report, Lawrence Livermore National Laboratory, Livermore, Calif.

Hansen, R. A., F. Ringdal, and P. G. Richards (1990). The stability of RMS Lg measurements and their potential for accurate estimation of the yields of Soviet underground explosions, *Bull. Seis. Soc. Am.*, **80**, Part B, 326-338.

Harris, D. B (1990). Comparison of the direction estimation performance of high-frequency seismic arrays and three-component stations, *Bull. Seis. Soc. Am.*, 80, Part B, 1951-1968.

Haskell, N. A. (1967). Analytic approximation for the elastic radiation from a contained underground explosion, *J. Geophys. Res.*, **72**, 2583-2587.

Hearn, T., N. Beghoul, and M. Barazangi (1991). Tomography of the western United States from regional arrival times, Submitted to the *J. Geophys. Res.*

Helmberger, D. V. and D. M. Hadley (1981). Seismic source functions and attenuation from local and teleseismic observations of the NTS events Jorum and Handley, *Bull. Seis. Soc. Am.*, **71**, 51-67.

Howard, K. A. (1980). Metamorphic infrastructure in the northern Ruby Mountains, Nevada, *Geologic Society of America Memoir*, **153**, 335-347.

Howard, K. A. and B. E. John (1987). Crustal extension along a rooted system of imbricate low-angle faults: Colorado River extensional corridor, California and Arizona, In: Coward, M. P., Dewey, J. F., and Hancock, P. L. (eds.), *Continental Extensional Tectonics*, Geologic Society Special Publication No. 28, 299-311.

Ingat, S. F., E. S. Husebye, and A. Christoffersson (1985). Regional arrays and optimum data processing schemes, *Bull. Seis Soc. Am.*, **75**, 1155-1177.

Jepsen, D. C. and B. L. N. Kennet (1990). Three-component analysis of regional seismograms, *Bull. Seis. Soc. Am.*, **80**, Part B, 2032-2052.

Jurkevic, A. (1988). Polarization analysis of three-component array data, *Bull. Seis. Soc. Am.*, **78**, 1725-1743.

Kvaerna, T. (1989). On exploitability of small-aperture NORESS type arrays for enhanced P-wave detection, *Bull. Seis Soc. Amer.*, **79**, 888-900.

Leonard, M. A., and L. R. Johnson (1987). Velocity structure of Silent Canyon Caldera, Nevada Test Site, *Bull. Seis. Soc. Amer.*, **77**, 597-613.

Lawson, C. L. and R. J. Hanson (1974). Solving Least Squares Problems, Prentice-Hall, Englewood Cliffs, New Jersey.

Mavko, G. M. (1979). Frictional attenuation: an inherent amplitude dependence, *J. Geophys. Res.*, **84**, 4769-4775.

Menke, W., A. L. Lerner-Lam, B. Dubendorff, and J. Pacheco (1990). Polarization and coherence of 5 to 30 Hz seismic wave fields at a hard-rock site and their relevance to velocity heterogeneities in the crust, *Bull. Seis. Soc. Am.* , **80**, 430-449.

Minster, J. B. and S. M. Day (1986). Decay of wave fields near an explosive source due to high-strain, nonlinear attenuation, *J. Geophys. Res.*, **91**, 2113-2122.

Mrazek, C. P., Z. A. Der, B. W. Barker, and A. O'Donnell (1980). Seismic array design for regional phases, in *Studies of Seismic Wave Characteristics at Regional Distances*, Teledyne Geotech, Alexandria, Virginia, AL 80-1.

Mueller, R. A. and J. R. Murphy (1971). Seismic characteristics of underground nuclear detonations, Part I. Seismic spectrum scaling, *Bull. Seis. Soc. Am.*, **61**, 1675-1692.

Mykkeltveit, S., K. Astebol, D. J. Doornbos, and E. S. Husebye (1983). Seismic array optimization, *Bull. Seis. Soc. Am.*, **73**, 173-186.

Nuttli, O. W. (1981). On the attenuation of Lg waves in western and central Asia and their use as a discriminant between earthquakes and explosions, *Bull. Seis. Soc. Amer.*, **71**, 249-261.

Nuttli, O. W. (1986). Yield estimates of Nevada Test Site explosions obtained from seismic Lg waves, *J. Geophys. Res.*, **91**, 2137-2151.

Pomeroy, P. W., W. J. Best, and T. V. McEvilly (1982). Test ban treaty verification with regional data - a review, *Bull. Seis. Soc. Am.*, **72**, S89-S129.

Priestley, K. F., W. R. Walter, V. Martynov, and M. V. Rozhkov (1990). Regional seismic recordings of the Soviet nuclear explosion of the joint verification experiment, *Geophys. Res. Lett.*, **17**, 179-182.

Pulli, J. J. and P. S. Dysart (1987). Spectral study of regional earthquakes and chemical explosions recorded at the NORESS array, Technical Report, C87-03, Center for Seismic Studies, Arlington, Virginia.

Rodgers, P. W. and R. F. Rohrer (1987). Seismic noise spectra at Elko, Kanab, Landers, and Mina, Lawrence Livermore National Laboratory, Livermore, CA, UCID-21049.

Schmidt, R. O. (1986). Multiple emmiter location and signal parameter estimation, *IEEE Trans. on Antennas and Propagation*, **34**, 276-280.

Sharpe, J. A. (1942). The production of elastic waves by explosion pressures. I. Theory and empirical field observations, *Geophyiscs*, **7**, 144-154.

Snoke, A. W. (1980). Transition from infrastructure to suprastructure in the northern Ruby Mountains, Nevada, *Geologic Society of America Memoir*, **153**, 287-332.

Sykes, L. R.and D. M. Davis (1987). The yields of Soviet strategic weapons, *Scientific American*, **256**, 29-37.

Taylor, S. R., N. W. Sherman, and M. D. Denny (1988). Spectral discrimination between NTS explosions and western United States earthquakes at regional distances, *Bull. Seis. Soc. Am.*, **78**, 1563-1579.

Taylor, S. R., M. D. Denny, E. S. Vergino, and R. E. Glasor (1989). Regional discrimination between NTS explosions and western United States earthquakes, *Bull. Seis. Soc. Am.*, **79**, 1142-1176.

Taylor, S. R. and G. E. Randall (1989). The effects of spall on regional seismograms, *Geophys. Res. Lett.*, **16**, 211-214.

Thomson, D. J. (1982). Spectrum estimation and harmonic analysis, *IEEE Proc.*, **70**, 1055-1096.

U.S. Congress (1988). Office of Technology Assessment, *Seismic Verification of Nuclear Testing Treaties*, OTA-ISC-361 (Washington, DC: U.S. Government Printing Office)

Vernon, F. L. and Jon Fletcher (1991). Coherence of seismic body waves from local events as measured by a small-aperture array, accepted by the *J. Geophys. Res.*

von Seggern, D. and R. Blandford (1972). Source time functions and spectra for underground nuclear explosions, *Geophys. J. R. Astr. Soc.*, **31**, 83-97.

Wang, H. and M. Kaveh (1985). Coherent signal subspace processing for the detection and estimation of angles of arrivals of multiple wideband sources, *IEEE Trans. Acoust. Speech Signal Processing*, **33**, 823-831.

Wang, C. Y., C. Ruppert, T. Guo, G. A. Davis, D. A. Okaya, Z. Zhong, and H.-R. Wenk (1989). Seismic reflectivity of the Whipple Mountain shear zone in Southern California, *J. Geophys. Res.*, **94**, 2989-3005.

Appendix A

Spectral Amplitude Estimation

This purpose of this appendix is to describe a few of the details of the multiple taper spectral estimation procedure of Thomson (1982), and to examine how these tapers compare in synthetic tests for which the true amplitude spectrum is known. Results from the more common method of simple cosine tapering, described immediately below, are also included. The principal advantage of the multi-taper method is its ability to form relatively low bias, low variance spectral estimates. A more complete description of multi-taper spectral estimation and its statistical advantages over other spectral estimation procedures can be found in Thomson (1982) and Park *et al.*, (1987).

Cosine Tapering

Let $u_j(t_n)$; $t_n=n\tau$; $n=1,\ldots,N$ be a time series of sample length N (time length T) and sampling interval τ recorded at the jth station. The discrete Fourier transform (DFT) is expressed by

$$u_j(f) = \tau \sum_{n=1}^{N} v(t_n)\, u_j(t_n)\, e^{-i2\pi f t_n}, \tag{A.1}$$

where $v(t_n)$ is the data taper and f is the frequency. The estimate of the amplitude spectrum is then given by $A_j(f) = |u_j(f)|$.

A common choice of data taper is the p% split-cosine bell taper. Shown in Figure A1a is the 20% taper, i.e., 20% of the time series is modulated by the cosine function. In the frequency domain, the operation in (A.1) is equivalent to a convolution between the true fourier transform of the time series and the transform of the data taper. In effect, the spectral estimate is blurred and biased by the effects of the spectral resolution and leakage characteristics of the taper. The resolution and spectral leakage characteristics of this taper can be seen in its DFT

amplitude spectrum, shown in Figure A2a. The spectrum is plotted as a function of frequency bin number J, where J/T are the Rayleigh frequencies, which are the sampled frequencies returned from a fast fourier transform. The resolving width, i.e., the width of the main lobe, for this taper is approximately 2/T, and the amplitude of the first sidelobe is quite large, within one order of magnitude of the main lobe.

Multiple Taper Method

An alternative to conventional tapering is the method of Thomson (1982), which employs the use of multiple data tapers, or "eigentapers". These tapers $v_l(t_n;T,W)$; $l=1,\ldots,L$ are specifically designed to minimize spectral leakage outside a chosen frequency band of width 2W. For each time series one computes a total of L spectra, or "eigenspectra":

$$u_{jl}(f) = \tau \sum_{n=1}^{N} v_l(t_n)\, u_j(t_n)\, e^{-i2\pi f t_n}. \tag{A.2}$$

If the local variations in the spectrum are not too extreme, the eigenspectra will be nearly uncorrelated and the estimate of the amplitude spectrum $A_j(f)$ can be formed from a weighted sum of the eigenspectra (Thomson, 1982),

$$A_j^2(f) = \frac{\sum_{l=1}^{L} |w_l(f)\, u_{jl}(f)|^2}{\sum_{l=1}^{L} |w_l(f)|^2}. \tag{A.3}$$

The amount of spectral leakage associated with each eigentaper is reflected in its corresponding eigenvalue λ, where the amount of fractional leakage from outside the 2W bandwidth is $1 - \lambda$. A set of tapers having WT = P belongs to the family of "Pπ" tapers. Values of λ for the 2π, 3π, and 4π tapers are given in Table A1. Here we will consider only the first L=2P-1 lowest order tapers. From Table A1, this ensures that the fractional leakage remains below, at most, 6% for each taper. This amounts to using the first 3, 5, and 7 of the 2π, 3π, and 4π tapers, respectively.

The first $L_{P\pi}$ tapers are shown in Figure A1; tapers of higher order cross the time axis a greater number of times. Any single taper will weight the time series very unevenly. However, when all tapers are combined, the time series is much more evenly sampled. The DFT amplitude spectra of each of the tapers are shown in Figure A2 and reflect the differences in resolution width and leakage between the families of tapers. The whole-width of the main lobes can be seen to be 4/T, 6/T, and 8/T for 2π, 3π, 4π tapers, respectively. Within a family of tapers, the higher order tapers have a successively greater amount of spectral leakage. In general, the spectral leakage from most of the $P\pi$ tapers shown is less than that from the cosine taper. Between families of tapers, the amount of spectral leakage increases with decreasing resolution width. The number of eigenspectra L=2P-1 used in the spectral estimate increases going from 2π, 3π, 4π . Therefore, while, for example, the 2π estimate will have greater resolution, it will also have greater variance and leakage relative to the 3π and 4π estimates.

The frequency dependent weights $w_l(f)$ are computed through an adaptive iteration technique and provide a means of reducing the bias due to spectral leakage of the higher order tapers. The details of this weighting scheme can be found in Thomson (1982) and Park *et al.*, (1987). In regions where the spectrum is relatively constant $w_l(f)$ is approximately equal to one. However, in regions where spectral leakage is more significant, i.e., where the spectra is changing more rapidly, the higher order weights (which correspond to higher order tapers having relatively greater spectral leakage) are reduced. The method therefore provides an objective means of trading off variance, which is increased by the weighting, and bias, which is decreased.

Synthetic Tests

The characteristics of multi-tapering can be further illuminated by analyzing a synthetic seismic time series for which the true amplitude spectrum is known. Here we can use the displacement time series from a spherically symmetric compressional point source having a step source time function, as given by Sharpe (1942), and shown in Figure A3a for a chosen set of

physical parameters. The 20% cosine, 2π, 3π, and 4π tapered DFT spectra are compared in the three synthetic tests described below. A time window of approximately 0.5 seconds is used, which amounts to spectral resolution widths of 4 Hz, 8 Hz, 12 Hz, and 16 Hz for the 20% cosine, 2π, 3π, and 4π estimates, respectively. In all tests, to further reduce spectral leakage, the tapered time series were prewhitened using a sixth order auto-regressive filter determined from the tapered time series.

Test 1: Displacement pulse only

Here amplitude spectral estimates of the time series as shown in Figure A3a are computed. The theoretical amplitude spectrum is shown at the top of Figures A3b and A3c. For clarity, both log-log and log-linear plots of the spectra are shown. The true spectrum is quite simple, characterized by a constant low frequency level, a corner frequency near 4 Hz, and a constant high-frequency log-log slope of -2. All of the tapering methods estimate the high frequency slope and corner frequency about equally well. The 20% cosine taper, however, does a relatively poor job at low frequencies, underestimating the true amplitude level. This is a result of its relatively heavy tapering at the ends of the time series, effectively shortening the length of the time series and therefore removing some of the low frequency energy. A number of the multiple tapers, however, still apply relatively large weighting at the ends of the time series and so do not lose so much low frequency energy (see Figure A1). Of the multi-tapers, the 2π tapers downweight the ends of the time series the most, and so some underestimation of the low frequency levels is also evident in its spectral estimate.

The eigenspectra and corresponding computed weights for each taper are shown in Figure A4. The differences in eigenspectra reflect the differences in the data tapers used. For example, the second order 2π taper goes through a node near where the amplitude of the time series is greatest, resulting in the relatively low spectral amplitude estimate in Figure A4a. The weighting for any taper basically depends on the amount of leakage associated with it and the variation in the true spectrum. The tapers with the least amount of leakage, the zeroth order

3π and 4π tapers, have essentially constant weighting of one. Tapers with increasing leakage are weighted progressively less.

Test 2: Displacement pulse with added noise

Here spectra are computed from the same time series with a slight amount of white noise added, as shown in Figure A5a. These spectral estimates differ from those in Figure A3 only beyond about 20 Hz, where the signal to noise level becomes relatively low. The 20% cosine taper displays the most variation here, while the 4π tapers, because of their large resolution width, produce the smoothest estimate.

The eigenspectra and weights for this case are shown in Figure A6. The weights, in general, are reduced relative to Test 1 due to the increased spectral variation caused by the added noise. The relative reduction in weights becomes greater for the higher order tapers, even at the low frequencies where the signal to noise ratio is relatively large.

Test 3: Displacement pulse with two added harmonics

To contrast resolution and leakage characteristics among the tapers, harmonics at 20 Hz and 55 Hz, differing in amplitude by a factor of ten, are added to the time series, as shown in Figure A7. No noise has been added to the time series. The 20% cosine estimate produces the best resolution of the harmonics, as well as the greatest amount of spectral leakage. Were the relative amplitude difference between the harmonics larger, the presence of the smaller amplitude harmonic could easily be lost in the leakage of the larger harmonic. The multi-taper estimates are all quite smooth, displaying very little spectral leakage effects. The resolution differences between the multitaper estimates are clearly evident at the harmonic frequencies. All estimates retain the high-frequency slope about equally well, however, there is a progressive blurring of the corner frequency proceeding from the 2π to the 4π estimate due to increased smoothing of the 20 Hz harmonic. This effect would not be as pronounced were the time series of longer duration, which would narrow the resolved width of the harmonics.

The eigenspectra and weights for this case are shown in Figure A8. Rather than monotonically decay as in the first test, here the weights increase around the frequency of the harmonics. Note that the weighting of the higher frequency harmonic is scaled by the background weighting, (i.e. the weighting shown in Figure A4b) and so for any taper it is weighted relatively less than the lower frequency harmonic.

Comments

These synthetic tests have displayed some of the features of the multi-taper spectral estimation method. For each test case we saw how reduced spectral leakage from higher order tapers trades off with increased variance through the adaptive weighting of eigenspectra. We also examined variance and resolution characteristics. In Tests 1 and 2, the multi-taper method reproduced the spectrum for a simple explosive source better than that from simple cosine tapering, particularly at low frequencies. The accuracy of the estimate improved proceeding from the 2π to the 4π estimate, as more and more tapers were added, which reduced the variance. However in Test 3, where small bandwidth structure was added to the true spectrum, the low-variance 4π estimate was no longer the obvious choice as the best estimate. The higher-resolution 2π tapers appeared to provide a better overall estimate for this case. And it was the 20% cosine estimate that best reproduced the harmonics by virtue of its narrow resolution width.

In general, the choice of spectral estimation method should depend on what is known about the data, what one is looking for in the spectrum, and the statistical requirements of the estimate. For example, if one is looking for harmonics, then high-resolution methods, such as the split cosine and maximum entropy estimates, would be appropriate. However, if details in the spectrum on scales smaller than the relatively larger resolution widths of the multi-tapers is not terribly significant and not of great interest, then the multi-taper estimate may be favored. Such could be the case, for example, when analyzing time series from explosive sources, as suggested by the above test cases. In any case, it is instructive to experiment with all tapers

for a particular data set to get a feel for the differences and for which estimate may be appropriate. This is done below for data recorded at the Ruby Valley array.

Ruby Valley Example

In this section we compare the differences in the spectral estimates for seismic data recorded at the Ruby Valley array and the LLNL seismic station. The time series here consists of a 2.6-second window of the radial Pn wave from the explosion HARDIN, the same window analyzed in section 3.3.1. Figure A9 shows the instrument corrected spectral estimates for each type of taper. The Ruby Valley spectrum shown is actually the mean of the spectra computed for each of the twelve stations at the array, assuming a log-normal spectral distribution. Also shown is the recording system noise level at the Ruby Valley array.

The differences here are similar to the differences found in the synthetic cases, namely the decreasing spectral leakage and decreasing resolution proceeding from the 20% taper to the 4π tapers. All estimates produce essentially the same high-frequency slope of approximately -7 beyond 10 Hz. The spectra, even though from an explosive source, do show prominent peaking, possibly due to site response effects. These features, near 6 Hz at the array and near 3 Hz and 8 Hz at the LLNL site, remain visible even up to the low-resolution 4π estimate. Here one might choose to favor the 3π estimate as a compromise between the 2π and 4π estimates, retaining relatively low variance, characteristic of the 4π estimate, and acceptable resolution characteristic of the 3π estimate.

For comparison to the test cases, the eigenspectra and multi-taper weights for station #1 of the Ruby Valley array are shown in Figure A10. The eigenspectra shown here have not been instrument corrected. Notice the significant drop in weighting for the lower order tapers near 30 Hz. Referring to Figure A9, this is just where the signal runs into the noise and the spectral variation greatly increases, resulting in the low weighting.

References Cited

Park, J., C. R. Linberg, and F. L. Vernon III (1987), Multitaper spectral analysis of high-frequency seismograms, *J. Geophys. Res.*, 92, 12675-12684.

Sharpe, J. A. (1942), The production of elastic waves by explosion pressures. I. Theory and empirical field observations, *Geophyics*, 7, 144-154.

Thomson, D. J. (1982), Spectrum estimation and harmonic analysis, *IEEE Proc.*, 70, 1055-1096.

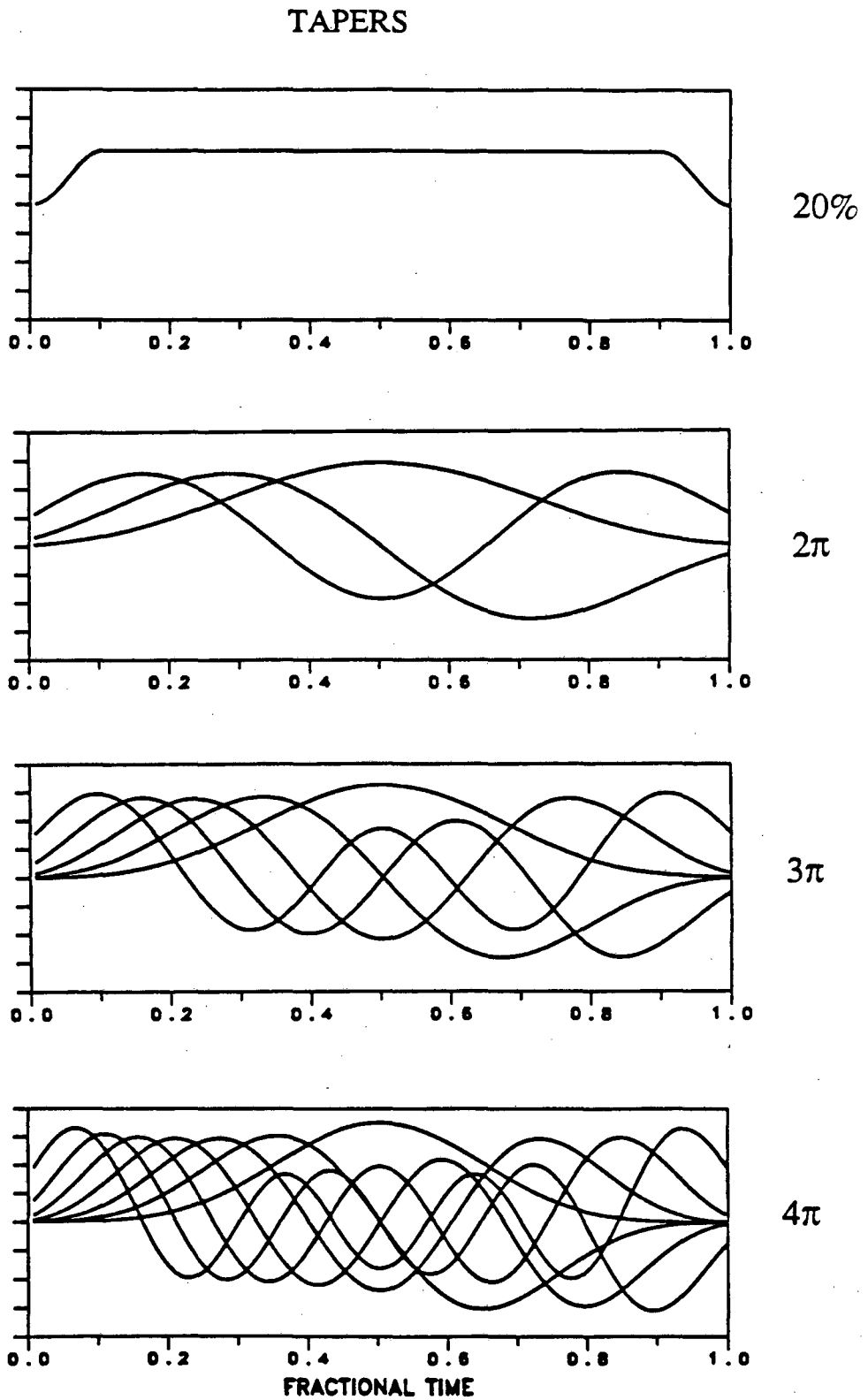

FIG. A1 20% split cosine taper and the first L = 2P - 1 multiple tapers, for P = 2, 3, and 4, respectively.

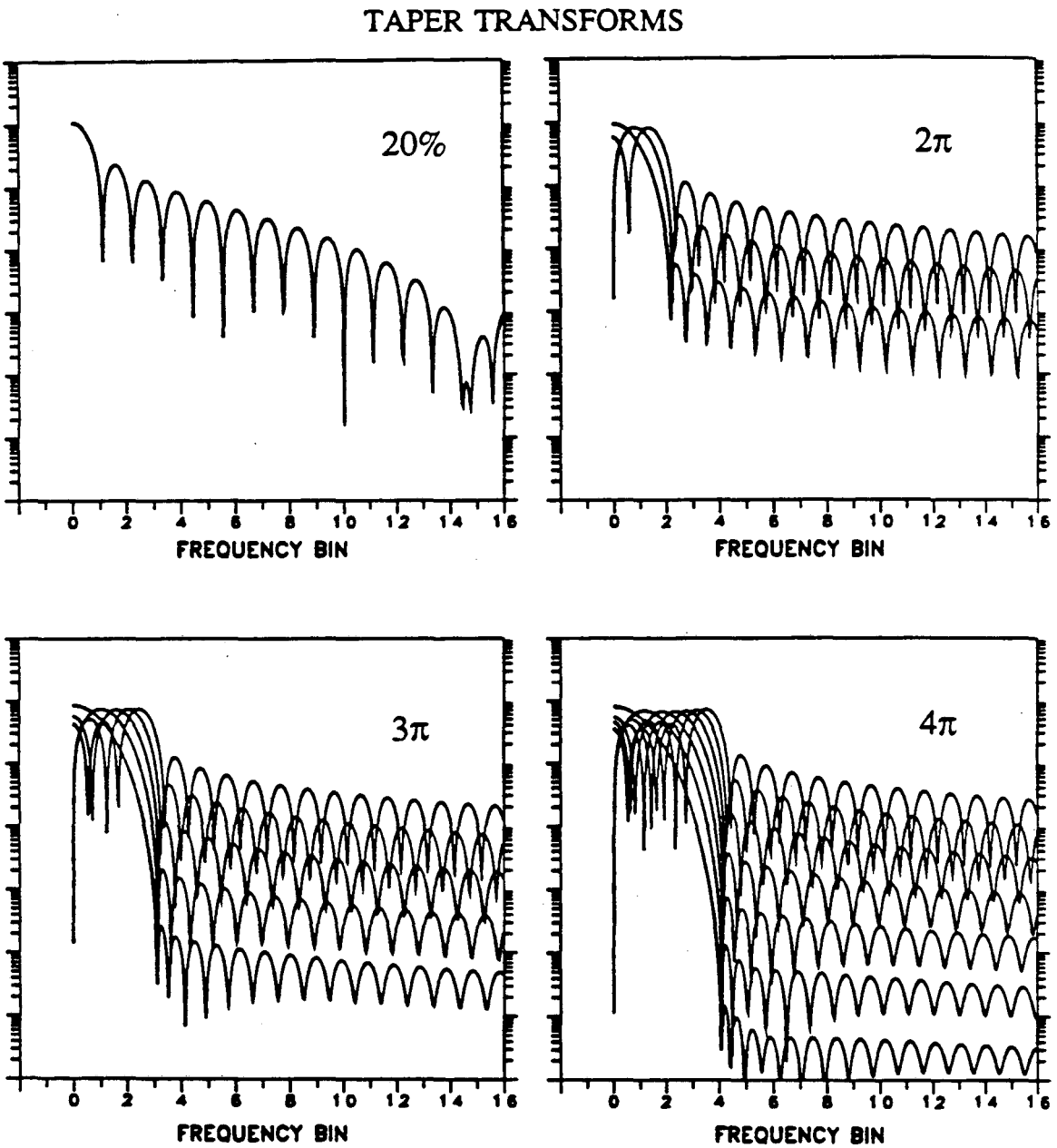

FIG. A2 Discrete Fourier Transform amplitude spectra of the tapers shown in Figure A1, plotted as a function of frequency bin number J, where J/T are the sampled frequencies returned from a fast fourier transform, T being the length of the time series in seconds.

Multi-taper Eigenvalues			
order	2π	3π	4π
0	0.99994	0.99999987	0.9999999997
1	0.998	0.999991	0.99999997
2	0.96	0.9997	0.9999988
3	0.73	0.995	0.99997
4		0.95	0.9994
5		0.72	0.993
6			0.94
7			0.72

Table A1 Eigenvalues λ for the lower order tapers of the 2π, 3π, and 4π families of tapers. The amount of fractional spectral leakage for each taper is $1 - \lambda$.

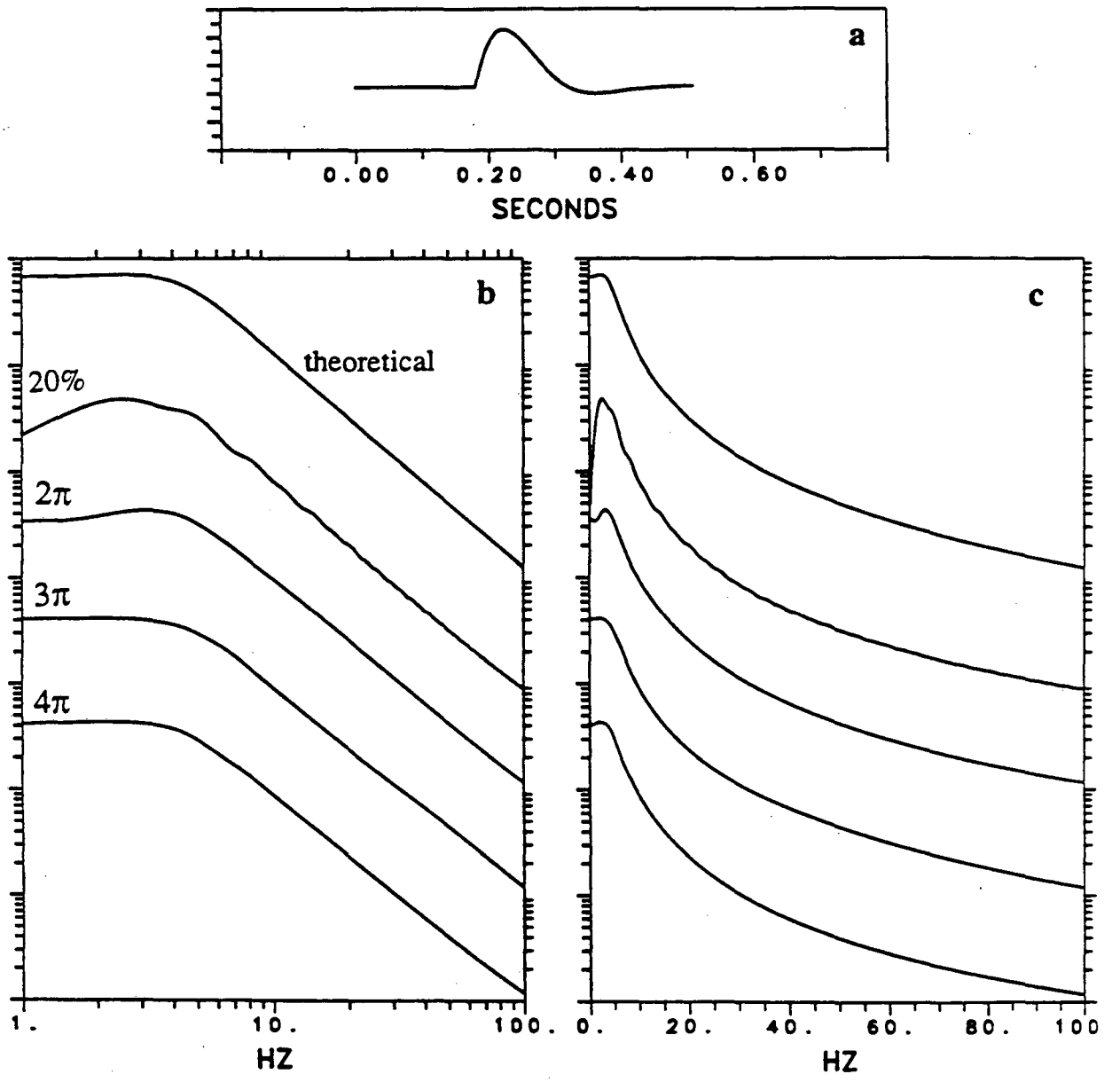

FIG. A3 (a) Discrete time series of the theoretical displacement from a spherically symmetric explosive source. (b) Corresponding theoretical displacement amplitude spectrum and estimates based on the tapers indicated. (c) Log-linear plot of (b).

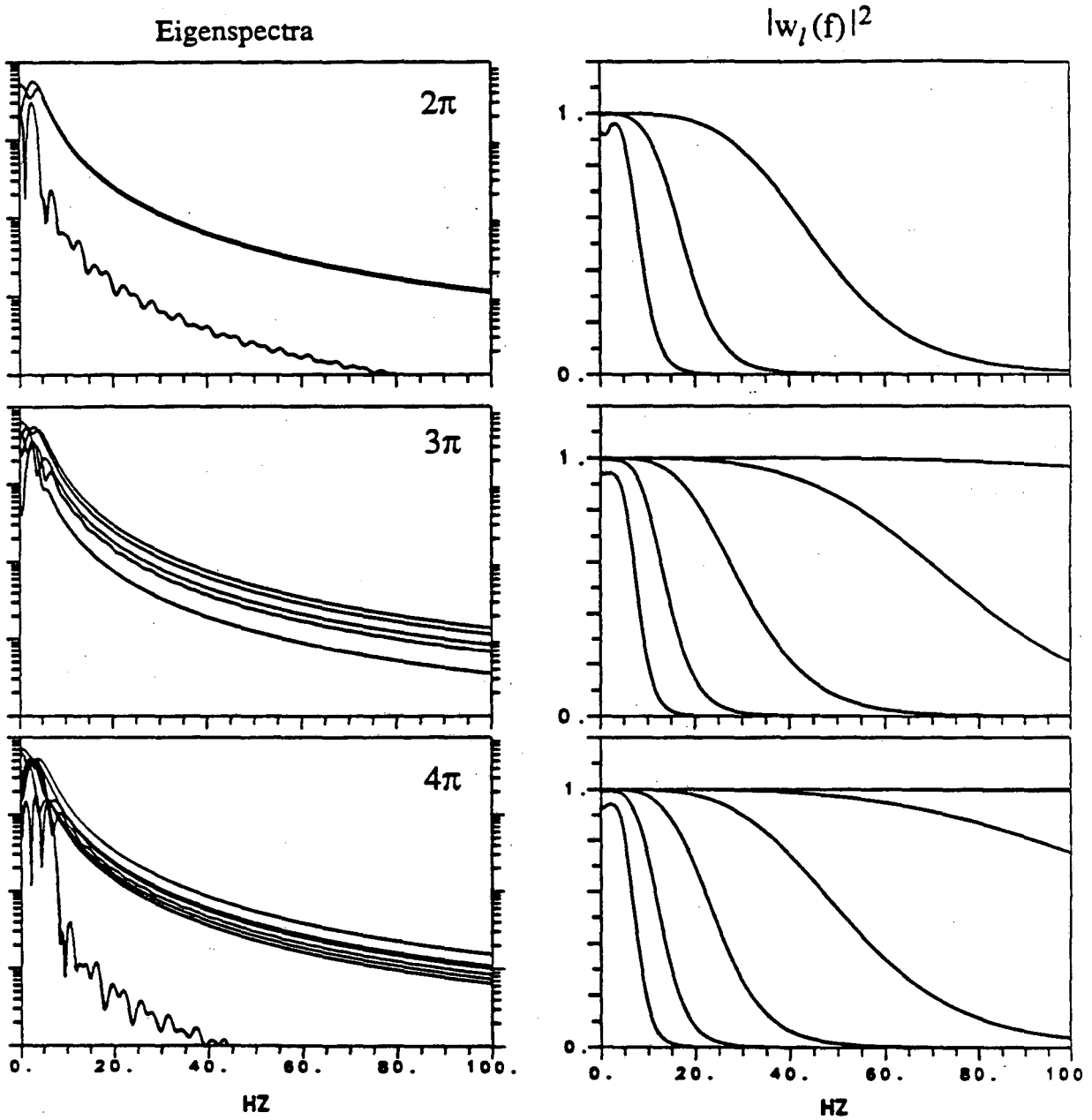

FIG. A4 Eigenspectra for the 2π, 3π, and 4π families of multiple tapers computed from the time series in Figure A3. The corresponding frequency dependent eigenspectra weighting functions $|w_l(f)|^2$ are shown to the right.

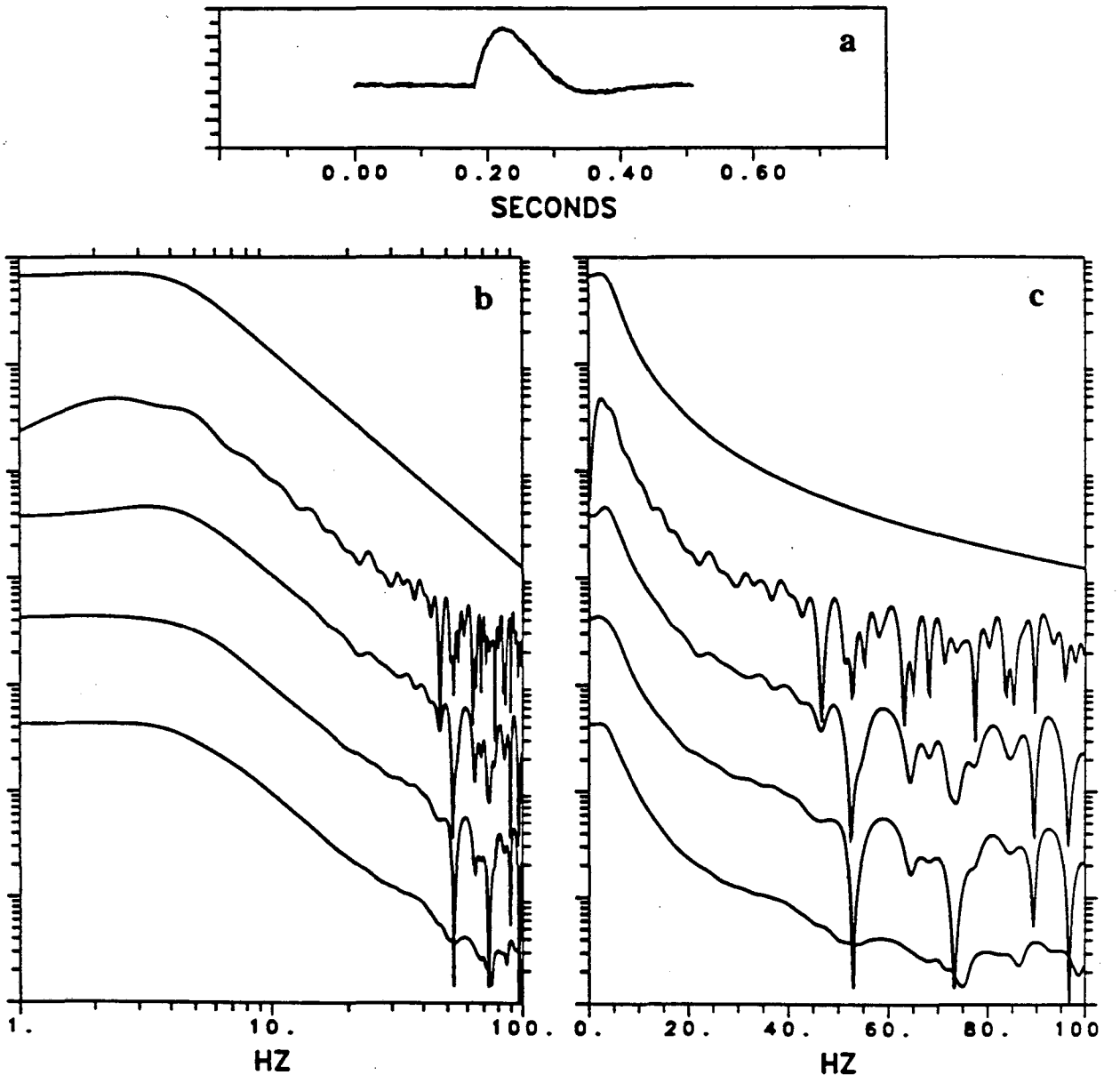

FIG. A5 Same as Figure A3 with white noise added to the time series.

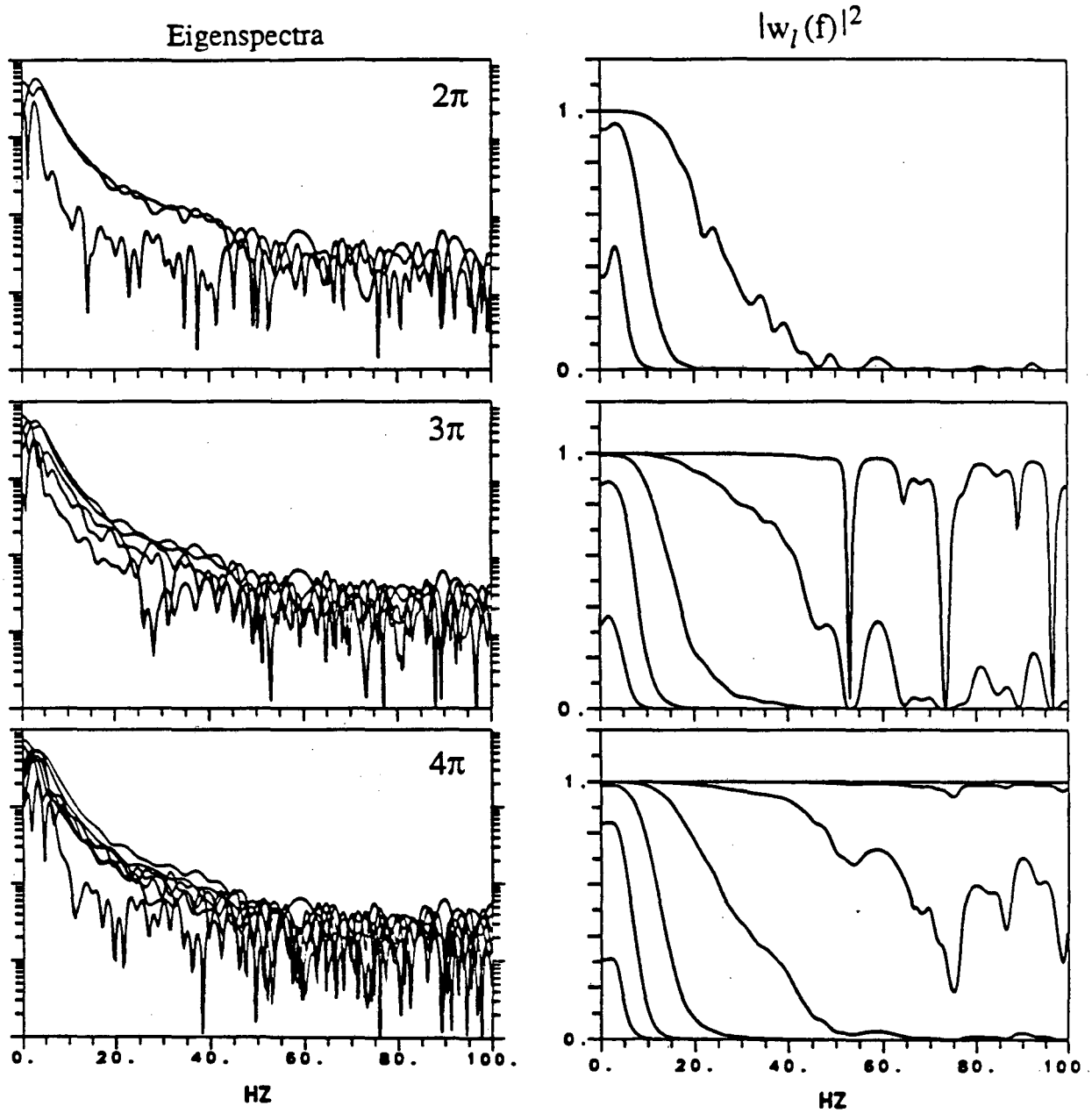

FIG. A6 Same as Figure A4 with white noise added to the time series.

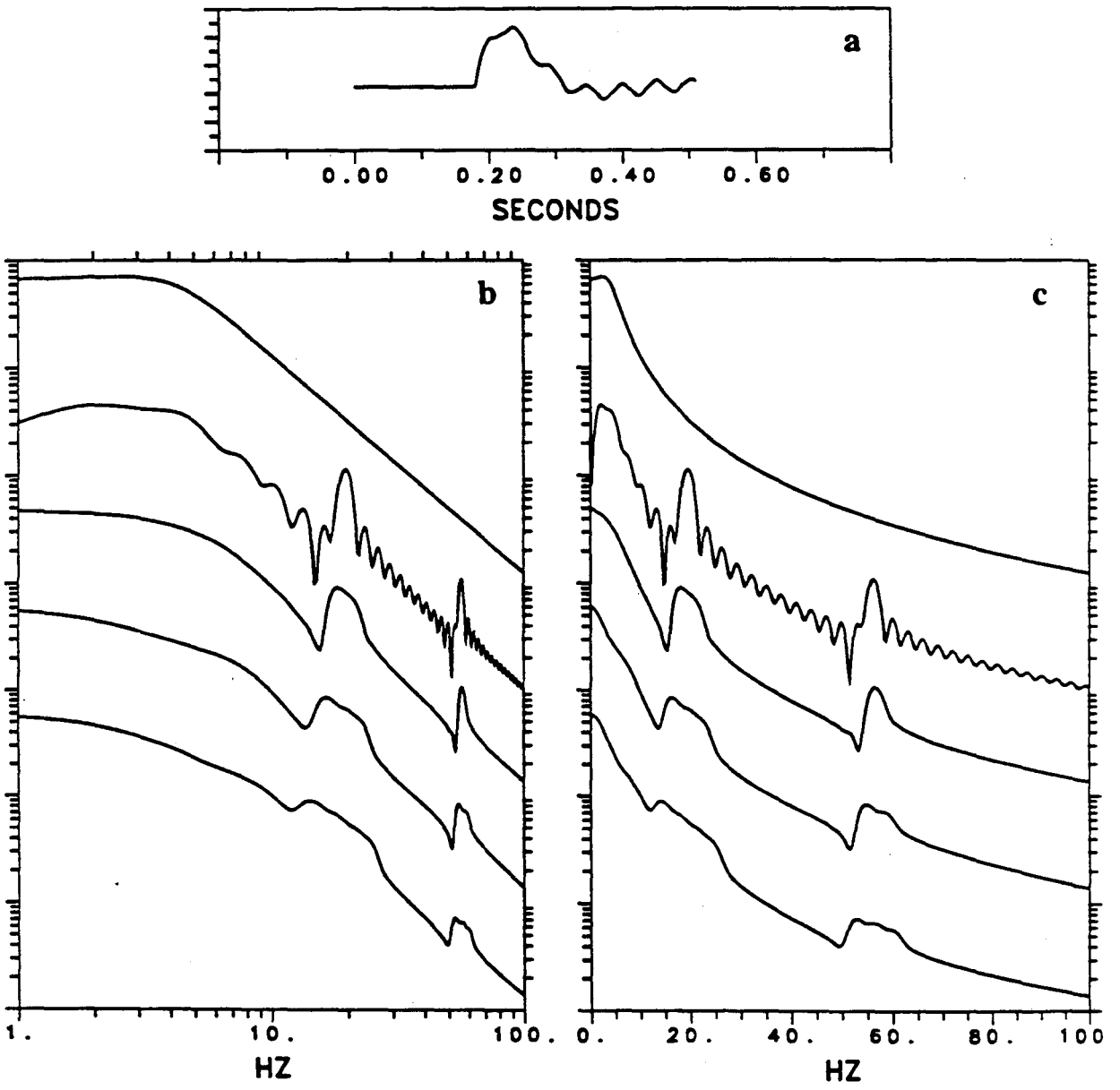

FIG. A7 Same as Figure A3 with harmonics added to the time series at 20 Hz and 55 Hz. No noise added.

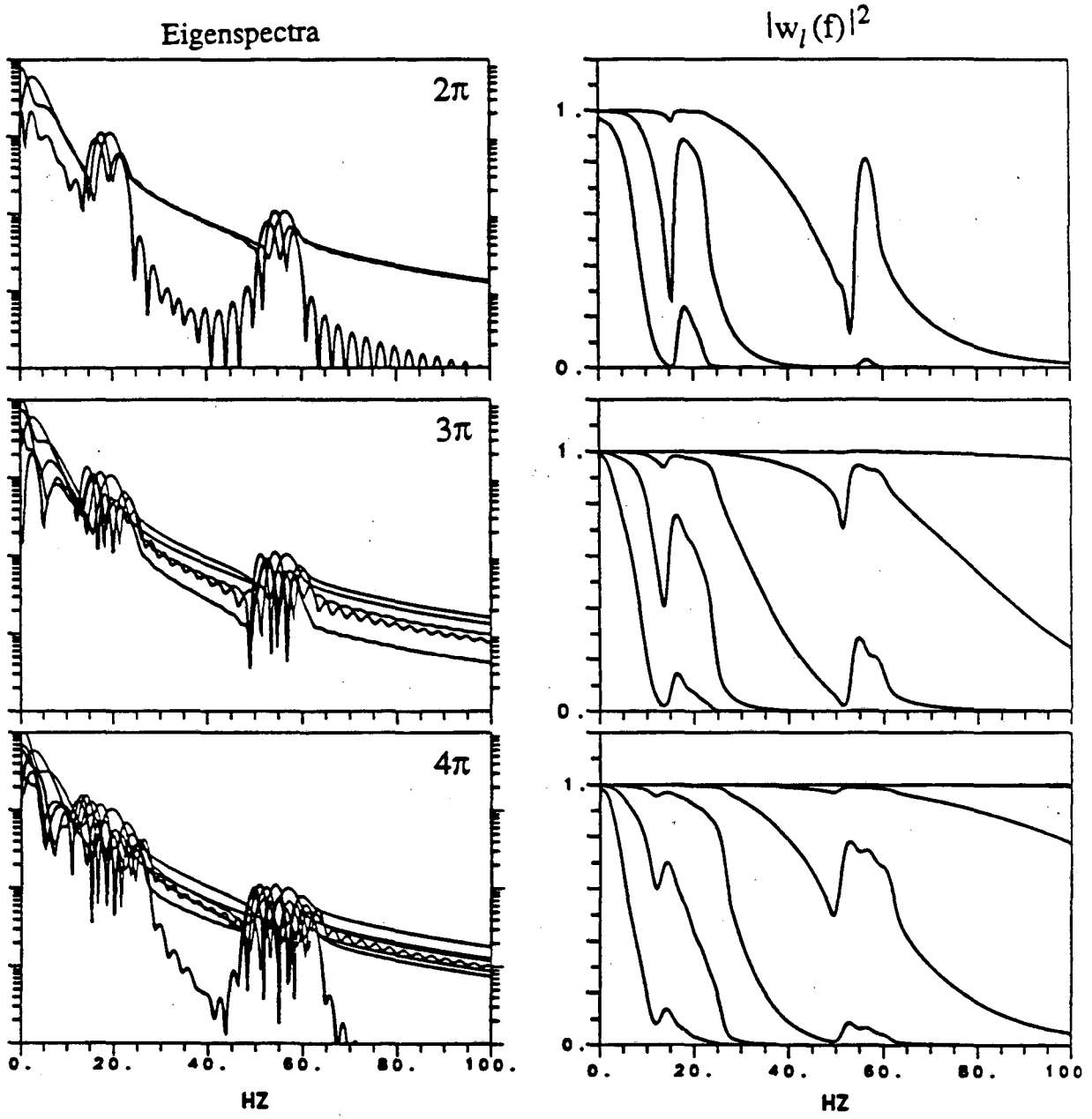

FIG. A8 Same as Figure A4 with harmonics added to the time series at 20 Hz and 55 Hz. No noise added.

HARDIN Pn

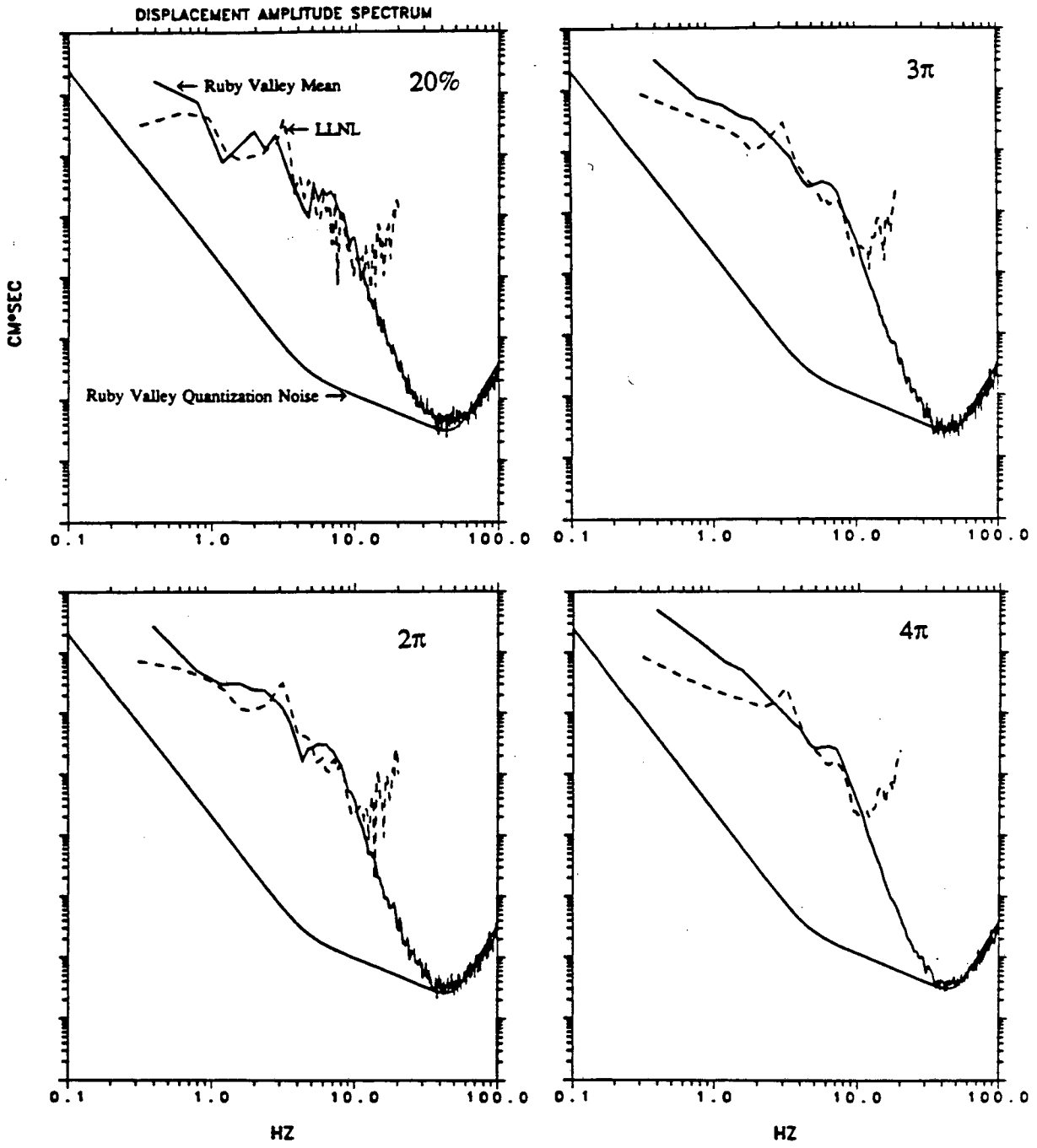

FIG. A9 Instrument corrected displacement amplitude spectral estimates of the Pn wave from the explosion HARDIN recorded at the Ruby Valley array and at the LLNL site for the tapers indicated. The Ruby Valley spectrum shown represents an average of the spectra computed at each of the 12 array recording stations. The Ruby Valley system noise is also shown.

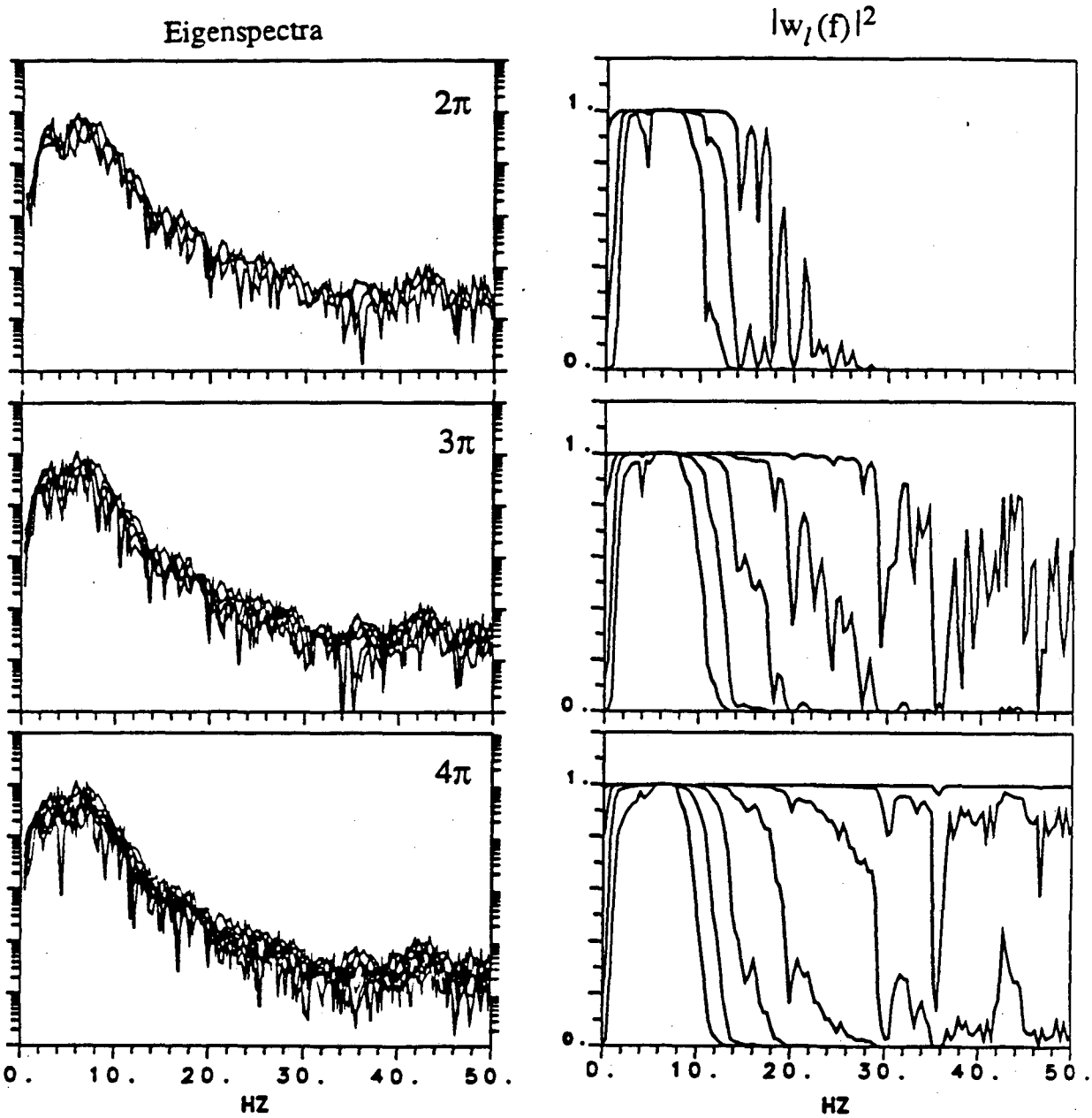

FIG. A10 Eigenspectra and corresponding weights at station # 1 of the Ruby Valley array for the Pn wave of the explosion HARDIN.

Appendix B

Bandpass Filtering Example of a Regional Waveform

An important task of regional seismic monitoring is the detection and isolation of regional phases. This is often done in the time domain with the use of STA/LTA algorithms, which may be made more effective by first bandpass filtering the data. For example, regional data recorded at the NORESS array often reveal otherwise concealed Pg and Sn phases when bandpassed filtered toward the higher frequency end (Mykkeltveit *et al.*, 1990)

As an example of our western U.S. data, bandpass filtered waveforms from one of the Ruby Valley array recordings of the explosion HARDIN are displayed in Figure B1. The raw three-component data are shown at the top of the figure. A 12 pole zero-phase Butterworth filter was used to compute the filtered traces. The corner frequencies, or bandpass, of the filters increase in octave steps, as indicated in the figure. Each waveform is plotted to 74 seconds and is normalized by its maximum amplitude. On the raw traces can be seen the onsets of Pn near 2 seconds, Pg near 10 seconds, and, on the horizontals, Lg near 60 seconds. In the 0.5-4 Hz range the waveforms are dominated by Pg and Lg. In the 4-8 Hz range Pn has surpassed Pg in amplitude on the vertical component and Lg is greatly attenuated. By the 8-16 Hz range, Pn has reached equal or greater amplitude relative to Pg on all components and Lg appears undetectable. Here the peak amplitude of Pn is about the same on all three components. Finally, in the 16-32 Hz range Pn on the vertical component sustains the largest amplitudes, while on the horizontals Pn falls back below Pg. In this frequency band Pg is detectable only on the horizontals, and here the detectability is not great. In no instance was a clear new arrival revealed in the filtering process. However we do see that the detectability of Pn, Pg, and Lg, measured here simply by the signal amplitude relative to the preceding ground motion, is dependent on frequency and component of ground motion. Overall the detectability of Pn appears greatest on the vertical component. The detectability of Pg appears comparable

on all components, while Lg is greatest on the horizontals at the lowest frequencies.

References

Mykkeltveit, S. Ringdal, T. Kvaerna, and R.W. Alewine (1990), Application of regional arrays in seismic verification, *Bull. Seis. Soc. Amer.*, **80** , Part B, 1777-1800.

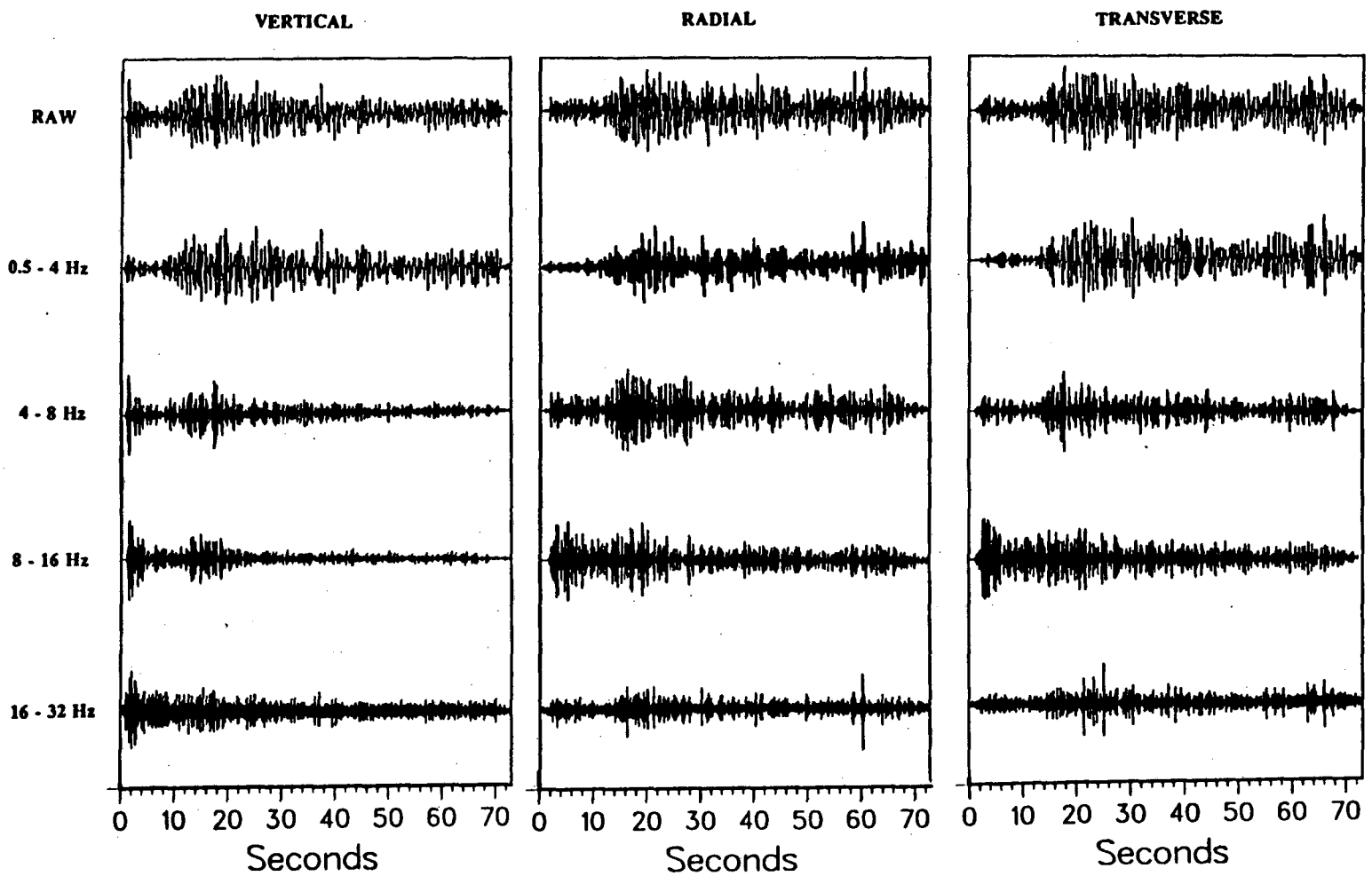

FIG. B1 Three-component recordings of the explosion HARDIN recorded at station #8 of the Ruby Valley array bandpassed filtered in octave frequency steps.

Appendix C

Coherence Estimation and Statistics

The purpose of this appendix is to describe the procedure used in the estimation of coherence and to describe the corresponding statistics of the estimate. Both the multiple taper spectral estimation procedure of Thompson (1982), and the more conventional frequency averaging method (e.g. Beauchamp and Yuen, 1979) are considered.

First, recall that the estimate of coherence between two time series $u_j(t)$ and $u_k(t)$ at frequency f is given by

$$|\gamma_{jk}(f)| = \frac{|S_{jk}(f)|}{[S_{jj}(f)\ S_{kk}(f)]^{1/2}} \quad , \tag{C.1}$$

where S_{jk} is the cross-spectral estimate given by

$$S_{jk}(f) = E\,[u_j(f)\ u_k(f)^*] \ , \tag{C.2}$$

where E is the expectation operator, $u_j(f)$ and $u_k(f)$ are the Fourier transforms of the time series, and * denotes the complex conjugate. The value of $|\gamma_{jk}|$ depends fundamentally on the means by which the expectation in $S_{jk}(f)$ is computed. The non-stationarity typical of our seismic data precludes averaging cross-spectra over multiple time windows, as can be done with stationary time series (e.g. Beauchamp and Yuen, 1979). Therefore some other means of spectral averaging must be used. Two alternatives are described below.

Frequency Averaging Method

In this method the assumption is made that the cross-spectrum varies slowly with frequency, so that we can average the cross-spectrum over a frequency band centered about the frequency of interest. A single data taper, such as a split cosine taper, is used on each of the two time series. An estimate of the cross-spectrum between the time series at a "center

frequency'' f_c is obtained by a weighted average over a frequency band of width 2M/T centered at f_c, i.e.,

$$S_{jk}(f_c) = \sum_{m=-M}^{M} a(f_m)\, u_j(f_m)\, u_k(f_m)^*, \tag{C.3}$$

where 2M+1 discrete Rayleigh frequencies are used in the averaging ($f_m = f_c + m/T$) and $a(f_m)$ is a weighting function. Typical weighting functions are the boxcar, triangle, and Hamming functions. The weights are normalized such that $\sum a_m = 1$ to prevent biasing the estimate. Again, this estimate of $S_{jk}(f_c)$ assumes that the cross-spectral values at each frequency within the averaging bandwidth are independent and identically normally distributed.

Multiple Taper Method

An alternative to the above frequency averaging is the method of Thomson (1982), which employs the use of multiple data tapers. As described in Appendix A, these tapers $v_l(t_n;T,W)$; $l=1,\ldots,L$ are designed to minimize spectral leakage outside a chosen frequency band and are used to construct eigenspectra $u_{jl}(f)$. If the local variations in the spectrum are not too extreme, the eigenspectra will be nearly uncorrelated and the estimate of the cross-spectrum can be constructed from an ensemble average at a single frequency, rather than over a bandwidth as before:

$$S_{jk}(f) = \sum_{l=1}^{L} a_l\, u_{jl}(f)\, u_{kl}(f)^*. \tag{C.4}$$

The coherence is then given as before in (C.1). Here the weights a_l are a function of taper order number rather than frequency in (C.3). The cross-spectrum estimated in this way was used by Thomson (1982) in synthetic coherency calculations, and later by Park *etal.*, (1987) in a polarization analysis of seismic data. Because the conerence is essentially a correlation coefficient, if only one realization of $u_j(f)u_k(f)^*$ is used in the averaging for $S_{jk}(f)$ the correlation will be perfect and $|\gamma_{jk}|$ will always equal 1. Therefore, to obtain meaningful results we must have M significantly greater than 0 in (C.3) and L significantly greater than 1

in (C.4).

Notice that in (C.4) frequency dependent weights have not been applied to the eigenspectra as they were in the multi-taper estimate of the amplitude spectrum described in Appendix A. This is because the low weighting which would be applied to the higher order tapers is effectively equivalent to decreasing L in (C.4). This would result in a high-variance estimate of $|\gamma_{jk}|$, biased towards a value of one. However, without weighting, spectral leakage of higher order tapers can be significant. We can reduce this effect by using fewer higher-order tapers in (C.4). If instead of considering the first 3, 5, and 7 of the 2π , 3π, and 4π tapers, respectively, as we did in the spectral amplitude estimate, and instead consider the first 1, 3, and 5 tapers, the maximum amount of leakage from any taper will be reduced to below 1% (see Table 1 in Appendix A). In doing so, we have reduced the bias from spectral leakage, but now we may be in danger of unacceptably large variance due to the smaller number of tapers used. To further quantify this, and to compare the frequency averaging and multi-taper coherence estimation methods, we now look at the statistics of the estimates.

Coherence Statistics

The statistics of coherence are quite complicated. It is not normally distributed and does not have a constant variance, i.e., the variance of $|\gamma_{jk}|$ depends on the value of $|\gamma_{jk}|$. This makes least squares fitting of coherence data non-trivial. However, under a $\tanh^{-1}$ variance stabilizing transformation, $|\gamma_{jk}|$ can be transformed to a variable which is normally distributed and has a constant variance (Enochson and Goodman, 1965), thus making it more suitable to least squares procedures (e.g. Abrahamson, 1988).

Let $|\hat{\gamma}_{jk}|$ denote the true coherence. If the value of $|\gamma_{jk}|$ is not too small and, again, assuming that the Fourier coefficients in (C.3) or (C.4) are independent and normally distributed, then the distribution of $\tanh^{-1}|\gamma_{jk}|$ is approximately normal with mean and variance given by

$$E\left[\tanh^{-1}|\gamma_{jk}|\right] = \tanh^{-1}|\hat{\gamma}_{jk}| + \frac{g^2}{2(1-g^2)} \tag{C.5}$$

and

$$\mathrm{var}\left[\tanh^{-1}|\gamma_{jk}|\right] = \frac{g^2}{2} \tag{C.6}$$

(Brillinger,1981; Bloomfield,1976). The quantity g^2 is given by Bloomfield (1976) to approximate the statistical effect of the data taper $v(t_n)$ and frequency averaging, where

$$g^2 = N\frac{\sum_{n=1}^{N} v(t_n)^4}{\left[\sum_{n=1}^{N} v(t_n)^2\right]^2} \sum_{m=-M}^{M} a_m^2. \tag{C.7}$$

Analogously, with multi-taper ensemble averaging, one can show that

$$g^2 = N \sum_{l=1}^{L} \frac{\sum_{n=1}^{N} v_l(t_n)^4}{\left[\sum_{n=1}^{N} v_l(t_n)^2\right]^2} a_l^2. \tag{C.8}$$

In general, a taper which downweights the time series more will have a larger g^2 factor and therefore produce a larger bias $g^2/2(1-g^2)$ and variance $g^2/2$. However, at the same time, such a taper typically results in relatively less spectral leakage. Such is the case, for example, in contrasting the 20% cosine taper with the lower order multiple tapers (refer to Figures A1 and A2 in Appendix A). Therefore, we should expect the multi-tapers to produce somewhat greater bias and variance as defined in (C.5) and (C.6). Keep in mind, however, the significant reduction in bias due to spectral leakage for the multi-tapers, not accounted for in (C.5) and (C.6).

In regard to frequency averaging, by increasing the value of M in (C.7), i.e., the number of frequencies over which S_{jk} is averaged, one gains a decrease in the above bias (C.5) and variance (C.6). However, in doing so, resolution is lost as the averaging bandwidth increases with increasing M. Additionally, increasing M increases the bias which will result when the spectra are not identically distributed over the averaging bandwidth. Concentrating the frequency averaging weights towards the center frequency, such as with a Hamming or triangle

function, will reduce this bias but at the same time will tend to increase the bias in (C.5).

The multi-taper estimate in (C.4), in addition to its resistance to spectral leakage, has the added advantage of not losing resolution or gaining additional bias from frequency averaging. However, as mentioned above, the ensemble average over only L tapers may produce unacceptable variance, where we have now reduced L to 1, 3, and 5 for the 2π, 3π, and 4π estimates, respectively. To reduce the variance, one can supplement the multi-taper ensemble average with a small amount of frequency averaging. Having multiple cross-spectral estimates at each frequency, one can still achieve relatively better resolution than that from the single-taper frequency averaging method without suffering greatly increased bias and variance.

To demonstrate this more clearly, the bias from (C.6) and the standard deviation $\sigma = g/\sqrt{2}$ from (C.7) are plotted in Figures C1 and C.2, respectively, as a functions of N_X, the number of the cross-spectra averaged in the estimate of $|\gamma_{jk}|$. For frequency averaging, $N_X = 2M+1$, where a_m is a Hamming window function and $v(t_n)$ is a 20% cosine data taper. For the multi-tapers, a boxcar weighting function is used, $a_l = 1/L$. The multi-taper curves begin as a function of increasing taper order up to $N_X = L$. This taper sequence is then continuously repeated to demonstrate the effect of including frequency averaging over additional frequencies to either side of a center frequency. For example, $N_X = 5$ on the 3π curve indicates that in addition to the $L_{3\pi} = 3$ tapers used at the center frequency f_c, the lowest order 3π taper was also used on the two adjacent frequencies, $f = f_c \pm 1/T$. Similarly, $N_X = 9$ implies all three 3π tapers used on the two adjacent frequencies.

Below about $N_X = 5$, the bias and variance are exceedingly large for each of the four methods. Beyond about $N_X = 5$, the tapers which downweight the time series relatively less, such as the 20% cosine and the 2π tapers, do produce the lowest bias and variance as expected, however the differences between the four methods are not great. The principal differences here lie in the resolution of the estimates. Consider an example where one decides that acceptable values of the bias and σ occur near $N_X = 15$ (all four estimates give about the same values here). To achieve $N_X = 15$, the 20% cosine single-taper estimate would require

averaging over the seven adjacent Rayleigh frequencies to either side of the center frequency. With its 2/T spectral resolution width, where T is the record length, this results in a coherence estimate averaged, primarily, over a total of 16/T Hz. The 2π estimate, with $L_{2\pi} = 1$ and having a greater 4/T resolution width, will average over 18/T Hz. However, the 3π and 4π estimates, with $L_{3\pi} = 3$ and $L_{4\pi} = 5$, and having resolution widths of 6/T and 8/T, respectively, will both average over a total of only 10/T Hz. Thus we see that, in addition to their resistance to spectral leakage, the 3π and 4π coherence estimates will produce essentially the same statistics, as defined by (C.5) and (C.6), as the 20% cosine single-taper estimate but with significant improvement in spectral resolution, 10/T Hz as opposed to 16/T Hz for $N_X = 15$. Also, with this better resolution, the estimates are not as susceptible to bias due statistical variations in cross-spectra over wide averaging bandwidths.

The other important statistic is the null distribution of coherence. This is the value of coherence above which one can be 100p% confident that the estimate was not produced from random noise. The 100p % confidence point of the null distribution of $|\gamma_{jk}|^2$ can be approximated by

$$\rho^2(p) = 1 - (1-p)^{g^2/(1-g^2)} \tag{C.9}$$

(Bloomfield, 1976). The 50% and 90% confidence levels for both $\tanh^{-1}|\gamma|$ and $|\gamma|$ are shown in Figure C3 as functions of N_X for the taper and frequency-averaging parameters described above. These curves, like those in Figures C1 and C2, can be used to determine how much frequency averaging is required for acceptable statistics for the four different estimation procedures. Here again, the 20% cosine frequency-averaged estimate produces somewhat more optimum statistics, in this case lower values for the null distribution. However, as before, the differences here are not terribly great and, as discussed above, the multi-taper method offers significant advantages in resolution and decreased bias from spectral leakage, making it a more attractive estimation procedure for coherence, and cross-spectra in general, for non-stationary time series.

References Cited

Abrahamson, N. (1988), Empirical models of spatial coherency of strong ground motion, personal manuscript.

Beauchamp, K. and C. Yuen (1979), Digital Methods for Signal Analysis, George Allen & Unwin, London.

Bloomfield, P. (1976), Fourier Analysis of Time Series: An Introduction, John Wiley & Sons, New York.

Brillinger, D. R. (1981), Time Series, Data Analysis and Theory, Expanded edition, Holden-Day, San Francisco.

Enochson, L. D. and N. R. Goodman (1965), Gaussian approximations to the distribution of sample coherence, Tech. Rep. AFFDL-TR-65-57, Wright-Patterson Air Force Base.

Park, J., F. L. Vernon III, and C.R. Linberg (1987), Frequency dependent polarization analysis of high-frequency seismograms, *J. Geophys. Res.*, 92, 12664-12674.

Thomson, D.J. (1982), Spectrum estimation and harmonic analysis, *IEEE Proc.*, 70, 1055-1096.

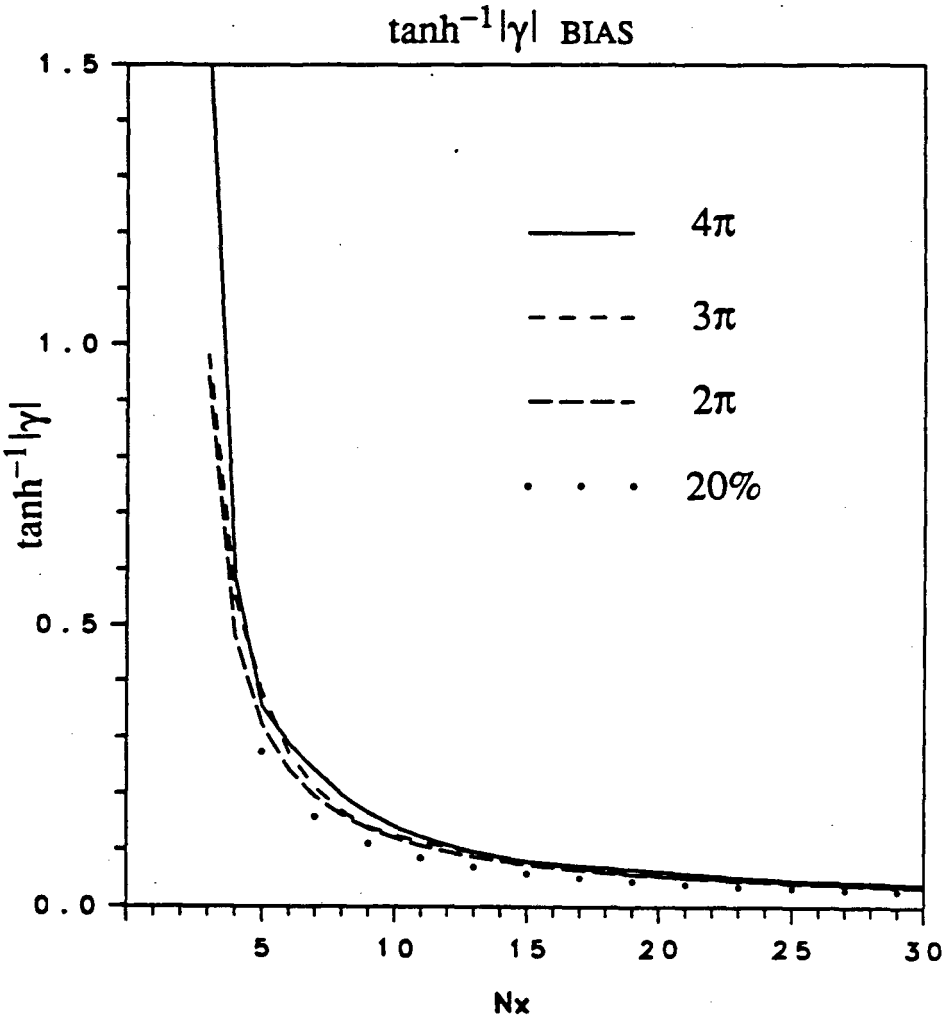

FIG. C1 Bias of $\tanh^{-1}|\gamma|$ as a function of N_X, the number of cross-spectra used in the estimate of $|\gamma|$, for each of the four estimates described in the text. This does not include the bias which will result from frequency averaging when the cross-spectra are not identically statistically distributed, nor the bias due to spectral leakage.

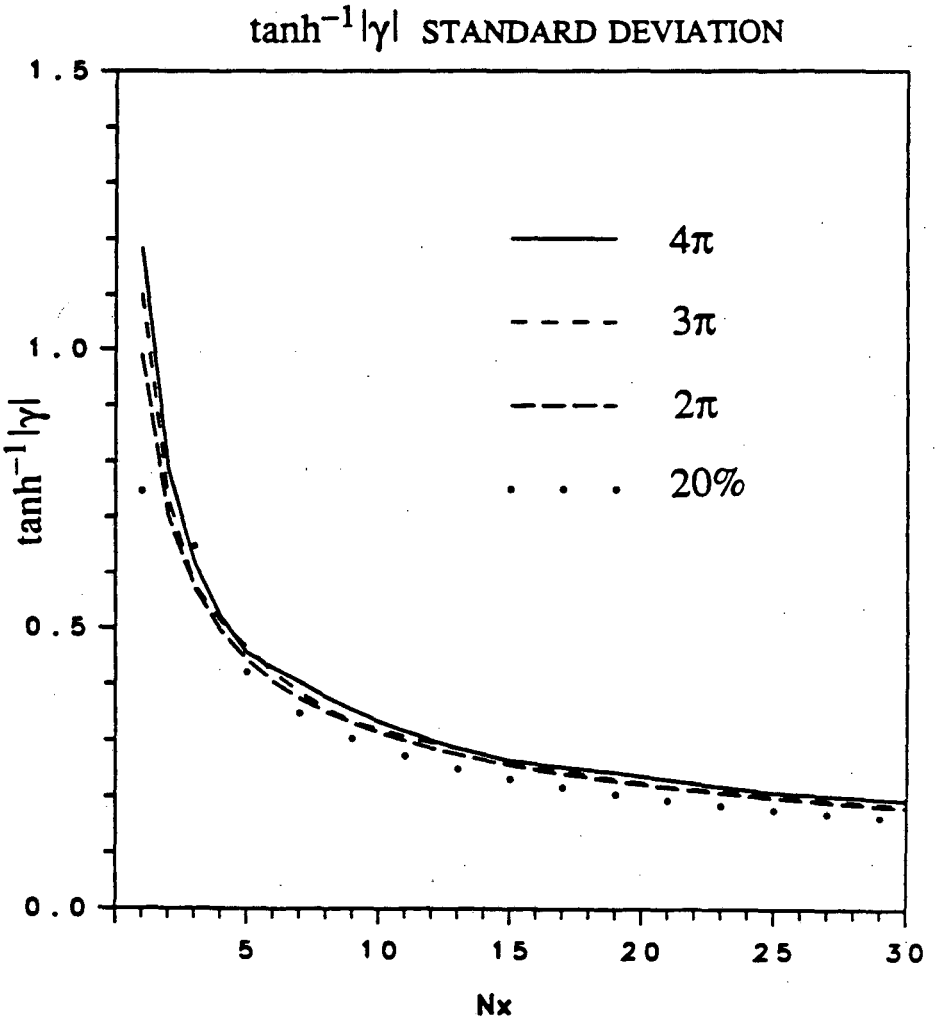

FIG. C2 Standard deviation of $\tanh^{-1}|\gamma|$ as a function of the number of cross-spectra used in each of the four estimates.

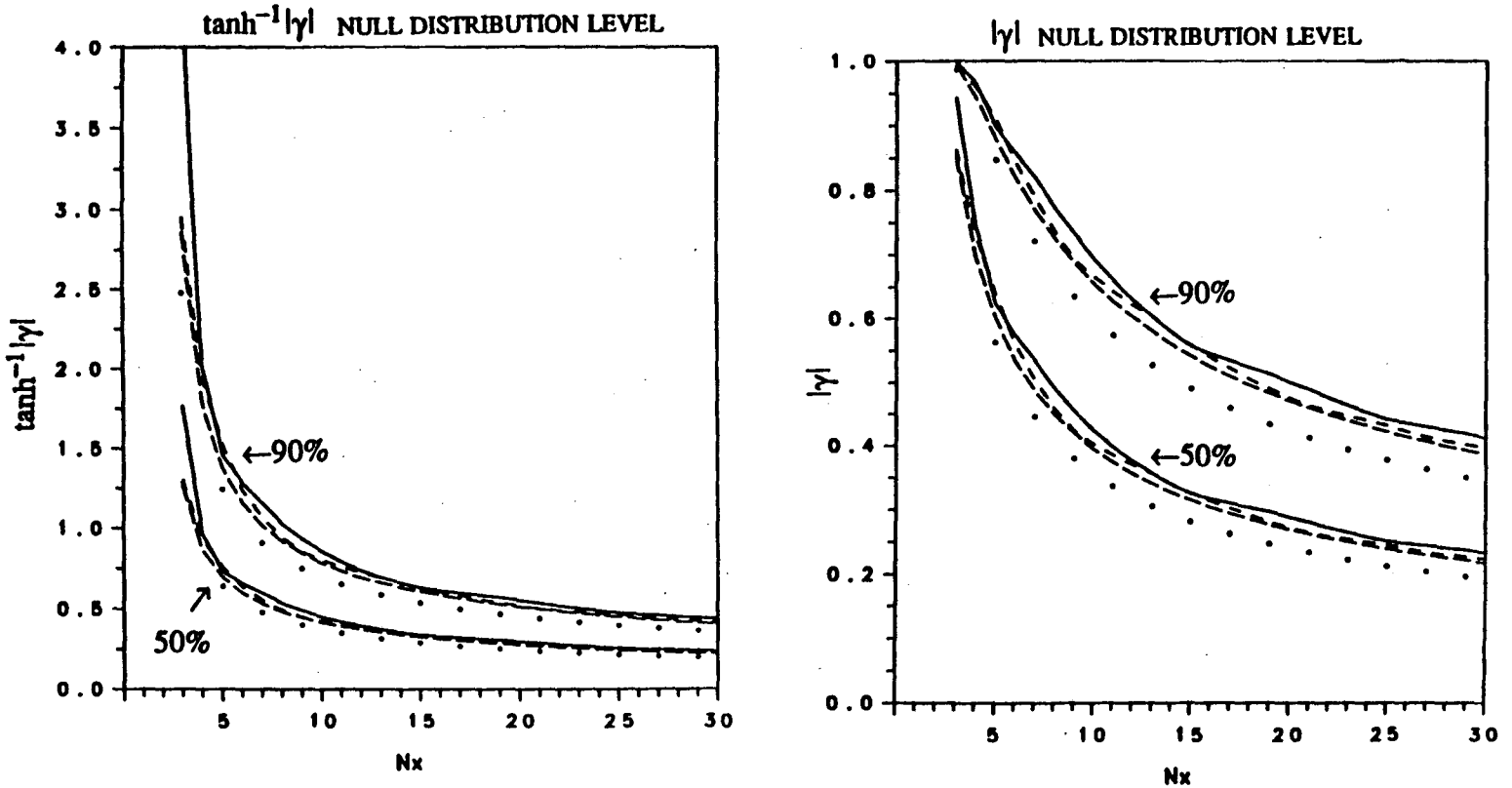

FIG. C3 (a) 50% and 90% null distribution levels for $\tanh^{-1}|\gamma|$ as a function of of the number of cross-spectra used in each of the four estimates. The curve symbols have the same meaning as in Figures C1 and C2. (b) Same as (a) but for coherence $|\gamma|$.

Appendix D

Estimates of $\tanh^{-1}|\gamma|$ Used in Chapter 5 Inversions

This appendix contains the estimates of $\tanh^{-1}|\gamma|$ used in the inversions for coherence model parameters in Chapter 5. Estimates for Pn and Pg at each array site up to 14.9 Hz are displayed. The best-fitting isotropic models are superimposed on the estimates.

Pn: Ruby Valley

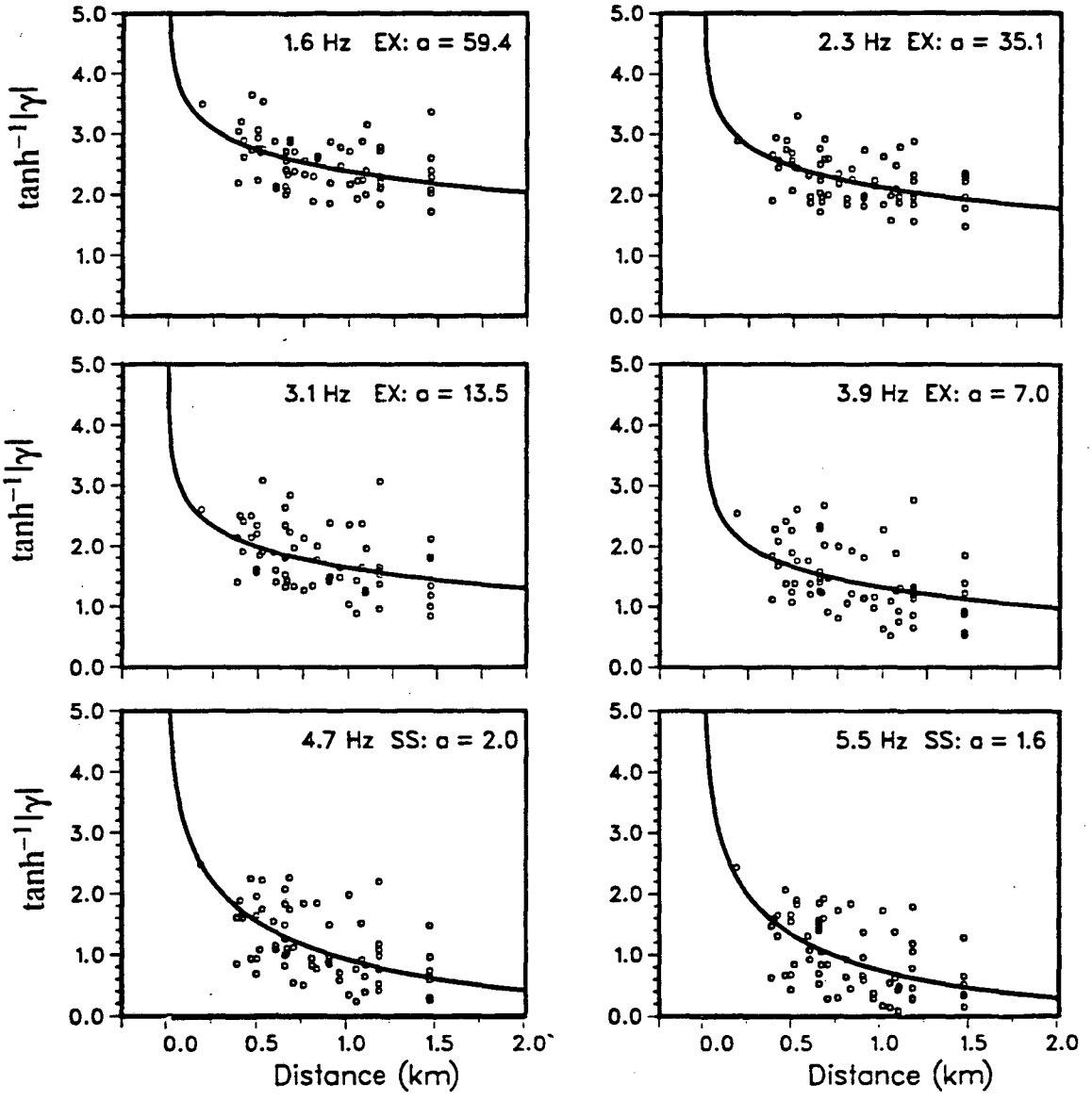

FIG. D1a

Pn: Ruby Valley

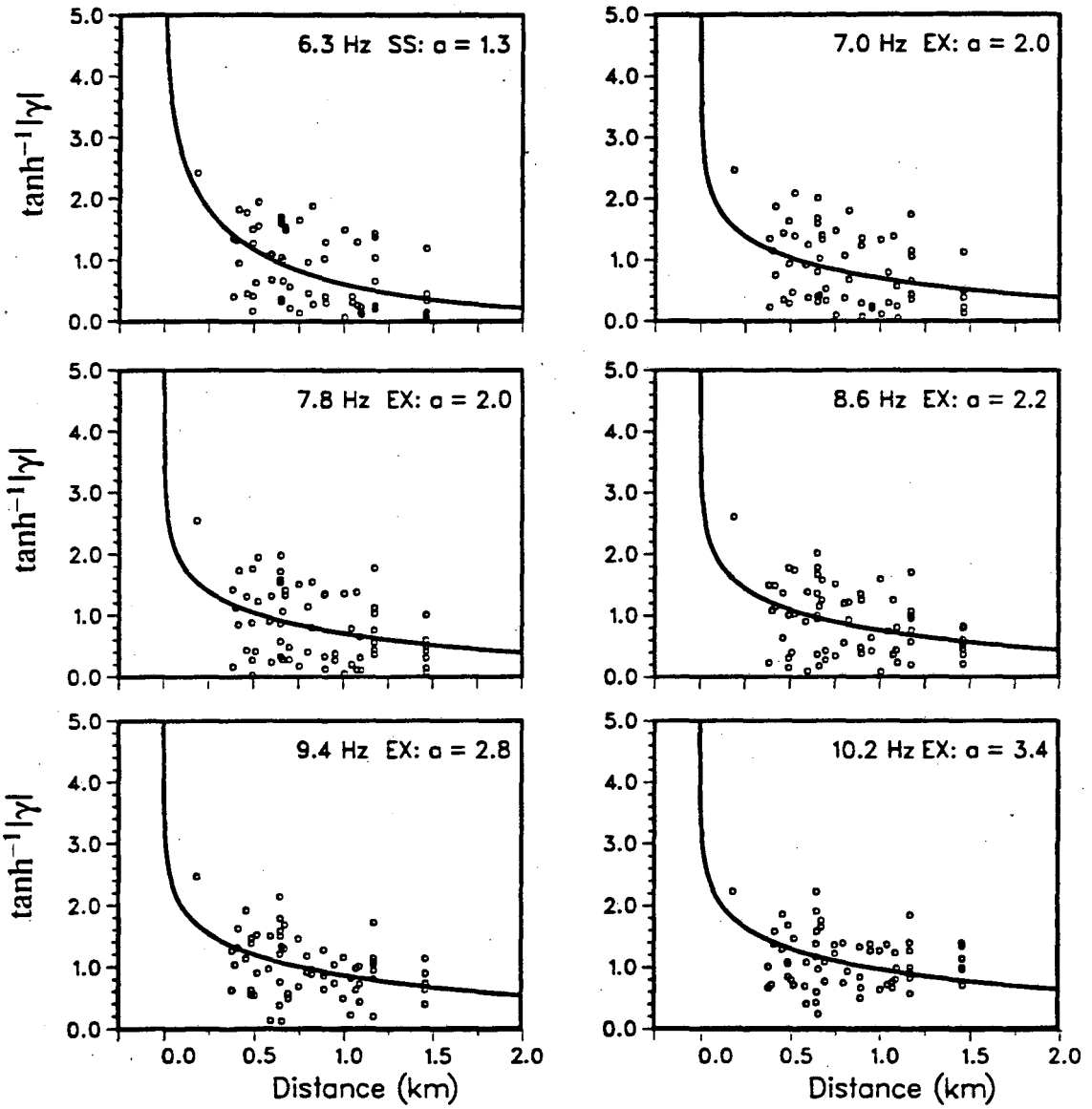

FIG. D1b

Pn: Ruby Valley

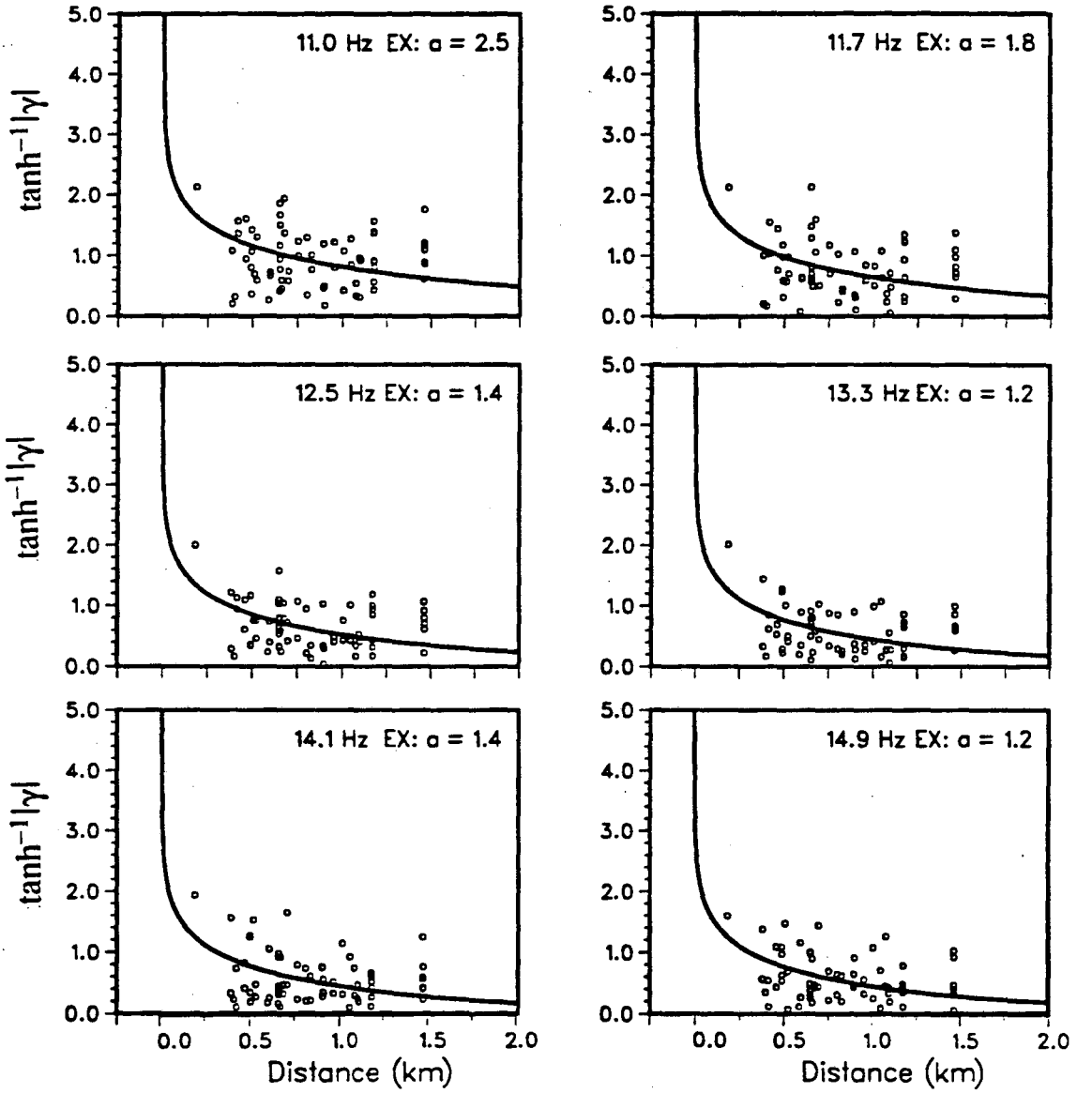

FIG. D1c

Pn: Rice Valley

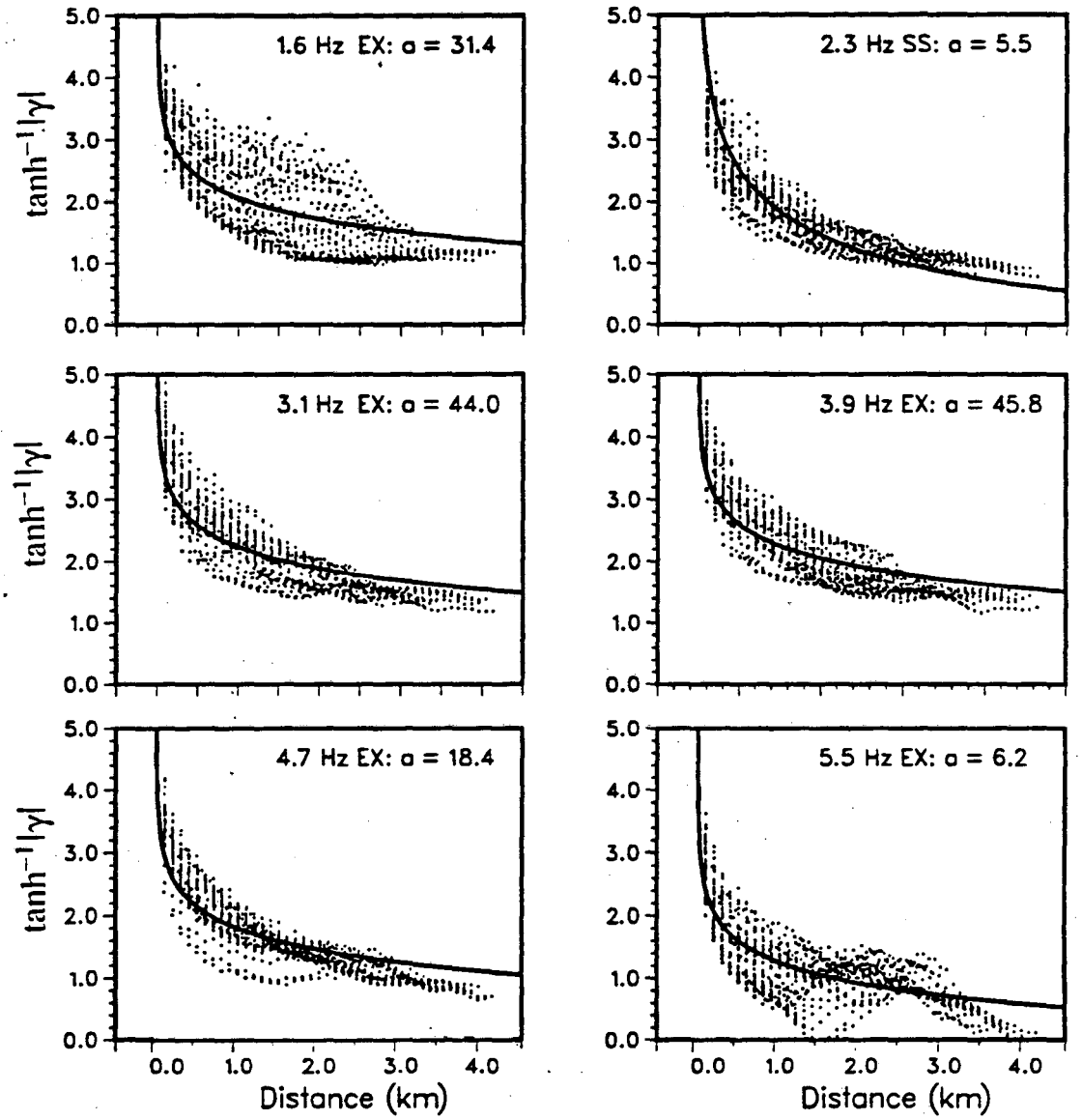

FIG. D2a

Pn: Rice Valley

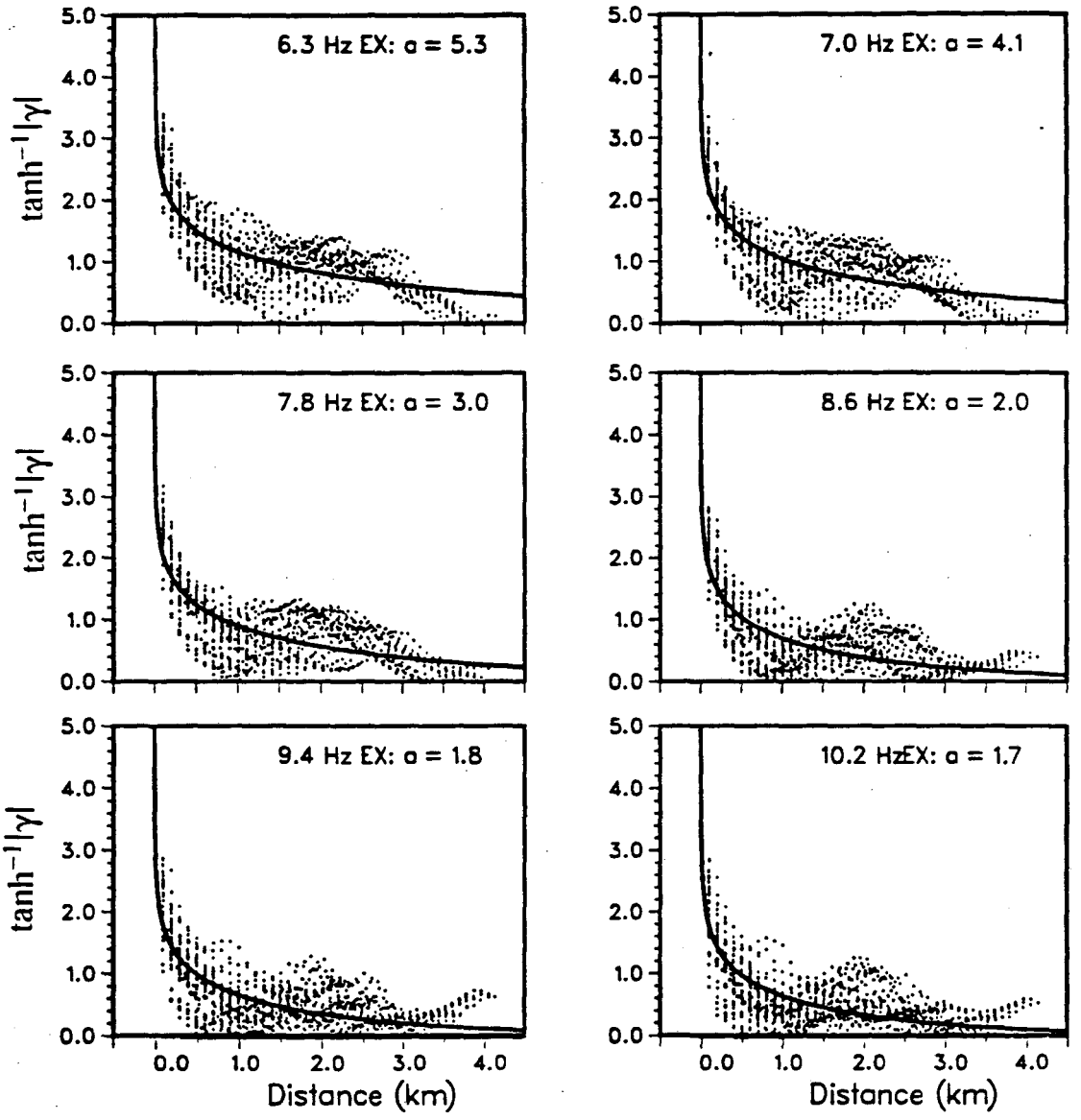

FIG. D2b

Pn: Rice Valley

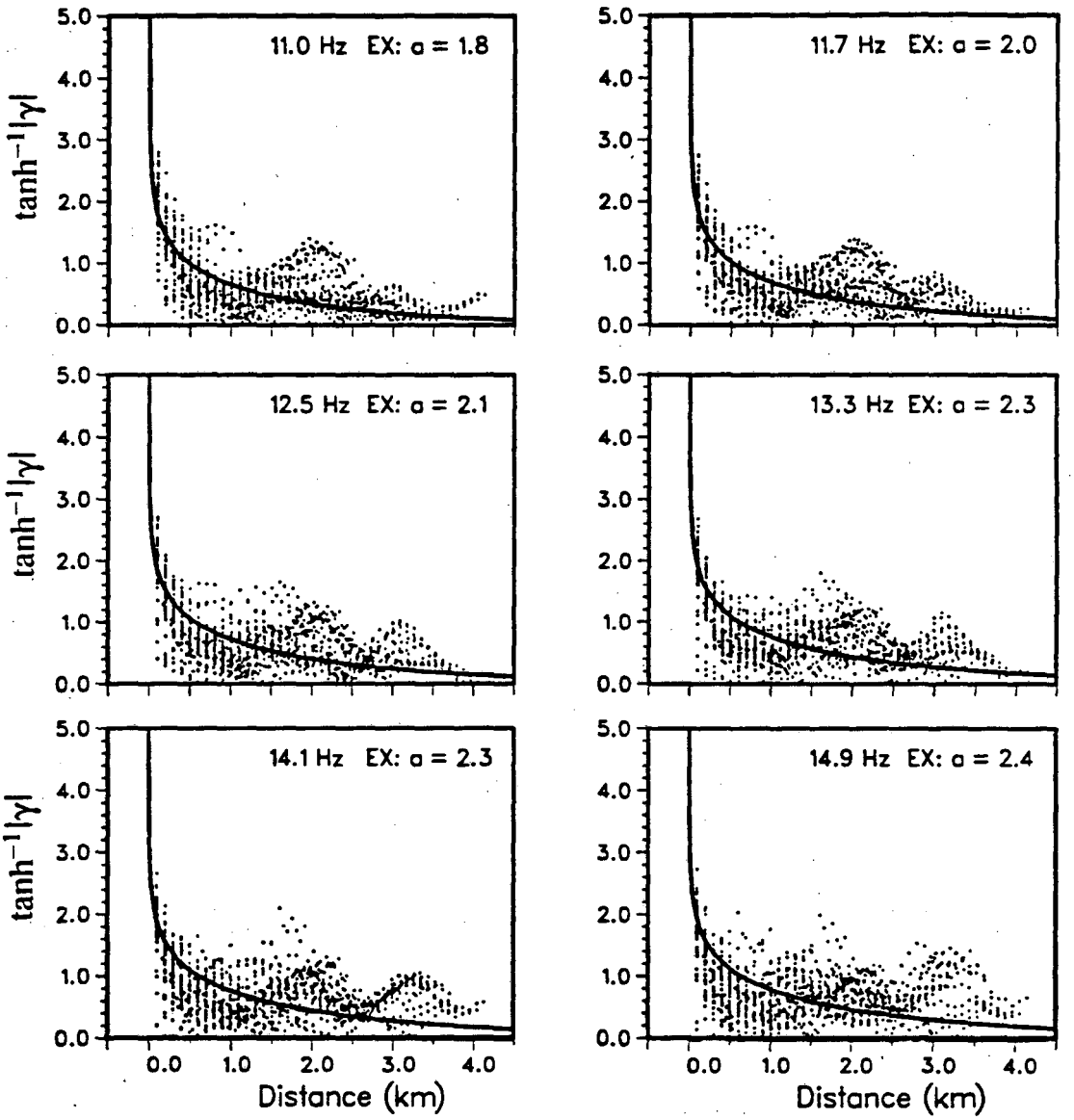

FIG. D2c

Pn: Savahia Mountain

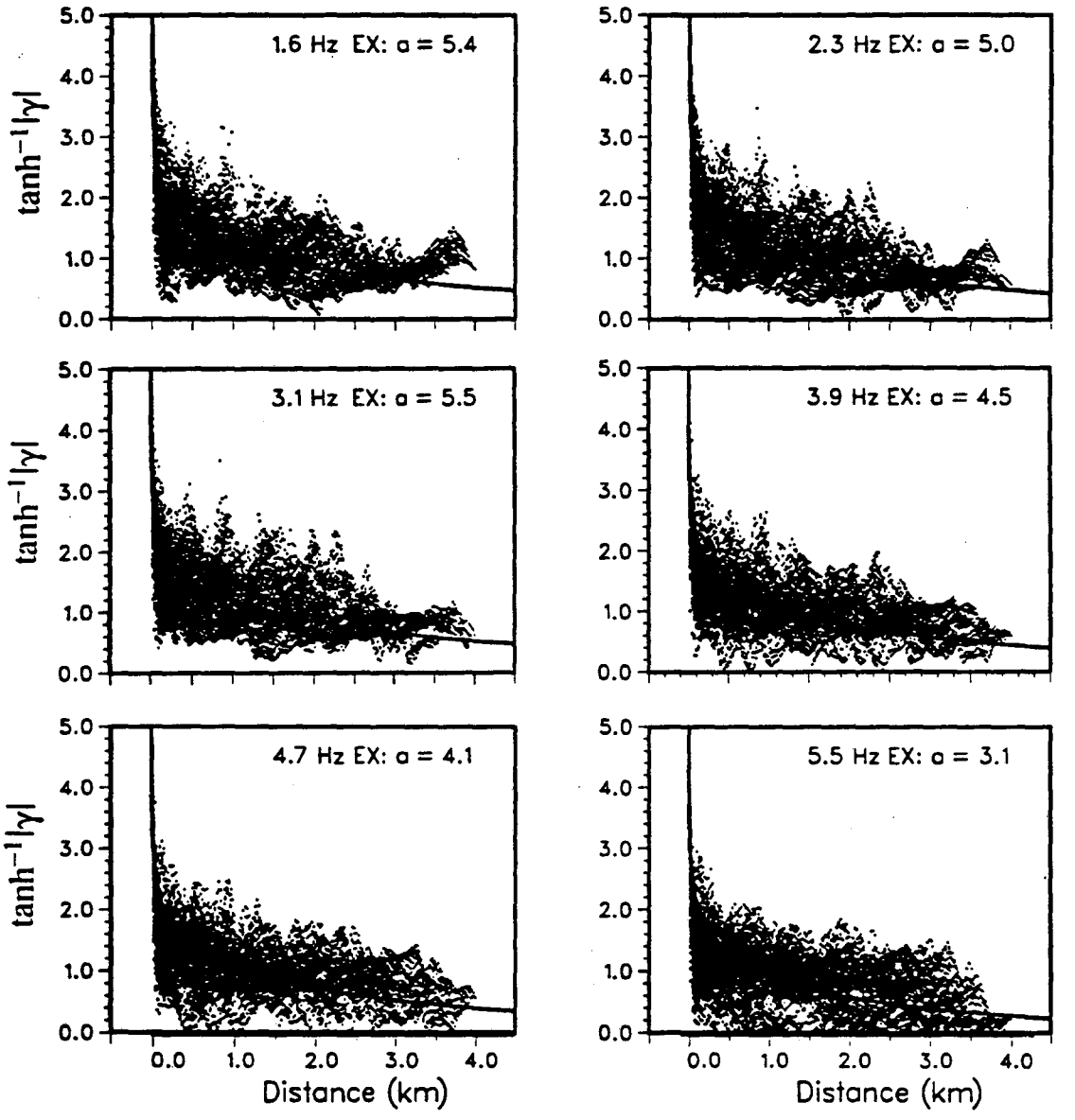

FIG. D3a

Pn: Savahia Mountain

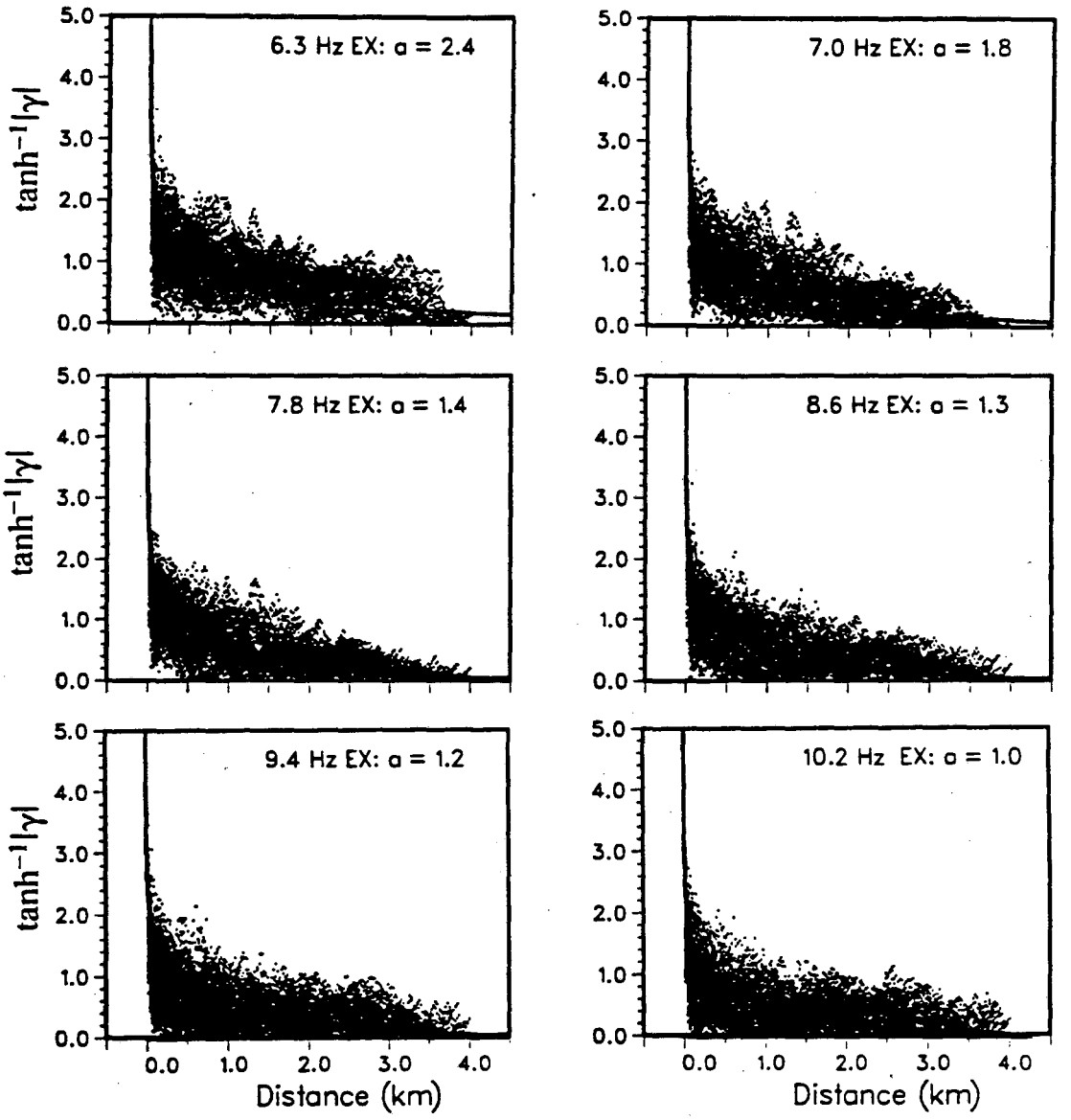

FIG. D3b

Pn: Savahia Mountain

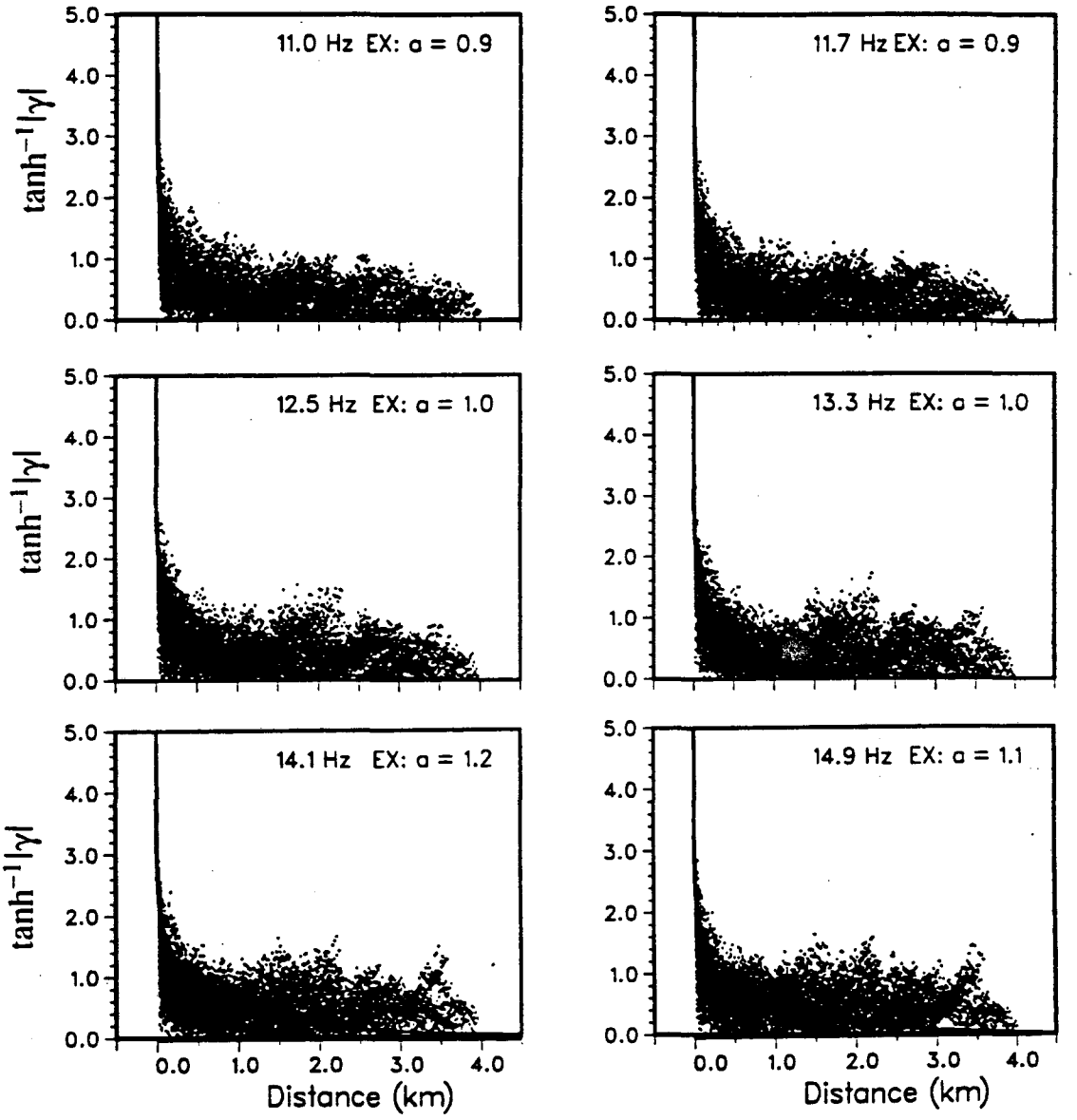

FIG. D3c

Pg: Ruby Valley

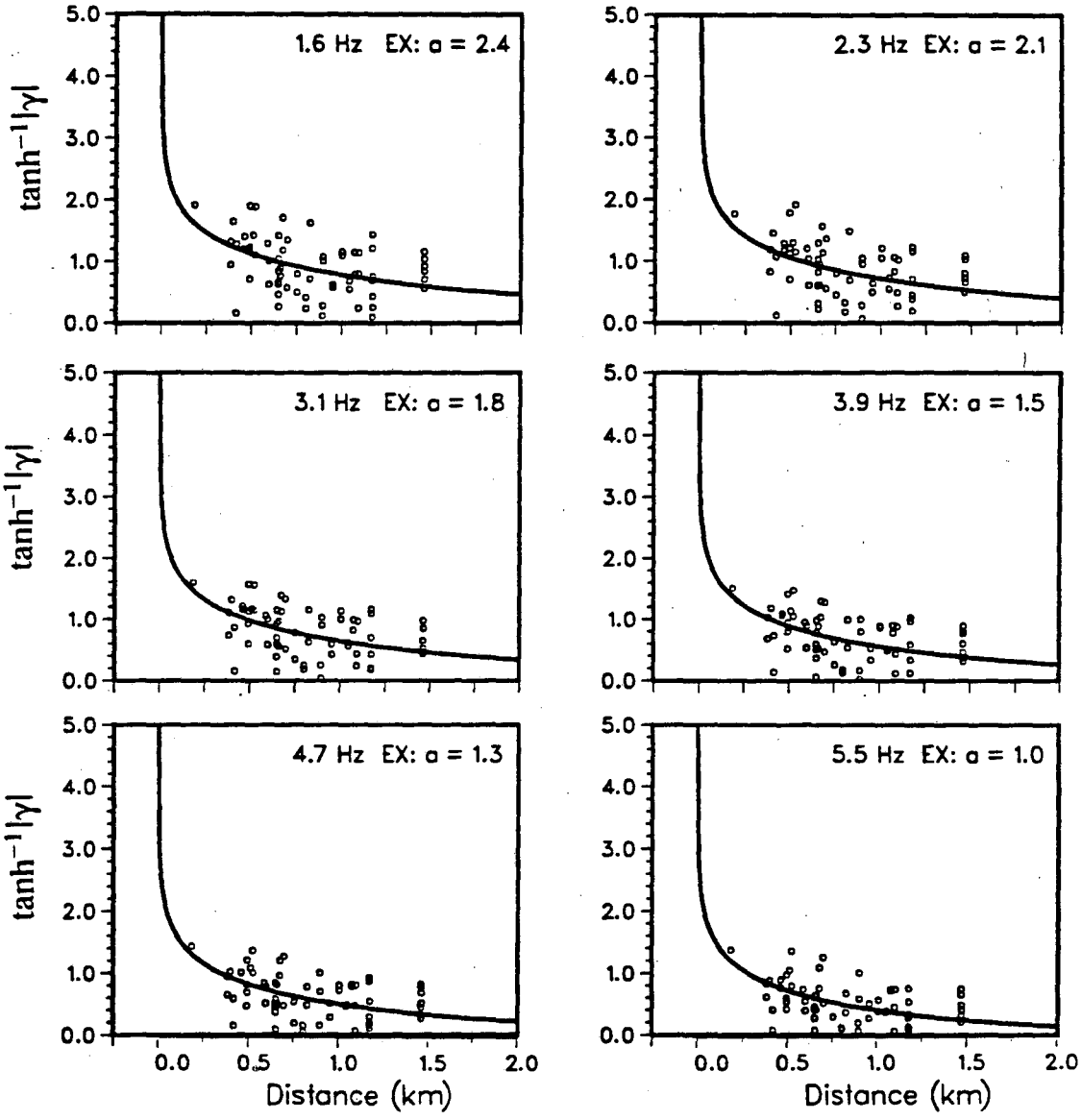

FIG. D4a

Pg: Ruby Valley

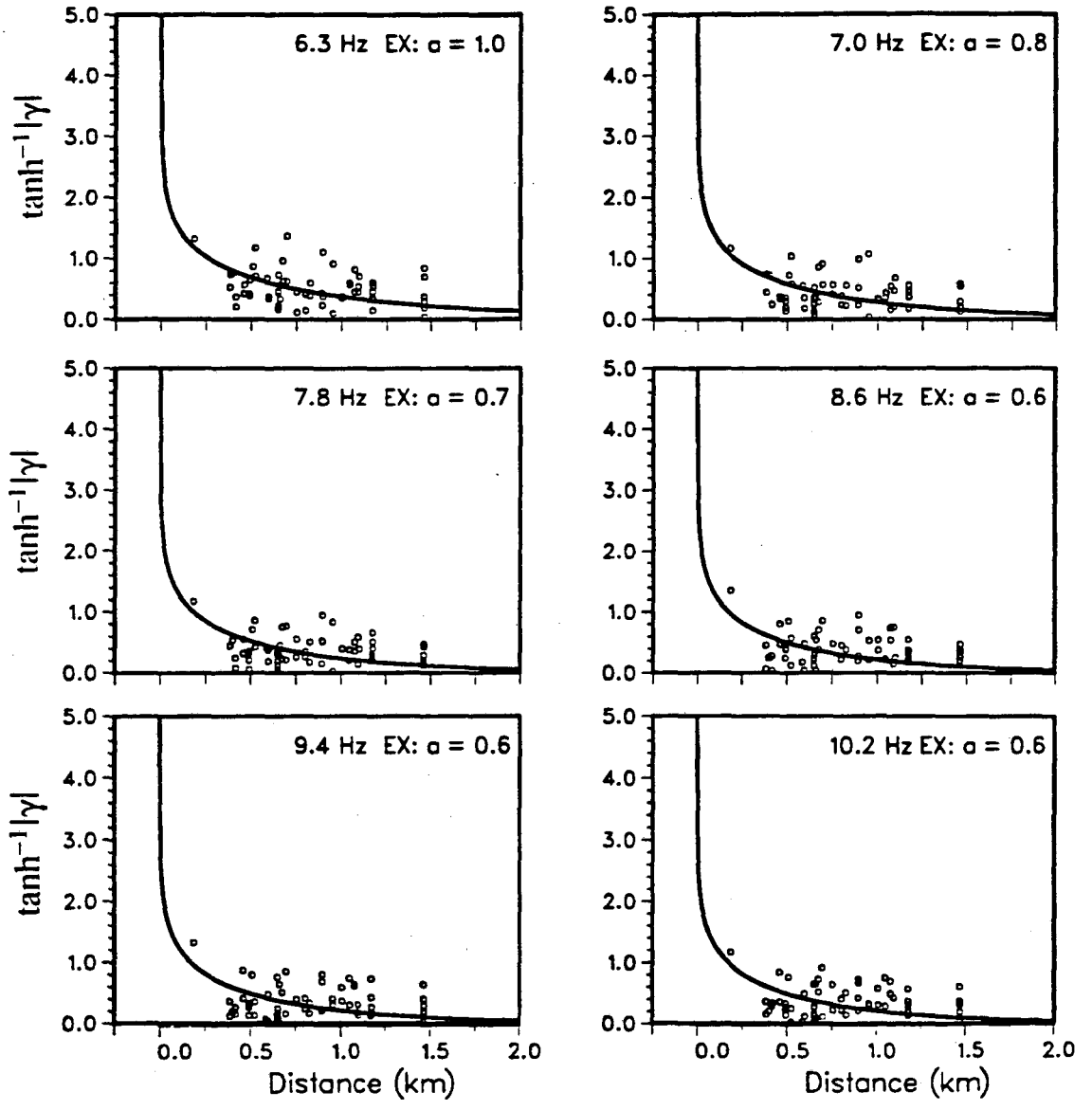

FIG. D4b

Pg: Ruby Valley

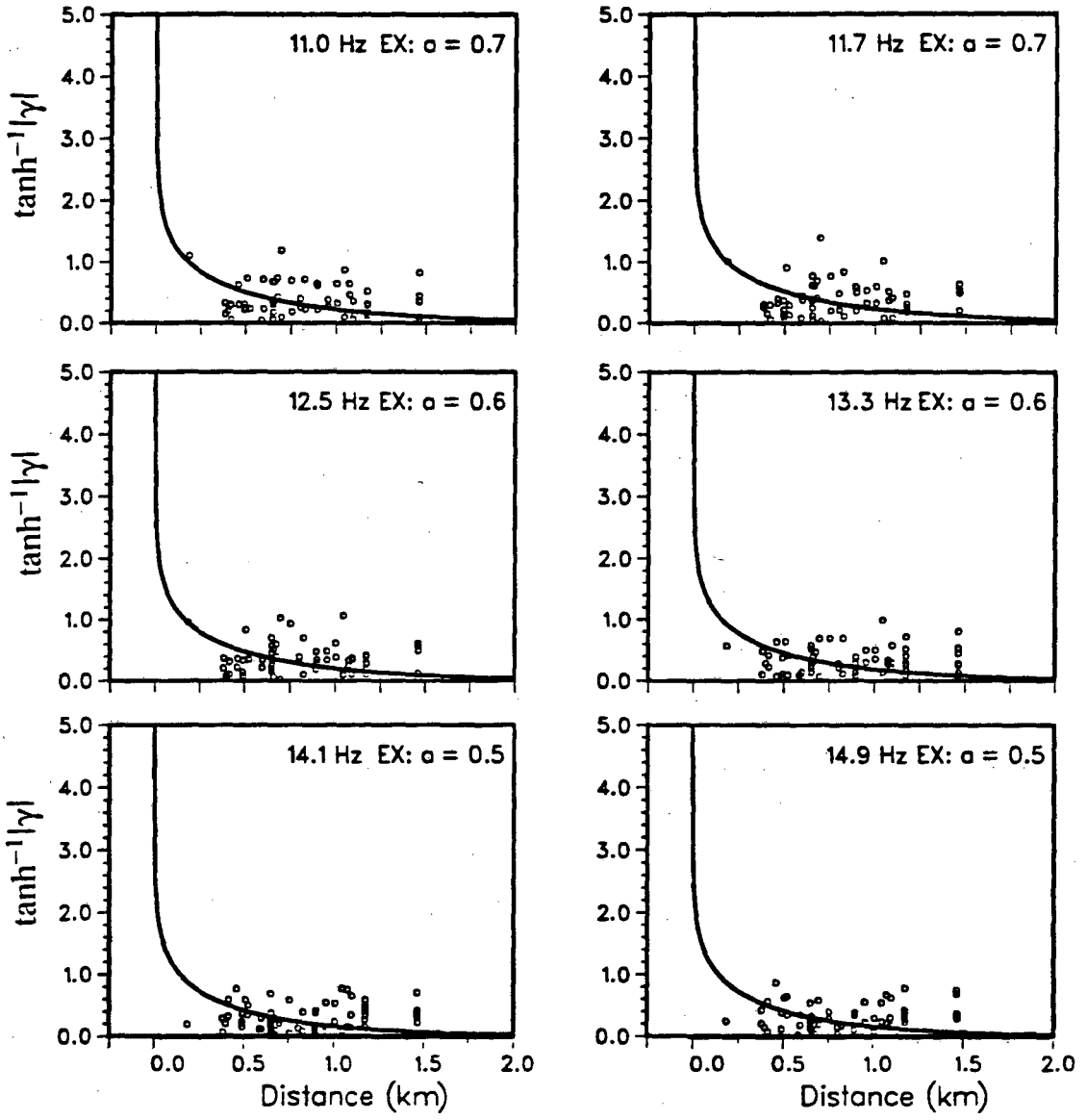

FIG. D4c

Pg: Rice Valley

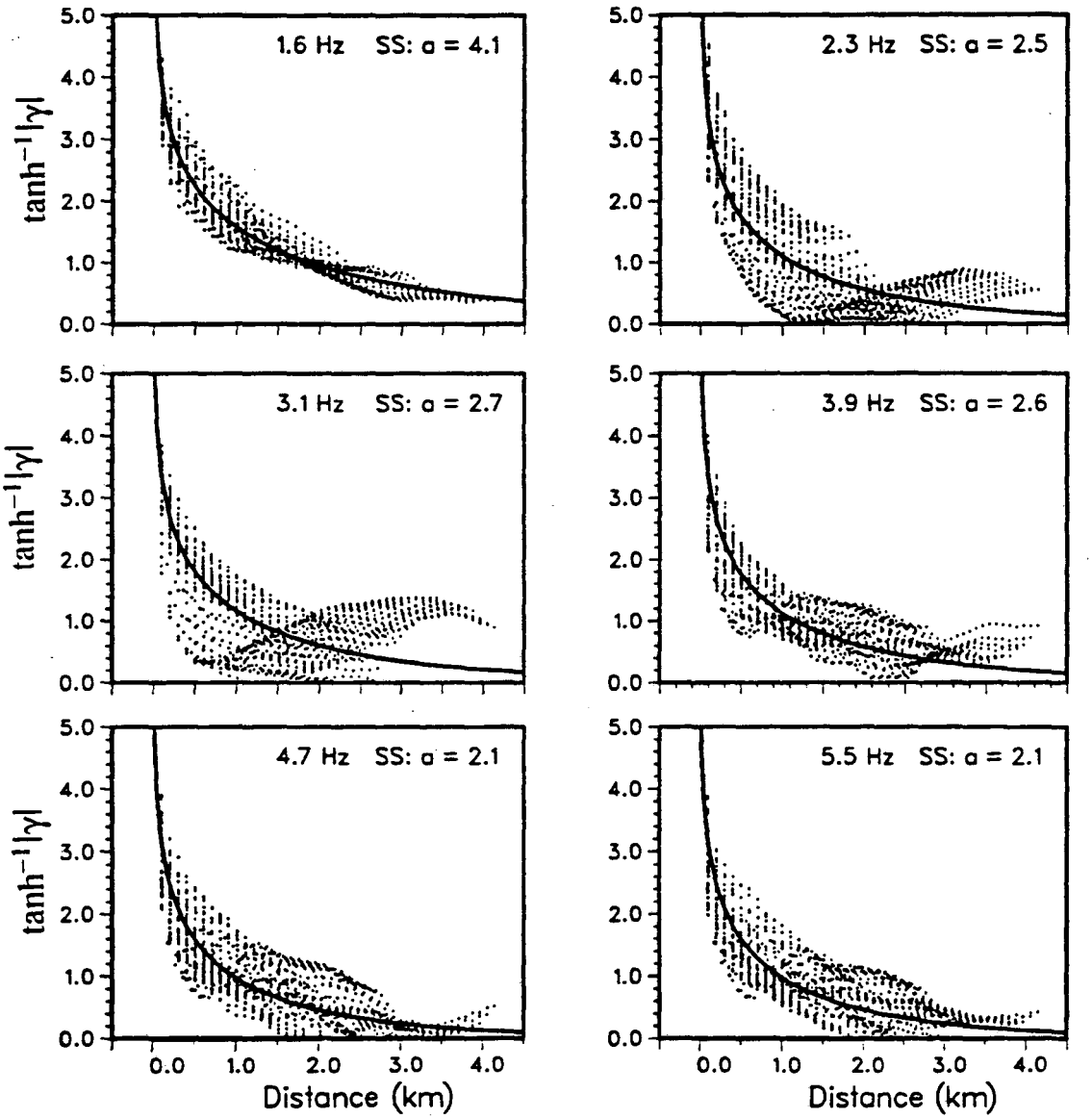

FIG. D5a

Pg: Rice Valley

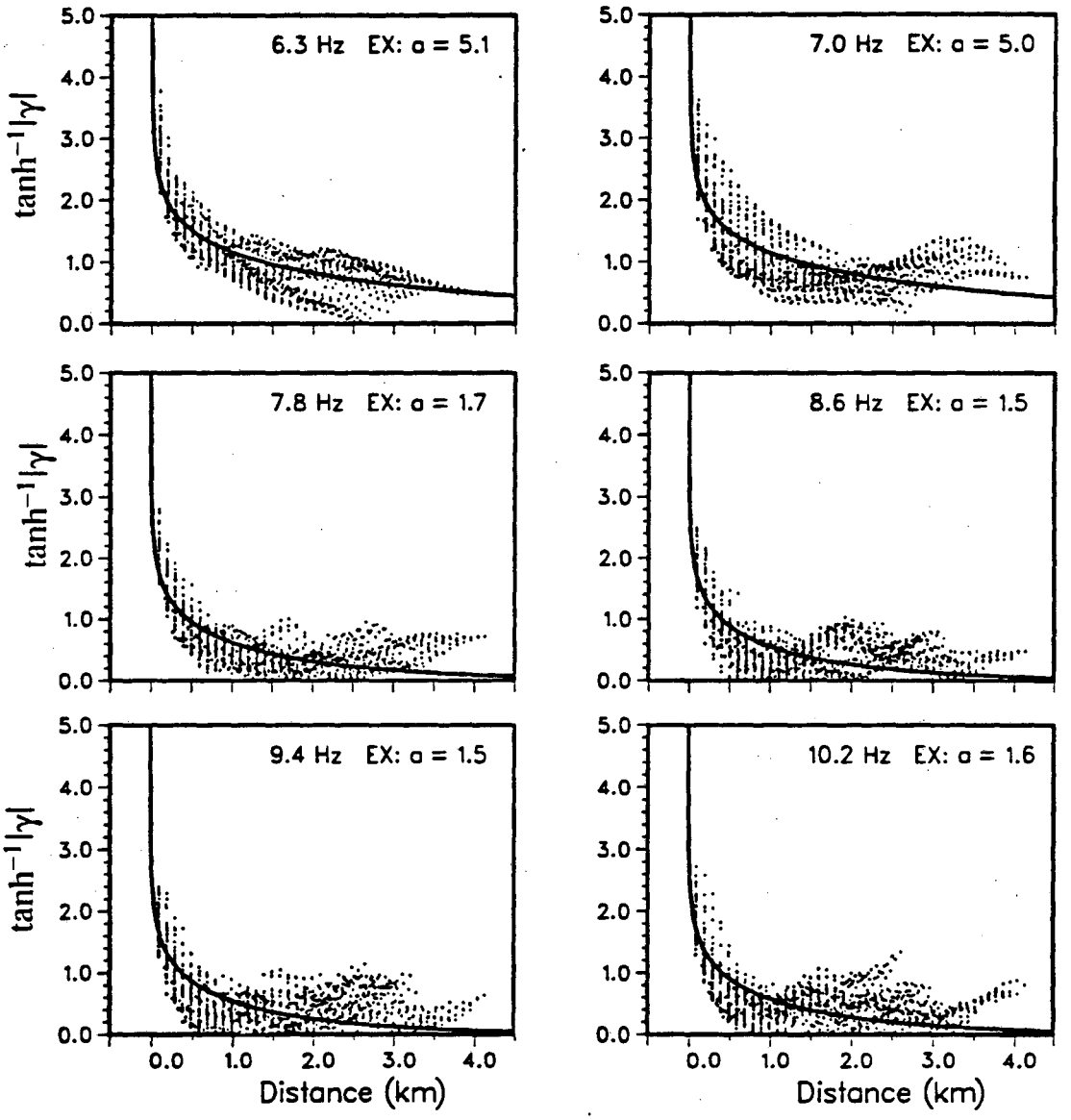

FIG. D5b

Pg: Rice Valley

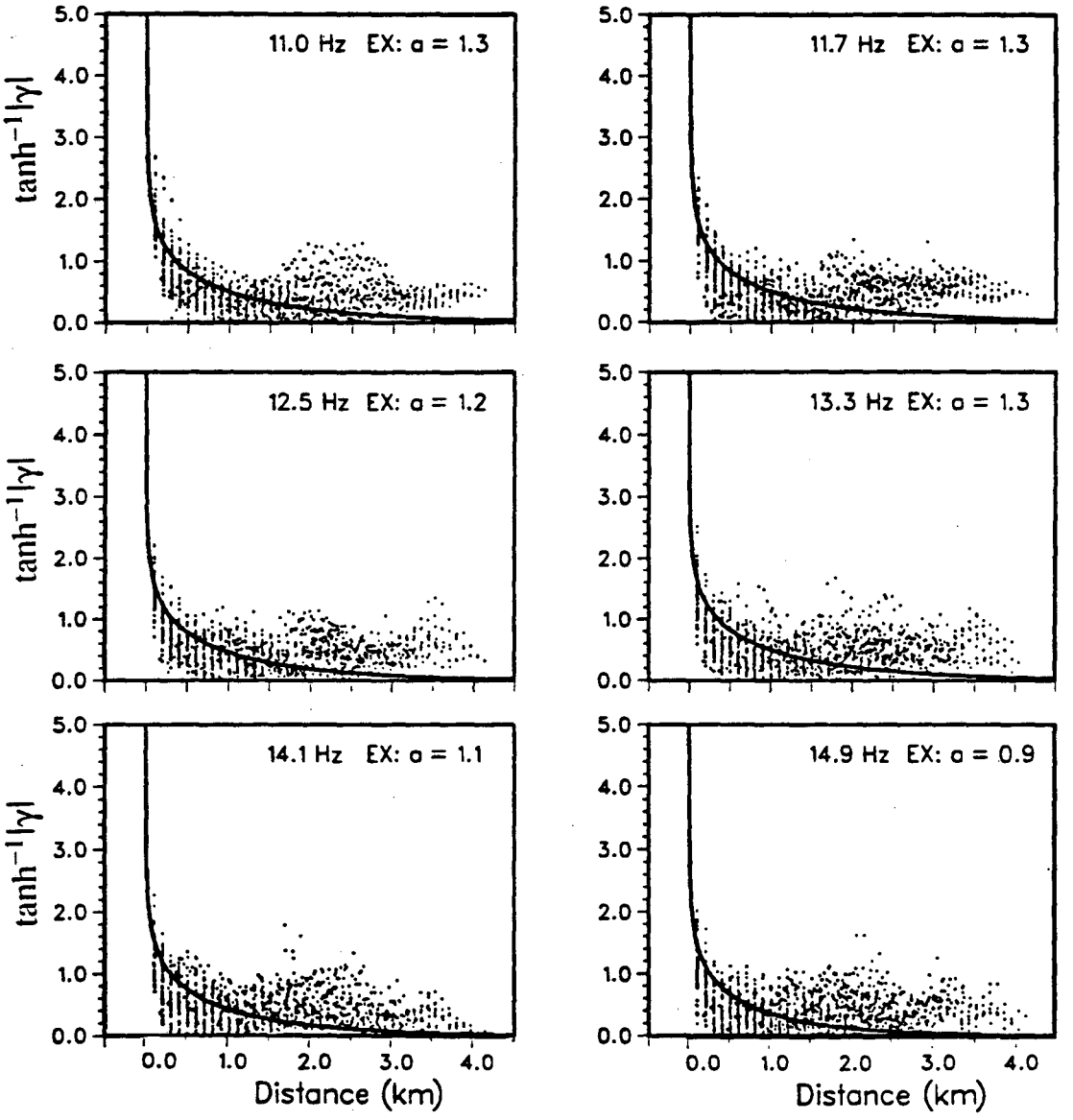

FIG. D5c

Pg: Savahia Mountain

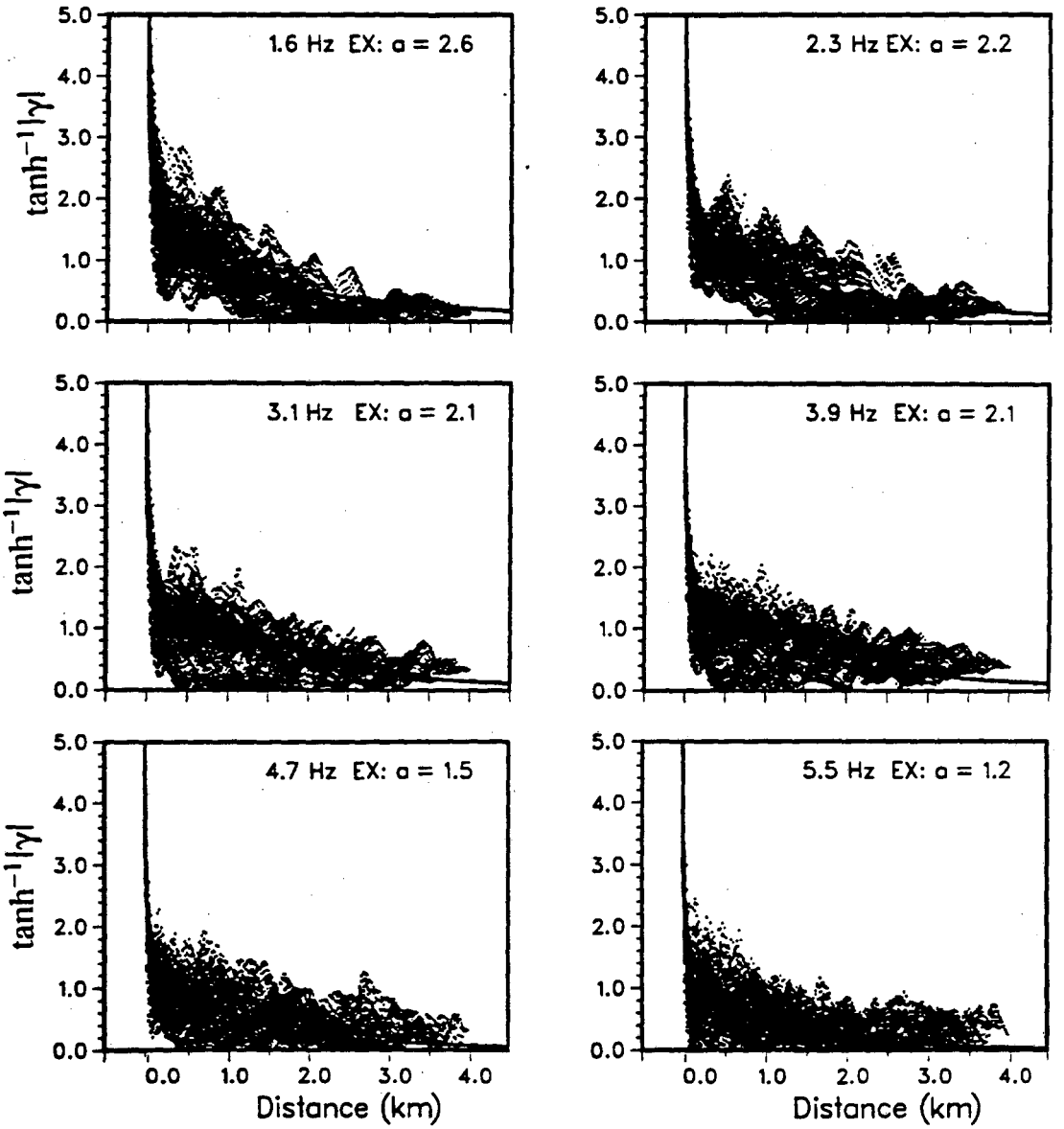

FIG. D6a

Pg: Savahia Mountain

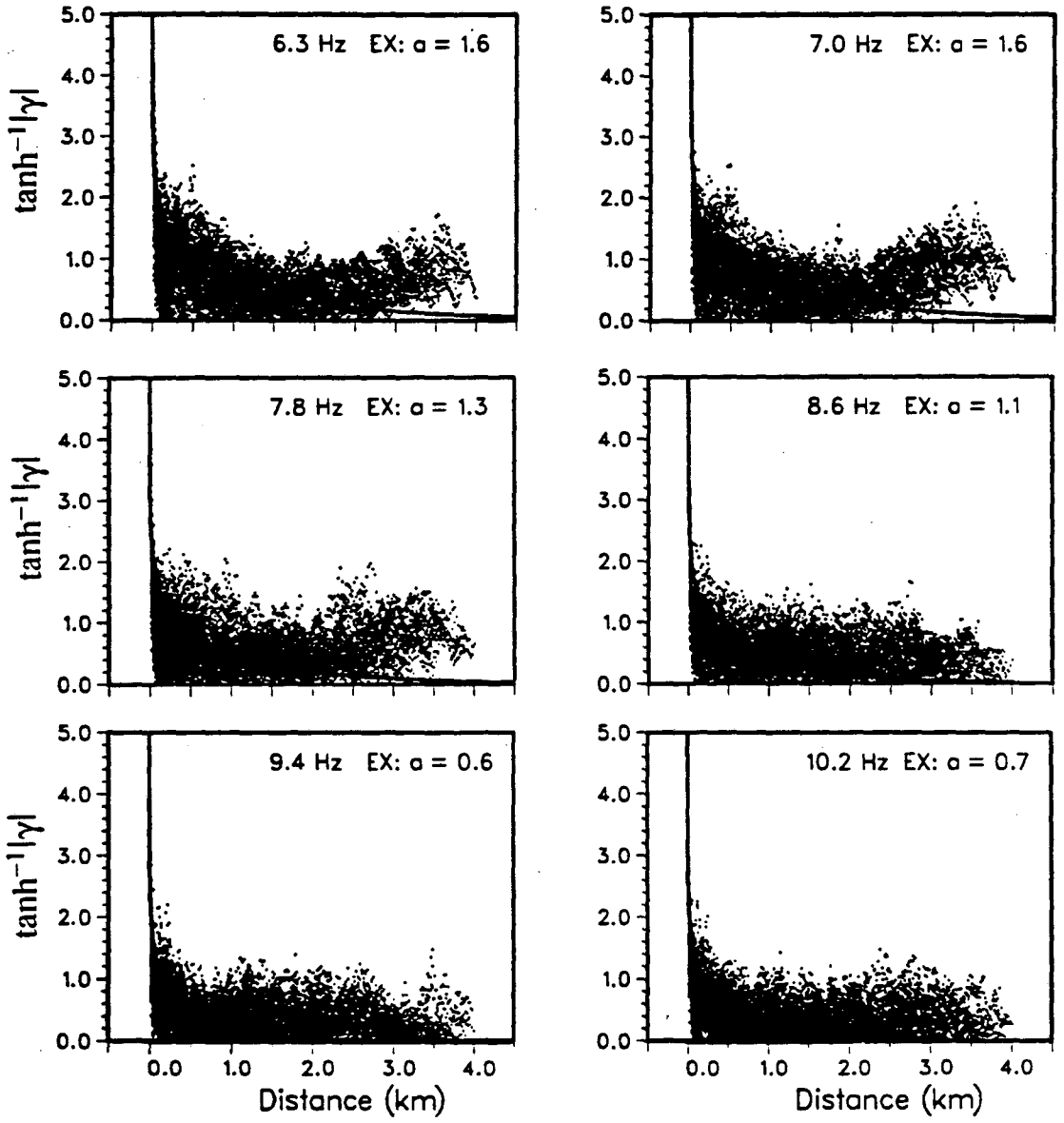

FIG. D6b

Pg: Savahia Mountain

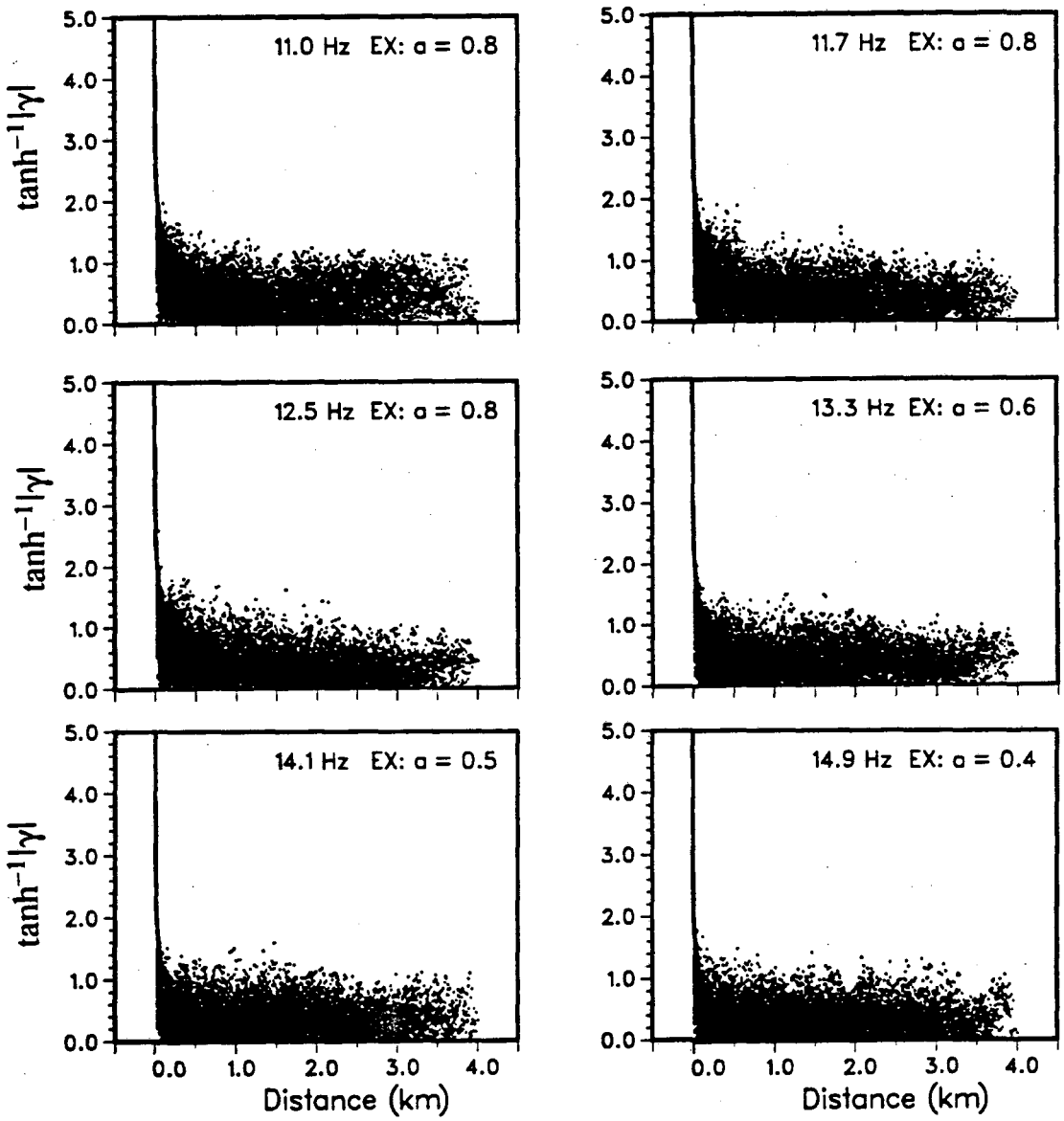

FIG. D6c

LAWRENCE BERKELEY LABORATORY
UNIVERSITY OF CALIFORNIA
INFORMATION RESOURCES DEPARTMENT
BERKELEY, CALIFORNIA 94720